Turkey

EISSN 2791-6049

TEPES

TURKISH JOURNAL OF ELECTRICAL POWER AND ENERGY SYSTEMS

VOLUME 2 • ISSUE 1 • APRIL 2022

tepesjournal.org

TEPES
TURKISH JOURNAL OF
ELECTRICAL POWER
AND ENERGY SYSTEMS

AVES

Founder
İbrahim KARA

General Manager
Ali ŞAHİN

Publishing Director
İrem SOYSAL

Editor
Gizem KAYAN TEKAÜT

Publication Coordinators
Arzu ARI
Deniz KAYA
Bahar ALBAYRAK
Gamze BİLGEN
Irmak BERBEROĞLU
Alara ERGİN
Ebru BOZ

Web Coordinator
Sinem Fehime KOZ

Finance Coordinator
Elif YILDIZ ÇELİK

Contact
Address : Büyükdere Cad. No: 105/9 Şişli, İstanbul, Turkey
Phone : +90 212 217 17 00
E-mail : info@avesyayincilik.com

TEPES
TURKISH JOURNAL OF
ELECTRICAL POWER
AND ENERGY SYSTEMS

cigre Turkey

TEPES
TURKISH JOURNAL OF
ELECTRICAL POWER
AND ENERGY SYSTEMS

AIMS AND SCOPE

Turkish Journal of Electrical Power and Energy Systems (TEPES) is an international, scientific, open access periodical published in accordance with independent, unbiased, and double-blinded peer-review principles. The journal is the official online-only publication with the support of Association of Turkish Electricity Industry (TESAB) and led by CIGRE Turkish National Committee. and it is published biannually in April and October. The publication language of the journal is English.

TEPES aims to contribute to the literature by publishing manuscripts at the highest scientific level on all fields of electrical power and energy systems. The journal publishes original research and review articles that are prepared in accordance with ethical guidelines.

The scope of the journals includes but not limited to:

1. Power Generation, Transmission and Distribution
- Conventional and renewable power generation
- Transmission systems
- Distribution Systems, automation and control
- Energy efficiency
- Electromagnetic analysis and compatibility in power systems
- HVDC and flexible AC transmission system (FACTS)
- Renewable energy technologies and system
- Transmission and distribution equipment
- Insulated cables
- Overhead lines
- Substations
- Electrical Power System Protection
- Smart-Grid
- Plasma physics and the pulsed power technology
- Information systems and telecommunication
- Electric vehicles and charging networks
- Measurement
- Power System control
- Demand Response

2. Power System Management
- Power system development and economics
- Power system operation, planning and control
- Power system environmental performance
- Power system technical performance
- Electricity markets and regulation
- Load modeling, estimation and forecast

3. High-Voltage Techniques
- Measurement systems
- Electrical materials
- Emerging test techniques
- Insulation condition and coordination in power systems
- Over-voltage, lightning protection and grounding
- Ultra-High Voltage (UHV) technologies
- Electrical installations

4. Electrical Machines
- Power electronics
- Electrical Machines and Drives
- Power transformers and reactors
- Design of Electrical Machines for Sustainable Energy Applications

TEPES is currently indexed in Gale.

The target audience of the journal includes academicians, specialists, researchers and professionals who are working and interested in the field of electrical power and energy systems.

The editorial and publication processes of the journal are shaped in accordance with the guidelines of the Institute of Electrical and Electronics Engineers (IEEE), the World Commission on the Ethics of Scientific Knowledge and Technology (COMEST), Council of Science Editors (CSE), Committee on Publication Ethics (COPE), European Association of Science Editors (EASE), and National Information Standards Organization (NISO). The journal is in conformity with the Principles of Transparency and Best Practice in Scholarly Publishing (doaj.org/bestpractice).

Processing and publication are free of charge with the journal. No fees are requested from the authors at any point throughout the evaluation and publication process. All manuscripts must be submitted via the online submission system, which is available at www.tepesjournal.org. The journal guidelines, technical information, and the required forms are available on the journal's web page.

All expenses of the journal are covered by the CIGRE Turkish National Committee. Potential advertisers should contact the Editorial Office. Advertisement images are published only upon the Editor-in-Chief's approval.

Statements or opinions expressed in the manuscripts published in the journal reflect the views of the author(s) and not the opinions of the CIGRE Turkish National Committee, editors, editorial board, and/or publisher; the editors, editorial board, and publisher disclaim any responsibility or liability for such materials.

You can find the current version of the Instructions to Authors at https://tepesjournal.org/.

Editor in Chief: Belgin EMRE TÜRKAY
Address: Department of Electrical Engineering, İstanbul Technical University (ITU) Faculty of Electrical and Electronics Engineering, İstanbul, Turkey
E-mail: info@tepesjournal.org

Publisher: AVES
Address: Büyükdere Cad., 105/9 34394 Mecidiyeköy, Şişli, İstanbul, Turkey
Phone: +90 212 217 17 00
Fax: +90 212 217 22 92
E-mail: info@avesyayincilik.com

TEPES
TURKISH JOURNAL OF
ELECTRICAL POWER
AND ENERGY SYSTEMS

CONTENTS

RESEARCH ARTICLES

REVIEW

*These papers are selected from ELECO 2021.

TEPES
TURKISH JOURNAL OF ELECTRICAL POWER AND ENERGY SYSTEMS

TEPES, Vol. 2, Issue. 1, 1-10, 2022 **DOI:** 10.5152/tepes.2021.21041

RESEARCH ARTICLE

Energy Modeling and Optimization in a Radio and Television Broadcasting Facility

Titus Oluwasuji Ajewole[1], Adedapo Olaitan Alao[2], Kabiru Alani Hassan[3], Abdulsemiu Alabi Olawuyi[4]

[1]Department of Electrical and Electrronic Engineering, Osun State University, Osogbo, Nigeria
[2]Department of Engineering, Osun State Broadcasting Corporation, Osogbo, Nigeria
[3]Department of Electrical and Electronics Engineering, Federal Polytechnic, Ede, Nigeria
[4]Department of Electrical and Electronic Engineering, Osun State Polytechnic, Iree, Nigeria

Cite this article as: T. O. Ajewole, A.O. Alao, K.A. Hassan & A. A. Olawuyi. Energy modeling and optimization in a radio and television broadcasting facility. *Turk J Electr Power Energy Syst,* 2022; 2(1): 1-10.

ABSTRACT

This paper evaluates the energy consumption pattern of the Osun State Broadcasting Corporation, Osogbo, Nigeria. Using HOMER software, installation and operating costs of a renewable energy-based hybrid power system, over a multi-year lifetime, is investigated towards deployment of the hybrid at the broadcasting facility. Information dissemination is very important in the society, and requires propagation media. Broadcasting station is an important medium of dissemination, therefore, constant and cost-effective power supply needs to be put in place. By optimizing hybrid renewable energy systems, the choice of components is controlled and thus enable cost-effective power solution with the use of different combinations of renewable energy resources. In the study, four energy resources are considered for hybridization: Solar photovoltaic (SPV), diesel engine generator (DEG), wind energy converter (WEC) and battery energy storage system (BESS). The input parameters considered in the optimization are project lifespan; capital, operating and maintenance costs; and resource specifications. From energy audit, it is obtained that the ,peak electrical demand of the corporation's facility is 361.61kW, while the peak daily intake and annual mean use are 4577.38kWh and 835011.71kWh respectively. Four different configurations of the energy sources are recommended for their advantage cost effectiveness, with SPV/DEG/BESS hybrid taking the lead as the optimum configuration.

Index Terms—Cost of energy, hybrid, net present cost, optimization, techno-economic, total capital cost, total operating cost.

I. INTRODUCTION

Energy is an important ingredient of modern life, as it is the lifeline of our everyday life. However, energy is not free. It comes at a financial price for users and at an even bigger cost to the environment [1]. Therefore, energy can be aptly described as a significant factor for socio-economic development. The essence of the energy system is to make provisions for energy services that are desirable and may used for activities such as transportation, air-conditioning, lighting, refrigerated storage, indoor climate control, industrial processes, conversion of raw materials to final products, and selection of appropriate temperatures for cooking [1]. The energy chain to power these services starts with the extraction of primary energy [2].

Furthermore, the demand for energy is rapidly increasing everyday [3]. A published report revealed that there are two possible ways to resolve the problem of the rising energy demand [4]: the first is the generation and production of additional energy, while also exploring other alternative sources of energy production; the second is an efficient and more optimal utilization of available resources. The first approach is highly capital-intensive and time-consuming, and therefore, the second approach is highly recommended due to its affordability and its efficiency; with efficient energy usage, there is no need to produce additional energy [5]. Moreover, technologies are improving and various methods have been advanced for energy use and optimization. The efficient use of energy is currently one of the major challenges, because it impacts nearly every human activity such as vacation, leisure, entertainment, sports, hospitality, academic, commercial, and industrial activities [6]. The consumption of energy in residential buildings is fast increasing, making the efficient use of energy in the real estate sector a significant challenge. Recently, energy consumption and optimization, both in business centers and official buildings, have attracted much attention from researchers [7]. Most scholars have attempted to resolve this challenge, with the majority of these attempts having been made in the

Corresponding author: Adedapo Olaitan Alao, engrdapo@gmail.com

Received: August 16, 2021
Accepted: October 13, 2021
Available online: December 29, 2021

past decade [8]. However, the challenge of efficient energy utilization and optimization still remains, because the more the usage of electronic equipment in a building, the higher the consumption of energy [9]. A majority of the available energy management systems are concerned more with the substantial amount of energy utilized in the broadcasting facility, and not much has been done on energy management in such a facility. Therefore, this research developed a model that will cover the complete energy spectrum, such as energy supply, utilization, and optimization, in a broadcasting station. The model will also be used to identify and estimate energy loss or wastage that may be hindering optimization in the system.

Energy conservation provides the cheapest way to remedy the supply and demand gap with minimal capital investment. It also helps to improve the plant load factor of electricity-generating plants that will help in reducing the price of electricity. The need to monitor and lower energy use now receives even greater attention than ever before. The use of energy conservation approaches definitely reduces the general energy consumption [4]. According to [6], global warming is now a worldwide issue and one of the major reasons is the emissions produced from greenhouse gases. Emissions will continue to rise because of industrialization and the increasing need for electricity supply.

Though many novel methods have been employed for conserving energy, they also need to take into consideration the structural design of the building, in order to work according to design. Challenges occasioned by nonlinear features in the control parameters are also one of the shortcomings of conventional control systems [4]. [10] stated that studies have shown that most of the existing energy management systems focus on energy monitoring systems rather than systems with efficient utilization and optimization functions. Therefore, a study aimed at developing a bottom–up model which will focus on the efficient utilization and optimization of energy, especially at the consumption side, is highly expedient.

II. MATERIALS AND METHODS

Considering the duration and the wattage, the daily power requirement of group of equipment was estimated, and the yearly and peak daily power consumption for each group of equipment was calculated from the estimate. For convenience, the pieces of equipment were thereafter arranged by grouping similar electrical loads together, as shown in Table I.

The following materials were used in the collection, analysis, and presentation of data and the results that will be obtained from this study:

(i) Structured questionnaires,
(ii) HOMER Pro software, and
(iii) Digital clamped meter.

A. Administration of Structured Questionnaires

Structured questionnaires will be administered to selected members of staff who work in the administrative offices, staff personal offices, workshops, libraries, and technical areas across the length and breadth of the Osun State Broadcasting Corporation, Oke Baale, Osogbo. The structured questionnaires will be administered to collect data on the quantity of energy supplied to the Osun State Broadcasting Corporation buildings.

B. Determination of Energy Consumption

The data that was obtained from the administration of structured questionnaires was used to determine the power supply and consumption, through the application of some specific formula or methods according to [11] and [12]. Energy auditing was also carried out using the digital clamped meter. The load profile of the Corporation was also derived from the result of the energy audit

C. Location/Brief History of the Study Area

The Osun State Broadcasting Corporation, which is located in Osogbo, Osun State, Nigeria, consists of four stations (two radio stations and two television stations), and it all began on August 27, 1991. A television and a radio station of frequencies 559.25 MHz and 104.5 FM, respectively, are located in Osogbo; a radio station known as Orisun FM on frequency 89.5 FM is located in Ile-Ife; and a television station called New Dawn TV on frequency 479.25 MHz is located at Ibokun. The picture of the study area is shown in Fig. 1.

D. System Components Modeling

The components of the energy optimization system involve hybrid modeling, in order to achieve its performance under various circumstances. The following mathematical model is used to demonstrate the proposed hybrid renewable energy system (HRES) components:

TABLE I.
ARRANGEMENT OF ELECTRICAL LOADS

Identity	Class	Type of Loads
1	Lighting	Lamps include, but are not limited to, security lamps, office lamps, rechargeable lamps, and others
2	Technical Supplies	Television transmitter, radio transmitter, computer accessories, photocopier, and printers
3	Air-conditioners	Fans, AC units, and refrigerators
4	Computers	Intercoms, computers, mobile phones, network switch, and other communication devices
5	Entertainment System	TVs, DVD players, and decoders
6	Miscellaneous Equipment	Electric jugs, pumping machine

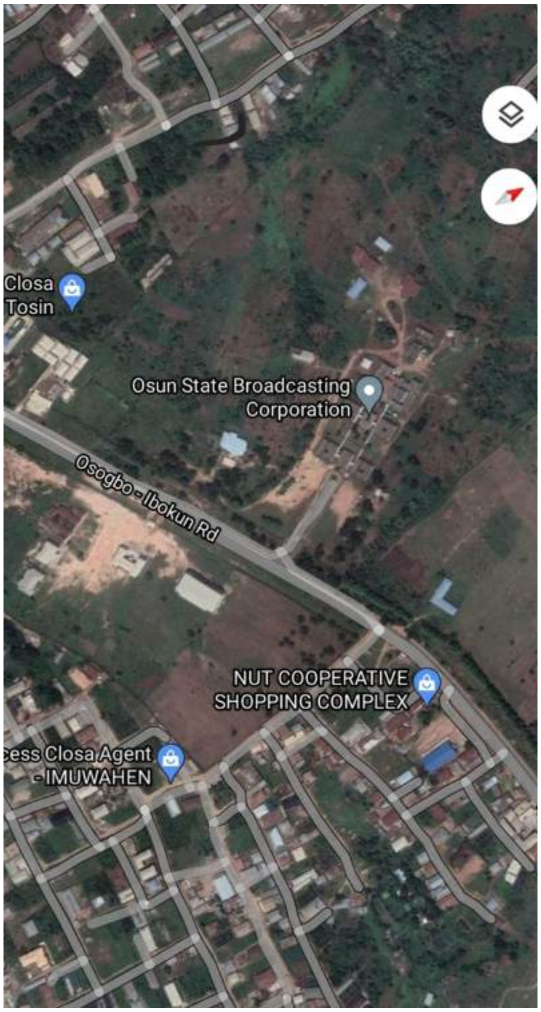

Fig. 1. Location of the study area.

1) Modeling of Solar PV System

This research utilizes the Canadian Solar MaxPower CS6X-325P. After an extensive literature research, two PV modules were selected. The two kinds of PV cells are defined by their production procedures and materials used [13]. The PV was based on the manufacturing techniques employed. Canadian Solar offers two types of solar cell in their Solar MaxPower CS6X-325P: monocrystalline and polycrystalline. While standard modules are known to have a very high degradation rate, the PV has excellent protection and durability. It is a dependable and long-lasting alternative throughout the lifetime. It obtains energy from the sun throughout the day, using PV technology.

To keep the surrounding temperature below the appropriate temperature, the PV panel must be positioned correctly with respect to the sun's rays, since both inadequate and excessive solar radiation can damage the PV panel's derating factor.

Table II shows the simulation parameters for the solar PV system used in this study.

TABLE II.
SIMULATION PARAMETERS FOR THE SOLAR PV SYSTEM

Parameters	Values
Capital cost ($)	300
Replacement cost ($)	100
Operation and maintenance cost ($/year)	5
Rated capacity (kW)	0.325
Lifetime (years)	25
Temperature coefficient	−0.41
Operating temperature (°C)	45
Efficiency (%)	16.94

TABLE III.
SIMULATION PARAMETERS FOR DIESEL GENERATOR (DEG)

Parameters	Values
Capital cost ($)	150 000
Replacement cost ($)	150 000
Operation and maintenance cost ($/op. hour)	5
Minimum load ratio (%)	25
Lifetime (hours)	15 000

2) Modeling of Diesel Generator

This research used a Generic 500 kW fixed-genset generator. The genset's specifications are shown in Table III. In Nigeria, the price of diesel is $0.59 per liter. The minimum load ratio to protect the engine exhaust system is set as 25%.

3) Modeling of BESS

This analysis reveals that 12VRE-3000TF batteries are being utilized. Table IV gives the techno-economic details. Batteries are crucial when renewable energy sources are not accessible, as they help provide stability, quality, and dependable power delivery. The discharge ability of a battery is computed using (3) [14].

$$P_{bi}(t) = E_{bi}(t-1)(1-\sigma) - [(E_{req}(t)/\eta_{bj} - E_{bih}(t)] \quad (3)$$

$Ereq(t)$ = energy required at time (t)

E_{bi} = total battery energy in time (t),

E_{bih} = PV component total energy generated

η_{bj} = converter efficiency,

σ = self-discharge rate.

TABLE IV.
SIMULATION FOR BATTERY ENERGY STORAGE SYSTEM (BESS)

Parameters	Values
Capital cost ($)	410
Replacement cost ($)	410
Operation and maintenance cost ($/year)	0
Round-trip efficiency (%)	80
Lifetime (years)	20
Throughput (kWh)	3581.60
Nominal voltage (V)	12
Nominal capacity (kWh)	3.11
Maximum capacity (Ah)	260

The capacity of a battery must be adapted in order for it to maintain enough charge to sustain a planned system when PV power is tailored, by using (4) [15].

$$C_{BAT} = [E_{load}(t):DA(t) \,/\, \eta_{bj}.\ \eta_{bat}:DOD(t)] \tag{4}$$

where:

η_{bat} = efficiency of battery

E_{load} = Avg. demand of energy (kWh/day)

DA = Autonomy day

η_{bj} = efficiency of converter

DOD = the battery's charge depth

The amount of energy accessible in a battery at any one moment is determined by its state of charge (SOC). The following formulas are used to compute energy and charge state:

$$E_b\,(t) = (t - \Delta t)\; E_b - P_b\,(t) \cdot \Delta t \tag{5}$$

$$SOC\,(t) = (t - \Delta t)\; SOC - (P_b\,(t) \cdot \Delta t\, /En) \tag{6}$$

$P_b\,(t)$ = Battery's power

En = battery nominal capacity.

4) Modeling of Conversion Unit
The converter used for this study is the Generic System Converter. In order for a hybrid energy power system to work, it must have a converter unit, which connects the various current applications. Table B contains all the information on the capital cost for the converter unit as well as the replacement cost utilized in this research. This time period is 15 years, with a percentage of 95 percent. The converter's power rating is calculated using (7).

TABLE V.
SIMULATION PARAMETERS FOR CONVERTER UNIT

Parameters	Values
Capital cost ($)	300
Replacement cost ($)	300
Operation and maintenance cost ($/year)	0
Efficiency (%)	95
Lifetime (years)	15

$$P_{con} = P_{peak}/\eta_{con} \tag{7}$$

where:

η_{con} = converter efficiency

P_{peak} = max consumption load

5) Modeling of the Wind Energy Converter
The wind turbine system used for this study is the Generic 10 kW and the mathematical model, which was obtained from the power curve of the wind turbine derived by the manufacturer. Table VI below shows the parameters for the WEC.

III. RESULTS AND DISCUSSION

The daily load profile of Osun State Broadcasting Corporation is presented in Fig. 2. The peak daily and annual energy use was estimated to be 45 77.38 kWh and 83 5011.71 kWh, while the Corporation daily power requirement was estimated to be 361.61 kW.

TABLE VI.
SIMULATION PARAMETERS FOR WIND ENERGY CONVERTER (WEC)

Parameters	Values
Capital cost ($)	50 000
Replacement cost ($)	50 000
Operation and maintenance cost ($/year)	500
Rated capacity (kW)	10
Hub height (m)	24
Lifetime (years)	20

Fig. 2. OSBC daily load profile.

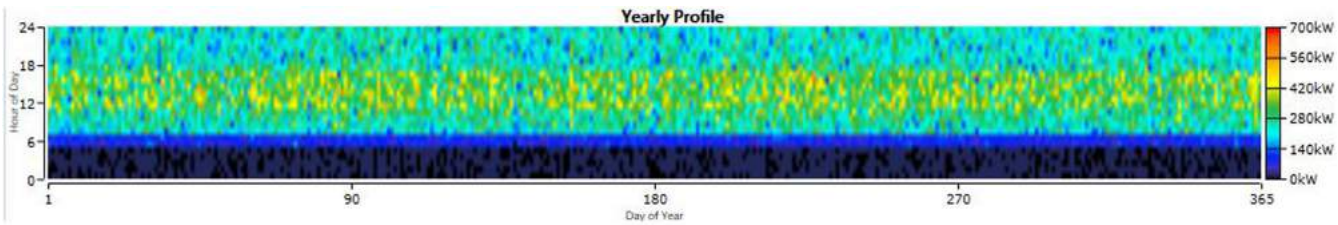

Fig. 3. Monthly average solar GHI data for OSBC.

While peak daily and annual energy use is 4577.38 kWh and 835 011.71 kWh, the Corporation needs 361.61 kW of electricity per day. The latitude and longitude of the research region (7°46.6′N and 4°35.4′E) were used to estimate the average solar irradiation and wind speed particulars of the area of study. The average wind speed and solar irradiation were calculated using HOMER Pro across these longitudes and latitudes. The monthly average solar global horizontal irradiance (GHI) graph is shown in Fig. 3. The maximum monthly solar irradiation level seen was 5.8 kWh/m^2/day in February, while the minimum level seen was 3.7 kWh/m^2/day in August. Furthermore, Table. VII shows where the simulation resources are. The estimated daily peak electrical demand (kW), the estimated peak daily intake (kWh), and the estimated annual mean use (kWh) for each section of the Corporation were computed and stated in Table VIII.

A. Simulation Results from the HOMER Method

Several possible setups and parameters are created when the simulation complete. Many combinations exist; four out of these combinations have been proposed, and the effects of each are explained below.

1) SPV–DEG–BESS Without WEC Combination

Allocations of energy sources for satisfying the requirement of energy demand in the research region include a mixture of solar photovoltaic (SPV) system, diesel engine, and battery energy storage system (BESS). The system may be described as consisting of 1424 kW photovoltaic

TABLE VII.
SIMULATION RESOURCES

S/N	Configuration Parameter	Equity
1	The project’s life expectancy	25 years
2	Diesel fuel price (for DEG)	\$0.59/L
3	The average annual amount of solar radiation received	5.80 kWh/m^2/day
4	Wind speed averages each year	3 m/s
5	Output of the battery	12V/260 Ah per unit

TABLE VIII.
ESTIMATED SECTIONAL DEMAND AND CONSUMPTION

Sections/Departments	Estimated Daily Peak Electrical Demand (kW)	Estimated Peak Daily Intake (kWh)	Estimated Annual Mean Use (kWh)
Engineering	32.98	230.02	745 80.60
Programs	26.90	163.04	50 754.78
News	26.57	161.80	53 290.68
Radio and TV studio	77.42	1312.96	466 099.38
Radio and TV transmitter building	125.30	2236.56	44 468.69
Administrative	27.09	173.12	52 382.45
Marketing	27.55	193.29	59 948.13
Director general’s office	17.80	106.59	33 487.00
Grand total	361.61 kW	4577.38 kWh	835 011.71 kWh

capacity and a 500 kW diesel engine, together with 2512 batteries. The anticipated energy consumption was estimated to 2 461 829 kWh/year. An additional 10.4% of surplus energy is available.

2) SPV–WEC–DEG–BESS Combination
In combination 2, SPV system, wind energy converter (WEC), diesel engine, and BESS are taken into account. For sizing purposes, the size of the system is defined as SPV, WEC, DEG, and BESS, which have system power ratings of 1461 kW, 1 unit, 500 kW, and 2502 units respectively. The anticipated energy consumption was estimated to 2 518 674 kWh/year. The excess energy percentage is 12.4%.

3) SPV–BESS Without WEC and DEG Combination
Combination 3, SPV–BESS, lacks WEC and DEG. The SPV and BESS are accounted for in the combination. The system sizes are assumed to be 1751 kW of SPV and 4720 units of BESS, with an estimated energy consumption of 2 907 626 kWh/year. Availability of extra energy is projected at 23.7%.

4) SPV–WEC–BESS, But Without DEG Combination
Combination 4 takes into consideration SPV, WEC, and BESS, but DEG is not considered. The system sizes, estimated as SPV, WEC, and BESS, were 1743 kW, 1 unit, and 4730 units. respectively. With regard to energy consumption, 2 899 030 kWh/year was estimated; and availability of surplus energy was estimated at 23.5%.

B. Component Simulation Results

1) Solar Panel Simulation Result
The solar PV system used for this study has a maximum power output of 1317 kW and a minimum output of 0 kW in a year. The PV penetration is 122% and the number of hours of operation is 4380 h/year.

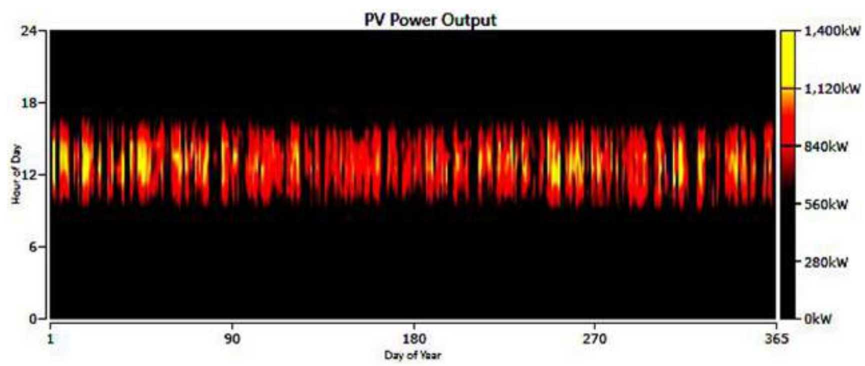

Fig. 4. PV power output.

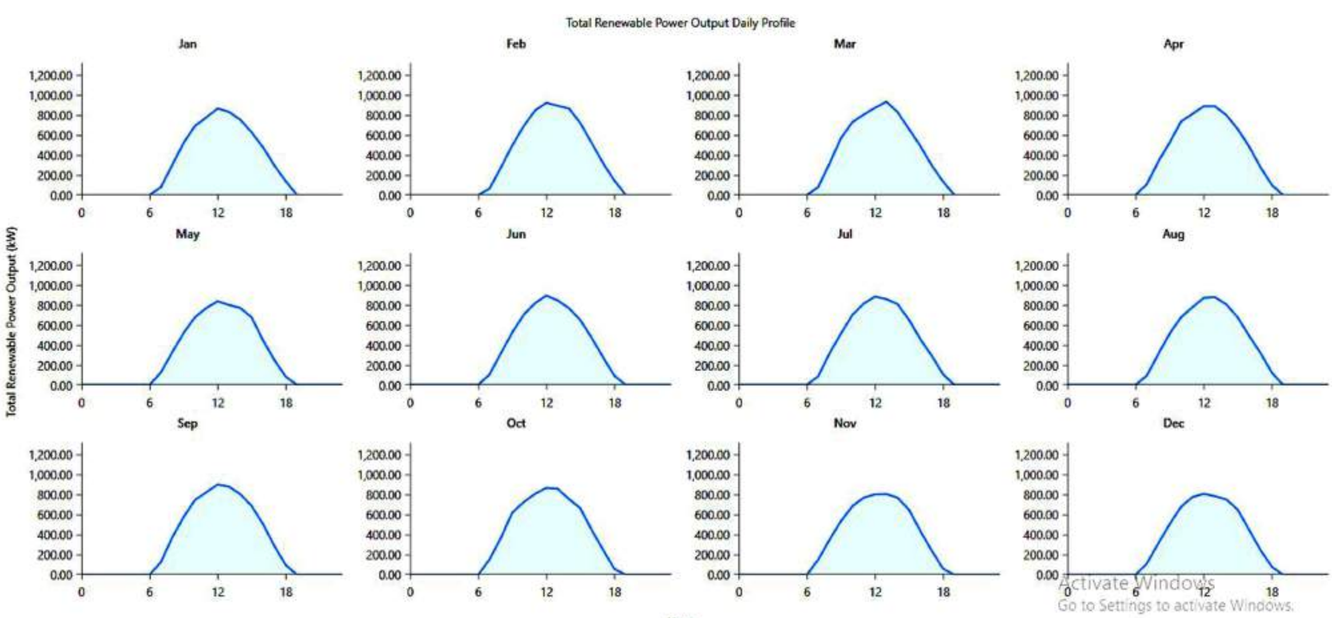

Fig. 5. Total renewable power output daily profile.

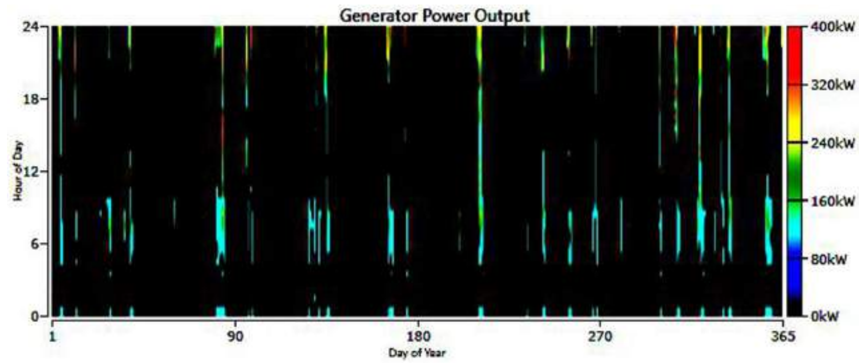

Fig. 6. Generator power output.

The plot showing PV power output for the year is shown in Fig. 4. The daily profile of total renewable power output is shown in Fig. 5. It can be seen that the majority of energy is generated from 9:00 hours to 17:00 hours.

2) Generator Simulation Result

Simulation of the generator output is presented in Fig. 6. The simulation result shows the hourly generator output in kW for the year. The total fuel consumed is 27 863 L/year, the average fuel per day is 76.3 L/day and the average fuel per hour is 3.18 L/h. The generator power output daily profile is presented in Fig. 7. It shows that the area requires generation of energy from a generator, mostly during morning and evening hours.

3) Battery Simulation Result

The battery SOC simulation is presented in Fig. 8, with high SOC falling mostly between 10:00 hours and 24:00 hours. The SOC daily profile is presented in Fig. 9.

4) Optimization Results

Fig. 10 shows the cost summary of all the components for combination 1. WEC gives the best overall price, at $415.82, while BESS gives the highest price of $1,693,661.42. The optimization result for the total operating cost ($) and the total capital cost ($) is given in Fig. 11 while the optimization result for the energy cost ($) and the total net present cost ($) is shown in Fig. 12 .

IV. CONCLUSION

Electric power supply system design relies on software modeling and energy audits. This is for powering the Osun State Broadcasting Corporation, Osogbo. DEG/BESS/PV is the optimum hybrid configuration, according to sensitivity analysis. DEG and PV work together to meet the power demands of the system; the converter subunit allows the PV array to directly provide the appropriate amount of electricity without emptying the battery. As a result, the battery bank and BESS unit will both have longer life spans, while simultaneously encouraging the DEG unit to engage in fewer, but more frequent on/off tasks.

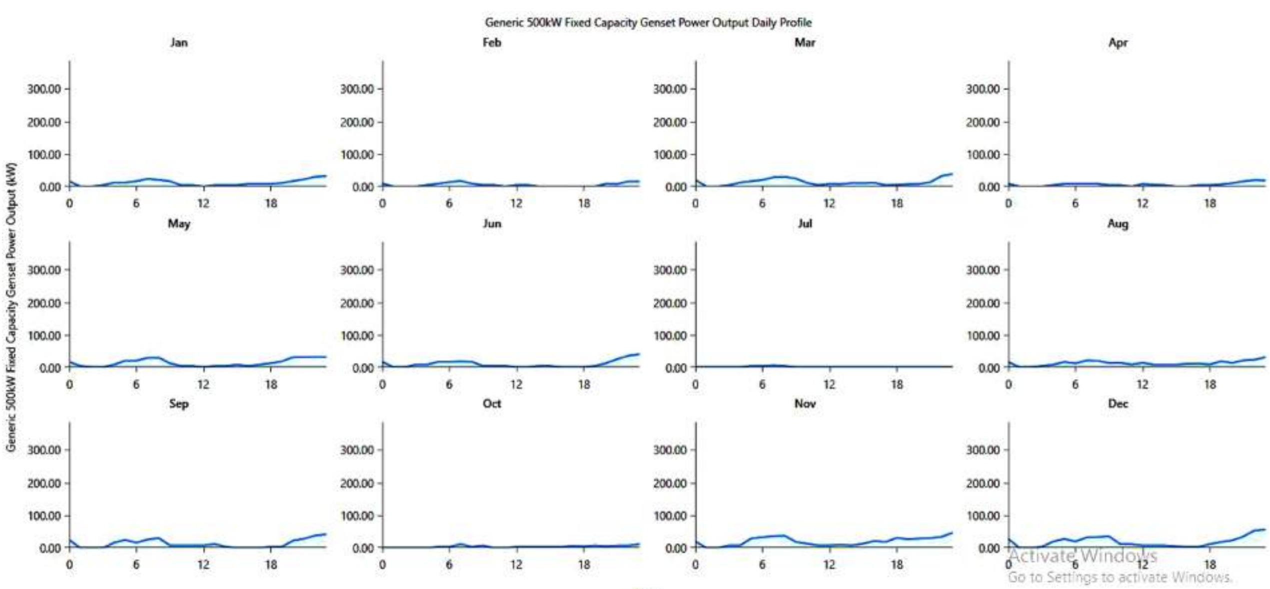

Fig. 7. Generator power output daily profile.

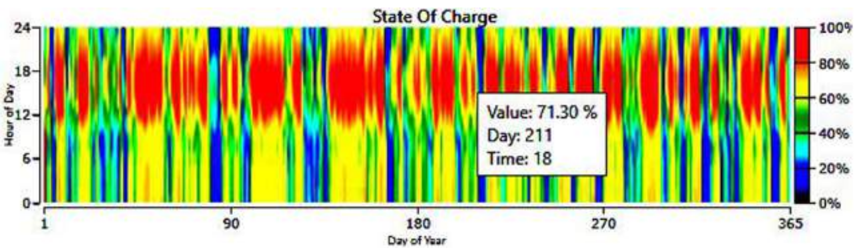

Fig. 8. State of charge.

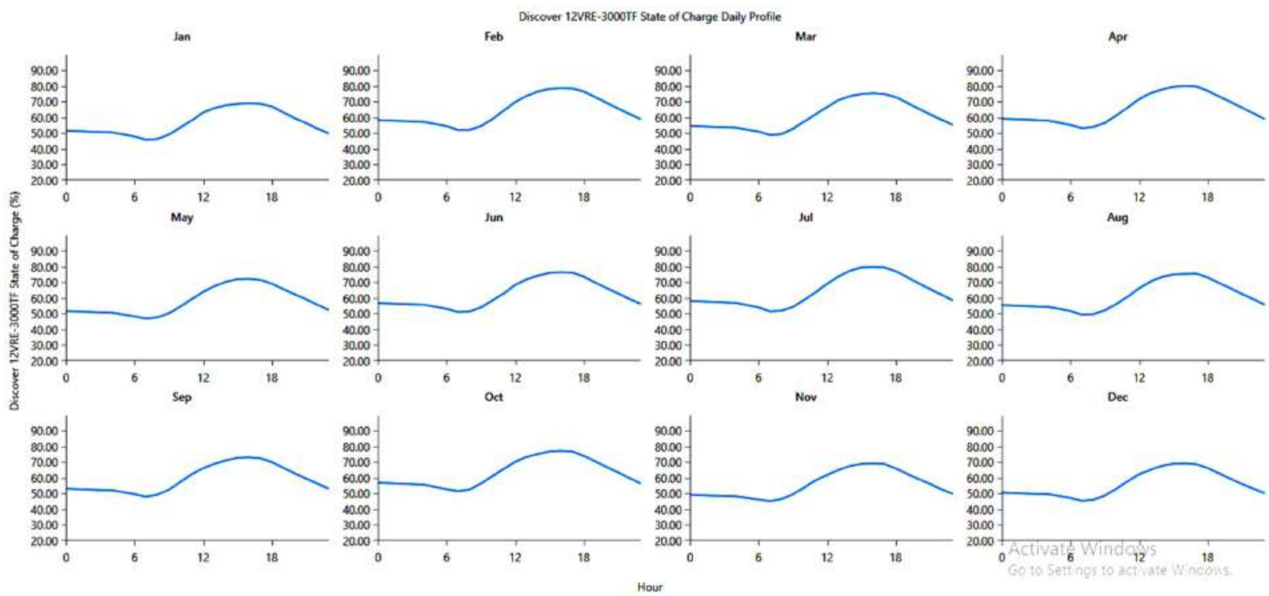

Fig. 9. State of charge daily profile.

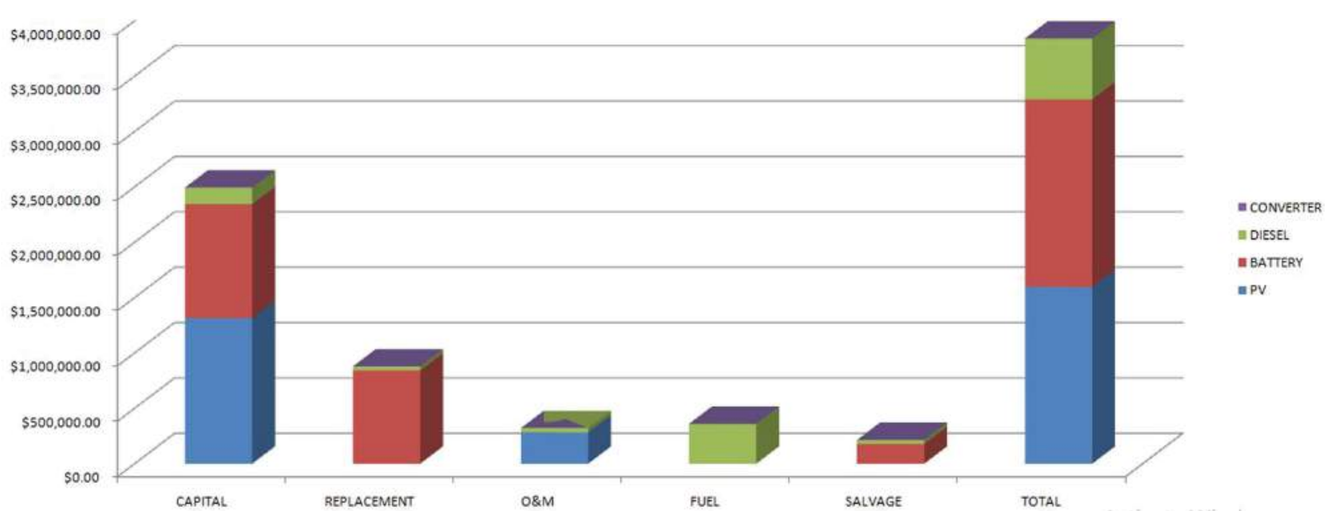

Fig. 10. General summary of cost of all the components of combination 1.

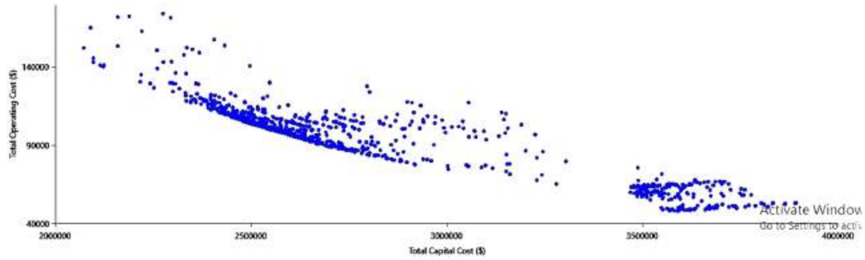

Fig. 11. Total operating cost ($) against the total capital cost ($).

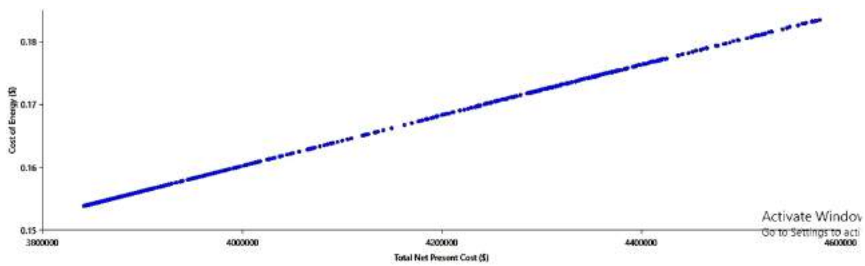

Fig. 12. Cost of energy ($) against the total net present cost ($).

Architecture						COE ($)	NPC ($)
CS6X-325P (kW)	G10	500kWGen (kW)	Dis12V	Converter (kW)	Dispatch		
1,424		500	2,512	722	LF	$0.154	$3.84M
1,461	1	500	2,502	743	LF	$0.156	$3.90M
1,751			4,720	888	LF	$0.168	$4.18M
1,743	1		4,730	886	LF	$0.170	$4.24M
594		500		776	LF	$0.320	$7.99M
587	1	500		894	LF	$0.322	$8.05M

Fig. 13. Optimization results by HOMER Pro.

HOMER Pro has also examined four different combinations of hybrid energy systems. The four combinations, which are: (1) SPV–DEG–BESS, often known as WEC-free; (2) SPV–WEC–DEG–BESS; (3) The SPV–BESS without WEC and DEG requirements; and (4) SPV–WEC–BESS without DEG. The total net present cost and cost of energy in the research region are both considered when making a decision based on the findings from these four combinations. HOMER is examined via four different HRES configurations. The first combination provides a minimum net present cost of $3.84 million and a cost of energy of $0.154/kWh.

Fig. 13 shows the optimization results by HOMER pro. The result of the sensitivity analysis shows that the first combination, a DEG/SPV/BESS hybrid, has many merits over the other four combinations. As its two energy sources, the diesel engine and the SPV array complement each other, and the converter subunit allows delivery of the needed amount of power directly from the PV array without running down the battery when there is enough solar radiation. As a result, the lifespan of the whole BESS unit and battery bank is increased, which also allows limited operation of the DEG unit. The first combination can therefore be considered as the most feasible means of power supply for the broadcasting station. The availability of both diesel fuel and solar radiant energy in Osogbo Nigeria made the option reliable.

Peer-review: Externally peer reviewed.

Acknowledgments: The authors are thankful to the Department of Engineering in Osun State Broadcasting Corporation Osogbo, Nigeria for providing an enabling environment to carry out this research work.

Conflict of Interest: The authors have no conflict of interest to declare.

Financial Disclosure: The authors declared that this study has received no financial support.

REFERENCES

1. T. O. Ajewole, W. A. Oyekanmi, A. A. Babalola, and M. O. Omoigui, “RTDS modelling of a hybrid-source autonomous electric microgrid,” *Int. J. Emerg. Electr. Power Syst.*, vol. 18, no. 2, 2017. Available: https://www.degruyter.com/view/j/ijeeps.2017.18.issue-2/ijeeps-2016-0157/ijeeps-2016-0157.xml.
2. S. O. Oyedele, “Energy efficiency and conservation measures: Tools for sustainable energy development in Nigeria,” *IJEE*, vol. 1, no. 2, pp. 86–98, 2017.
3. W. Fazli, and D. H. Kim, “An efficient approach for energy consumption optimization and management in residential building using artificial bee colony and fuzzy logic,” *Hindawi Publ. Corp. Mathematic. Prob. Eng.*, vol. 18, no. 5, pp. 1–14, 2018, [CrossRef].
4. S. Ali, and D. H. Kim, “Effective and comfortable power control model using Kalman filter for building energy management,” *Wirel. Personal Commun.*, vol. 73, no. 4, pp. 1439–1453, 2013, [CrossRef].
5. World Steel Association, *Steel Statistical Yearbook 2012*. Brussels, Belgium: World Steel Committee on Economic Outlook, 2012, pp. 34–42.
6. W. Yang, G. He, and W. Wang, “Design and implementation of user energy management archetype system,” *Autom. Electr. Power Syst.*, vol. 36, pp. 74–79, 2017.
7. A. Kusye, M. Li, and Z. Zhang, “A data-driven approach for steam load prediction in buildings,” *Appl. Energy*, vol. 87, no. 3, pp. 925–933, 2014, [CrossRef]
8. Z. Lang, R. Yang, and L. Wang, “Multi-agent intelligent controller design for smart and sustainable buildings,” In *Proc. 4th Ann. IEEE Syst. Conf.*, San Diego, CA, USA: IEEE Publications, 2019, pp. 277–282.
9. K. Bunse, M. Vodicka, P. Schonsleben, M. Brulhart, and F. O. Ernst, “Integrating energy efficiency performance in production management - Gap analysis between industrial needs and scientific literature,” *J. Cleaner Prod.*, vol. 19, no. 6–7, pp. 667–679, 2019, [CrossRef].
10. J. Sidiqqi, F. Oldewurtel, J. Cigler, and S. Prıvara, “Experimental analysis of model predictive control for an energy efficient building heating system,” *Appl. Energy*, vol. 88, no. 9, pp. 3079 – 3087, 2018.
11. G. S. Lukas, and V. I. Ugursal, “Modelling of end-use energy consumption in the residential sector: A review of modelling techniques,” *Renew. Sustain. Energy Rev.*, vol. 13, pp. 1819–1835, 2018, [CrossRef].
12. Z. Wang, L. Wang, A. I. Dounis, and R. Yang, “Multi-agent control system with information fusion based comfort model for smart buildings,” *Appl. Energy*, vol. 99, pp. 247–254, 2012, [CrossRef].
13. H. Kang, T. Hong, S. Jung, and M. Lee, “Techno-economic performance analysis of the smart solar photovoltaic blinds considering the photovoltaic panel type and the solar tracking method,” *Energy Build.*, vol. 193, pp. 1–14, 2019, [CrossRef].
14. K. V. Konneh *et al*. “Optimal design and performance analysis of a hybrid off-grid renewable power system considering different component scheduling, PV modules, and solar tracking systems,” *IEEE Access*, vol. 9, pp. 64393–64413, 2021, [CrossRef].
15. M. R. Elkadeem, K. M. Kotb, Z. A. E. G. Ullah, E. G. Atiya, A. Dán, and S. Wang, “A two-stage multi-attribute analysis method for city-integrated hybrid mini-grid design,” *Sustain. Cities Soc.*, vol. 65, p. 102603, 2021, [CrossRef].

TEPES
TURKISH JOURNAL OF
ELECTRICAL POWER
AND ENERGY SYSTEMS

TEPES, Vol. 2, Issue. 1, 11-20, 2022 **DOI:** 10.5152/tepes.2021.21026

RESEARCH ARTICLE

Validation of Passive Islanding Detection Methods for Double Line-to-Ground Unsymmetrical Fault in a Three-Phase Microgrid System

Bangar Raju Lingampalli, K. Subba Rao

Department of Electrical and Electronics, Koneru Lakshmaiah Educational Foundation, Guntur, Andhra Pradesh, India

Cite this article as: B. R. Lingampalli & K. S. Rao. Validation of passive islanding detection methods for double line-to-ground unsymmetrical fault in a three-phase microgrid system. *Turk J Electr Power Energy Syst*, 2022; 2(1): 11-20.

ABSTRACT

Microgrid islanding detection has become challenging with the penetration of distributed generation (DG). IEEE-1547-2018 specifies that islanding is to be detected in less than 2 seconds if voltage $0.88 \leq V \leq 1.1$ *p.u.* (per unit) and frequency $49 \leq f \leq 51$ Hz (for 50 Hz) exceed these limits. The available methods of islanding detection are active, passive, hybrid, and communication. The active methods affect power quality due to injections; passive methods have a larger non-detection zone (NDZ); and communication type methods are expensive. The hybrid approach is a combination of the active and passive methods, which also deteriorate the power quality. To obviate all this, this paper proposes the rate of change of voltage phase angle (ROCOVPA) method, a passive islanding detection method which reduces NDZ and detection time when compared to other methods. The methodology is based on retrieving the voltage phase angle at the targeted output of DG first. Then, the phase angle is differentiated to get ROCOVPA to detect islanding and to isolate the microgrid seamlessly from the main grid during unintentional unsymmetrical fault. In this paper, the islanding condition is tested for double line-to-ground fault, which occurs when two lines are grounded. The non-islanding condition is also tested in MATLAB/Simulink with capacitor load connection and disconnection. The simulations are carried on ROCOVPA and compared with the widely used rate of change of frequency (ROCOF) at zero percent mismatch power. The analysis of the results depicts that ROCOVPA is effective and better than ROCOF.

Index Terms—Distributed generators (DG), double line-to-ground fault (L-L-G-Fault), non-detection zone (NDZ), point of common coupling (PCC), rate of change of frequency (ROCOF), rate of change of voltage phase angle (ROCOVPA).

I. INTRODUCTION

The microgrid is meant to feed the loads and import the mismatch power from the grid, which is the normal operation. Based on the load demand, the mismatch power is supplied by the grid. To achieve this, the inverters are designed to operate in constant current control during grid mode and droop control in islanding mode. The microgrid is to be seamlessly islanded from the main grid during unintentional, unsymmetrical, and symmetrical faults and is to be stable during non-islanding periods like load connection and disconnection. To detect these faults, many islanding detection methods already exist. These are active, passive, hybrid, and communication methods. The active methods are good but the power quality is affected due to injections. Passive islanding detection methods are good in view of the power quality as there are no injections; however, they leave behind a large NDZ. The hybrid method is a combination of passive and active methods. The communication methods are good but expensive, and the cost depends on the size of the microgrid and criticality of the loads. To obviate all these drawbacks, a simple passive islanding detection method, ROCOVPA is proposed, to detect faults even at 0% mismatch power. The detection time of ROCOVPA is less than that of ROCOF, according to the results analysis in Section 6.

In this paper, the passive islanding detection method ROCOVPA is tested for detecting unsymmetrical L-L-G fault [1]. This method can also be extended to all unintentional faults. Double line-to-ground unsymmetrical faults occur in the system due to two lines short circuiting and grounding to the earth. This occurs due to the line snapping, falling on another line, and earthing to the ground. This type of fault leads to unequal currents with unequal phase shifts in a three-phase system. The IEEE-1547-2018 standards prescribe that these unintentional faults are to be detected in less than 2 seconds and the microgrid is to be islanded from main grid for stability and to feed power to local loads without interruption [2].

Corresponding author: Bangar Raju Lingampalli, lsmlbr@yahoo.in

Received: May 29, 2021
Accepted: November 7, 2021
Available online: December 17, 2021

The methodology suggested in this paper is to first retrieve the voltage signals at the targeted DG and estimate the phase angle. Then, the rate of change of phase angle is calculated to detect the fault condition. In the normal condition, the values are within the threshold. However, during fault conditions, the phase angle variations are sufficient to exceed the threshold values and trip the circuit breaker to isolate the microgrid from the main grid. The simulation results obtained during fault conditions, and sudden load connection and disconnection are discussed elaborately in Section 7. The simulation results prove the purpose for which the method is intended. The methodology suggested is justified with the results and comparison with ROCOF [3].

The advantages and disadvantages of the proposed phase angle variation method over the other two methods, ROCOF and ROCOV, are as follows:

A. Advantages

- It is simple to implement.
- It is effective, accurate, and reliable.
- It detects islanding at zero percent power mismatch (0% NDZ).
- It discriminates between islanding and non-islanding, thus avoiding nuisance tripping.
- The detection time is 10 ms, which is lower compared to other methods, and does not depend on frequency and voltage.
- The detection time is almost consistent irrespective of percentage of mismatch power.
- The method does not affect power quality as there are no injections during testing.

B. Disadvantages

- The ROCOVPA method is not suitable for microgrid with hybrid DGs, as proportional load sharing becomes a problem.
- The inverter control topologies have to be designed specially to suit DGs.
- High quality factor loads will have more problems in detecting the islanding condition.

Main Points

- The main purpose of the microgrid is to supply uninterrupted quality power to loads.
- As per IEEE-1547-2018 standards, the microgrid is to be islanded in less than 2 seconds from the main grid and has to supply power to loads in autonomous mode.
- The proposed ROCOVPA method detects islanding at zero percent power mismatch and isolates the microgrid to feed connected loads, as the methodology is based on phase angle variation instead of frequency and voltage.
- According to the analysis of the results, the proposed method discriminates islanding during faults and is stable without nuisance tripping during non-islanding conditions, like capacitor load connection and disconnection at PCC.
- The proposed ROCOVPA method is compared with the widely used ROCOF method and is found to be a better alternative.

- Loads with resonance frequency which are nearly equivalent to system frequency will also have difficulty in islanding detection.
- This method is not suitable for unbalanced loads.

Because of its simplicity, reliability, and effectiveness over the active and communication methods, ROCOVPA, the passive method, is more preferable than other methods. It also avoids nuisance tripping as it distinguishes islanding and non-islanding very accurately. The islanding detection is perfect even at 0% power mismatch. This method seamlessly detects islanding and transfers the microgrid from grid to islanding mode in less than 1 cycle detection time with almost zero NDZ. This is verified with the MATLAB simulation results and proved to be as proposed. The paper is organized as follows: Section 2 explains the network and mathematical model. Section 3 discusses the NDZ. Section 4 deals with the proposed methodology. Section 5 gives the design parameters. Section 6 discusses and analyzes the results of MATLAB simulations. Finally, the paper is concluded in Section 7.

II. LITERATURE REVIEW

Dejan Milosevic et al. in [1] have used both voltage magnitude and phase angle at PCC, for obtaining balance between active power and reactive power to achieve stability in the microgrid. The proposed method considers only rate of change of phase angle for the protection during islanding. The phase angle variations will increase after a certain time, and hence, the islanding is detected. Thus, the method exactly caters to the need of the islanding detection without additional components.

Haidar Samet et al. in [2] used the voltage phase angle in their method. However, they used the energy involved in the phase angle by collecting five energy samplings. Although there may be an error in calculating energy samplings, the proposed method directly monitors rate of change of phase angle at output of the DG, and hence, is more reliable.

Ch. Rami Reddy et al. in [3] utilized the active method of injecting low-frequency current harmonics on the q-controller with the ROCOF method. It increases power quality issues and is ineffective at lower power mismatches.

Behrooz Bahrani et al. in [4] used the active method of injecting negative sequence current on the inverter, which raises power quality issues. However, the NDZ will of course be reduced considerably.

Min-Sung Kim et al. in [5] reviewed different islanding techniques including ROCOV and ROCOF. However, the proposed method ROCOVPA is better than all those methods, as it detects at zero percent power mismatch in less time, as per IEEE-1547-2018 standards.

Mehdi Hosseinzadeh et al. in [6] reviewed islanding methods and their merits and demerits. However, the proposed method is a better alternative to detect islanding

F. Namdari et al. in [7] considered the passive islanding detection method of rate of change of voltage over active power, which is good for power quality retention but not efficient at zero power mismatch.

Onkemetse Tshenyego et al. in [8] used artificial intelligence(AI) with wide-area monitoring protection and control (WAMPAC). This method is less reliable, as it uses communication support.

Hajir Pourbabak et al. in [9] used the variations in the phase angle of active and reactive powers. Though the method reduces NDZ, the variations are not consistent, leading to nuisance tripping.

Walid Ghzaiel et al. in [10] used phase shift between real and imaginary values of voltage, to detect islanding. The method depends on voltage, and nuisance tripping cannot be avoided; the NDZ is also large enough.

III. NETWORK AND MATHEMATICAL MODEL

The network model is shown in Fig. 1. The ROCOVPA islanding detection method is tested on a DG with 2.5 KW with an interfaced inverter. A parallel-connected Resistive, Inductive and Capacitive (RLC) load is connected to the DG with a quality factor of 1.8 at PCC. The DG inverter is connected to the main grid via PCC through a three-phase circuit breaker. The inverter is connected to the PCC with a series filter.

The mathematical model of the islanded microgrid in frame abc is given by the following equations,

$$V_{t,abc} = L_t di_{t,abc} / dt + R_t i_{t,abc} + V_{abc} \tag{1}$$

$$i_{t,abcc} = V_{abc} / R + i_{L,abc} + C \frac{d}{dt} V_{abc} \tag{2}$$

$$V_{abc} = L \,{}^{d}\!/_{dt}\, i_{L,abc} + R_L i_{L,abc} \tag{3}$$

where $V_{t,abc}$, $i_{t,abc}$, $i_{L,abc}$ are terminal three-phase voltages and currents, V_{abc} is PCC voltage,R_t, L_t are line resistance and inductance, respectively.

These three-phase instantaneous voltages and currents are to be transformed to a synchronous rotating frame dq0, due to the following reasons:

- to have control of active power (d-axis) and reactive power (q-axis)
- to keep mutual inductance constant
- to achieve the desired output
- to have infinite gain control on PI and PID, by adjusting integrators, and to make steady-state error to zero to enable ease of computations

$$X(t) = AX(t) + Bu(t) \tag{4}$$

$$y(t) = CX(t) \tag{5}$$

$$u(t) = V_{td}. \tag{6}$$

The A, B, C, and D are constants given by

$$A = \begin{bmatrix} \frac{-Rt}{L_t} & \omega_0 & 0 & \frac{-1}{L_t} & \\ \omega_0 & \frac{-R_t}{L} & -2\omega_0 & \frac{RlC\omega_0}{L} & -\frac{\omega_0}{R} \\ 0 & \omega_0 & \frac{-Rl}{L} & \frac{1}{L} - \omega_0^2 C & \\ \frac{1}{C} & 0 & \frac{-1}{C} & -\frac{1}{RC} & \end{bmatrix} \tag{7}$$

$$B^T = \left[\frac{1}{L_t} 000 \right] \tag{8}$$

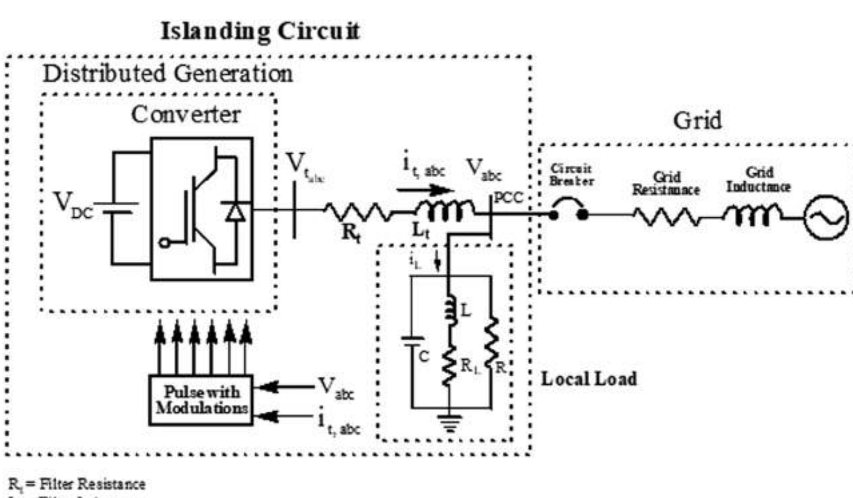

Fig. 1. Network model for testing the islanding detection method, ROCOVPA.

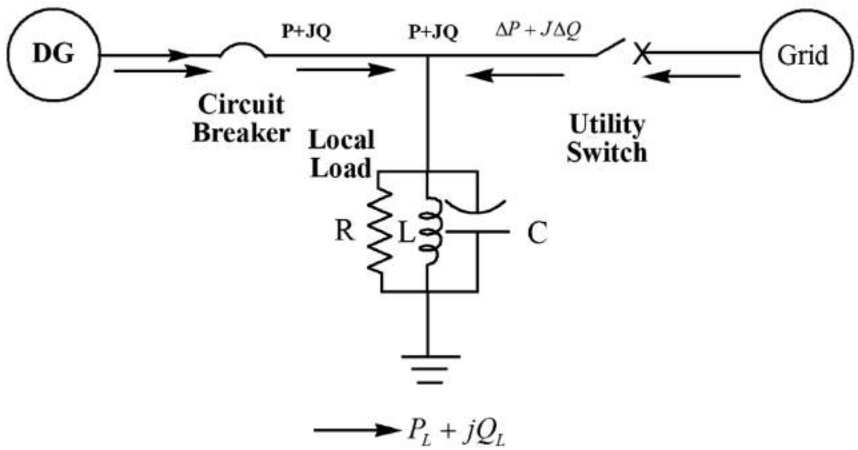

Fig. 2. DG network connected with grid system.

$$C = \begin{bmatrix} 0 & 0 & 0 & 0 \end{bmatrix} \tag{9}$$

$$D = [0] \tag{10}$$

$$X^T = \begin{bmatrix} i_{td} & i_{tq} & i_{Ld} & V_d \end{bmatrix}. \tag{11}$$

These equations give the transfer functions of V_d/V_{td}, where V_d and V_{td} are input and output components of the d axis.

IV. NON DETECTION ZONE

The efficiency of islanding detection depends on minimizing the NDZ [4, 5]. The method depends on the percentage of active power mismatch, which, as per IEEE-1547, has to be < 15%. and the detection time has to be < 2 seconds. The network for the NDZ study is shown in Fig. 2. The DG is connected to the grid through an interfacing inverter, PCC, and utility switch [6]. The three-phase parallel RLC load is connected at PCC [7]:

$$P + \Delta P = \frac{v^2}{R} \tag{12}$$

$$Q + \Delta Q = \frac{V^2}{2\pi f L} \tag{13}$$

Equations (12) and (13) give the voltage, and frequency at PCC and is given by,

$$V = \sqrt{R(P + \Delta P)} \tag{14}$$

$$f = \frac{V^2}{2\pi L(Q + \Delta Q)}. \tag{15}$$

However, in islanding conditions, ΔP and ΔQ become zero, as there is no main grid. The voltage V′ and frequency f′ under islanding mode are given by

$$V' = \sqrt{R(P)} \tag{16}$$

$$f' = \frac{v'^2}{2\pi L(Q)} = \frac{RP}{2\pi L(Q)}. \tag{17}$$

With these, the voltage and frequency deviations due to power mismatch are given by

$$\Delta V = V' - V = \sqrt{R(P)} - \sqrt{R(P + \Delta P)} \tag{18}$$

$$\Delta f = f' - f = \frac{v'^2}{L(Q)} - \frac{v'^2}{L(Q + \Delta Q)} = \frac{R \times P}{L \times Q} - \frac{R \times (P + \Delta P)}{L \times (Q + \Delta Q)} \tag{19}$$

Equations (18) and (19) show the variations in voltage and frequency due to power mismatch [2]. If the power mismatch is substantial, the variations in voltage and frequency can be identifiable. However, if the mismatch is too small leading to less than 15%, the islanding cannot be detected and hence the formation of NDZ. Fig. 3 shows the NDZ for different percentages of power mismatches [8, 11].

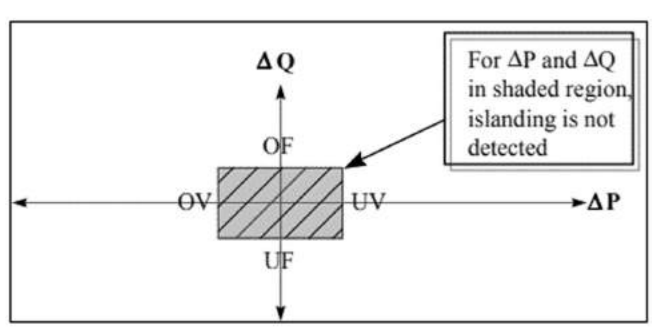

Fig. 3. Mapping of the NDZ in ΔP versus ΔQ for over/under voltage and over/under frequency relays.

NDZ is the operating region in which islanding detection methods cannot detect islanding as specified by IEEE-1547 standards. It is expressed in terms of percentage of power mismatch or in terms of the parameters like R, L, and C of the load. In Fig. 4, the NDZ representation for OVP/UVP was derived as an approximate representation of the NDZ [12, 13].

The NDZ of OVP/UVP (over / under voltage protection) and OFP/UVP (over / under frequency protection) islanding schemes are shown in Fig. 3. These techniques fail to detect islanding in mismatch power less than 15%. In the distribution network, voltage values, as per the standards of IEEE-1547-2018, are between 0.88 p.u. and 1.1 p.u. for voltage relays. These voltage levels are equivalent to 456 V to 365 V (ΔV=91 V), for a 415V nominal voltage level. Similarly, the frequency levels are between 49 Hz and 51 Hz (Δf=2 Hz), for a 50 Hz nominal frequency level. The calculated 15% active power mismatch for our test network (the inverter rated output power is 2.5 kw), is between 2.125 kw and 2.875 kw (Δkw=0.75). Similarly, the 15% reactive power mismatch is between 1.3 kvar and 1.7 kvar (Δkvar=0.4).

In grid mode, the load consumes the reactive power [14]. However, in islanding, DGs cannot inject reactive power to load, as DGs operate at unity power factor, because load behaves like resistance [15], and the load resonance frequency is equal to system frequency at PCC. Hence, to find more deviations in frequency, the load selected is parallel RLC with a high quality factor of 1.8 in islanding mode [9, 10]. The quality factor is given by

$$Q_f = \omega_0 RC = \frac{R}{\omega_0 L} = R\sqrt{\frac{C}{L}} \tag{20}$$

In which, $\omega_0 = 2\pi f_0 = \frac{1}{\sqrt{LC}}$.

Equation (20) gives the energy stored in the RLC circuit. High quality factor loads have high capacitance and small inductance with or without high parallel resistance [16, 17]. The islanding detection is complex, with resonant frequency loads of higher quality factor [18, 19]. The percentage mismatch is not the criterion for load parameters [20, 21]. The load reactive power is given by

$$Q_{\text{Load}} = Vrms^2\left[\frac{1}{\omega L} - \omega c\right] = \Delta Q \tag{21}$$

Equation (21) depicts the variation in reactive power for different values of L and C. The percentages of mismatch power for OVP/UVP and OFP / UFP relays are shown in Fig. 3 and are given by equations for active power imbalance, as

$$\Delta P = 3V \times I - 3(V + \Delta V) \times I = -3 \times \Delta V \times I \tag{22}$$

$$\Delta Q = 3\frac{v^2}{\omega_n L}\left(1 - \omega^2 LC\right) = 3\frac{v^2}{\omega_n L}\left(1 - \frac{\omega_n^2}{\omega_r^2}\right) \tag{23}$$

where ω_n and ω_r are system and resonance frequencies [22, 23]. The system frequency varies till it reaches the resonant frequency of the load in islanding mode and is given by

$$\omega_r = \frac{1}{\sqrt{LC}} \tag{24}$$

and the reactive power imbalance is given by

$$\Delta Q = 3\frac{v^2}{\omega_n L}\left(1 - \frac{fn^2}{\left(f_n \pm \Delta f\right)^2}\right). \tag{25}$$

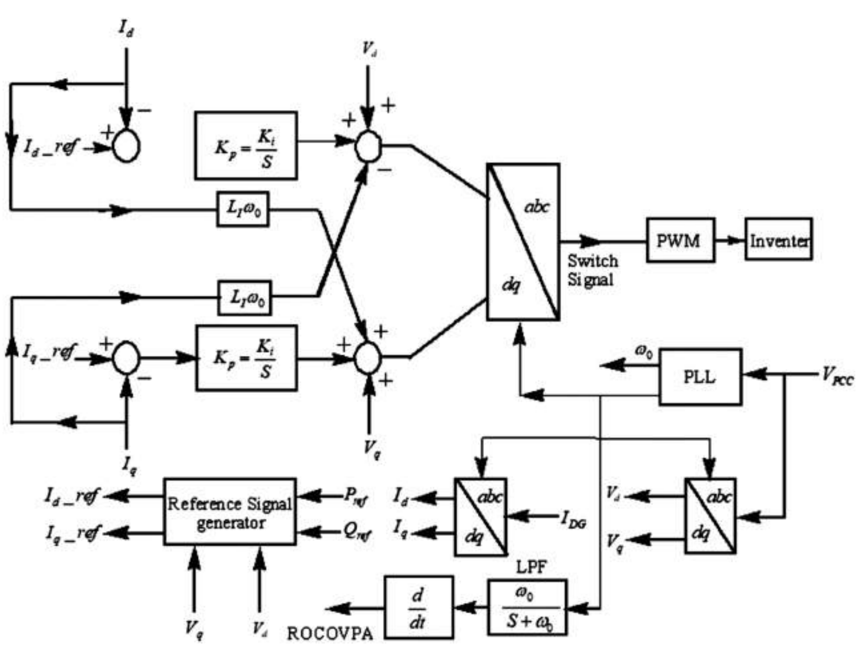

Fig. 4. Current controller block diagram.

TABLE I.
ISLANDING STANDARDS

Standard	Detection Time (Seconds)	Quality Factor	Trip Frequency Range, Nominal Frequency f_0(Hz)	Trip Voltage Range (V)
IEC 62116	t < 2	1	f_0 - 1.5 $Hz \leq f \leq f_0$ + 1.5 Hz	$0.88 \leq V \leq 1.15$
Korean	t < 0.5	1	59.3 $Hz \leq f_0 \leq$ 60.5 Hz	$0.88 \leq V \leq 1.10$
IEEE-1547-2018	t < 2	1	58.8 $Hz \leq f_0 \leq$ 61.2 Hz	$0.88 \leq V \leq 1.10$
IEEE-929-2000	t < 2	2.5	59.3 $Hz \leq f_0 \leq$ 60.5 Hz	$0.88 \leq V \leq 1.10$

As per IEEE-1547-2018, the frequency range is between 49 and 51 Hz and the voltage range is 0.88 to 1.1 V p.u. [24]. The different islanding standards for voltage, frequency, and detection time are shown in Table I.

V. PROPOSED METHODOLOGY FOR ISLANDING DETECTION

The proposed method can detect at zero percent power mismatch, and the detection time is also less than that of ROCOF. In this method, the voltage phase angle is first measured at the targeted DG and then the rate of change of voltage phase angle is calculated, to detect the islanding phenomenon. In non-islanding, the rate of change of phase angle is negligible after certain time; but in islanding, this becomes substantial so that the islanding is detected. ROCOVPA also avoids nuisance tripping, thus protecting the stability of the microgrid.

The ROCOVPA method is tested with the 2.5 KW DG with current control mode inverter connected to an RLC load with a quality factor of 1.8. Fig. 4 shows the current control mode to control active and reactive power of load. The proposed method, ROCOVPA islanding detection, is tested on the DG with the control methodology used in Fig. 4.

In the proposed method, the variation of voltage phase angle is monitored at the specified DG. If there is change in the voltage phase angle, the rate with respect to time is calculated. During the islanding, the deviations of the rate of change of phase angle are high enough to detect the islanding condition. If the relay threshold is fixed, then the trip command for tripping the breaker can be initiated.

A. Algorithm for ROCOVPA

The flow diagram of ROCOVPA is explained in the Fig. 5. The voltage phase angle at DG is measured first. After measurement of the phase angle of voltage, the rate of change of voltage phase angle is calculated. In a normal situation, this value is < 1 deg/s (fixed threshold value); but during islanding, the value suddenly crosses the threshold, depending on the fault severity, by means of which the islanding is detected. During non-islanding mode, this value is within limits, hence nuisance tripping is avoided.

VI. DESIGN PARAMETERS OF INVERTER

The proposed method of ROCOVPA is tested on the network shown in Fig. 1 and the parameters are given in in Table II.

The DG capacity with interfaced inverter is 2.5 KW. The interfaced inverter is connected to the main grid through a breaker via the PCC. A three-phase parallel RLC load is connected at the PCC. The input DC voltage to the inverter is 500 V. The output line to line voltage of the inverter is 415 V. The inverter filter resistance and inductance are 0.05 mΩ and 3 mH respectively. The nominal grid frequency is 50 Hz. The inverter switching frequency is 10 KHz. The load parameters with a quality factor of 1.8 are, R = 5.5 Ω, L = 7.8 mH, and C = 900 μF. The load resonant frequency is 50 Hz. Current controller gains are $K_P = 0.4$ and $K_i = 500$.

VII. ANALYSIS AND DISCUSSION OF RESULTS

The designed network is tested in MATLAB / Simulink for islanding cases of unintentional unsymmetrical L-L-G fault and non-islanding cases of connection and disconnection of capacitor load at PCC. The MATLAB simulation results of ROCOVPA and ROCOF are compared. It is proved that ROCOVPA is better than ROCOF.

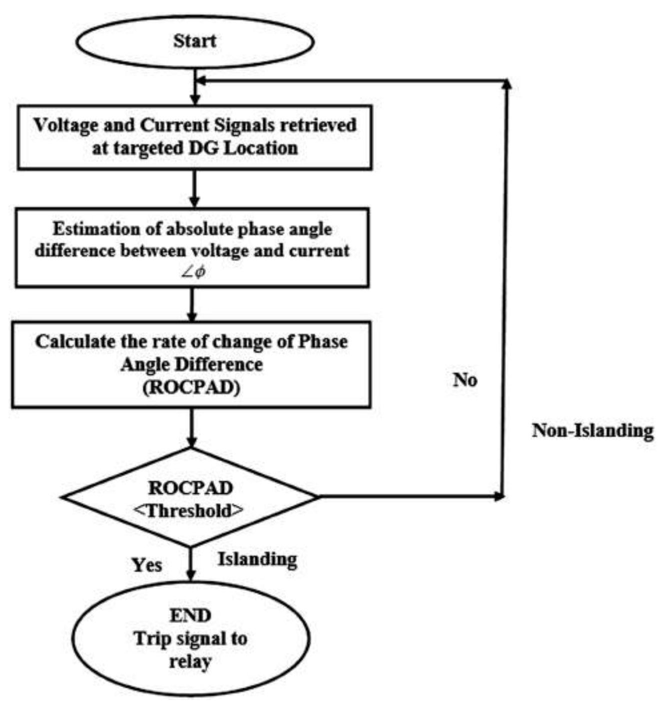

Fig. 5. Flow chart of proposed islanding for the detection of ROCOVPA.

TABLE II.
INVERTER PARAMETERS FOR SIMULATION

Component	Value and Units
DG Power	2.5 KW
Switching frequency	10 KHz
DC input voltage	500
Line voltage	415 V
Inverter Filter inductance Lt	3 m H
Inverter Filter resistance Rt	0.05 Ω
Nominal frequency	50 Hz
Load resistance R	5.5 Ω
Load inductance L	7.8 m H
Load capacitance C	900 μ F
Load quality factor $\left(Q = R\sqrt{C/L}\right)$	1.8
Load resonant frequency $\left(fr = \frac{1}{2\pi\sqrt{LC}}\right)$	50 Hz
Current controller proportional gain, k_p	0.4
Current controller integral gain, k_i	500

A. Islanding case for unsymmetrical fault on the system

The proposed method is tested and compared with ROCOF for islanding case of unintentional unsymmetrical fault L-L-G at 0% power mismatch. In this section, the simulations are discussed for both ROCOVPA and ROCOF, for comparison.

Islanding Testing for L-L-G Unsymmetrical Fault

An L-L-G unsymmetrical fault is initiated on the system at PCC at 0.4 seconds in MATLAB Simulink at 0% power mismatch. PL = PG is the condition for 0% power mismatch, and at that load, a double line-to-ground fault is initiated on the grid side at 0.4 secs on a simulation time of 1 sec. The simulation graph is shown below in Fig. 6. The proposed ROCOVPA detected islanding in 10 ms within a fixed threshold of 1 deg/sec and the relay can exactly detect and send command to trip the circuit breaker to bring the Microgrid to islanding mode from grid mode. The total time is the sum of relay time and breaker time. Any type of the fault is to be cleared within 4 cycles (2 cycles, i.e., 0.04 seconds of relay operation + 2 cycles, 0.04 seconds of breaker operation). Hence, the ROCOVPA can detect the fault condition in less than 1 second and island the microgrid by tripping the circuit breaker, which is less than 2 seconds, as per the standards of IEEE-1547-2018.

The same fault conditions were applied and tested with ROCOF in MATLAB, as shown in Fig. 7, and the islanding was detected in 40 ms. The threshold value was fixed based on the number of simulations, and the threshold value did not cross 0.02 Hz/s in any of the simulations. If the threshold value is fixed at 0.02 Hz/s, the tripping of the circuit breaker can be actuated in around 1 second, which is much below the standards of 2 seconds. The detection time of ROCOF is more than that of ROCOVPA. As the ROCOF is dependent on frequency, at lower percentages of power mismatch, the threshold value cannot be fixed exactly. Hence, detection time varies inversely with the percentage of power mismatch.

To obviate all these issues, ROCOVPA is proposed and proved to be a better islanding detection method for unsymmetrical faults. The MATLAB simulation results of both ROCOVPA and ROCOF are shown in this section.

B. Non-islanding Case for Capacitor Load Connection and Disconnection at PCC on the System

System stability has been studied for different transient conditions during load connection and disconnection at PCC with capacitor load, for ROCOVPA and ROCOF in MATLAB /Simulink. Both methods, ROCOVPA and ROCOF, proved their stability by keeping within the threshold values to avoid nuisance tripping. The ROCOVPA threshold value was fixed at 1 deg/s and that of ROCOF at 0.02 Hz/s based on the number of simulations. The simulation results for non-islanding cases are shown in the following sections.

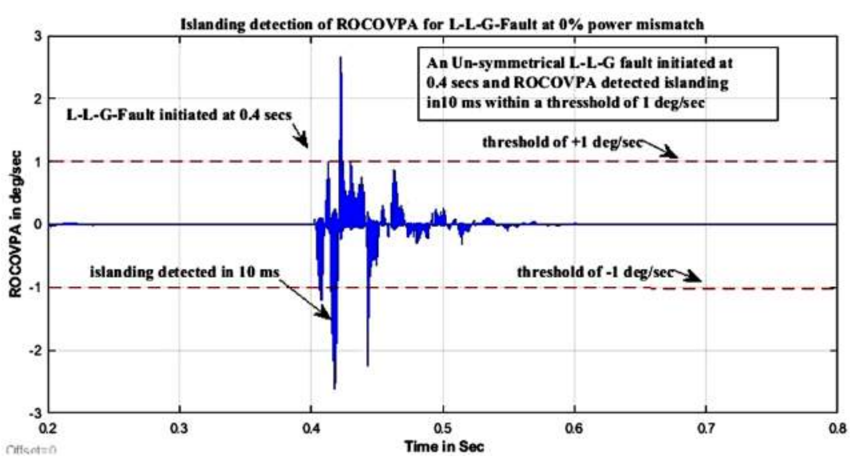

Fig. 6. Islanding detection of ROCOVPA for an L-L-G Fault on the system.

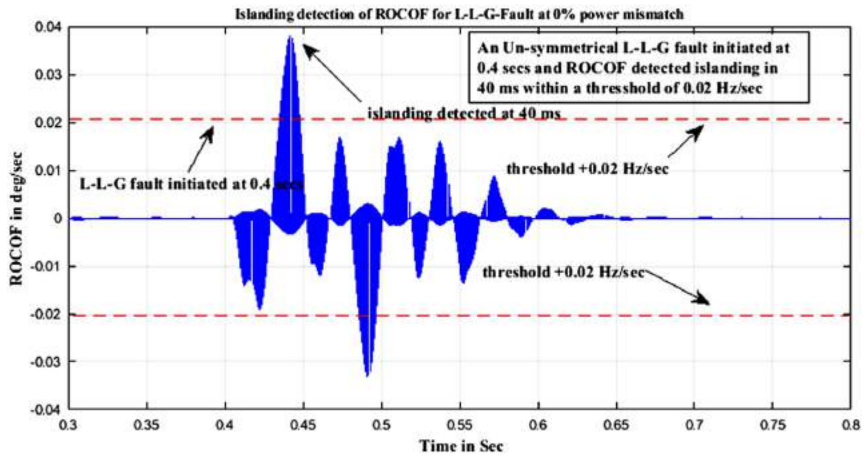

Fig. 7. Islanding detection of ROCOF for an L-L-G Fault on the system.

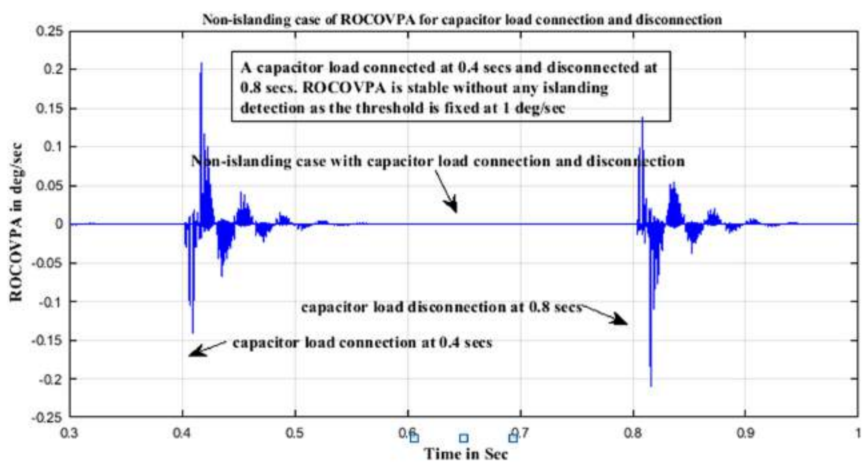

Fig. 8. Non-islanding case of ROCOVPA for capacitor load connection and disconnection.

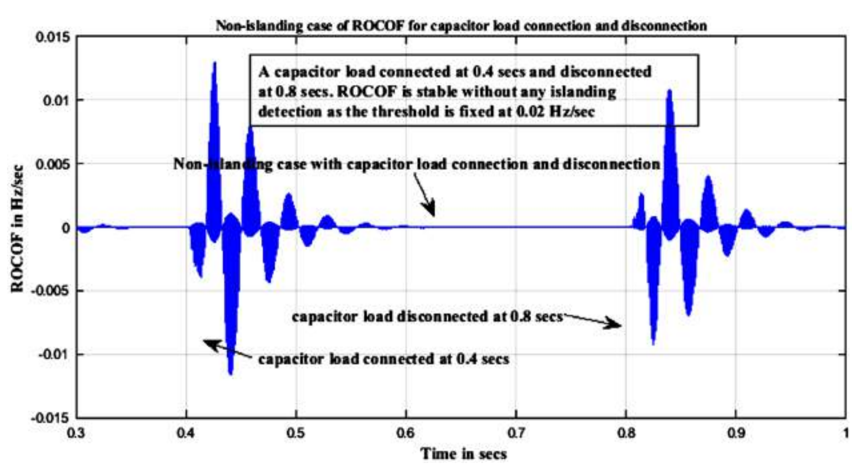

Fig. 9. Non-islanding case of ROCOF for non-linear load connection and disconnection.

Non-islanding Case with Capacitor Load

The stability of the microgrid during non-islanding operation of ROCOVPA and ROCOF during connection and disconnection of capacitor load are tested in MATLAB/Simulink. A capacitor load is connected at PCC at 0.4 seconds and disconnected at 0.8 seconds. The stability of microgrid without nuisance tripping is analyzed through MATLAB simulations. The simulations show that the variations of both ROCOVPA and ROCOF are within threshold values and hence avoid nuisance tripping. The non-islanding conditions with capacitor loads are shown in Fig. 8 and 9. The readings of ROCOVPA and ROCOF show that the thresholds are at higher values, 1 deg/s and 0.02 Hz/s, respectively. Hence, the system is stable without any nuisance tripping of the circuit breaker.

VIII. CONCLUSION

Islanding detection is the main challenge for microgrids. The most common unintentional faults on the system are supposed to be unsymmetrical L-L-G fault, in which two lines are short-circuited and are earthed to the ground. The passive islanding detection method proposed in this paper is ROCOVPA, which is tested for detecting islanding at 0% power mismatch (0% NDZ), with a faster detection time than the widely used ROCOF, and proved to be a better alternative, according to the MATLAB simulation results. This ROCOVPA method was also tested for its stability to avoid nuisance tripping during capacitor load connection and disconnection, and was found to be effective. It is simple to implement in view of methodology, faster in islanding detection (time), safe, and secure. The method discriminates between islanding and non-islanding perfectly, for microgrid operations. The detection is more accurate as the phase angle does not depend on voltage or frequency, and the islanding detection is perfect at almost zero percent mismatch power. Future work is being extended for the detection of symmetrical faults with the same proposed ROCOVPA method and with hybrid DGs.

Peer-review: Externally peer reviewed.

Acknowledgments: The authors acknowledge with thanks the Electrical and Electronics Department of Koneru Lakshmaiah Educational Foundation, Guntur-522502, Andhra Pradesh, India, for bringing this research work into a presentable form and shape.

Conflict of Interest: The authors have no conflict of interest to declare.

Financial Disclosure: The authors declared that this study has received no financial support.

REFERENCES

1. D. Milosevic, and Z. Durisic, “Technique for stability enhancement of microgrids duringunsymmetrical disturbances using battery connected by single phase converters,” in *IET Renew. Powergener. J.*, vol. 14, no. 9, pp.1629–1640, 2020. [CrossRef]
2. H. Samet, F. Hashemi, and T. Ghanbari, “Islanding detection method for inverter-based distributed generation with negligible non-detection zone using energy of rate of change of voltage phase angle,” *Inst. Eng. Technol. Gener. Transm. Distrib. J.*, vol. 9, no. 15, pp. 2337–2350, 2015. [CrossRef]
3. C. R.. Reddy and K. Harinadha Reddy, “Islanding detection for inverter based distributed generation with low frequency current harmonic injection through Q controller and ROCOF analysis,”*J. Electr. Syst.*, vol.14, no. 2, pp. 179–191, 2018.
4. B. Bahrani, H. Karimi, and R. Iravani, “Nondetection zone assessment of an active islanding detection method and its experimental evaluation,” *IEEE Trans. Power Deliv.*, vol. 26, no. 2, pp. 517–525, 2011. [CrossRef]
5. M.-S. Kim, R. Haider, G.-J. Cho, C.-H. Kim, C.-Y. Won, and J. Chai, “Comprehensive review of islanding detection methods for distributed generation systems,” *Energies*, vol. 12, no. 5, p. 837, 2019. [CrossRef]
6. M. Hosseinzadeh and F. R. Salmasi, “Islanding fault detection in microgrids—A survey,” *Energies*, vol. 13, no. 13, p. 3479, 2020. [CrossRef]
7. F. Namdari, M. Parvizi, and E. Rokrok, “A novel passive method for islanding detection in microgrids,” *Iran. J. Electr. Electron. Eng.*, vol. 12, no. 1, pp. 82–90, 2016.
8. O. Tshenyego, R. Samikannu, and B. Mtengi, “Wide area monitoring, protection, and control application in islanding detection for grid integrated distributed generation: A review,” *Meas. Control. Sage J.*, vol. 54, no. 5–6, pp. 585–617, 2021. [CrossRef]
9. H. Pourbabak and A. Kazemi, “A new technique for islanding detection using voltage phase angle of inverter-based DGs,” *Int. J. Electr. Power Energy Syst.*, vol. 57, pp. 198–205, 2013. [CrossRef]
10. W. Ghzaiel, M. J.–B. Ghorbal, and I. Slama-Belkhodza, “Grid impedance estimation based hybrid islanding detection method for AC microgrids”, in Mathematics and Computers in Simulation (2015), MATCOM-4253, pp. 1–15. [CrossRef]
11. P. Kumar, V. Kumar, and B. Tyagi,“Islanding detection for reconfigurable microgrid with RES,” in *IET Gen., Trans. Distrib*. Chichester: Wiley, 2020.
12. M. H. Cintuglu and A. M. Osama, “Islanding detection in microgrids,” in *IEEE Power Ener. Soc. General Meet.*, vol. 2013, pp. 1–5, 2013. [CrossRef]
13. B. Li, J. Wang, H. Bao, and H. Zhang, “Islanding detection for microgrid based on frequency tracking using extended Kalman filter algorithm,” *J. Appl. Math.*, vol. 2014, no. 186360, 2014. [CrossRef]
14. K. Subramanian and A. K. Loganathan, “Islanding detection using a micro-synchrophasor for distribution systems with distributed generation,” *Energies*, vol. 8, p. 5180, 2020. [CrossRef]
15. A. A. Abdelsalam, A. A. Salem, E. S. Oda, and A. A. Eldesouky, “Islanding detection of microgrid Incorporated inverter based DGs using long short-term memory network,” *IEEEE Access*, vol. 13, no. 19, pp. 106471–106486, 2020. [CrossRef]
16. S. Dutta, P. K. Sadhu, M. J. B. Redyy, and D. K. Mohanta, “Shifting of research trends in islanding detection method: A comprehensive survey,” *Prot. Control Mod. Power Syst.*, vol. 3, no. 1, 2018. [CrossRef]
17. N. C. Munukutla, V. S. K. Rao Gadi, and R. Mylavarapu, “A simplified approach to controlled islanding of power system,” in *8th Int. Conf. Power Syst.*, in, “Transition Toward Sustainable, Smart and Flexible Grids, IEEE, ICPS,” pp. 1–7, 2019. [CrossRef]
18. J. Sridevi, V. U. Rani, and B. L. Rao, “Integration of renewable DGs to radial distribution system for loss reduction and voltage profile improvement,” in *1st Int. Conf. Electri. Control Instrument. Eng. (ICECIE)*, 2019, vol. 2019, pp. 1–6. [CrossRef]
19. K. Pranavi, P. L. Reddy, and S. V. N. L. Lalitha, “Optimal sizing and siting of BESS in distribution networks,” *Int. J. Innov. Technol. Explor. Eng.*, vol. 8, no. 6, pp.1073–1078, 2019.
20. B. Srinivasa Rao, S. V. N. L. Lalitha, and Y. Sreenivasarao, “Evaluation of closed-loop-P.I.D, fractional order-P.I.D and proportional resonant controlled micro-grid-schemes,” *J. Comp. Theor. Nanosci.*, vol. 16, no. 5–6, pp.2479–24879, 2019. [CrossRef]
21. C. R. Reddy, K. H. Reddy, and K. V. S. Reddy, “Recognition of islanding data for multiple distributed generation systems with ROCOF shore up analysis,” *Smart Innov. Syst. Technol.*, vol. 1040, pp.547–558, 2019. [CrossRef]

22. B. V. Rajanna and K. S. Srikanth, “Grid connected inverter for current control by using anti-islanding technique,” *IJPEDS*, vol. 9, no. 2, pp. 926–932, 2018. [CrossRef]
23. M. Kiran Kumar, C. Veeranjaneyulu, and N. P. Surya, “Interfacing of distributed generation for micro grid operation,” *J. Adv. Researh Dyn. Control Syst.*, vol. 10, no. 4, pp. 472–447, 2018.
24. K. Jyothi, K. S. Srikanth, and H. S. Jain, “Control of standalone and grid connected distributed energy resource: A review,” *J. Adv. Res. Dyn. Control Syst.*, vol. 10, no. 12 (Special Issue), pp. 1603–1615, 2018.

cigre Turkey

TEPES
TURKISH JOURNAL OF
ELECTRICAL POWER
AND ENERGY SYSTEMS

TEPES, Vol. 2, Issue. 1, 21-30, 2022 **DOI:** 10.5152/TEPES.2022.21048

RESEARCH ARTICLE

Online Parameter Identification of a Simplified Composite Load Model by Voltage Sag Events

Mehmet Karadeniz[1], M. Timur Aydemir[2], Saffet Ayasun[3]

[1]Department of Electrical and Electronics Engineering, Kyrgyz-Turkish Manas University, Bishkek, Kyrgyzstan
[2]Department of Electrical and Electronics Engineering, Kadir Has University, İstanbul, Turkey
[3]Department of Electrical and Electronics Engineering, Gazi University, Ankara, Turkey

Cite this article as: M. Karadeniz, M. T. Aydemir & S. Ayasun. Online parameter identification of a simplified composite load model by voltage sag events. *Turk J Electr Power Energy Syst,* 2022; 2(1): 21-30.

ABSTRACT

Monitoring power quality events that occur in a power grid and determining their causes are important in terms of taking preventive actions. Power quality events are generally caused by structural changes in the network. Network loads are also affected by power quality events as a part of the network or they may cause power quality events themselves due to a sudden change in their structure. In this respect, when a power quality event occurs, the estimation of the behavior of the network loads contributes to the determination of the causes of the power quality events. In this study, a new method is developed to identify the parameters of a composite load model to estimate the response of network loads to certain power quality events. The method identifies model parameters using the voltage sag or swell data. By this model, it is possible to estimate the response of the loads and detect whether there is a change in the load. In this way, it becomes easier to understand whether the event is caused by the load or the network, which eventually helps us find the causes of power quality events. Simulation studies show that the load parameters identified by the method using a voltage sag are close to the actual load parameters, and the load behavior estimated by the load model in case of any power quality event is very close to the real load.

Index Terms—Voltage sag/swell, composite load modeling, parameter identification, power quality

I. INTRODUCTION

Power quality issues have been drawing a lot of attention in modern power systems. For customers to sustain quality service, the identification of events that negatively affect power quality is crucial to reduce their adverse effects. Observed power quality events as transients distort waveforms within the network. Voltage dips, transients, peeks, or voltage fluctuation is types of power quality problems. These events reduce the quality of the power supplied to the customers and have negative effects on other components and devices in the network. In order to take the necessary precautions against power quality events, it is vital to determine the types and causes of power quality problems. Power quality is defined as “a set of electrical boundaries that allows an equipment to function in its intended manner without significant loss of performance or life expectancy[1].”

Events affecting the power quality in the network are generally caused by structural changes such as changes in network lines or network loads. In order to find the causes of an event, possible scenarios should be examined and their results should be compared. For that purpose, a load model that can estimate the response of loads to events is contributive to analyzing an event. As a result of an event in the network, when the voltages at certain points of the network go beyond the normal operating range, obtaining a model that can accurately estimate the instantaneous response also has the following important advantages: (1) providing the status and characteristics of network loads and (2) allowing the detection of the changes in the loads in the network, thus making it possible to observe the changes of these loads over time. Having a load model for each load on the grid, it will be easier to determine if there is a change in the grid and at what point the change occurred.

In the literature, there are studies on several load models. Polynomial model or constant impedance (Z), constant current (I), constant power (P) (ZIP) model is one of the first among these load models based on the assumption that a load is composed of constant impedances, constant current, and constant power drawing components [2]. However, it is a static model and does not take

Corresponding author: Saffet Ayasun, saffetayasun@gazi.edu.tr

Received: November 26, 2021
Accepted: February 14, 2022

into account the load dynamics. There are studies in which the ZIP model and induction motor model are used to model dynamics of load, which is called composite load [3-5]. In these models, there are difficulties in parameter identification. To overcome these difficulties, a simplified composite load model is presented which consists of only one impedance and an induction motor [6-9]. The parameters of this model can be obtained using data from a detected power quality event. Another form of a load model is the transfer function-based load model [10]. More recent studies dedicated to Western Electricity Coordinating Council (WECC) [11-13] were encountered to more severe identification problems. However, WECC composite load model has too many parameters, an effort to reduce the number of parameters is needed [14].

Apart from the accurate model selection, method selection is also another consideration. There are several methods used in parameter identification mainly based on statistical and heuristic techniques. In the group of statistical methods, there are weighted least square-based estimation [15], least square-based parameter estimation [16], and maximum likelihood-based estimation [17]. In the group of heuristic methods, there are genetic algorithms [18], neural networks [19], and simulated annealing algorithms [20]. In [21], it was reported that: (1) the maximum likelihood approach was a time-consuming task, and the probability density function of measurements is needed to define the likelihood function, which may be unknown in practice and (2) The gradient-based approach was vulnerable to data pollution. Although the genetic algorithm is a multi-point search algorithm and can be adapted to different problems, it requires too much computation. Artificial neural networks can be trained with measurement data without requiring knowledge of the structure of the load model. However, the convergence rate of this method is quite slow. The simulated annealing method does not require the knowledge of the structure of the load model. However, the repeated annealing process is slow.

Based on the discussion given above, this study aims to obtain the load model as quickly as possible and to examine the causes of the events, and for this reason, the focus is given on the simple composite load model. The simplified composite load model is based on the assumption that a grid load can be modeled with an impedance and an induction motor. According to the study of Savio et al., many induction motors connected to a bus behave like a single induction motor [22]. Accordingly, it is understood that a real load consisting of *N* number of induction motors and *M* number of impedance loads can be modeled with an induction motor and an impedance connected with each other in parallel.

Main Points

- The effect of power quality events on the load model and dynamics.
- A new method to identify composite load parameters using voltage sag or swell data.
- Fast identification of composite load parameters and model with sufficient accuracy.

There are studies on identifying the parameters of the simplified composite load model. In [3] and [23], an online method was proposed based on parameter tuning. In [7], the most important parameters of the composite load were identified with a two-step approach. In these methods, the identification process has calculation loops: amount of impedance and motor parts of the load are obtained after the trial-and-error process. Power quality events occur frequently and it is possible for an event to affect the load and causes permanent changes in the load. In this case, when a power quality event occurs, the load model will need to be determined quickly. Therefore, while these methods mentioned can be used in stability analysis, they may not be fast enough to catch up with power quality events. For this reason, the main purpose of this study is to develop a less sensitive but faster method.

In this study, a method has been developed in which model parameters can be identified with the data of voltage sag or swell that occurred in the network. The model consists of an impedance in which the resistance and inductance are connected in series and an induction motor connected in parallel. This aggregated load model is able to estimate the response of a load to events that occurred, and more generally to estimate the current drawn. An event that occurred in the network causes instantaneous changes in the voltage of the load, and the current drawn by the load can be estimated by the proposed approach. Once the parameters of the model have been identified, the load response to new events can now be estimated, and whether there is a change in the load in each event can be determined with the available measurement data. The parameters of the model are identified by the data of voltage drop events. The model of which parameters are identified by the method can estimate the load response for any event that may occur afterward. With this method, the impedance part of the load and the important parameters that affect the motor dynamics are determined. Compared to the studies in the literature, it is observed that these parameters are obtained with less computational effort in a shorter time. By comparing the estimation results obtained with the response of the actual load, it can be determined whether the load has changed in the following events. Furthermore, by including the load model in the network model, events that may occur in the network can be examined. The most important advantage of the method is that the process of parameter determination provides the result in a short time and with less processing. With this method, load parameters are identified with a certain error rate and the response of the load can be estimated successfully. The amount of error in the determination has little negative effects on estimating the response of the load. Therefore, the results of the method can be used directly in estimating the response of the load or the values identified by this method can provide initial values to other methods.

II. COMPOSITE LOAD MODEL

The simplified composite load model takes impedance and motor loads into account. In Fig. 1, the structure of the composite load recommended by IEEE is presented [25]. Note that the composite load model consists of a static impedance load and an equivalent induction motor part. The equivalent induction motor part of this model has been developed by neglecting the stator transients based on the dynamic model of the induction motor and was generally used in

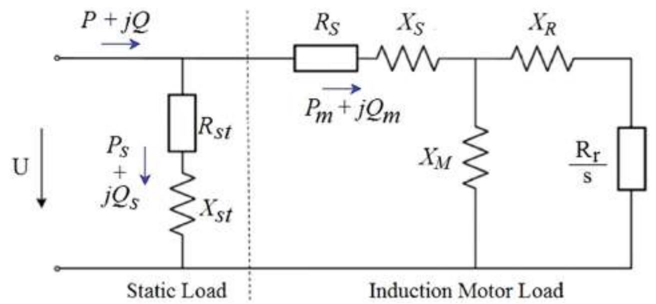

Fig. 1 . Simplified composite load structure and circuit.

system stability studies [24, 25]. The state equations of equivalent induction motor can be written as:

$$\begin{aligned}
\frac{dE_d}{dt} &= -\frac{1}{T_0'}\left(\frac{X}{X'}E_d - \frac{X-X'}{X'}U_d\right) + \omega_0 s E_q \\
\frac{dE_q}{dt} &= -\frac{1}{T_0'}\left(\frac{X}{X'}E_q - \frac{X-X'}{X'}U_q\right) - \omega_0 s E_d \\
\frac{ds}{dt} &= -\frac{1}{H}\left(P_{mt} - P_{mt0}\left(A\omega_r^2 + B\omega_r + C\right)\right)
\end{aligned} \quad (1)$$

where

$$X' = X_S + X_M // X_R ; T_0' = \frac{\left(X_M + X_R\right)}{\omega_0 R_r} ; X = X_S + X_M ; A+B+C=1 \quad (2)$$

There are many parameters to be determined in this model and it is very difficult to determine all of them. Here, some assumptions can be made to simplify and thus, the reduced number of parameters are to be determined. It is stated in the literature that the effect of the stator resistance R_s, the magnetization impedance X_M,and the mechanical coefficients *A*, *B*, and *C* on the electromechanical dynamic characteristics of the motor is quite low [7]. These parameters, which have little effect on the load, can be excluded from the load model, and this simplifies parameter identification process. With these assumptions, the new approximate model of the composite load is shown in Fig. 2.

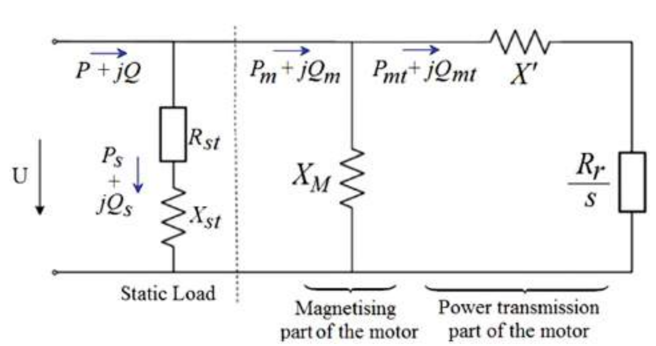

Fig. 2 . Simplified composite load with a modified motor model.

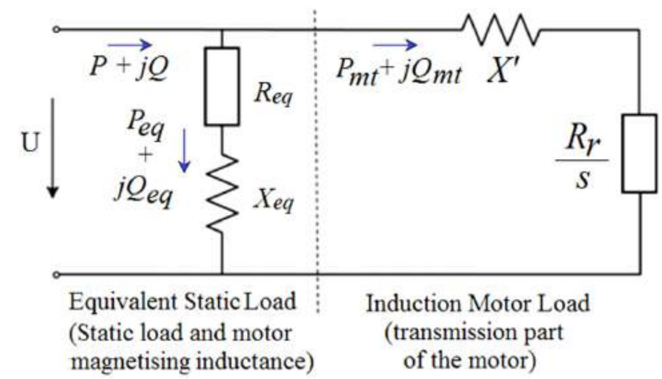

Fig. 3 . Simplified composite load circuit.

As a result, the induction motor part of the load model can be represented in two parts as "magnetizing part" and "power transmission part" as shown in Fig. 2. X_M is a negligible term in the motor part since the value of magnetizing reactance is much greater than the other reactances of the motor in practice and therefore, the current on it is much smaller. Besides, since X_M essentially exhibits an impedance behavior, it can be displayed in the static impedance part of the load. Thus, the static load and the magnetizing reactance are represented as an equivalent impedance as follows:

$$R_{eq} + jX_{eq} = jX_M // \left(R_{st} + jX_{st}\right) \quad (3)$$

Additionally considering that $X \gg X'$, $\omega_r \simeq 1$ and $A+B+C=1$, the motor part of the model shown in Fig. 3 can be further simplified as

$$\begin{aligned}
\frac{dE_d}{dt} &= -\frac{\omega_0 R_r}{X'}\left(E_d - U_d\right) + \omega_0 s E_q \\
\frac{dE_q}{dt} &= -\frac{\omega_0 R_r}{X'}\left(E_q - U_q\right) - \omega_0 s E_d \\
\frac{ds}{dt} &= -\frac{1}{H}\left(P_{mt} - P_{mt0}\right)
\end{aligned} \quad (4)$$

Stator currents I_d and I_q are given as

$$I_d = \frac{U_q - E_q}{X'} ; I_q = \frac{E_d - U_d}{X'} \quad (5)$$

Active and reactive powers drawn by the motor (power transmission part) are given as follows:

$$P_{mt} = U_d I_d + U_q I_q ; \quad Q_{mt} = -U_d I_q + U_q I_d \quad (6)$$

It must be noted here that the reactive power in (6) does not include the reactive power drawn by the magnetization impedance since it is included in the reactance X_{eq}. Furthermore, the following equations for the active, reactive and apparent power in the power transfer part of the motor, which are valid for steady-state conditions, will be used in load identification:

$$
\begin{aligned}
P_{mt0} &= \frac{R_r}{s_o} I_0^2 \\
Q_{mt0} &= X' I_0^2 \\
P_{mt0}^2 + Q_{mt0}^2 &= U_0^2 I_0^2
\end{aligned}
\tag{7}
$$

At this point, it will be informative to discuss the similarities and differences between the active and reactive powers (P_m, Q_m) drawn by the motor in Fig. 1 and the active and reactive powers (P_{mt}, Q_{mt}) of the power transmission part of the motor presented in Fig. 3: (1) Active powers are very close to each other ($P_m \approx P_{mt}$) and (2) Since the main reactive power of the motor is in the magnetizing reactance, the reactive power Q_m drawn by the motor is much bigger than the reactive power in the power transfer part of the motor ($Q_m \gg Q_{mt}$).

Based on these assumptions, it can be assumed that the current drawn by the power transmission part of the motor is proportional to the active power drawn by the motor. It must be stated here that the state variables of the model are *d*- and *q*-axis transient electromotive forces E_d and E_q, rotor slip *s*, and current of equivalent reactance X_{eq}. Model response to any further event can be obtained by set of equations in (4) and (8):

$$
\begin{aligned}
\frac{d}{dt} i_{eq\_d} &= \frac{1}{L_{eq}} \left(U_d - R_{eq} i_{eq\_d} + L_{eq} \omega_0 i_{eq\_q} \right) \\
\frac{d}{dt} i_{eq\_q} &= \frac{1}{L_{eq}} \left(U_q - R_{eq} i_{eq\_q} - L_{eq} \omega_0 i_{eq\_d} \right)
\end{aligned}
\tag{8}
$$

where i_{eq} is current on impedance $R_{eq}+jX_{eq}$ at rotor reference frame.

III. PARAMETER IDENTIFICATION OF THE LOAD MODEL

In this study, the model parameters are identified in two steps. In the first step, the steady-state values before and after voltage sag/swell events that occur at least one or more times are used, and with these data, the equivalent impedance in Fig. 3 and the transient reactance values of the motor are identified. In the second step, the rotor resistance of the motor and mechanical rotation inertia parameters is identified by using the instantaneous measurement data of only one event, and the rotor slip values are estimated. Since this method does not contain cyclic or loop operations based on trial and error, the amount of calculation is low and has a forward-oriented algorithm. The steps involved in determining the model parameters are given in Fig. 4.

A. Parameter Identification of Static Impedance and Transient Reactance of the Motor

In this first step, only pre- and post-event steady-state measurement values are used for voltage sag or swell events. The values that can be measured are the network voltages and the active and reactive powers of the load. However, symmetrical component analysis is processed, and positive sequence components of active and reactive values are used for identification. After estimating the impedance part of the load and the active and reactive powers drawn by the motor part from the measured values, the values of the impedance part of the load and the transient reactance of the motor can be identified. First of all, some assumptions are required in order to estimate the active and reactive powers drawn by the induction motor and impedance parts of the load. The assumptions developed step by step for steady-state conditions in this study are as follows:

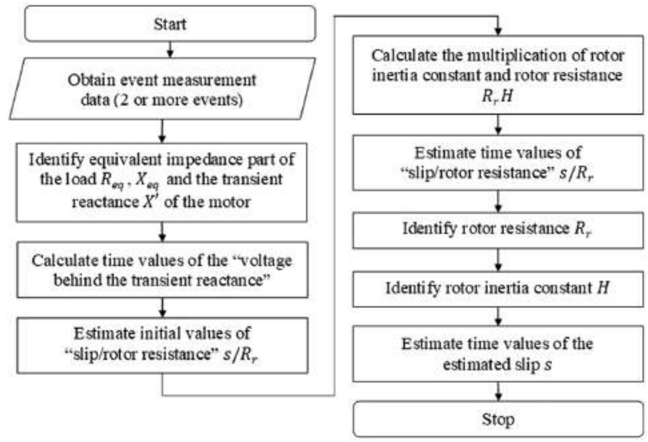

Fig. 4. Algorithm for identification of model parameters.

i) Positive sequence components of active and reactive power of the equivalent impedance part of the load are expected to be approximately proportional to the square of the busbar voltage at steady-state ($P_{eq0}^{+} \propto U_0^2$, $Q_{eq0}^{+} \propto U_0^2$).

ii) At the steady-state condition, it is observed that the effect of the busbar voltage level on the active power drawn by the motor is quite low. The active power values drawn by the motor part before and after the event are very close to each other. Such a feature is observed because the power demand of the mechanical load is not affected much by the voltage sag/swell and the motor continues to operate to meet the mechanical load demand. Although the active power values of the motor are very close to each other, also a difference can be explained by the thermal losses in the resistances and the effect of the mechanical load. Therefore, it is assumed that a significant part of the active power drawn by the motor part is a constant value ($P_{mt0}^{+} \cong y_{p2}$, where y_{p2} is a constant value).

iii) Since the active power of the induction motor does not change much with respect to the voltage changes and there is a small amount of reactive power in the motor power transfer part, it can be assumed that the current drawn by the motor power transmission part in a given operating range is inversely proportional to the busbar voltage ($I_0 \propto U_0^{-1}$).

iv) The reactive power drawn by the motor power transmission part depends on the transient reactance X' ($Q_{mt0}^{+} = X' I_0^2$). Therefore, the reactive power of the motor power transmission part is inversely proportional to the square of the busbar voltage ($Q_{mt0}^{+} \propto U_0^{-2}$ or $Q_{mt0}^{+} \cong y_{q2} U_0^{-2}$ where y_{q2} is a constant value).

v) The amount of reactive power drawn by the impedance part of the load is expected to be proportional to the square of the grid voltage ($Q_{eq0}^{+} \cong y_{q1} U_0^2$, where y_{q1} is a constant value).

Finally, the active and reactive powers drawn by the load are the sum of the powers drawn by the two parts of the load:

$$\begin{aligned} P_0^+ &= P_{eq0}^+ + P_{mt0}^+ \\ Q_0^+ &= Q_{eq0}^+ + Q_{mt0}^+ \end{aligned} \tag{9}$$

The subscript "0" in (9) denotes the steady-state values of the attributes. Based on these features and assumptions, any arrays $Y_p = [y_{p1}, y_{p2}]^T$ and $Y_q = [y_{q1}, y_{q2}]^T$ with constant elements, the following equations can be written:

$$\begin{aligned} P_{eq0}^+ &= y_{p1}U_0^2 \\ Q_{eq0}^+ &= y_{q1}U_0^2 \\ P_{mt0}^+ &= y_{p2} \\ Q_{mt0}^+ &= y_{q2}U_o^{-2} \end{aligned} \tag{10}$$

Substituting these expressions in (9), the following equations are obtained:

$$\begin{aligned} P_0^+ &= y_{p1}U_o^2 + y_{p2} \\ Q_0^+ &= y_{q1}U_o^2 + y_{q2}U_o^{-2} \end{aligned} \tag{11}$$

At least voltage sag/swell events must occur in order to solve these equations. If the values to be used in the solution for different steady-state voltage levels as a result of the events that occur are enumerated, the following equations in a compact form are obtained:

$$\underbrace{\begin{bmatrix} P_{01}^+ \\ P_{02}^+ \\ \vdots \\ P_{0N}^+ \end{bmatrix}}_{P} = \underbrace{\begin{bmatrix} U_{01}^2 & 1 \\ U_{02}^2 & 1 \\ \vdots & \vdots \\ U_{0N}^2 & 1 \end{bmatrix}}_{U_a} \underbrace{\begin{bmatrix} y_{p1} \\ y_{p2} \end{bmatrix}}_{Y_p} ; \underbrace{\begin{bmatrix} Q_{01}^+ \\ Q_{02}^+ \\ \vdots \\ Q_{0N}^+ \end{bmatrix}}_{Q} = \underbrace{\begin{bmatrix} U_{01}^2 & U_{01}^{-2} \\ U_{02}^2 & U_{02}^{-2} \\ \vdots & \vdots \\ U_{0N}^2 & U_{0N}^{-2} \end{bmatrix}}_{U_a} \underbrace{\begin{bmatrix} y_{q1} \\ y_{q2} \end{bmatrix}}_{Q_p} \tag{12}$$

or

$$Y_P = \left(U_a^T U_a\right)^{-1} U_a^T P \tag{13}$$

$$Y_Q = \left(U_a^T U_a\right)^{-1} U_a^T Q$$

According to this formulation, at least two voltage level values are required and, in this case, steady-state data of at least an event is required. The voltage, active, and reactive powers are measured values, and from the values obtained from the solution of the equations, the equivalent impedance and transient reactance parameters are found:

$$y_{p1} = \frac{R_{eq}}{\left|Z_{eq}\right|^2};\, y_{q1} = \frac{X_{eq}}{\left|Z_{eq}\right|^2};\, y_{q2} = Q_{mt0}^+ U_0^2 = X' U_0^2 I_0^2 \tag{14.a}$$

or equivalently,

$$\left|Z_{eq}\right| = \sqrt{y_{p1}^2 + y_{q1}^2};\, R_{eq} = y_{p1}\left|Z_{eq}\right|^2;\, X_{eq} = y_{q1}\left|Z_{eq}\right|^2 \tag{14.b}$$

equations are obtained. After R_{eq} and X_{eq} are identified, the equivalent impedance and then the stator current of the induction motor are calculated. After the steady-state current of the motor I_0 is found, the transient reactance is obtained as described below:

$$X' = \frac{y_{q2}}{U_0^2 I_0^2} \tag{15}$$

B. Parameter Identification of Motor Side

Once the parameter X' is obtained, the voltage values behind the transient reactance are obtained as a function of time:

$$\begin{aligned} E_d(t) &= U_d(t) + X' I_q(t) \\ E_q(t) &= U_q(t) - X' I_d(t) \end{aligned} \tag{16}$$

Let s_r be the ratio of slip to rotor resistance with slip s:

$$s_r(t) = \frac{s(t)}{R_r} \tag{17}$$

At the steady-state, the ratio of slip/rotor resistance s_{r0} is given below:

$$s_{r0} = \frac{s_0}{R_r} = \frac{I_{d0}}{E_{d0}} = \frac{I_{q0}}{E_{q0}} \tag{18}$$

is valid and from these equations above the initial values of $s_r(t)$ are determined before the event. It is possible to write the power equation as follows for any event where t_a is the start and t_b is the ending time of the event:

$$s_r(t) = s_r(t_b) - \frac{1}{R_r H}\int_{t_a}^{t_b}\left(P_{mt}^+(t) - P_{mt0}^+\right) \tag{19}$$

With this equation, instantaneous values of $s_r(t)$ during the event are estimated. After that, it becomes possible to identify the rotor resistance. State equations regarding voltages can be written as

$$\frac{dE_d}{dt} = R_r\left(-\frac{\omega_0}{X'}\left(E_d - U_d\right) + \omega_0 s_r E_q\right) \tag{20}$$

$$\frac{dE_q}{dt} = R_r\left(-\frac{\omega_0}{X'}\left(E_q - U_q\right) - \omega_0 s_r E_d\right)$$

Since the voltage values are obtained instantaneously, the identification process becomes easier. After labeling the integrals as

$$A_d = \int_{t_a}^{t_b}\left(-\frac{\omega_0}{X'}\left(E_d(t) - U_d(t)\right) + \omega_0 s_r(t) E_q(t)\right)dt \tag{21}$$

$$A_q = \int_{t_a}^{t_b}\left(-\frac{\omega_0}{X'}\left(E_q(t) - U_q(t)\right) - \omega_0 s_r(t) E_d(t)\right)dt$$

the rotor resistance can be identified as follows:

$$R_r = \sqrt{\frac{\left(E_d\left(t_a\right)-E_d\left(t_b\right)\right)^2+\left(E_q\left(t_a\right)-E_q\left(t_b\right)\right)^2}{A_d^2+A_q^2}} \tag{22}$$

After the rotor resistance is identified, slip values are obtained using (17).

It must be emphasized here that all equations have been developed for the identification of parameters of a composite load. The model of induction motor is a part of this composite load. The composite load model consists of an RL impedance and an induction motor. Impedance is a serially connected resistance and an inductance, which means an impedance of $\left(R_{st}+jX_{st}\right)$. The motor magnetizing impedance jX_m and RL impedance, which are considered to be connected parallel to each other, constitutes an equivalent impedance of $R_{eq}+jX_{eq}$. Moreover, the important parameters of the motor and the equivalent impedance part were identified. The identified motor parameters are X' (transient reactance of the motor), R_r (rotor resistance of the motor), and H or J (Rotor inertia constant) While the identified impedance parameter are R_{eq} and X_{eq}. In summary, the model has four state variables and five parameters. These 5 parameters are identified in the identification process through Eqs. (9)–(22). After identification is executed and parameters are obtained, model response to any event is obtained by Eqs. (4) and (8).

IV. RESULTS

Three case studies have been investigated to illustrate the performance of the method. The first study deals with a load consisting of only one impedance and an induction motor. The purpose of this case study is to show how accurately the method can estimate parameters and to investigate how to estimate the load behavior. In the second case study, the estimation performance of the method to a more realistic load is examined. In this study, the load consists of a voltage-reducing transformer, multiple impedances and induction motors, and reactive power compensators as well. The third case study shows the method's contribution in determining the cause of an event. In this study, a network consisting of a voltage supply and two loads is considered. The loads consist of a voltage-reducing transformer, multiple impedances and induction motors, and reactive power compensators as in case study 2. Both in studies 2 and 3, the measurements are taken on the high voltage side of the transformer connected to the network, since data are more available on the network side.

A. Case Study 1 Composite Load Consisting of an Impedance and an Induction Motor

The parameters of the impedance and the induction motor are given as: the impedance: R_{st} = *19.2 Ω* and X_{st} = *10.8573 Ω.* The induction motor data: 3 *HP*, 220 V_{LL}, 60 Hz, $X_{ls} = X_{lr}$ = 0.7540 Ω, X_m = 26.012 Ω, R_s = 0.435 Ω, R_r = 0.816 Ω, J = 0.089 kg·m^2. The load with these parameters will have equivalent impedance and transient reactance values as follows: Z_{eq} = 7.5182 + j11.5752 Ω = 13.802 ∠ 56.996^0 Ω, X' = 1.486 Ω, the rated rotational inertia of the motor is T_L = 11.9 N.m.

Event 1: While the amount of load T_L = 11.9 N m is applied to the rotor, a voltage drop event occurs at t = 1.0 s with a different depth of 9.1%, 22.73%, and 4.55% (20 V, 50 V, and 10 V drop) for each phase. With the data of this event, the parameters of the load model were estimated using the proposed method and the following values were obtained: Z_{eq} = 7.928273 + j11.663606 Ω = 14.103 ∠ 55.794° Ω, X' = 1.2744 Ω, R_r = 0.9407 Ω, J = 0.08609 kg m^2. It is clear that estimated parameters are very close to the real values. Moreover, in Fig. 5, the active and reactive powers drawn by the load and the results of the estimation of the model are shown for the case of voltage drop at t = 1.0 s to illustrate the accuracy of the method. It is clear from Fig. 5 that the real and reactive power estimated (solid red line) closely follows the actual ones (solid blue line). At steady-state, the error rate in active and reactive power estimation of the total load is 0.0104% and 0.01737%, respectively. Although its parameters are obtained with a certain error rate, the estimation results on the active and reactive powers of the model are more satisfactory. The identification process was executed within 0.17782 s using data sampled 2000 samples/second by a personal computer having Intel(R) Core(TM) i5-10210U CPU @ 1.60GHz microprocessor and 16 GB RAM.

Event 2: The model can identify the load when a much deeper voltage sag has occurred. In case of voltage drop at phases are 45%, 18% and 36% (100 V, 40 V and 80 V drop), following values were obtained: Z_{eq} = 8.046430 + j11.406010 Ω = 13.802 ∠ 56.996° Ω, X' = 1.411 Ω, R_r = 0.973 Ω, J = 0.0752 kg.m^2. At steady-state, the error rate in active and reactive power estimation of the total load is 0.91% and 1.75%,

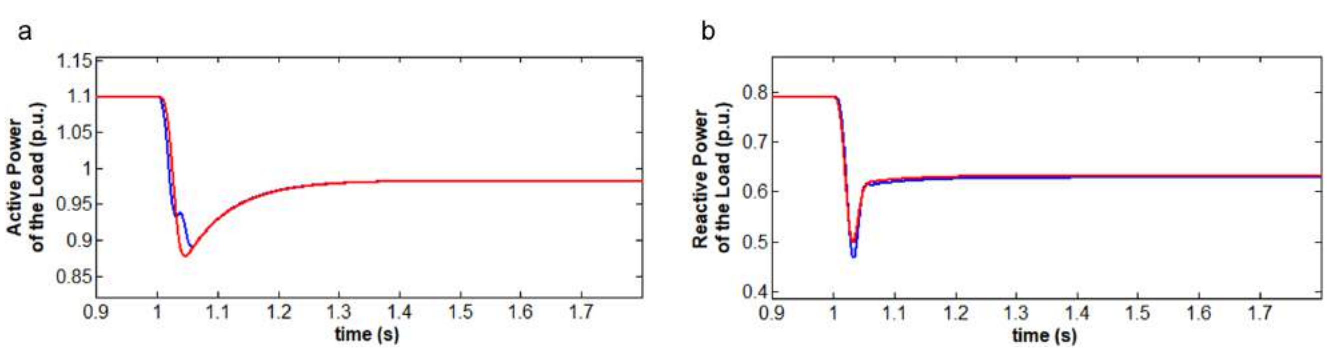

Fig. 5. Comparison of the actual and estimated real and reactive powers for case study 1, event 1: (a) actual and estimated active power and (b) actual and estimated reactive power (actual and estimated powers are presented in blue and red, respectively).

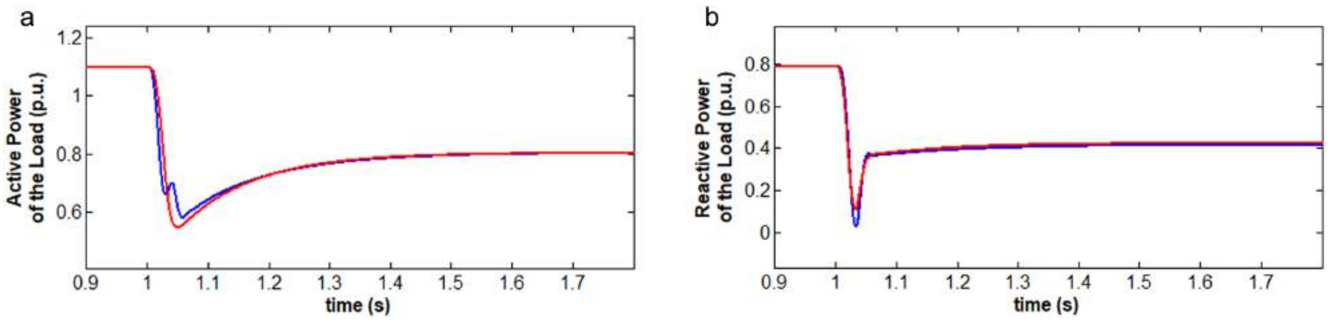

Fig. 6. Comparison of the actual and estimated real and reactive powers for case study 1, event 2: (a) actual and estimated active power and (b) actual and estimated reactive power (actual and estimated powers are presented in blue and red, respectively).

respectively, which shows that the less deep voltage sag results in better estimation. Results are presented in Fig. 6.

While discussing the performance of the proposed method, it is also necessary to estimate the parameter for different values of the network voltages, motor mechanical loads, and for several voltage sag/swell depths. In order to fulfill this requirement, firstly the network voltages and then the load of the motor and the depth of voltage drop are changed individually, and the results were compared. The estimated parameters of motor and impedance part obtained for different network voltage between 190 V and 260 V at a step of 10 V are shown in Table I. Z_{eq} =13.802∠56.996°Ω is the real and $Z_{eq(est)}$ is the estimated value of the equivalent impedance. Parameters are identified with a percentage error of 1.5% for the equivalent impedance $Z_{eq(est)}$, 11% for the rotor resistance $R_{r(est)}$, 4.4%, for mechanical inertia $J_{(est)}$, and *2–7%* for the transient reactance $X'_{(est)}$.

B. Case Study 2 Multiple Impedances and Induction Motors

Case 1 focuses on the identification of load parameters for a single impedance and induction motor. In practice, loads consist of many components and are compensated by compensation units. In this case study, the load to be identified is consists of 11 different impedances and 7 different induction motors having different parameters and mechanical loads and the load is compensated with a 0.85 power factor compensation. Additionally, it is considered that the composite load is connected to the grid by a transformer, and the measurement values are taken from the grid side of the transformer. The load is fed by 460 V (*L-L*), and its operating power is 390 kW. In Fig. 7, active and reactive powers drawn by the load and the estimation results of the model are shown for a voltage sag with different depths of 30%, 15%, and 5% (138 V, 69 V, and 23 V drop) for each phase at t = 1.0 s. At the steady-state condition, the error rate in active and reactive power estimation are found to be 0.1745 % and 1.857 %, respectively. As clearly seen in Fig. 7, the real and reactive powers estimated using the proposed method (solid red line) closely follow the actual real and reactive powers (solid blue line). In this case study, the load to be identified consists of more than one motor and impedance with different parameters as in real situations. Since the direct calculation of the motor-impedance load parameters equivalent to the identified load is another research subject in itself, the comparison of the estimated parameters has not been made here. Instead, the comparison for this case is performed only in terms of the real and reactive power estimation.

TABLE I.
ESTIMATED PARAMETERS FOR DIFFERENT GRID VOLTAGE LEVELS

Voltage *L-L* (V)	$X'_{(est)}$ (Ω)	$R_{r(est)}$ (Ω)	$J_{(est)}$ (kg m²)	$Z_{eq(est)}$ (Ω)
190	1.395	0.939	0.081	13.902∠55.267°
200	1.342	0.919	0.084	14.042∠56.060°
210	1.363	0.915	0.084	14.029∠56.133°
220	1.391	0.912	0.084	13.999∠56.083°
230	1.414	0.906	0.084	13.978∠56.047°
240	1.429	0.900	0.085	13.965∠56.028°
250	1.439	0.894	0.085	13.958∠56.022°
260	1.446	0.888	0.085	13.953∠56.022°

C. Case Study 3 Identification of the Cause of an Event

This case study is considered to show the contribution of the method in determining the cause of an event. The main idea is to use load models to detect whether the load is changed. If a load and its model's responses match, then it can be deduced that this load is not changed. However, if the load's response and its model's response do not match from the beginning of a moment, it can be deduced that the load is changed at this moment and probably causes an event. A simple network shown in Fig. 8 is considered to have two loads are connected to a supply through lines. Loads have the same ratings as in case 2.

The aim of this study is to detect the cause of an event occurring at a time interval of 1.0–1.05 s. At this time interval, two large induction motors are started by closing their circuit breaker at load 2, and at time 1.05 s, circuit breakers are opened. These turning on and turning off of induction motors cause events in the network which affect load 1. After events occurred, if measurement data is not recorded, it is not possible to find which load has temporarily changes and causes an event since both loads seem to be unchanged after the event has occurred. From the models' responses, we can detect which one has changed and caused the event.

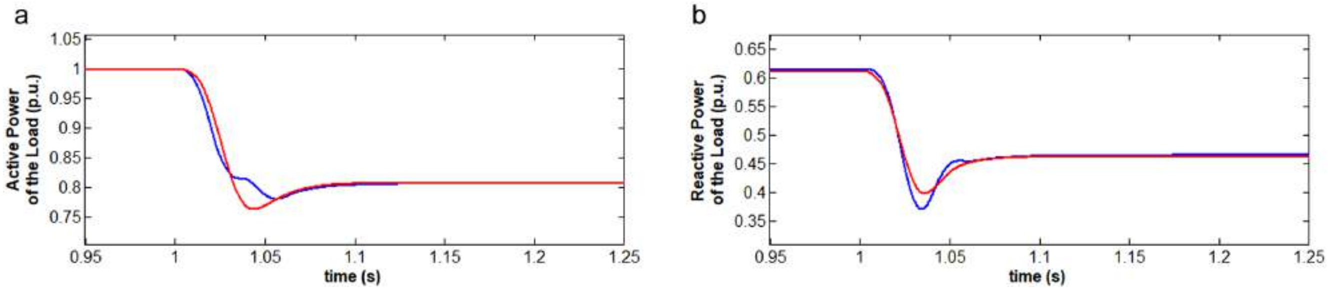

Fig. 7. Comparison of the actual and estimated real and reactive powers for case study 2: (a) actual and estimated active power and (b) actual and estimated reactive power (actual and estimated powers are presented in blue and red, respectively).

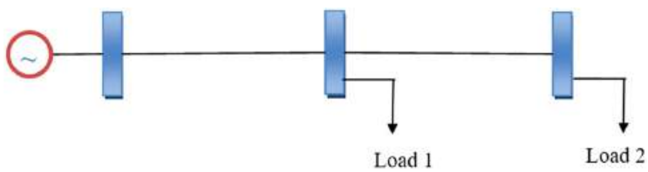

Fig. 8. The network is considered in case study 3.

The scenario considered is as follows: Between 0.3 s and 0.7 s a voltage sag event occurs. At 1.0 s, one of the large motor's circuit breakers of load 2 is closed, and at 1.05 s the circuit breakers are opened and load 2 remains as it was in before the time 1.0 s. After 1.05 s, Load 2 has the same characteristics as before and now it is not possible to find out if the load is changed and caused an event by steady-state measurement values after the event occurred. Referring to load models, it can be deduced when and if the load is changed.

In Fig. 9, actual and model responses of loads 1 and 2 are shown. Fig. 9a and 9b show the actual and estimated active and reactive power of load 1, and Fig. 9c and 9d show the actual and estimated active and reactive power of load 2 (actual and estimated values are represented by blue and red colors, respectively). Active and reactive power estimations of load 1 are quite close to actual values during the event as clearly seen in Fig. 9a and 9b. However, since the model of load 2 is changed temporarily between time 1.0 s and 1.05 s, active and reactive power estimation of its response by its model is wrong at this time interval. Actual load and model responses do

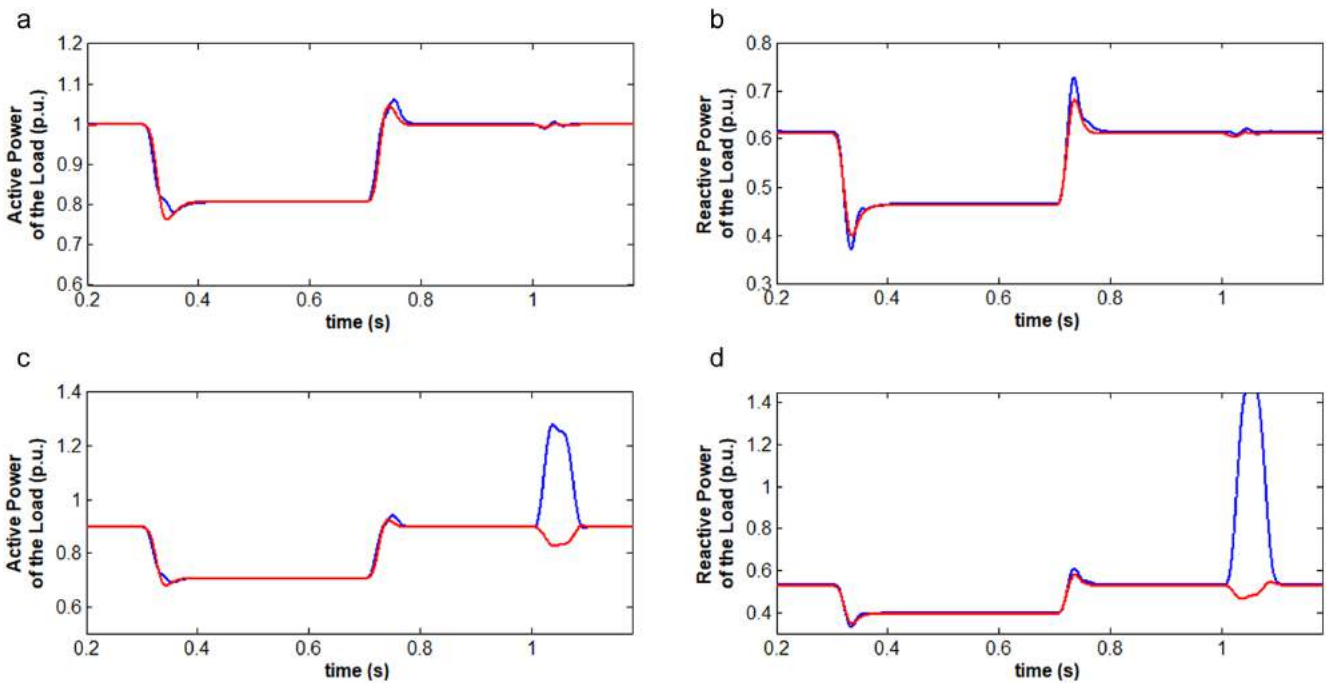

Fig. 9. Comparison of the actual and estimated real and reactive powers during event 1 at the time between 0.3 s and 0.7 s, and event 2 at the time between 1.0 s and 1.05 s of case study 3: (a) actual and estimated active power of load 1, (b) actual and estimated reactive power of load 1, (c) actual and estimated active power of load 2, and (d) actual and estimated reactive power of load 2 (actual and estimated powers are presented in blue and red, respectively).

TABLE II.
ESTIMATED PARAMETERS FOR DIFFERENT MOTOR MECHANICAL LOADS

Torque (Nm)	$X'_{(est)}$ (Ω)	$R_{r(est)}$ (Ω)	$J_{(est)}$ (kg m²)	$Z_{eq(est)}$ (Ω)
7.9	1.429	0.893	0.084	13.963∠56.079°
9.9	1.411	0.904	0.084	13.978∠56.083°
11.9	1.391	0.912	0.084	13.999∠56.083°
13.9	1.371	0.915	0.085	14.026∠56.081°
15.9	1.350	0.915	0.084	14.060∠56.078°

TABLE III.
ESTIMATED PARAMETERS FOR DIFFERENT VOLTAGE SAG DEPTHS

Sag Depth (V)	$X'_{(est)}$ (Ω)	$R_{r(est)}$ (Ω)	$J_{(est)}$ (kg m²)	$Z_{eq(est)}$ (Ω)
10	1.426	0.909	0.087	13.963∠55.953°
20	1.400	0.913	0.084	13.992∠56.060°
30	1.377	0.916	0.082	14.016∠56.130°
40	1.346	0.917	0.079	14.048∠56.220°
50	1.304	0.914	0.077	14.094∠56.344°

not match, and it can be deduced that structure of the load 2 has changed at this interval and this causes an event.

V. CONCLUSION

In this study, a load model has been proposed to estimate the response of network loads in response to network events and a method has been developed to estimate the parameters of this model. The aim of this model is to estimate the behavior of a load under power quality events. The feature of the method is to identify the parameters of the composite load model with less processing time by using measurement data from a voltage sag/swell. At least one sequential voltage sag/swell event is required to determine the parameters. In the case studies, it has been observed that the composite load model consisting of impedance and an induction motor gives results close to the actual load response. It is observed that the best results obtained by the developed method are obtained when the voltage sag/swell depth is less than 20%. Once the load model is obtained, it can be estimated how the load will behave under the occurrence of event such as voltage sag, voltage swell, or interruptions.

TABLE IV.
ESTIMATED PARAMETERS FOR DIFFERENT VOLTAGE SWELL DEPTHS

Swell Depth (V)	$X'_{(est)}$ (Ω)	$R_{r(est)}$ (Ω)	$J_{(est)}$ (kg m²)	$Z_{eq(est)}$ (Ω)
10	1.473	0.930	0.094	13.963∠55.951°
20	1.475	0.924	0.098	13.992∠56.057°
30	1.478	0.919	0.103	14.016∠56.127°
40	1.482	0.914	0.108	14.048∠56.218°

Peer-review: Externally peer-reviewed.

Declaration of Interests: The authors have no conflicts of interest to declare.

Funding: The authors declared that this study has received no financial support.

REFERENCES

1. U. Arumugam, N. M. Nor, and M. F. Abdullah, "A brief review on advances of harmonic state estimation techniques in power systems," *Int. J. Inf. Electron. Eng.*, vol. 1, no. 3, pp. 217–222, 2011. [CrossRef]
2. IEEE Task Force on Load Representation Performance, "Load representation for dynamic performance analysis (of power systems)," *IEEE Trans. Power Syst.*, vol. 8, no. 2, pp. 472–482, 1993. [CrossRef]
3. H. Renmu, M. Jin, and D. J. Hill, "Composite load modeling via measurement approach," *IEEE Trans. Power Syst.*, vol. 21, no. 2, pp. 663–672, 2006. [CrossRef]
4. S. Peerez-Londono, L. Rodriguez-Garcia, and J. Mora-Flores, "A comparative analysis of dynamic load models for voltage stability studies," In *Proceedings of 2014 IEEE PES Transmission & Distribution Conference and Exposition, Latin America (PES T&D-LA 2014)*, Medellin, Colombia, September 10-–13, 2014, pp. 1–6.
5. X. Qu, X. Li, J. Song, and C. He, "An extended composite load model taking account of distribution network," *IEEE Trans. Power Syst.*, vol. 33, no. 6, pp. 7317–7320, 2018.
6. L. Li, X. Xie, J. Yan, and Y. Han, "Fast online identification of the dominant parameters of composite load model using Volterra model and pattern classification," In *Proceedings of 2007 IEEE Power Engineering Society General Meeting*, Tampa, FL, USA, June 24-–28, 2007, pp. 1–8.
7. S. Yu, S. Zhang, and X. Zhang, "Two-step method for the online parameter identification of a new simplified composite load model," *IET Gener. Transm. Distrib.*, vol. 10, no. 16, pp. 4048–4056, 2016. [CrossRef]
8. M. Rasouli, R. Sabzehgar, and H. R. Teymour, "An efficient approach for measurement-based composite load modeling," In *Proceedings of 2018 IEEE Energy Conversion Congress and Exposition (ECCE)*, Oregon, Portland, September 23-–27, 2018, pp. 7310–7314.
9. L. Rodriguez-Garcia, S. Perez-Londone, and J. J. Mora-Florez, "Methodology for measurement-based load modeling considering integration of dynamic load models," In *Proceedings of 2020 IEEE International Autumn Meeting on Power, Electronics and Computing*, Ixtapa, GRO, México: ROPEC, November 4-–7, 2020, pp. 1–6.
10. H. Marma, and X. Liang, "Composite load model and transfer function based load model for high motor composition load," In *Proceedings of 2019 IEEE Canada Electrical Power and Energy Conference (EPEC)*, Montreal, Canada, 2019, pp. 1–5.
11. F. Bu, Z. Ma, Y. Yuan, and Z. Wang, "WECC composite load model parameter identification using evolutionary deep reinforcement learning," *IEEE Trans. Smart Grid*, vol. 11, no. 6, pp. 5407–5417, 2020. [CrossRef]
12. Z. Ma, Z. Wang, Y. Wang, R. Diao, and D. Shi, "Mathematical representation of WECC composite load model," *J. Mod. Power Syst. Clean Energy*, vol. 8, no. 5, pp. 1015–1023, 2020. [CrossRef]

13. R. Venkatraman, S. K. Khaitan, and V. Ajjarapu, “Application of combined transmission-distribution system modeling to WECC composite load model,” In *Proceedings of 2018 IEEE Power & Energy Society General Meeting (PESGM)*, Portland, Oregon, August 5–9, 2018, pp. 1–5.
14. Z. Ma, B. Cui, Z. Wang, D. Zhao, and D. Zhao, “Parameter reduction of composite load model using active subspace method,” *IEEE Trans. Power Syst.*, vol. 36, no. 6, pp. 5441–5452, 2021. [CrossRef]
15. I. A. Hiskens, “Nonlinear dynamic model evaluation from disturbance measurements,” *IEEE Trans. Power Syst.*, vol. 16, no. 4, pp. 702–710, 2001. [CrossRef]
16. Q. Liu, Y. Chen, and D. Duan, “The load modeling and parameter identification for voltage stability analysis,” In *Proceedings of 2002 International Conference on Power System Technology*, Kunming, China, October 13–17, 2002, pp. 2030–2033.
17. X. Zhang, C. Lu, and Y. Wang, “Identifiability analysis of load model parameter identification with likelihood profile method,” In *Proceedings of 2018 IEEE Power & Energy Society General Meeting (PESGM)*, Portland, Oregon, August 5–9, 2018, pp. 1–5.
18. M. E. Jahromi, and M. T. Ameli, “Measurement-based modelling of composite load using genetic algorithm,” *Electr. Power Syst. Res.*, vol. 158, pp. 82–91, 2018. [CrossRef]
19. X. Li, L.Wang, and P. Li, “The study on composite load model structure of artificial neural network,” In *Proceedings of Third International Conference on Electric Utility Deregulation and Restructuring and Power Technologies*, Nanjing, China, April 6–9, 2008, pp. 1564–1570.
20. V. Knyazkin, C. A. Canizares, and L. H. Soder, “On the parameter estimation and modeling of aggregate power system loads,” *IEEE Trans. Power Syst.*, vol. 19, no. 2, pp. 1023–1031, 2004. [CrossRef]
21. C. Wang, Z. Wang, J. Wang, and D. Zhao, “Robust time-varying parameter identification for composite load modeling,” *IEEE Trans. Smart Grid*, vol. 10, no. 1, pp. 967–979, 2019. [CrossRef]
22. K. O. Abledu, *Equivalent Load Model of Induction Machines Connected to a Common Bus*, Ph.D. dissertation. Iowa, US: Iowa State University, 1983.
23. S. Yu, S. Zhang, Y. Han, C. Lu, Z. Yu., and X. Zhang, “Fast parameter identification and modeling of electric load based on simplified composite load model,” In *Proceedings of 2015 IEEE Power & Energy Society General Meeting*, Denver, Colorado, July 26–30, 2015, pp. 1–5.
24. P. Kundur, *Power System Stability and Control*. California: McGraw-Hill, 1993.
25. P. S. E. C. System Dynamic Performance Subcommittee. “Standard load models for power flow and dynamic performance simulation”, *IEEE Trans. Power Syst.*, Vol. 10, no. 3, pp. 1302–1313, 1995.

Appendix

All symbols and variables in the text are defined as a list of nomenclature in the following:

Symbol	Explanation
f_0, ω_0	Base frequency and angular frequency of the power system
R_{st}, X_{st}	Resistance and reactance of the static impedance
R_{eq}, X_{eq}	Resistance and reactance of the equivalent static impedance
R_s, R_r	Stator and rotor resistance of the motor
X_S, X_R	Stator leakage and rotor leakage reactance of the motor
X_M	Magnetizing reactance of the motor
X	Stator circuit reactance
X'	Transient reactance of the motor
$T_0^{'}$	Transient open-circuit time constant
A,B,C	Constant torque coefficient
H	Rotor inertia constant
J	Rotor inertia coefficient
s	Slip of the motor
ω_r	Normalized rotor electrical speed
U,U_d,U_q	Bus voltage, d-axis, and q-axis bus voltage
I,I_d,I_q	Stator current, d-axis, and q-axis stator current
E,E_d,E_q	transient electromotive force, d-axis, and q-axis transient electromotive force
P,Q	Active and reactive power of the composite load
P_{st},Q_{st}	Active and reactive power of the static impedance
P_{eq},Q_{eq}	Active and reactive power of the equivalent static impedance
P_m,Q_m	Active and reactive power of the motor
P_{mt},Q_{mt}	Active and reactive power of the transmission part of the motor (excluding its magnetizing part)

TEPES
TURKISH JOURNAL OF
ELECTRICAL POWER
AND ENERGY SYSTEMS

TEPES, Vol. 2, Issue. 1, 31-45, 2022 **DOI:** 10.5152/tepes.2022.21049

RESEARCH ARTICLE

Ripple Signaling Control for Ancillary Services in Distribution Networks

Evangelos Boutsiadis, Dimitrios Tsiamitros, Dimitrios Stimoniaris

Department of Electrical & Computer Engineering, University of West Macedonia, Kozani, Greece

Cite this article as: E. Boutsiadis, D. Tsiamitros & D. Stimoniaris. Ripple signaling control for ancillary services in distribution networks. *Turk J Electr Power Energy Syst*, 2022; 2(1): 31-45.

ABSTRACT

The integration of distributed generation and electric vehicles' chargers into the electricity grid are two great challenges for distribution networks operators worldwide. In these cases, a reliable and cost-effective communication and control system is needed, in order to ensure stable operation of the grid and keep the power quality indices inside their limits. Such a control system is already in use by most of the distribution networks operators: the ripple signaling system. In this study, a part of a distribution network with increased penetration of Photovoltaic (PV) power plants is simulated, with and without ripple signaling control, for various operational scenarios. The results of the simulation scenarios indicate those PV plants where the ripple signaling control should be applied. The results also highlight the type of ancillary services that the proposed methodology can supply to the network, such as the improvement of the voltage profile and other power quality indices along with the feeders.

The first tests of the actual system on the real line are also demonstrated, showing also that the new method is highly reliable, inherently cyber-secure, and data-privacy protective.

Index Terms—Distributed generation, ripple signaling, renewable energy sources, smart grid, smart microgrid

I. INTRODUCTION

All European Union (EU) countries have the commitment to increase the share or renewable energy sources (RES), which however are fluctuating and uncertain. Therefore, in many EU countries, the laws allow premium access to the grid for RES. However, there are some well-known grid power quality indices, which limit the capacity of RES Distributed Generation (DGs) on any medium voltage (MV) grid line: i) the first has to do with the thermal capacity of the lines (conductors, overhead lines, or underground cables); ii) another restriction has to do with the lower and the upper limits of the grid's voltage [1]; and iii) there are also limits of the voltage variation through a complete year of operation [2].

Moreover, many distribution network operators (DNOs) had invested to cross grid lines (interconnected lines) between two main lines (Fig. 1) and had also invested in remote-controlled circuit breakers at the edges, toward their effort not to de-energize significant parts of a grid line, during repair or maintenance works, and finally to comply with the System Average Interruption Duration Index (SAIDI) and System average interruption frequency index (SAIFI) indices [2]. After the integration of DGs into the grid, the main issue with great impact on the grid operation has been identified: The interconnected lines impact due to high penetration of DGs, which gives rise to three specific problems:

1) The peak production of all the DGs of a line is allowed to reach up to 80% of the thermal limit of a line. When transporting the load and the DG to another line through the lines' interconnection, the substation actually feeds two lines in series. Thus, in the case of low consumption and maximum productivity of the two lines' DGs (such as a Sunday lunchtime period), the new line will be forced to operate with reverse currents near or above its thermal capacity or even to the 120% of its capacity (series connection). If there is such an unpleasant situation, then the line-feeder will trip.
2) An even more serious situation is the level of the voltage along the "new line" which consists now of two main lines in series. It is certain that at the Network Connection Point (NCP) of many PV plants, the rms voltage value will reach or exceed the upper voltage limits, and the protection relays will de-energize too many PV plants. After 3 minutes (synchronization period in Greece), if there is a voltage reset within the limits, the PV plant will supply energy to the grid again, raising the voltage value at its NCP [3] again. If this

Corresponding author: Dimitrios Tsiamitros, v.boutsiadis@deddie.gr

Received: December 11, 2021
Accepted: February 14, 2022

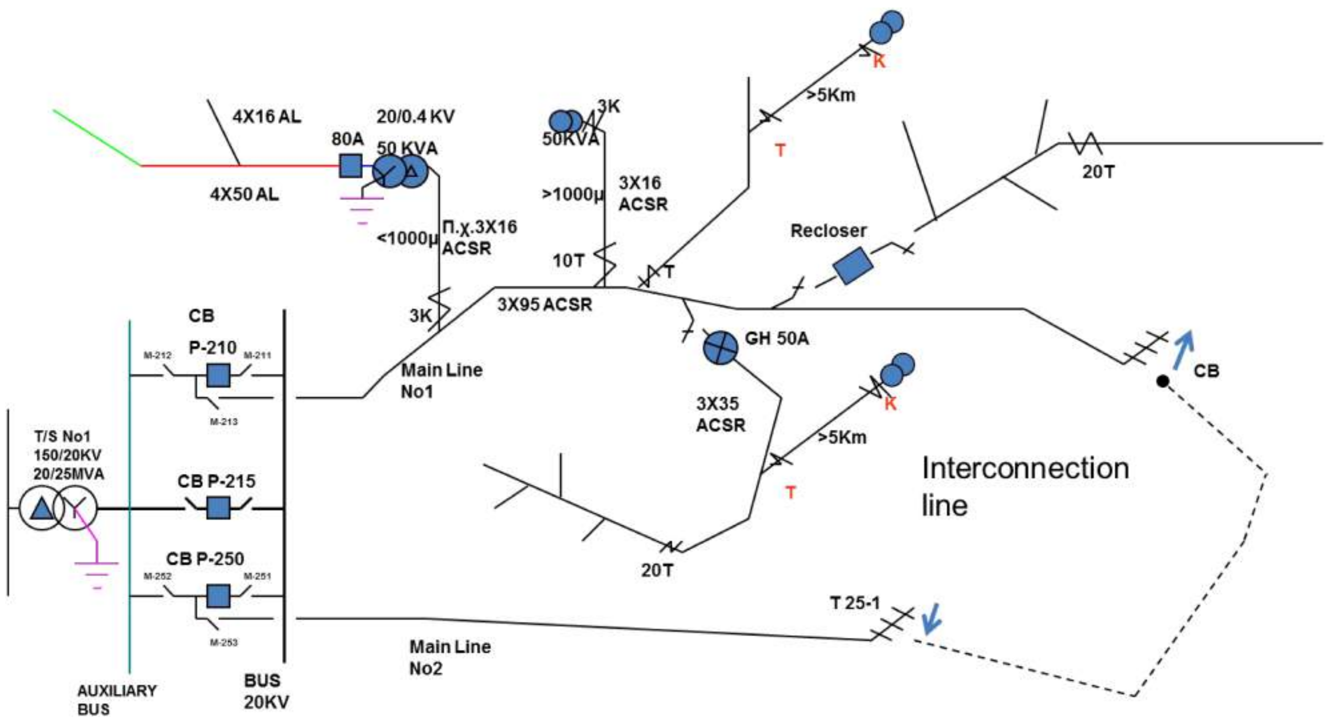

Fig. 1. Interconnection line example.

raise exceeds the upper limit, it will be disconnected, and this situation will be repeated again and again, at many PV plants of the "new line."

3) One-third of unpleasant situations may occur to the average voltage value at the consumers' facilities. The upper level of the voltage at the point of common coupling of a DG Unit is set to 253 V at the low voltage (LV) grid and to 22kV at the medium voltage (MV) lines. If there is a power production increase of DG units at the end of the "new line," and if there are consumers at the same "neighborhood," these consumers will experience increased voltage levels as well, especially if the DG units are connected to the LV grid (too many roof PV stations or DG connected to the LV network) (example of voltage curve with min and max DG at Figs. 2, 3). This situation is also verified by the results of simulations that are conducted by the authors in [4].

Main point

- Ripple signalling is a cost-effective, cyber-secure and efficient method to provide ancillary services to the grid.
- A grid simulation of the interconnected lines section under study is proposed, in order to apply even more efficiently the ripple signalling method.
- The ripple signal receivers can be applied in many ways directly to the inverters or even to smart loggers to activate the decrease or the increase in the solar station power output.

The aim of this study is to present a pilot system on a part of an MV network and simulate and test how the ripple signaling system can solve the aforementioned problems. The main objective is to develop and simulate easy-to-apply (both technically and in legal terms) and cost-effective solutions that utilize the ripple signaling system of the DNOs, in order to execute operations on the distribution network without worrying about violating the grid parameters and reliability indices, both of the consumers and of the producers. The following steps are followed and are described in this paper in the respective Sections.

1. Ripple signalling is a cost-effective, cyber-secure and efficient method to provide ancillary services to the grid.
2. A grid simulation of the interconnected lines section under study is proposed, in order to apply even more efficiently the ripple signalling method.
3. The ripple signal receivers can be applied in many ways directly to the inverters or even to smart loggers to activate the decrease or the increase in the solar station power output.

In the next section (section II), we describe the methodology to address the impact of interconnected lines by utilizing the ripple signaling system. Next, two actual interconnected lines of the MV network in Greece are selected to be simulated. The results of the simulation are presented in the fourth section. In the fifth section, the required equipment and procedure for installing, programming, and testing the ripple signaling system on the actual grid are presented, together with a comparison with other technologies that could tackle the same problems. Finally, the discussions section highlights more ancillary services, which the proposed system can offer to the grid.

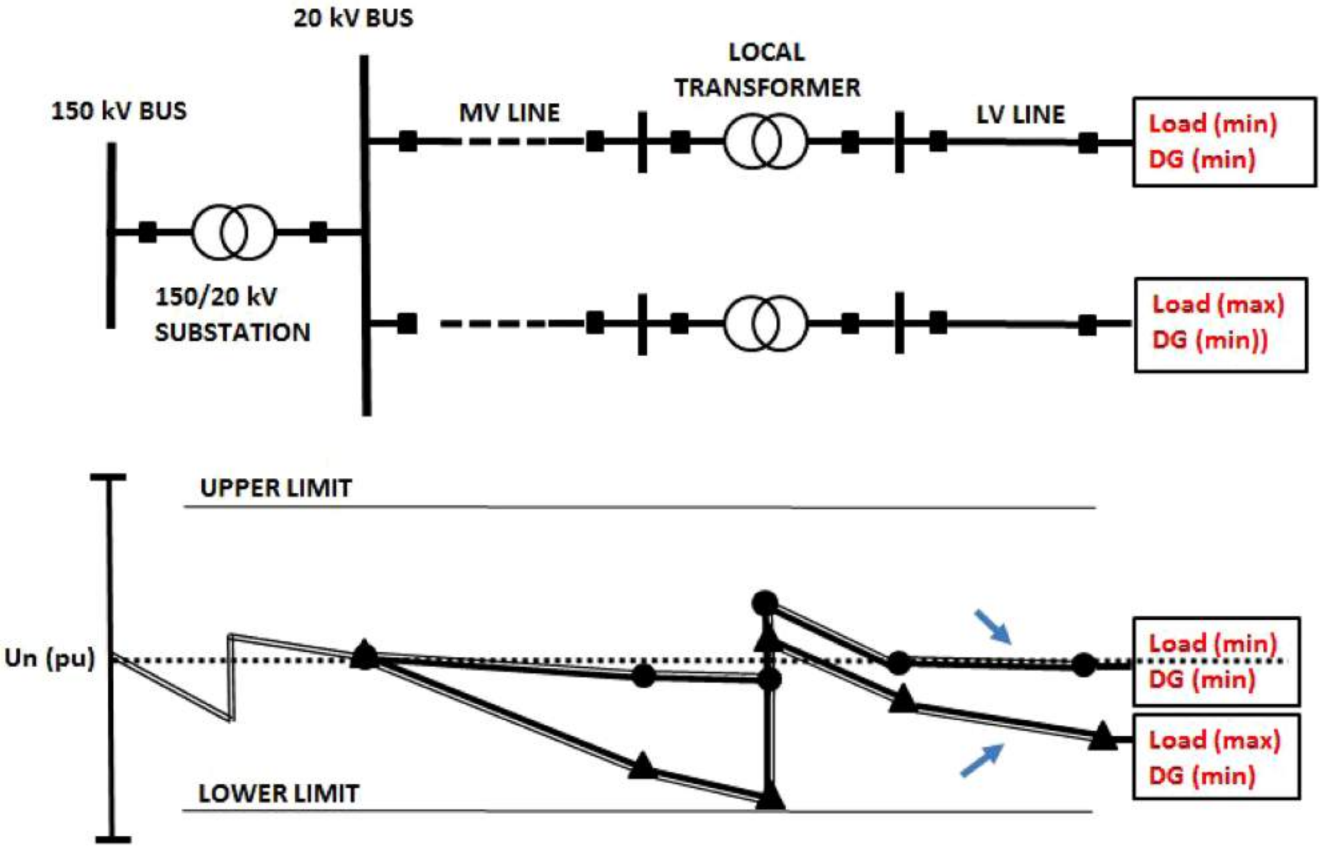

Fig. 2. Voltage profile including minimum DG penetration with min and max load situation.

II. ADDRESSING THE INTERCONNECTED LINES IMPACT VIA RIPPLE SIGNALING

Traditionally, DNOs around the world use the technique of injecting to the distribution network different frequency signals, in order to control the function of street lighting, tariff changeover, etc. They use a resonance circuit to inject a frequency signal. In this study, the network uses the Pulsadis system [5], according to which a 175 Hz signal (Fig. 4) is automatically injected into the DN, at specified time periods, and a number of appropriate receivers recognize when it is their turn to make an action (energize or de-energize some relay contacts).

A pair of time periods, like the ones in Fig. 5 and Fig. 6, is used every time to energize and de-energize certain receivers, respectively. So, when at a specified time of the day a signal is beginning to be injected for 1 second, followed by 2.75 seconds of silence, all the grid's receivers are sensing the incoming coded transmission (telegraph), and at the end of the 2.75 seconds of silence, the receivers are beginning to measure time periods of 1 second followed by 1.5 seconds silence [5-7].

If one receiver was preset to recognize the sixth transmission period, as an "ON" action for it, when and if the transmitted telegraph includes a transmission at the sixth period, the receiver will recognize, for example, that it has to close a relay and turn on the city lights.

When, in the morning, another transmitted telegraph includes a transmission signal at the seventh time period, the same receiver, as preset, will recognize that, for example, it has to turn off the relay and thus turn off the city lights.

The ripple control signal can usually be affected in two ways: 1) a significant reduction of the amplitude of the signal can occur when the load voltage value reduces to its lower limits at the end of the line and 2) researches have shown a rise to the signal's amplitude near DG units, especially when the reactive impedance of the grid equals to the capacitive reactance of the DG unit, leading to resonance phenomena. This issue could be solved by DNOs by obligating DG owners to install proper filters [2,8].

Summarizing the technical specifications of the ripple control signal, those which are involved in this study are:

1) the Pulsadis system theoretically could transmit 40 signals (20 pairs);
2) the time intervals of the transmissions and the silence are integral multiples of the 50 Hz period;
3) the signals 5, 10, 15, 20, 25, 30, 35, and 40 are not transmitted, due to DNO's restrictions;
4) 15 pairs of signals remain for use;

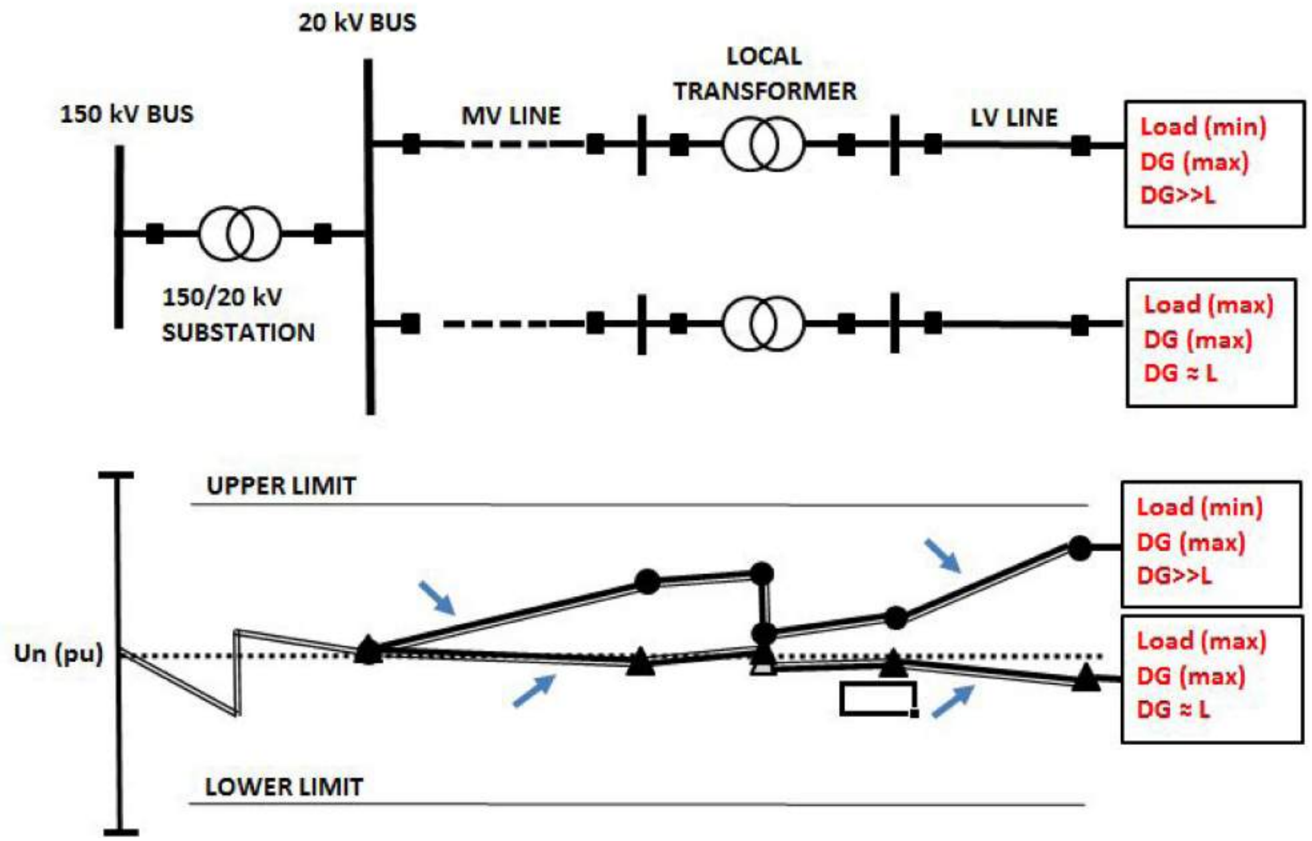

Fig. 3. Voltage profile including maximum DG penetration at min and max load situations.

5) the DNO uses, until now, five pairs for tariff changeover and street lightning control, so there are maximum of ten pairs available for other uses.

Therefore, the ripple control system can be used as follows:

All the modern PV inverters integrate remote control electrical contacts and are ready for use by a ripple control receiver. Many of the PV inverters allow to be connected in groups of five to the same ripple control receiver [9-12]. To reduce the cost of the ripple control receiver's installation more, if there is a motorized central circuit breaker at the production side of the DG unit, we can operate it via its auxiliary I-O contacts. The main idea is to affect only the production side of a PV station and not the auxiliary side in order to leave the PV station's area controlled by the owner (cameras, electric doors, fire detectors, internet connectivity, etc.) (Fig. 7).

To avoid miss-operation of the transmitting system, such as disability of the DG to reconnect to the DN (which can raise legal issues),

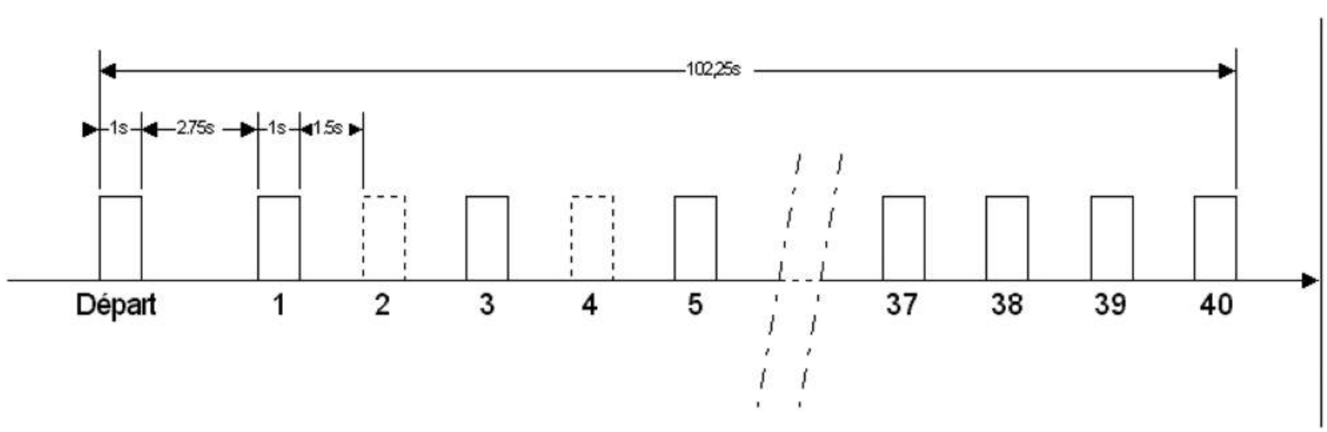

Fig. 4. Ripple control transmission telegraph.

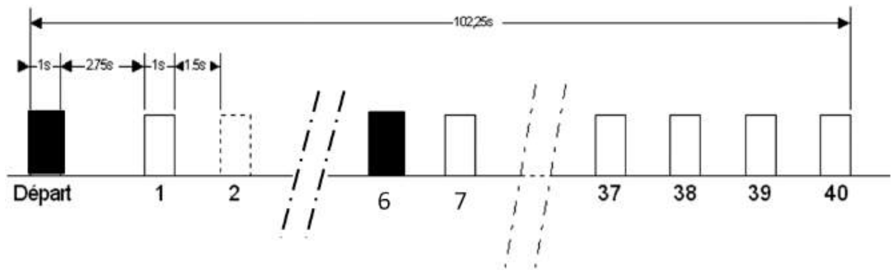

Fig. 5. Transmission of the signal no. 6.

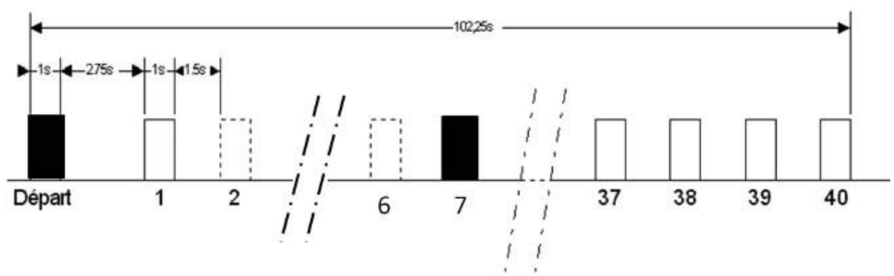

Fig. 6. Transmission of the signal 7.

there will be a safety net, applying backup solutions one by one or all together, such as:

1) there will be a preannouncement (to local papers, radio stations, sms, or e-mail) of the ancillary service period, so everyone could be prepared to monitor the state of their DG station;
2) to eliminate the possibility of "misunderstanding" of the signals by a receiver, we could use the traditional way of re-transmitting it after a few minutes.

The three specific problems that are mentioned in the Introduction Section above could be easily solved with the installation of ripple control receivers to every DG. Before the load and DG transfer to another line, with the help of the ripple control system, we can easily disconnect only the DGs of the line which is to be transferred. Therefore, the "new line" after the "interconnection" will consist of the main line connected in series to the new line without its DG units (since they are disconnected after the ripple signaling) (Fig. 8).

If this load transfer lasts for a long time period, for example, 8 hours, some very helpful solutions are proposed:

1) by grouping the DGs after simulation studies, we can install different ripple control receivers at separate DGs groups (same receivers, programmed to act at different pairs of signals), in order to disconnect or connect different group of DGs, with the biggest impact to voltage values (Fig. 9);

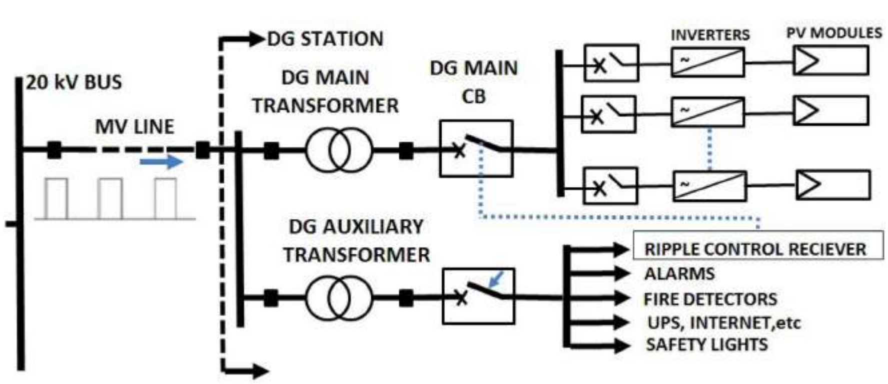

Fig. 7. Example of controlling the main circuit breaker of a DG via a ripple control receiver.

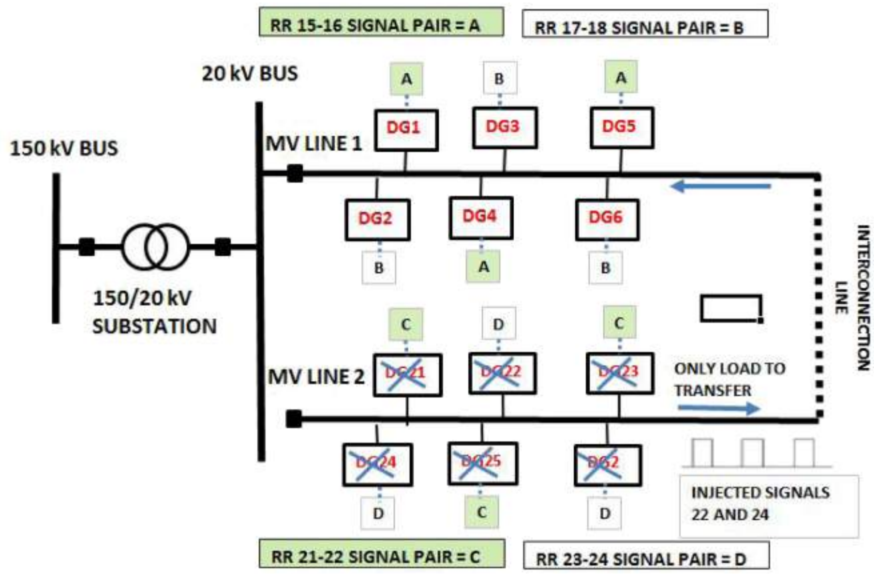

Fig. 8. Example of load transition from line 2 to the line 1, with DG disconnection at line 2.

2) by grouping the inverters in the same DG station and control these groups via different ripple control receivers (Fig. 10 below) or by installing one receiver per inverter (like Fig. 11) and finally set a number of receivers to act as a group at the same pair of signals and the others like another group acting to different pair of signals, we can disconnect a part of every station, thus decrease its power production. This operation can keep the voltage quality factors inside their limits and fairly decrease the production of all the DGs of the "new line" (Fig. 12). Similar techniques are proposed and tested by the authors on a laboratory scale [13-16].

III. DESCRIPTION OF THE MV GRID UNDER INVESTIGATION

The selection of the specific two main lines of Fig. 13 of the MV grid in Greece was based on the following criteria:

1) these two lines are interconnected;
2) both lines should present maximum PV installed capacity, compared to other regular lines in Greece;
3) the cumulative PV installed capacity of both lines exceeds the thermal capacity of each line (when they are connected in series).

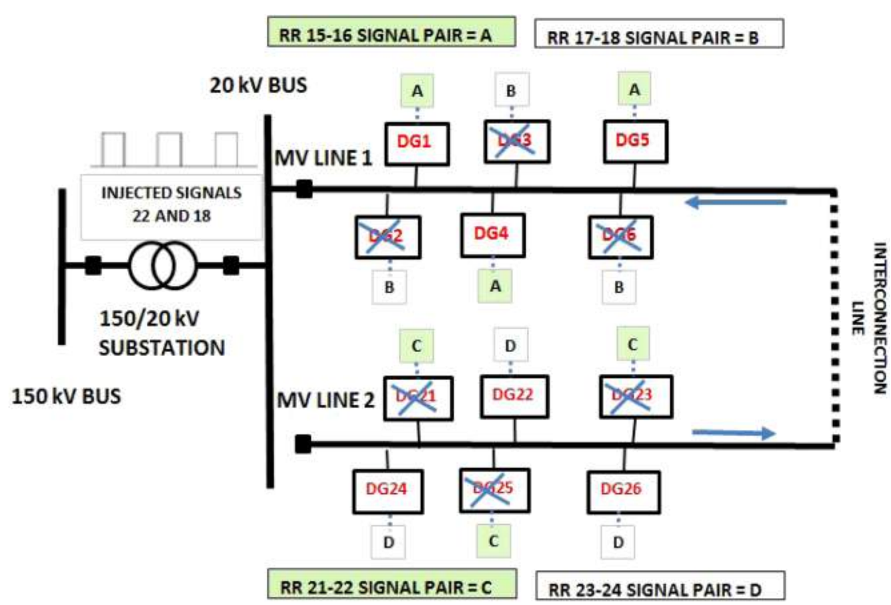

Fig. 9. Example of DGs in groups with different ripple control receivers, along load transition.

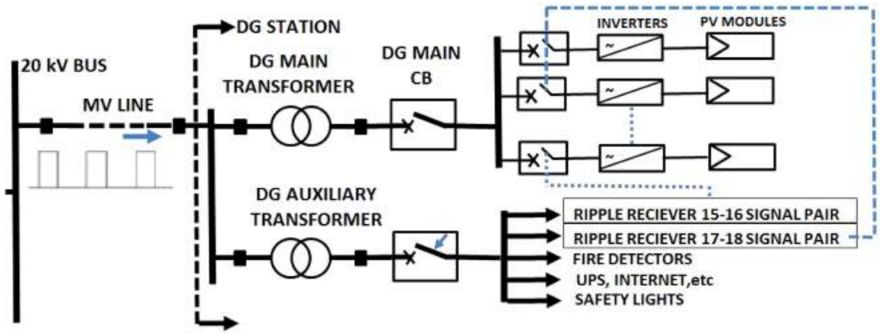

Fig. 10. Example of inverters in groups into the same DG station.

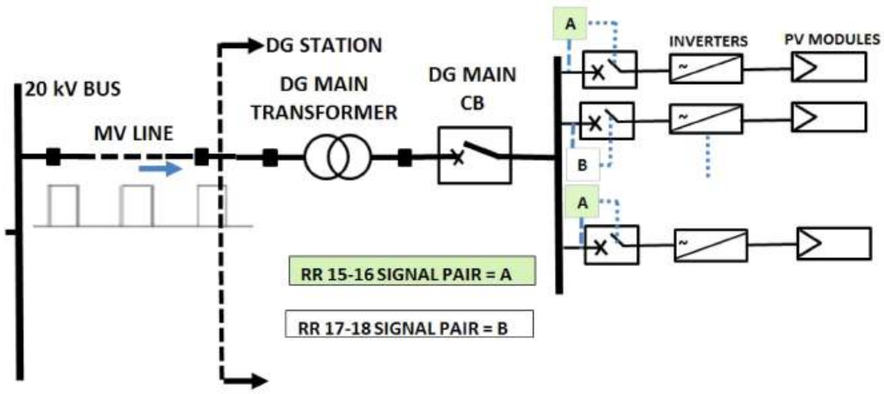

Fig. 11. Example of inverters in groups into the same DG station with one different receiver per inverter.

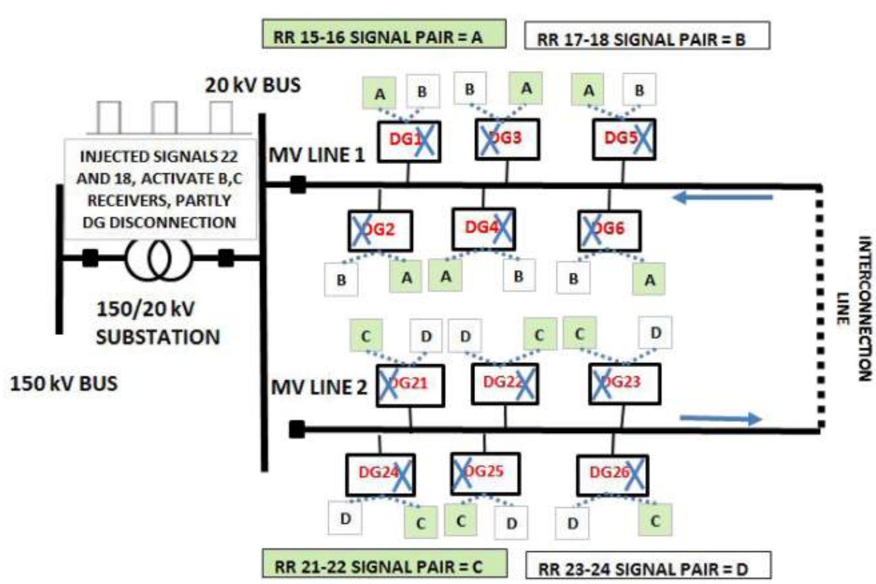

Fig. 12. Example of inverters in groups into the same DG station and partly disconnection of inverters.

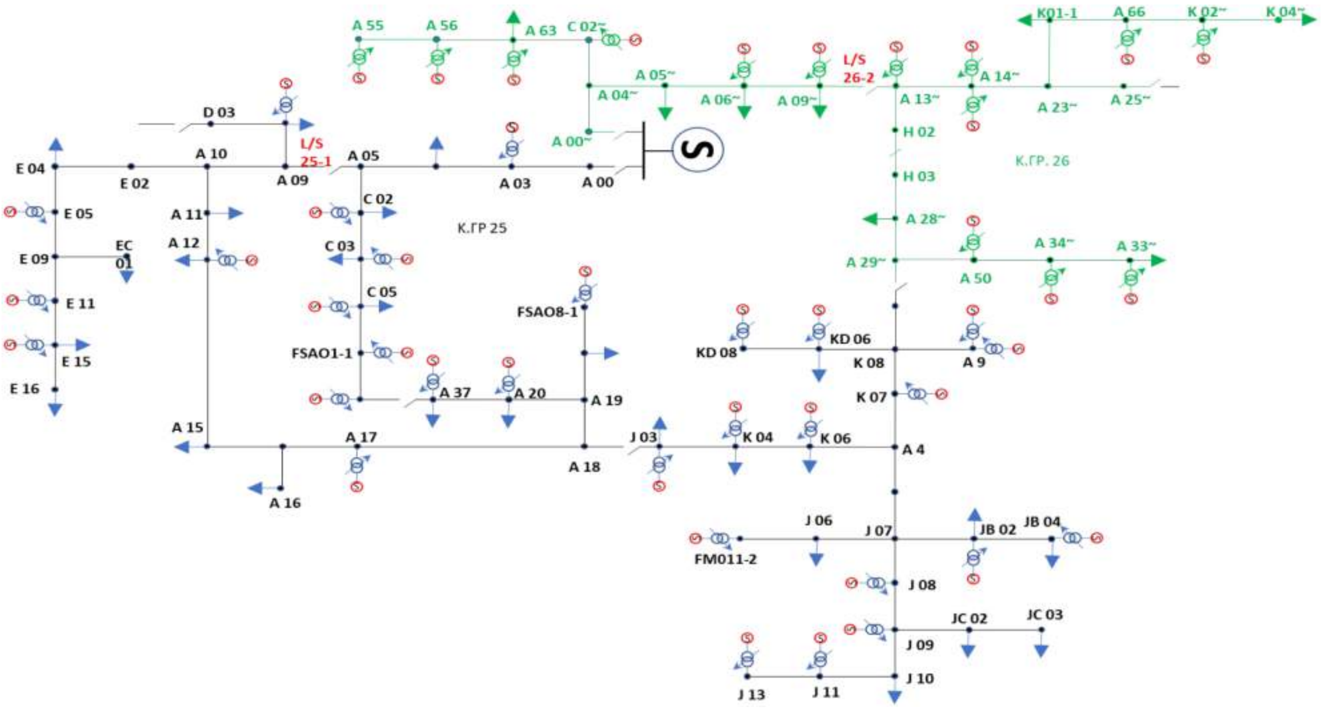

Fig. 13. The two selected MV lines: the black line is no. 25 and the green is no. 26. The red AC sources show where the PV distributed generators are located to.

The peak daily power production of the PV producers of these two lines occurs at the same time as the usual network operations of the DNO during weekends.

These two lines obtain 169 connected PV producers, while 45 of them have installed capacity larger than 95 kWp each. The total installed capacity of these 45 producers reaches 15 879 MWp and corresponds to 92% of the total PV installed capacity of the 2 lines. Therefore, for the purposes of the simulation, it is proposed that only these 45 PV producers are assumed to be controlled by the ripple signaling, although all PV producers of the lines are considered during modeling and simulation.

IV. SIMULATION RESULTS

The modeling of the two lines and the simulation results were obtained by the respective software of the DNO. Due to large amounts of DGs connected to the LV and MV parts of the lines, some parameters of the grid cannot be measured accurately, and many load transfer operations are prohibited due to thermal capability or voltage limits. In all simulated scenarios, the case of lowest recorded consumption is adopted (such as a Sunday lunchtime period), since it is the worst case. During the simulations, the voltage of the main busbar of the two lines is set to the usual value of 20 kV,7 kV, and 21 kV. In all scenarios, we compare the voltage level of various nodes of the lines with and without the ripple signal control over the 45 PV producers. The following four scenarios are the usual operations that occur due to scheduled maintenance works or due to grid reconfiguration because of a fault or due to underground cables works or because of adding new MV consumers to the grid:

(A) Feeding part of line no. 26 by line no. 25, through their interconnection (Fig. 14): the ripple signaling, in this case, decreases the power production of the 45 PV producers to 60% of their actual production. From Table I and Fig. 15, it is obvious that with ripple signaling control, the voltage level of every node is below or equal to the limit of 22 kV, which is not the case without applying ripple signaling, at the areas X of line no 26. and Y of Line no. 25.

(B) Feeding part of line no. 25 by line no. 26, through their interconnection (Fig. 16): the ripple signaling, in this case, decreases the power production of the 45 PV producers to 60% of their actual production. From Fig. 17, it is obvious that with ripple signaling control, the voltage level of every node is below the limit of 22 kV, which is not the case without applying ripple signaling, at the areas X1 and X2.

(C) Feeding line no. 25 by line no. 26, through their interconnection (Fig. 18): the ripple signaling, in this case, decreases the power production of the 45 PV producers to 60% and 50% of their actual production.

From Fig. 19, it is obvious that with ripple signaling control, the voltage level of every node is below the limit of 22 kV, which is not the case without applying ripple signaling, at the areas X1 and X2.

(D) Feeding line no. 26 by line no. 25, through their interconnection (Fig. 20): the ripple signaling, in this case, decreases the power production of the 45 PV producers to 60% and 50% of their actual production.

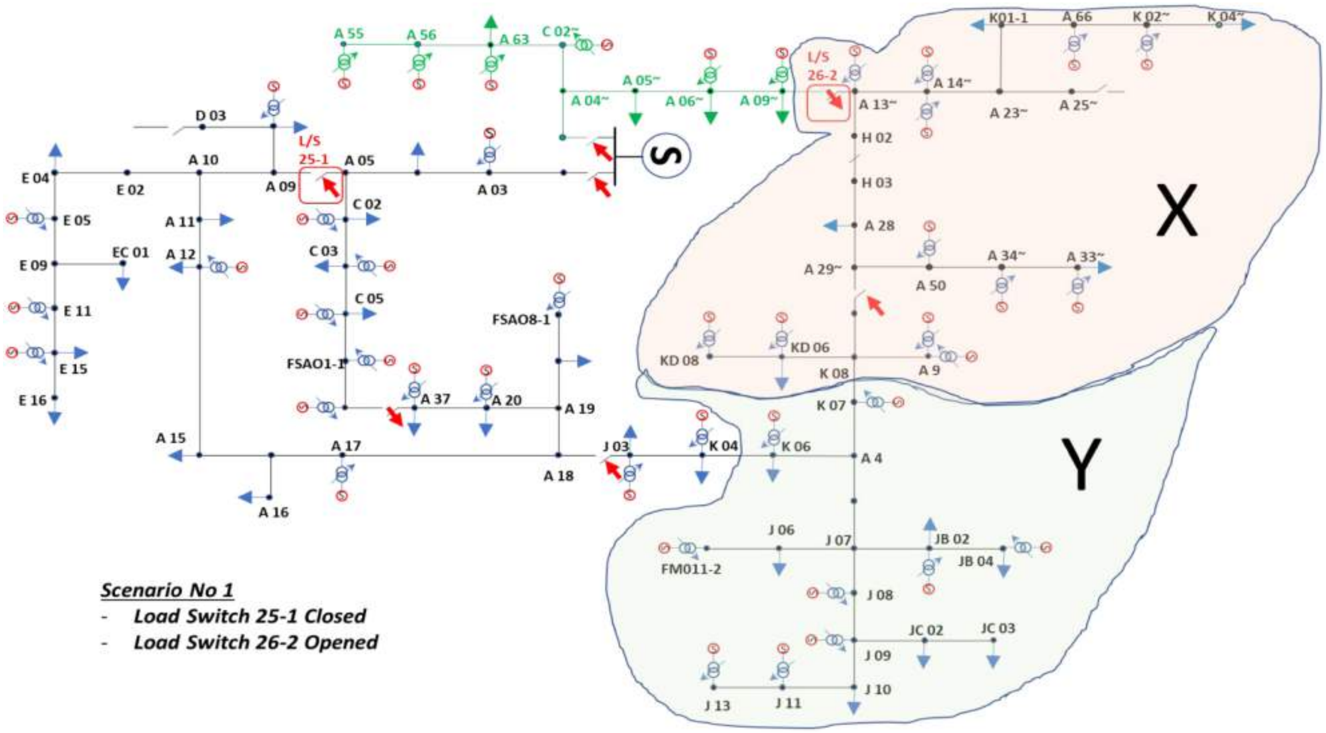

Fig. 14. Simulation scenario no. 1: The load switch 25-1 is closed and the load switch 26-2 is open. The X area is the part of line no. 26 that is fed by line no. 25 and the voltage level exceeds the limit of 22 kV, in case of no ripple signaling control. The Y area is the interconnection part of line no. 25 where the voltage level exceeds the limit of 22 kV, in case of no ripple signaling control.

This is the worst scenario since, from Fig. 21, it is obvious that only with ripple signaling control that leads to a 50% reduction of the actual PV output power of all PV producers, the voltage level of every node is sufficiently below 22 kV.

V. CONFIGURATION OF THE RIPPLE CONTROL EQUIPMENT AND COMPARISON WITH RTUs

What makes the proposed methodology so effective is that the required new ripple signaling control equipment includes only the receivers that will be installed at the PV producers' side, which are extremely cost-effective. The transmitters at the DNO side do not require any hardware or equipment change. The only software change is the graphical user interface added to the graphical environment of the human operator of the ripple signal at the control room. This addition enables the signal pair 18–19 for line no. 25 and the signal pair 23–24 for line no. 26.

On the other hand, the remote terminal units (RTUs) [17], which could be used to address the same problems, constitute a much more expensive solution, both in terms of installation cost as well as in terms of maintenance and operation cost. In Table II, a comparison between the ripple signaling and the RTU solutions is presented, including cyber-security issues.

Moreover, a testing of the ripple control system on an actual PV park at line 26 is presented here. In Fig. 22, the installation of the ripple signal receiver to the smart logger is shown at a PV park of the MV line no. 26, with an installed capacity of 489,60 kWp. The contact DI1 with status: normal open is connected to the ripple signal receiver. Then, due to the bad weather during the day of testing, the smart logger of the PV park is programmed to reduce significantly the PV active power production to 10% of its installed-nominal capacity (48,96 kW) when the ripple pulse no. 23 arrives to the receiver and to recover it when the ripple pulse no. 24 arrives to the receiver. The test that took place was totally successful: The ripple signal energized the smart logger and the PV power production reduced to 48,918 kW, from 233 kW. Moreover, when pulse no. 24 arrived, the PV park increased its production to the same value (233 kW). During regular operation in the future, the PV power production must not exceed 50 % (i.e., 240,58 kW), for the PV parks of line no. 26.

VI. CONCLUSION

Due to large amounts of DGs connected lately to the LV and MV network, some parameters of the grid cannot be measured accurately, and many load transfer operations are prohibited due to thermal capability or voltage values. With the help of the ripple control system, we can control the operation of the DGs. The solution involves already known systems, low-cost intervention, and legal compatibility. It is inherently cyber secure, since the signal transmission involves the distribution network only, and no broadcasting on the internet takes place. Compared to the RTU solution, the ripple signaling is much more effective, especially in terms of investment and Operation and Maintenance (O&M) cost

TABLE I.
VOLTAGE LEVEL OF THE TWO LINES NODES-SCENARIO NO 1 (VOLTAGE LIMIT: 22 KV)

Load Switch No. 26-2 Open					
PV production rate		**100.00%**		**60.00%**	
Feeding busbar initial voltage (kV)		**20.7 kV**	**21 kV**	**20.7 kV**	**21 kV**
Node	**Nominal voltage of each node (kV)**	**Simulated voltage level**	**Simulated voltage level**	**Simulated voltage level**	**Simulated voltage level**
K06	20	21.63	21.92	21.30	21.59
A4	20	21.65	21.94	21.31	21.60
K07	20	21.70	21.99	21.34	21.63
J07	20	21.71	22.00	21.35	21.64
J06	20	21.73	22.02	21.36	21.65
FM011-2	20	21.75	22.04	21.37	21.66
J08	20	21.77	22.06	21.38	21.67
JB02	20	21.79	22.08	21.40	21.69
JB04	20	21.79	22.08	21.40	21.69
JC03	20	21.80	22.08	21.39	21.69
JC02	20	21.80	22.08	21.39	21.69
J09	20	21.80	22.09	21.40	21.69
J10	20	21.81	22.10	21.41	21.70
J11	20	21.82	22.11	21.41	21.70
J13	20	21.82	22.11	21.41	21.70
K08	20	22.12	22.40	21.60	21.89
A29~	20	22.13	22.41	21.61	21.90
A50	20	22.13	22.42	21.61	21.90
A34~	20	22.14	22.42	21.62	21.90
A33~	20	22.14	22.42	21.62	21.90
A28~	20	22.14	22.43	21.62	21.91
KD06	20	22.16	22.45	21.63	21.92
KD08	20	22.16	22.45	21.63	21.92
H03	20	22.18	22.47	21.64	21.93
H02	20	22.18	22.47	21.64	21.93
A13~	20	22.19	22.47	21.65	21.94
A9	20	22.19	22.47	21.65	21.93
A14~	20	22.20	22.48	21.66	21.94
A25~	20	22.23	22.51	21.66	21.95
A23~	20	22.23	22.51	21.66	21.95
K01-1	20	22.31	22.59	21.70	21.99
K04~	20	22.31	22.59	21.70	21.98
A66	20	22.31	22.60	21.71	21.99
K02~	20	22.32	22.60	21.70	21.99

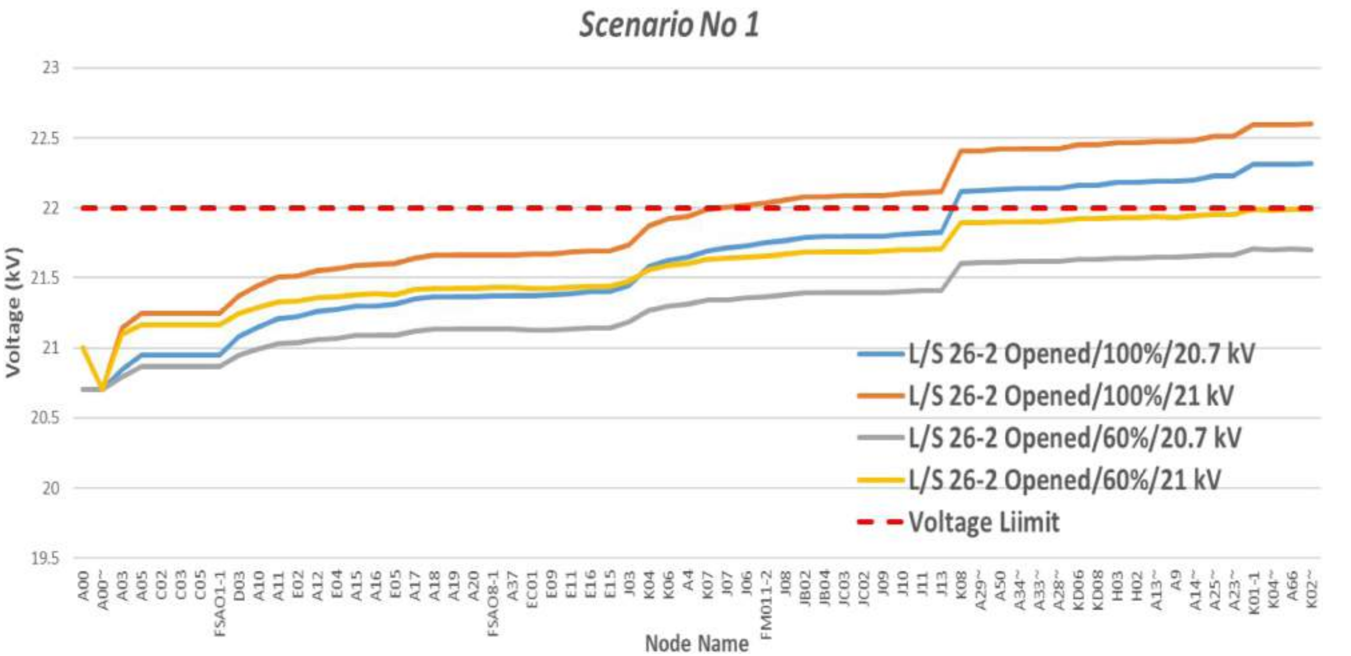

Fig. 15. Voltage profile of simulation scenario 1.

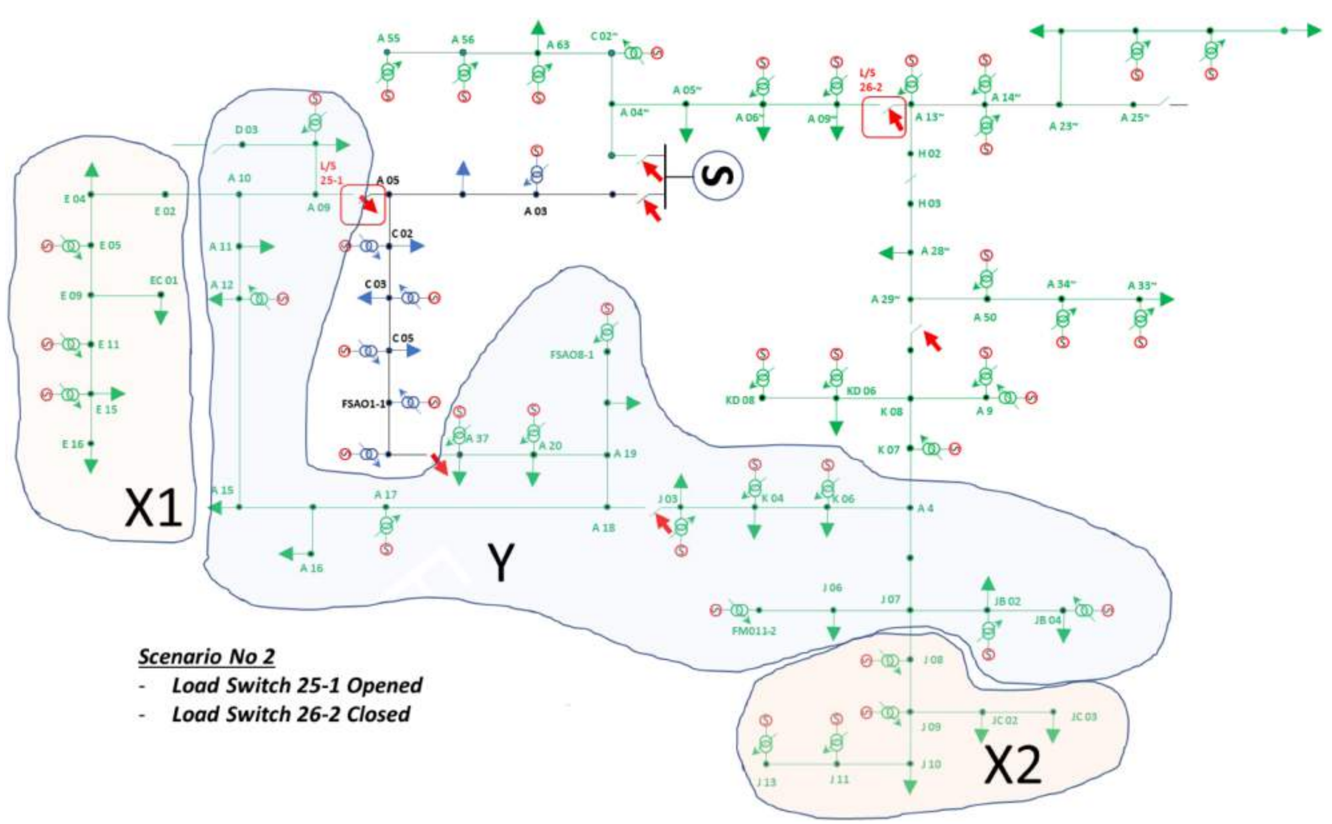

Fig. 16. Simulation scenario no. 2: The load switch 26-2 is closed and the load switch 25-1 is open. The X1 and X2 are the areas where the voltage level exceeds the limit of 22 kV, in case of no ripple signaling control. The Y area includes voltage levels almost 22 kV.

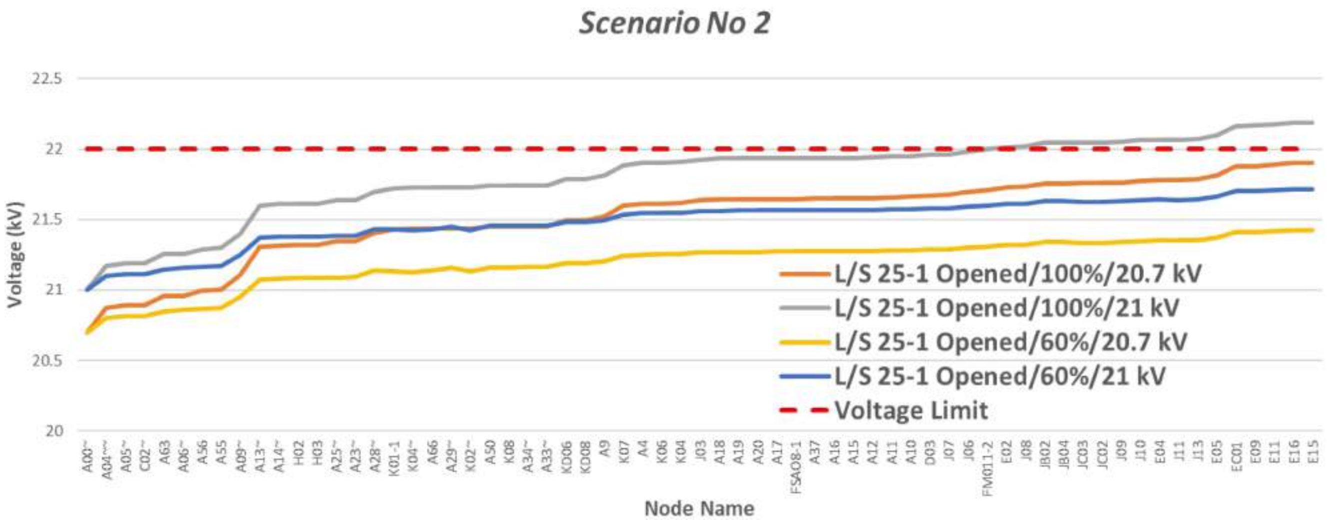

Fig. 17. Voltage profile of simulation scenario no. 2.

and of course much more cyber secure and data-privacy protective. The simulation results are absolutely encouraging: with ripple signaling control, the voltage level of every node of the MV network is below the limit of 22 kV, which is not the case without applying ripple signaling, especially at distant nodes from the substations.

VII. DISCUSSION

Further advantages, by placing ripple control receivers to the lines with significant penetration of DG stations, are:

1) measurement and control of the line's load development;
2) recognition, if it is needed, of the load flow direction.

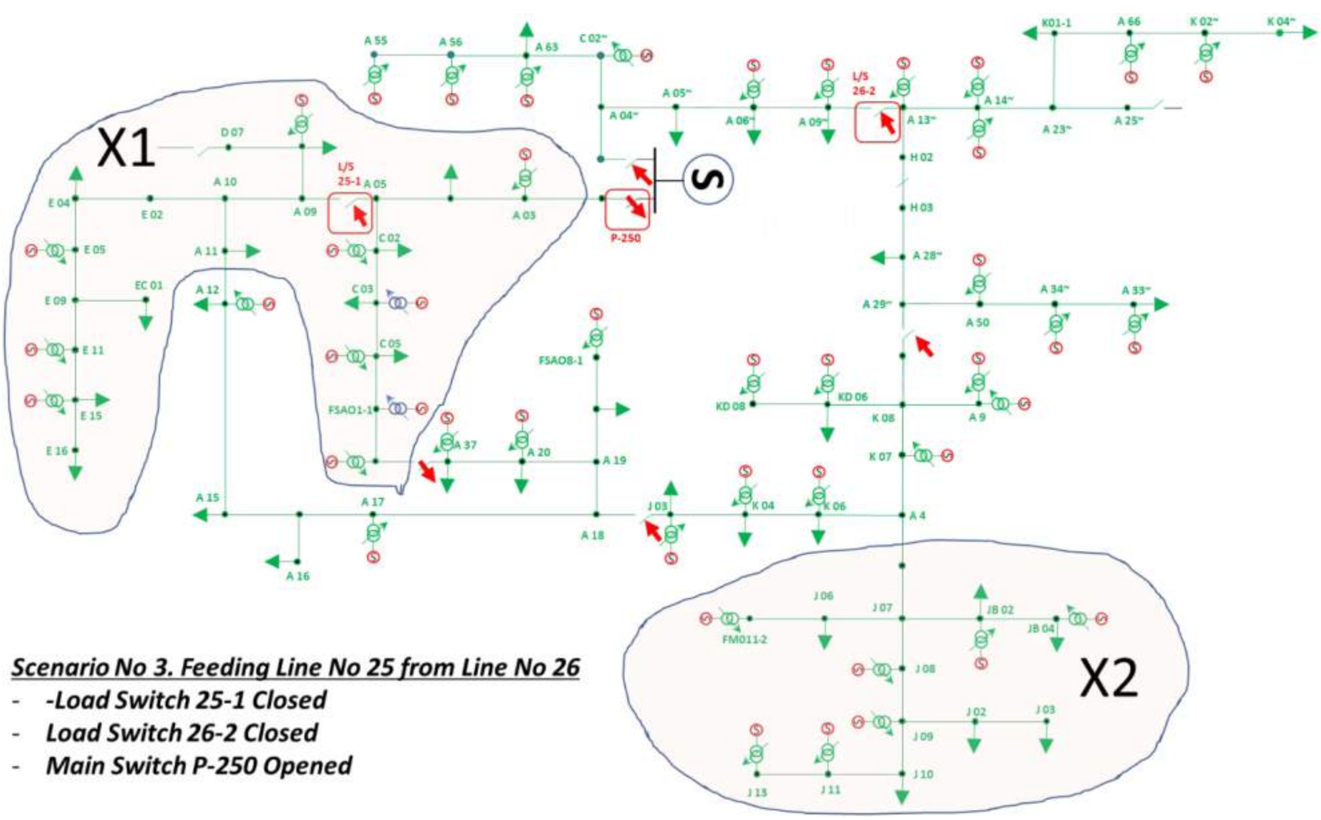

Fig. 18. Simulation scenario no. 3: Feeding line no. 25 from line no. 26. The X1 and X2 are the areas where the voltage level exceeds the limit of 22 kV, in case of no ripple signaling control.

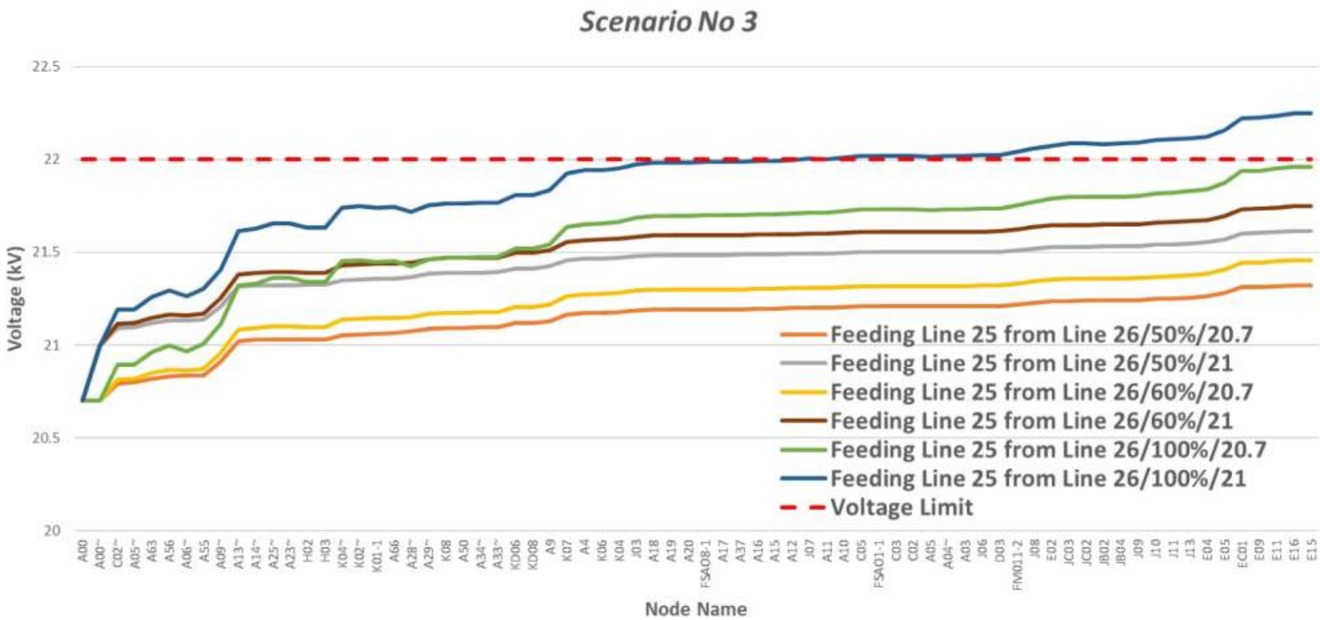

Fig. 19. Voltage profile of simulation scenario 3.

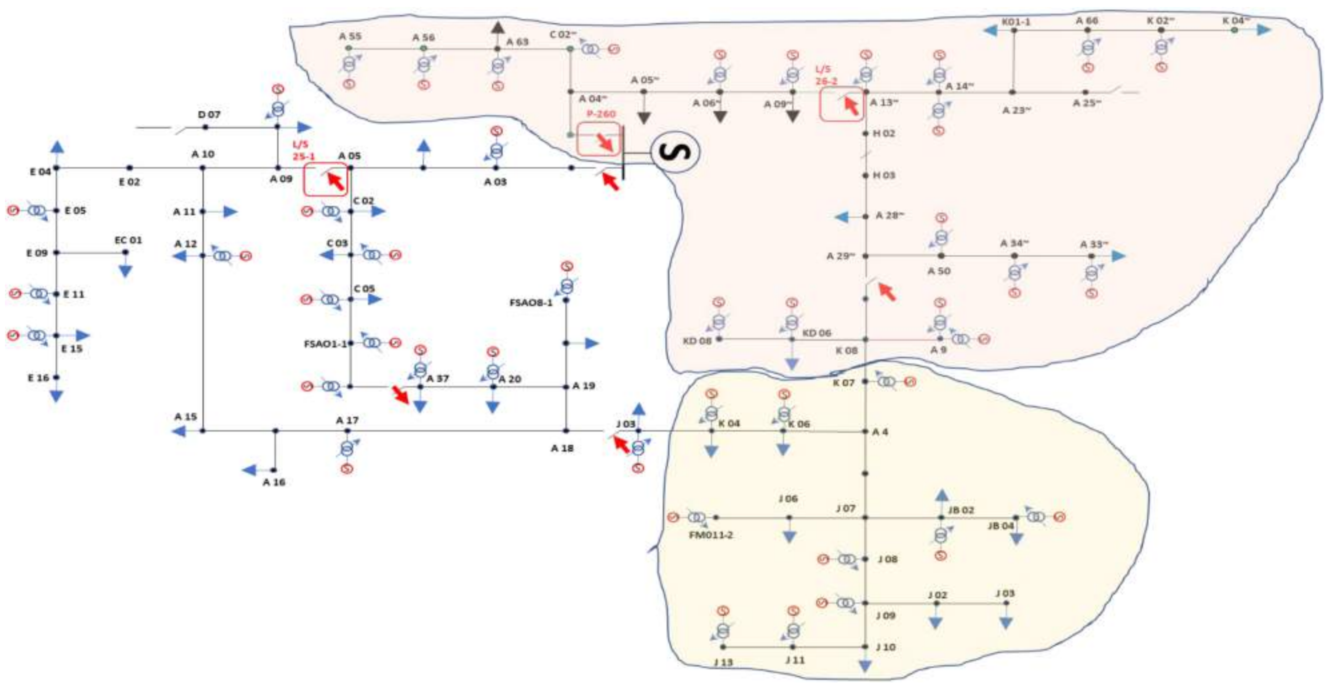

Fig. 20. Simulation scenario no. 4: Feeding line no. 26 from line no. 25. The colored areas are the ones where the voltage level exceeds the limit of 22 kV, in all cases except the ripple signal decrease control to 50% of PV actual production.

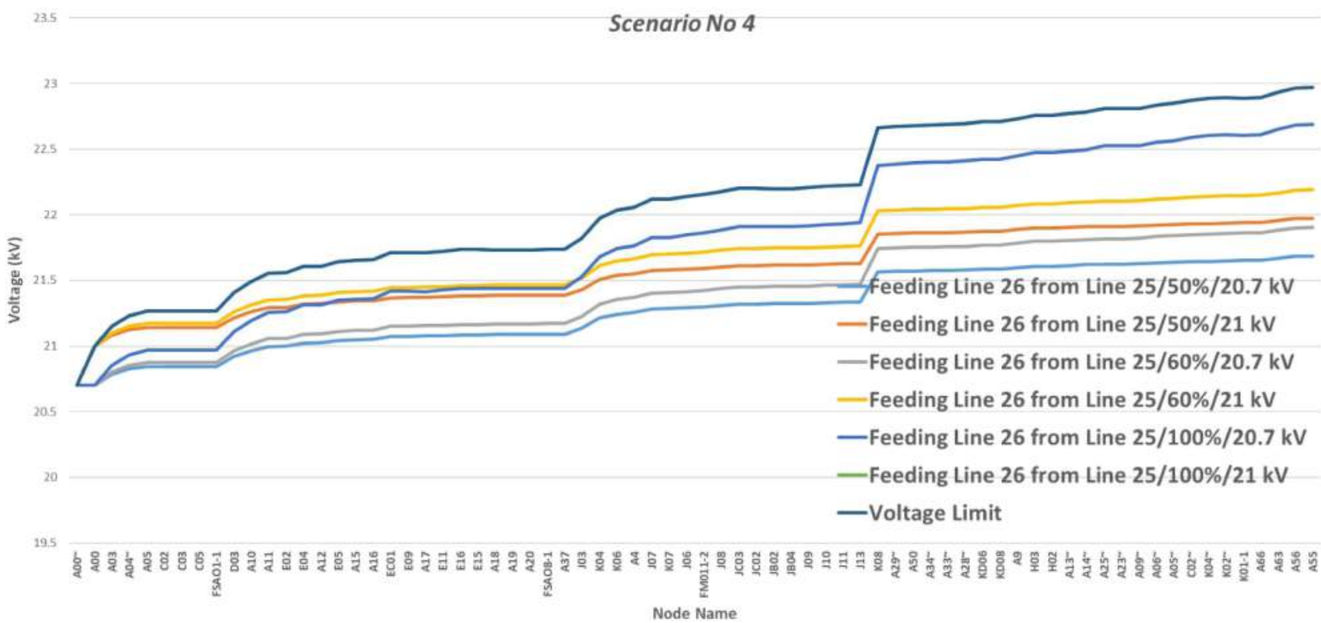

Fig. 21. Voltage profile of simulation scenario 4.

TABLE II.
COMPARISON BETWEEN RIPPLE SIGNALING AND RTU SOLUTIONS

Solution	Investment Cost Per Solar Power Plant (€)	Installation Cost Per Solar Power Plant (€)	MONTHLY O&M Cost Per Solar Power Plant (€)	Cybersecurity
Ripple signaling	2000	10 000	0.00	Inherently cyber secure: Internal network signal and no IP assignment
RTUs	1.000 00-1.500 00	10 000	1000 (for internet connection)	Vulnerable to IoT threats

RTU, remote terminal units.

Fig. 22. Installation of the ripple signal receiver to the smart logger.

Fig. 23. Active PV power before the ripple signal transmission (23,373 kW) and after the signal transmission (48,918 kW).

Although it is already known, how to duplicate the available pairs of the signals, in a substation with two or three transformers, we must still investigate the possibility to transmit signals with the same equipment at two different frequencies (175 Hz and 188 Hz as an example). The trouble-free emission at two different frequencies at different time periods duplicates the available pair of signals.

Peer-Review: Externally peer-reviewed.

Declaration of Interests: The authors have no conflicts of interest to declare.

Funding: The described work and further pilot testing are supported by the Hellenic Distribution Network Operator (HEDNO), through the contract No. 6765469B7K-5KΓ, and under the project with code 80579 of the Research Committee of the University of Western Macedonia.

REFERENCES

1. H. Markiewicz, and A. Klajn, Voltage Disturbances, Standard EN50160, Voltage Characteristics in Public Distribution Systems, Leonardo Power Quality Initiative; 2004.
2. REGULATORY AUTHORITY OF ENERGY (RAE)/Management code of the Greek Electricity Distribution Network. Available: rae.gr.
3. HEDNO/Low Voltage Photovoltaic Connection Guide.
4. M. A. Zehir *et al.*, "Impact of renewable based microgrid supply/demand profiles on low voltage distribution networks," *Energy Procedia*, vol. 103, pp. 231–236, 2016.
5. HEDNO directive No119.
6. THE REMOTE CONTROL FREQUENCIES by Jean Marie POLARD (Ternat, Belgium).
7. Orion/How to use ripple signals on Orion s network/Revision 5.
8. BDEW/ Technical Guideline/Generating Plants Connected to the Medium-Voltage Network/Guideline for generating plants' connection to and parallel operation with the medium-voltage network/June 2008 issue.
9. Installation Manual/SMA POWER CONTROL MODULE (PWCMOD).
10. HUAWEI/ Fusion solar/residential and commercial smart PV solution.
11. SOLAREDGE/.Application Note - SolarEdge Inverters, Power Reduction Control/ V3-December 2018.
12. ABB solar inverters/Product manual/PVS-50-TL / PVS-60-TL.
13. D. Stimoniaris, D. Tsiamitros, and E. Dialynas, "Improved energy storage management and PV-active power control infrastructure and strategies for microgrids," *IEEE Trans. Power Syst.*, vol. 31, no. 1, Iss, pp. 813–820, 2016.
14. D. Stimoniaris "Demand-side management by integrating bus communication technologies into smart grids," *Elsevier Electr. Power Syst. Res. (EPSR)*, vol. 136, pp. 251–261, 2016.
15. V. Zacharaki, M. A. Zehir, A. Thavlov, K. Heussen, A. Batman, D. Tsiamitros, D. Stimoniaris, A. Ozdemir, E. Dialynas, M. Bagriyanik, "Demand response with residential and commercial loads for phase balancing in secondary distribution networks," *6th International Istanbul Smart Grids and Cities Congress and Fair (ICSG)*, Date of Conference: 25–26 April 2018, IEEE Xplore: 12 July 2018.
16. A. Tsiakalos *et al.*, "Development of an innovative grid ancillary service for PV installations: Methodology, communication issues and experimental results", *Sustain. Energy Technol Assess*, vol. 44, p. 101081, 2021.
17. RTU configuration software user manual, Schneider Electric. Available: [CrossRef]

TEPES
TURKISH JOURNAL OF
ELECTRICAL POWER
AND ENERGY SYSTEMS

TEPES, Vol. 2, Issue. 1, 46-57, 2022 **DOI:** 10.5152/tepes.2022.22010

RESEARCH ARTICLE

Energy Management Planning According to the Electricity Tariff Models in Turkey: A Case Study

Sercan İşçan[1,2], Oktay Arıkan[2]

[1]Department of Construction and Maintenance, Boğaziçi University, İstanbul, Turkey
[2]Department of Electrical Power Systems, Yıldız Technical University, İstanbul, Turkey

Cite this article as: S. İşçan & O. Arıkan. Energy management planning according to the electricity tariff models in turkey: A case study. *Turk J Electr Power Energy Syst,* 2022; 2(1): 46-57.

ABSTRACT

In recent years, as a result of limited energy sources, growing populations all around the world, and increases in energy demand, many techniques penetrate into both the producer and consumer sides. One of the most important of these techniques is optimal energy management. Managing the energy use of public institutions, particularly in state universities with campus characteristics, should be an important part of local energy and climate policy. The International Organization for Standardization (ISO) 50001 standard constitutes an internationally recognized catalog of requirements for systematic energy management. Currently, this standard is mostly implemented by organizations. In this study, with reference to the ISO 50001 standard, the energy management system is handled as an energy planning which is the initial step of the ISO 50001 and also optimal tariff management study is exercised as the initial action of energy planning. Case studies are conducted to specify the optimal electricity tariffs model by analyzing different billing models in Turkey. Results show that invoice costs can be saved at the rate of 2.93%–3.71% by optimal tariff management that does not require any investment costs.

Index Terms—Energy management, electricity tariff management, ISO 50001, university campus

I. INTRODUCTION

In recent years, especially in emerging economies, the energy demand increased rapidly and became an explosive problem of the world as a result of limited energy sources, population growth, and economic development day by day [1-4]. Furthermore, as conventional energy resources such as fossil fuels, oils, natural gas, and coal are not dispersed uniformly among the world, the classification of resource-rich and resource-poor countries emerges too. Hence, countries form their foreign policies in this direction, develop methods to be competitive in the world, and tend to implement these optimally [5, 6]. In the context of severe and cascading sustainability challenges, critical strategies are shared among emerging economies [7, 8]. These countries are ascribing greater importance to energy efficiency, and energy management systems (EnMS) subtly balance the industry-driven economies and energy consumption [9–11]. These issues led numerous countries, especially in emerging economies, to take action about energy efficiency and EnMS and accelerated the steps to be taken in these regards.

In Turkey, ranked as an emerging economy, energy demand increases faster than developed countries due to its population growth, economic development, and industrialization. In addition, Turkey, whose imported energy rate is 73.21%, according to the primary energy data of 2019, is among the countries with a high external dependence on energy [12, 13]. Ultimate energy consumption was realized as 109.57 Million Tonne of Oil Equivalent (MTOE) on a sectoral basis in 2019 and increased by 39.47% in the 10-year period from 2009 to 2019. The ultimate energy consumption rates of sectors as of 2019 in Turkey are shown in Fig. 1. As illustrated in Fig. 1, the rates of ultimate energy consumptions in Turkey by sectors are as follows respectively: housing and service sector (32.58%), industry sector (31.46%), transportation sector (25.24%), agriculture and livestock (4.27%), and non-energy consumption group (6.45%) [13]. These rates clearly show that energy efficiency and EnMS have an important role in public institutions, especially in university campuses, that are placed in the housing and service sector and should be carried out in Turkey particularly. Thus, so as to energy efficiency studies to aim at sustainable and continuous improvement, it is strongly recommended that organizations in Turkey need to establish EnMS in line with the Energy Efficiency Law No 5627.

Due to the above-mentioned issues, EnMS becomes one of the popular research topics around the world and is considered the most effective way to prevent energy wastage [14]. With an EnMS,

Corresponding author: Sercan İşçan, e-mail: sercan.iscan@boun.edu.tr

Received: January 31, 2022
Accepted: March 11, 2022

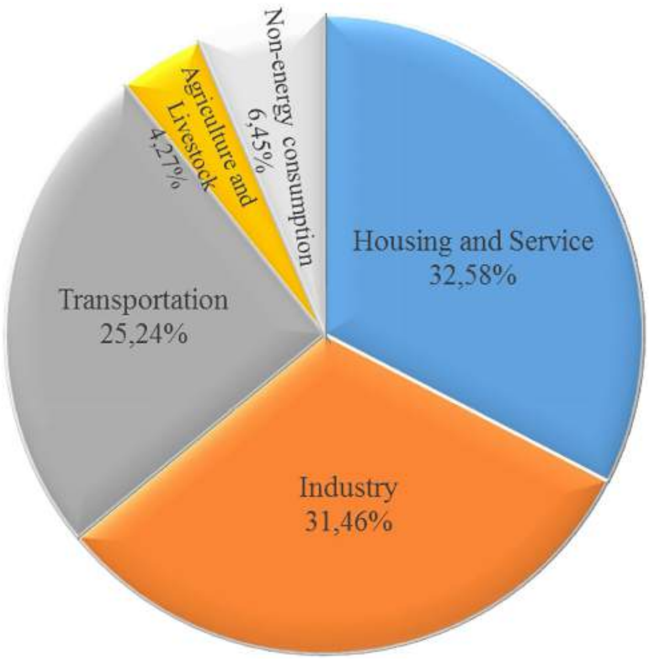

Fig. 1. Ultimate energy consumption rates on the basis of sectors in Turkey as of 2019.

an organization can specify energy targets and processes to achieve these targets [15]. Besides the energy efficiency potentials in almost all sectors, it is possible to improve the energy performance by 40% by EnMS and existing technologies, even in the countries that use energy efficiently [16]. In this regard, the International Organization for Standardization (ISO) 50001, which comprehensively gives guidance on the elements of an EnMS, is a significant standard [17]. The ISO 50001 standard defines good practice standards and guidelines for energy management and is widely applicable [11-18]. It permanently aims to enhance the energy performance of numerous organizations worldwide by ensuring them strategic practices to use their energy more optimally and effectively [19, 20–25]. A great number of studies in the literature have highlighted that significant energy efficiency gains and energy savings can be yielded cost-effectively through the long-term execution of an ISO 50001-based EnMS, even without requiring a large financial investment [18, 24–27].

Main Points

- Cost reduction without investment.
- The way of the successful initial step about energy management issue.
- Raise awareness about energy management issues in public institutions and organizations, especially in state universities that have campus zones.
- Winning the top management's trust, increasing its support, thus putting techniques into practice that require investment cost in a shorter time by the savings obtained from the actions that no need investment cost.

A great number of studies on energy efficiency and EnMS in various sectors have taken part in the literature. Most papers on EnMS deal with practices in the industrial, company, factory, and building and residence sectors that are used for various purposes and finally the transportation sector [28]. In [29], Roy studied sustainable energy management to promote energy efficiency in the public sector in Malaysia. This study makes recommendations regarding the applicability of energy management strategy in the public sector in Malaysia. In [30], the results of the research conducted among 121 German companies that are mostly (84%) from the manufacturing sector and EnMS certified by the ISO 50001 are analyzed. In this study, it is concluded that the reduction of energy costs is the main motivation of EnMS. Moreover, making use of subsidies, acceptance of EnMS by employees, and image advantages are regarded as additional motivators.

A case study in Latvia [31] recommends directions for implementing EnMS and stresses that having an energy team of employees tasked with establishing the EnMS and being equipped with the necessary instruments are a high priority. Another study on EnMS [32] concludes that having no energy manager, insufficient financial resources, and missing or incomplete data are major challenges that need to be overcome for functioning EnMS. In the case study of [33], the EnMS helps identify public buildings with high specific and absolute energy consumption and prioritize energy efficiency measures, including renovation. In this study, in 2019, the heat consumption of public buildings was 12% lower and electricity consumption was 8% lower than in 2016. In [34], the study on EnMS and clean production in the automotive sector, Ozdemir indicates that the electricity used in the factory could be reduced by 10%, thanks to energy efficiency actions. Moreover, the amount of waste could also be reduced by 40% with clean production activities. In [35], Onus, in his study on the automotive sector, indicates that the cheapest and the most effective way to reduce energy consumption, energy costs, carbon emissions, and wastes in the production process is to use EnMS standards. In studies [36–39], analyses are conducted based on energy audits to increase energy consumption transparency through a systematic investigation and for the identification of the different energy consumers within a production system. Methods in these studies allow for the identification of the most energy-consuming processes and represent a very significant step to improve the energy efficiency of the production process. Moreover, reviewing of utility bills or other operating data (e.g., rated power of the equipment and their number of operating hours) and a walk-through of the facility are analyzed in these studies.

Acosta, in [40], does scientific research on the 66 public schools in Louisiana and indicates that 70% of the energy consumed in schools is for heating–cooling, 22% for lighting, and 8% for office and kitchen needs. Moreover, in this study, it is also stated that the energy-saving potential is higher in schools with a large number of students and a wide usage area. Thus, in this study, it is concluded that energy consumption and costs can be reduced by 25% by implementing an EnMS in schools. In [41], Lee forms an EnMS model to evaluate the building energy performance by analyzing scenario-based case studies in 30 buildings that serve cross purposes on the campus of Georgia Technical University. The proposed model in the study aims to improve the energy and environmental performance of the buildings on the campus and concludes that it is economized energy consumption and prevents negative environmental effects as a result of the implementation of these specified scenarios. In [42], saving methods to reduce the energy costs of mosques are analyzed by Akdag. In this study, it is concluded that approximately 30% of energy savings could be achieved by applying thermal insulation to the mosques that are no thermal insulation studied. In addition, it is concluded that the lighting costs could be reduced by 75% by replacing the existing lighting in the examined mosques with energy-saving compact fluorescent or LED lamps. Sinha, in [43], develops a real-time energy performance model to reduce energy consumption and costs in residential buildings. This model is employed for controlling and forecasting the energy consumption of heating–cooling equipment, and 30% of energy saving has been achieved in the residences in this way.

It is clearly seen that the above-mentioned studies are the output of EnMS. In general, these studies aim to reduce both the negative environmental effects and provide financial saving opportunities as a result of actions that needed investment costs in small and medium-sized enterprises. However, the practicing rates of these studies in real life are surprisingly minimal since the proposed EnMS studies in the literature generally include issues that needed initial investment costs. As can be seen in Fig. 2, an organization can save about 3%–5% financially only through the energy reviewing process [44]. Therefore, the top management expectation of the organizations for EnMS, particularly public institutions subject to public funding, is to be given priority applications with no or very low investment costs in action plans.

In this study, firstly, an organizational EnMS flowchart that specifies all steps step by step is proposed in Fig. 3. As can be seen in Fig. 3, the proposed EnMS include the stages of planning, implementation, control, and taking precautions specified in the ISO 50001 standard. Next, the energy reviewing process, which is one of the initial steps of EnMS, given in Fig. 3 is performed as a case study. Thus, opportunities in EnMS are specified by energy consumption analysis on a zonal basis and costs. As shown in Fig. 2, financial opportunities that are approximately 3%–5% only through the energy reviewing process are the main motivation of this study. Thus, the main purpose of this study is to analyze the opportunities that do not need any investment costs but have financial returns within the scope of EnMS. Within this context, in our study, [45] is taken as a reference, the electrical energy consumed by the six campuses of Bogazici University located in different locations are analyzed and important consumption zones are specified for the years 2019–2020. Next, as a case study, scenario-based invoice cost (IC) analysis of the North Campus which is specified as one of the important consumption zones is conducted. As a result, the optimal tariff management strategy of the campus is specified, and it is concluded that there is a financial savings opportunity of 2.93%–3.71% per year by this strategy. The main contributions of this study are as follows:

(1) raising awareness about energy management issues in public institutions and organizations, especially in state universities that have campus zones;
(2) specifying important consumption zones and energy mapping of the organization;
(3) scrutinizing the tariff models in Turkey in electricity energy billing and specifying optimal tariff management of an organization;
(4) specifying opportunities that do not need any investment cost in EnMS, and analyzing the financial gain potential of the organization in line with these opportunities;
(5) winning the top management's trust, increasing its support, and thus implementing the applications that require investment cost in a shorter time by the savings obtained from the EnMS applications that do not require investment costs.

The paper is organized as follows. Section II explains the method and materials of the study. In section III, as a case study, scenarios are

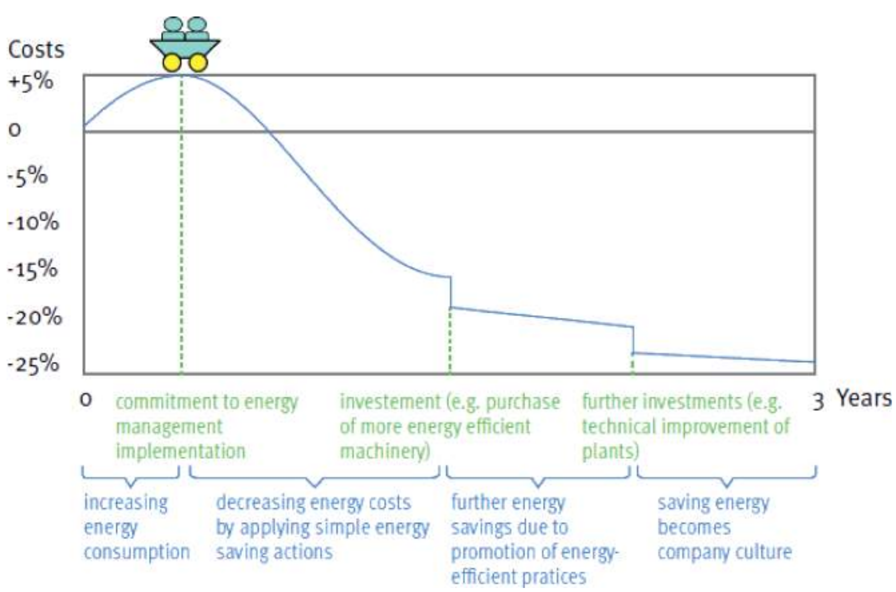

Fig. 2. Impact of EnMS on cost reduction [16].

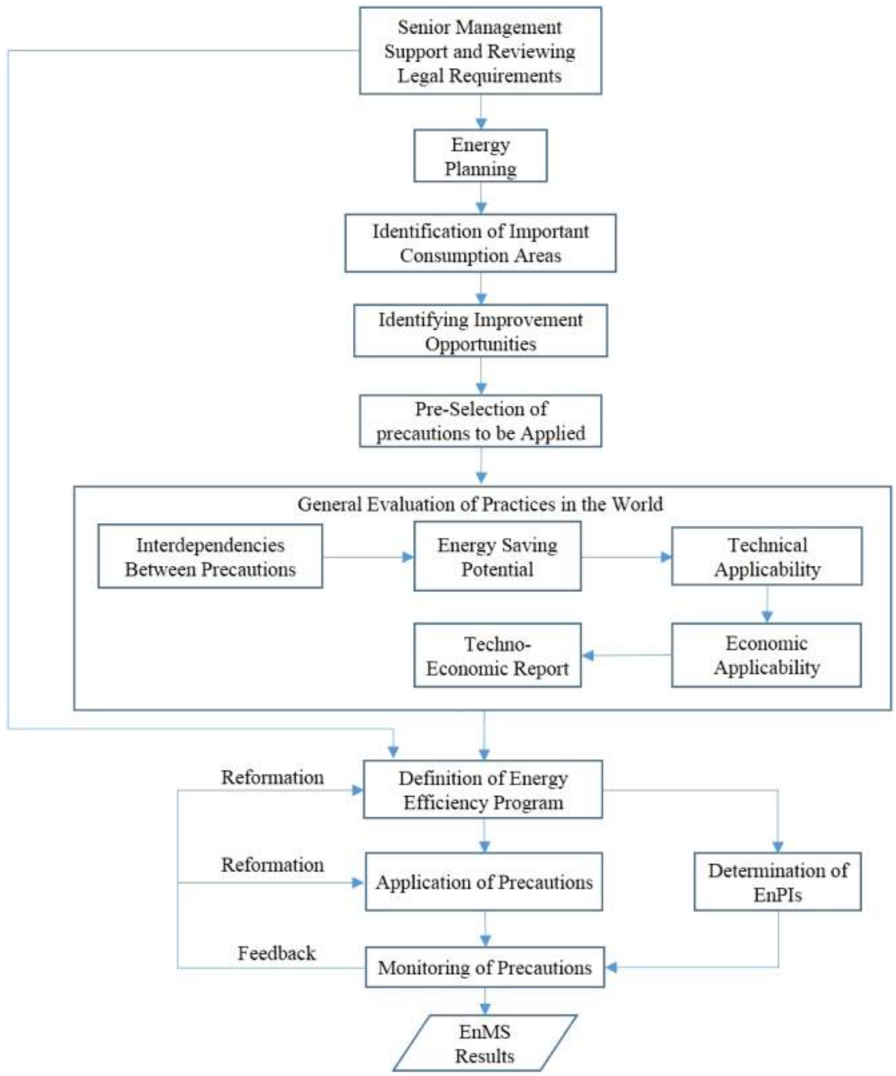

Fig. 3. Proposed EnMS flow chart.

analyzed and results and discussions are considered. Finally, the conclusion is drawn in section IV.

II. MATERIALS AND METHODS

In this section, the electrical energy consumed by the six different campuses of Bogazici University indicated in Table I was systematically measured and monitored (MM) between 2019 and 2020. Thus, important consumption zones (campuses) have been specified. MM was carried out via Otomatik Sayaç Okuma Sistemi (OSOS) system which does not need any investment cost at the transformer points, and recorded consumptions have been analyzed within the framework of the following points:

(1) energy consumptions on a monthly and seasonal basis;
(2) energy consumptions on a three-time tariff basis;
(3) peak load demands on a monthly basis;
(4) existing billing model versus alternative electricity tariffs models.

TABLE I.
BOGAZICI UNIVERSITY CAMPUSES WHERE ELECTRICAL ENERGY CONSUMPTION IS MEASURED AND MONITORED

Campus	Total Closed Area (m^2)	Attribute of Subscriber
South	58,783.85	2000 kVA, MV*
North	99,661.25	2000 kVA, MV
		1600 kVA, MV
Uçaksavar	37,304.42	1600 kVA, MV
Hisar	13,529.13	LV*
Sarıtepe	45,748.37	1600 kVA, MV
Kandilli	43,613.06	1600 kVA + 2500 kVA, MV

*MV is the medium voltage; LV is the low voltage.

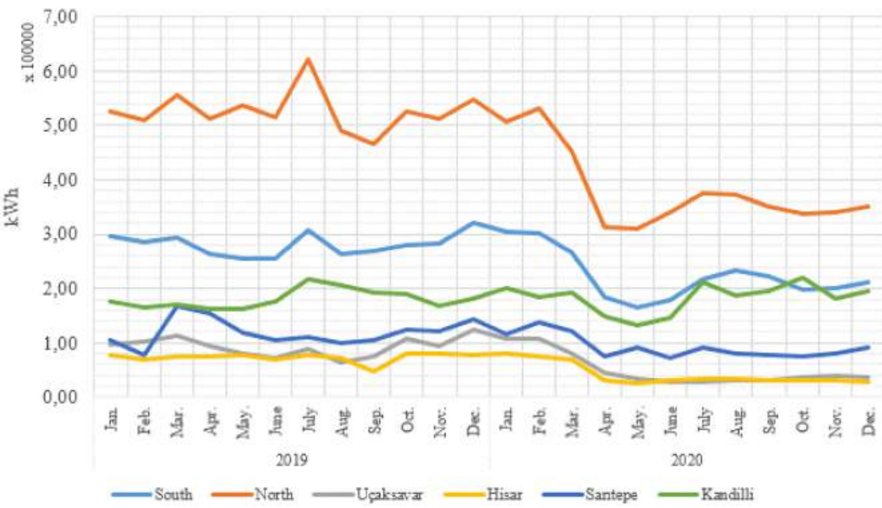

Fig. 4. Monthly basis campus consumptions of 2019–2020 years.

Thus, the second and third steps of the EnMS workflow diagram indicated in Fig. 3 have been carried out. These data are shown in Fig. 4 and Fig. 5. At this point, the main purpose is to determine the important consumption zones and the next step is to improve opportunities by making a preliminary study of the electrical energy consumption of the institution within the scope of EnMS. In this study, the priority of improvement opportunities is to identify actions with low investment costs but high impact and include these in the action plan of EnMS. Thus, as illustrated in Fig. 2, it is aimed to initially reduce energy costs by 3%–5% by simple measures and actions and to take the first step to ensure its continuity. Moreover, it is also aimed to win the top management's trust and to increase the awareness and support of EnMS through actions that need low investment costs but have a high financial incoming impact.

As can be seen clearly in Fig. 4 and Fig. 5, the highest total electrical energy consumption occurs in the North Campus by 40%. This is followed by South Campus by 23%, Kandilli Campus by 16%, Sarıtepe Campus by 10%, Uçsavar Campus by 6%, and Hisar Campus by 5%, respectively. When Fig. 4 is analyzed carefully, it is clearly seen that, since February 2020, electricity consumption has been decreased by nearly 32% as a result of online education throughout the university due to the coronavirus disease 2019 epidemic. Since this issue is important in terms of IC analysis, which is the main subject of our study, it is especially discussed.

Another indicator used in this study to specify the important consumption zones is the energy performance indicators (EnPI) of the campuses. In our model, as the EnPI, kWh/m^2, that is, the amount of energy consumed per unit closed area is used. Campus energy performances for the years 2019–2020 were calculated by using the closed area values specified in Table I and the consumption data in Fig. 4, and results are illustrated graphically in Fig. 6. As can be seen in Fig. 6, campuses with the worst energy performance are North, Hisar, Kandilli, South, Sarıtepe, and Uçaksavar campuses, respectively. As illustrated in Fig. 4–6, it is clearly concluded that the North Campus is the most critical campus in terms of both consumption and performance. Therefore, a case study on optimal IC analysis is conducted in the North Campus. We would like to point out in particular that other EnMS issues such as performance evaluation, the best and worst periods analysis, hourly consumption analysis, energy production rates, EnPI targets, etc., are not discussed because these lie outside the scope of the study.

A. Electricity Billing Tariffs in Turkey

The electrical energy billing tariffs in force in Turkey are shown in Table II briefly. As can be seen in this table, the electricity tariffs in Turkey are primarily categorized as Low Voltage (LV) and Medium Voltage (MV). Next, sub-categorization is made based on monomial (M) and binomial (B) regarding term type, based on fixed-time (FT) and three-time (3T) regarding the time of use (ToU), and finally user types. We would like to point out that since the green tariff specified in Table II entered into force as of date October 2020, it is not taken into consideration in the case study.

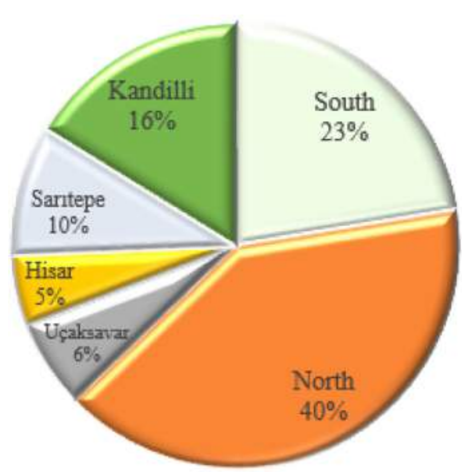

Fig. 5. The percental rates of the total electrical energy consumption in 2019–2020 by campuses.

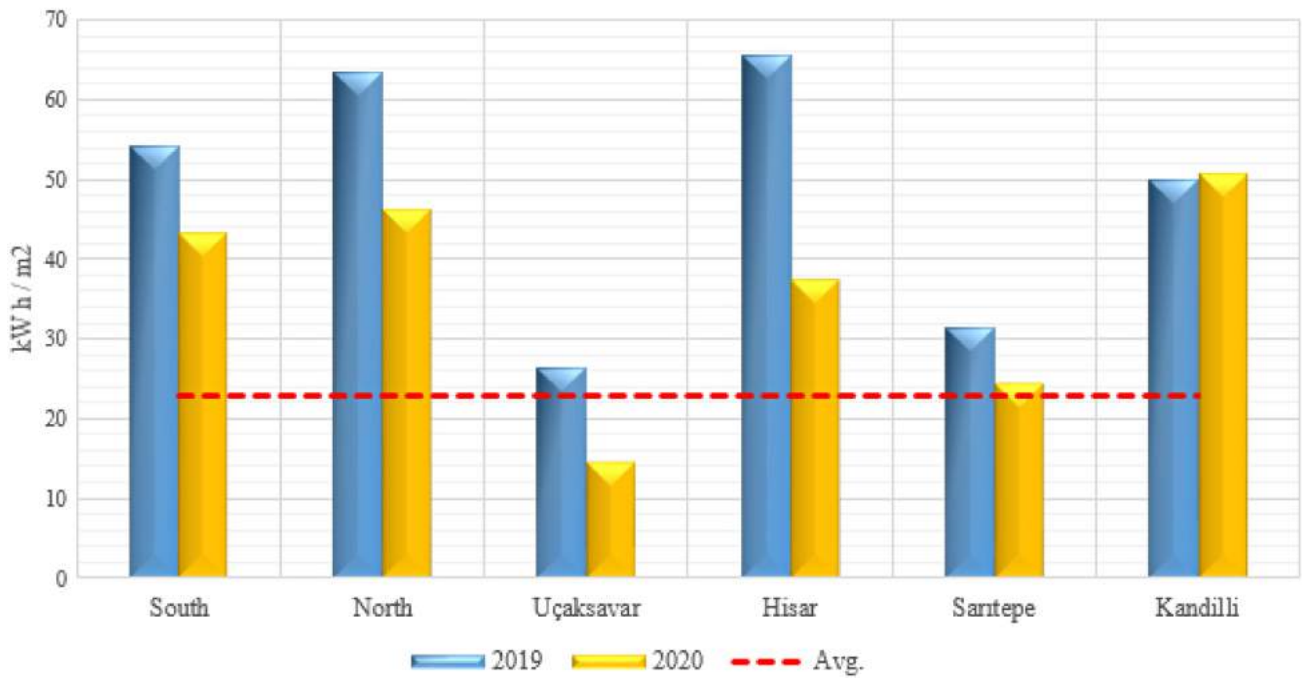

Fig. 6. Yearly basis campus EnPIs of 2019–2020 years and the reference line.

1) Monomial Tariff

In this tariff model, only the amount of electricity consumed (kWh) is used for IC [45]. In this tariff, Eq. (1) is used for calculating IC.

2) Binomial Tariff (Demand Charge Tariff)

In this tariff model, in other words, demand charge tariff (DCT), IC is calculated via both contract power (CP) (kW) that is promised not to exceed by the consumer during 1 month and monthly-based active power consumption of the consumer [45]. Customers subject to this tariff model can change their contract power up to three times in a calendar year [46]. The purpose of DCT is to know the demanded power (DP) of the customers and to keep this power ready for them by agreements made with consumers who demand high power [45]. A certain power fee (PF) is charged in this tariff model; however, a discount is also made on the active energy unit cost consumed. The most important issue in this tariff model is the determination of the CP optimally because the selected high value of the CP can cause more power cost and can remove the advantage of the tariff. On the

TABLE II.
THE ELECTRICAL ENERGY BILLING TARIFFS IN FORCE IN TURKEY

	Normal Tariff								Green Tariff							
	LV				MV				LV				MV			
	M		B		M		B		M		B		M		B	
Consumer Groups	**FT**	**3T**	**FT**	**3T**	**FT**	**3T**	**FT**	**3T**	**FT**	**3T**	**FT**	**3T**	**FT**	**3T**	**FT**	**3T**
Industry	✓	✓			✓	✓	✓	✓	✓				✓		✓	
Business	✓	✓			✓*	✓	✓	✓	✓				✓		✓	
Household	✓	✓			✓	✓	✓	✓	✓				✓		✓	
Agricultural Irrigation	✓	✓			✓	✓	✓	✓	✓				✓		✓	
Lighting	✓				✓		✓		✓				✓		✓	
Families of Martyrs and War Veteran	✓															
General Lighting	✓															

* The current (base) tariff class of the North Campus for which the case study is conducted.

contrary, when this power is exceeded as a result of which the CP is specified low value, the extra power overrun fee is applied and the customer is penalized. Therefore, the system should be analyzed very carefully for determining the optimal CP. In this tariff model, IC is calculated by using Eq. (2).

3) ToU Tariff as Fixed-Time and Three-Time

In the FT tariff model, ToU is fixed. On the contrary, in the 3T tariff model, ToU is categorized as follows: T1 is the normal price time slot between 06:00 and 17:00 hours, T2 is the higher price time slot between 17:00 and 22:00 hours, and T3 is the lower price time slot between 22:00 and 06:00 hours. In the 3T tariff model, the IC of electricity consumed specified time slots above are calculated separately. These time periods have been determined by considering the daily load curve of the Turkish electricity system by the Energy Market Regulatory Authority (EMRA). The main purpose of this model is to encourage the use of electrical home appliances that consume a lot of energy, such as washing machines, dishwashers, irons, after 22:00 hours. Because, at T2 time slot overlapping of various loads such as lighting, industry, generally the highest demand power occurs and this power needed should be provided by electricity generation companies. In this case, the power plants with the highest operating costs are commissioned and the production cost naturally increases. Thus, the electrical energy selling price in this model reaches the highest value at the T2 time slot. In this tariff model, for calculating ICs, Eq. (3) is used for M tariff and Eq. (4) is used for B tariff, in other words, DCT:

$$IC = \frac{1}{100} \times \sum_{t=1}^{n} \left(\exists_i \times \aleph \right) \tag{1}$$

$$IC = \frac{1}{100} \times \left[\left(\sum_{t=1}^{n} \left(\exists_i \times \aleph \right) \right) + \left(CP \times PF \right) \right] \tag{2}$$

$$IC = \frac{1}{100} \times \sum_{t=1}^{n} \left[\left(\exists_{T1_t} \times \aleph_{T1} \right) + \left(\exists_{T2_t} \times \aleph_{T2} \right) + \left(\exists_{T3_t} \times \aleph_{T3} \right) \right] \tag{3}$$

$$IC = \frac{1}{100} \times \left[\left(\sum_{t=1}^{n} \left(\exists_{T1_t} \times \aleph_{T1} \right) + \left(\exists_{T2_t} \times \aleph_{T2} \right) + \left(\exists_{T3_t} \times \aleph_{T3} \right) \right) + \left(CP \times PF \right) \right] \tag{4}$$

Where $\exists$ denotes the active energy consumption (kWh) and $\aleph$ denotes the energy unit cost of the relevant class (krş/kWh). *PF* is (krş/Month/kW) basis. Subscripts denoted *t* and *n* are periods of IC. Where time slots denoted as *t* and *n* are handled on a daily basis while ICs are calculated monthly.

III. SYSTEM DESCRIPTION AND DATA'S

As shown in Table I, the power of the North campus is supplied through two separate transformer subscriptions named North-TR1 and North-TR2. Load profiles and DP data of these subscriptions are shown in detail in Fig. 7, Fig. 8, Table III, and Table IV. Where $\ddot{Y}$ denotes the closest to the highest demand power (DP) value occurred during the years 2019–2020 and the safest maximum DP value that is not exceeded. On the other hand, λ denotes the safest maximum DP value that is closest to and does not exceed the highest DP value occurring in the periods specified in Table III and Table IV in 2019 and 2020. Another issue we would like to point out here is that the consumption of the North Campus illustrated in Fig. 4 is the sum of the consumption of these two subscriptions given in Fig. 7 and Fig. 8 during the same periods. For instance, the total consumption of January 2019 of the North Campus illustrated in Fig. 4 is equal to the sum of January 2019 consumptions in Fig. 7 and Fig. 8.

IV. CASE STUDY

Case studies are conducted on specifying the optimal tariff model analyzed through using electrical energy consumption data of the North Campus between 2019 and 2020 years. The current model, as a base case, is analyzed by being compared with the five alternative

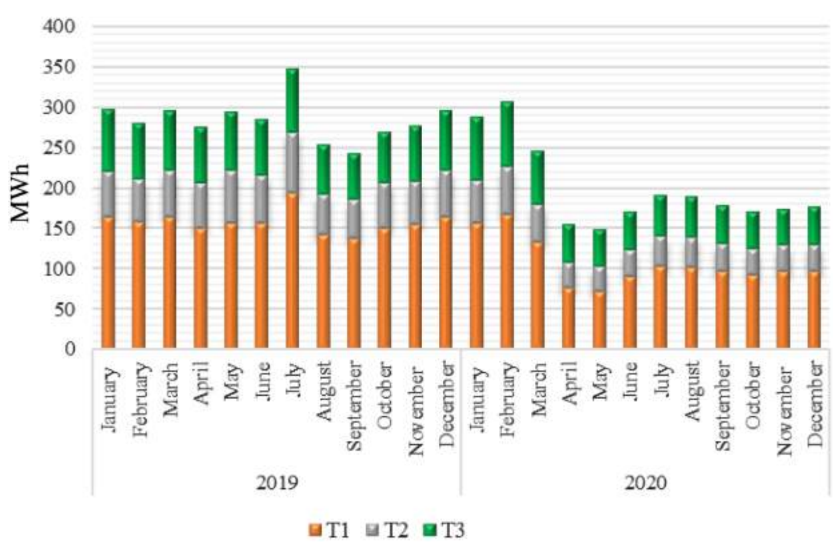

Fig. 7. Load profile of North-TR1.

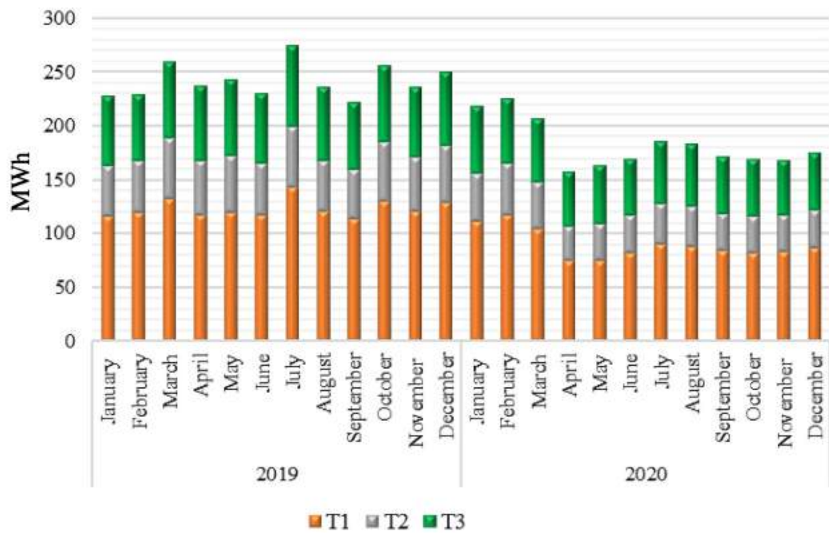

Fig. 8. Load profile of North-TR2.

scenario-based billing models. The case studies carried out in this section are briefly described below.

(1) Case 1: Base case: In this case, the ICs of the analyzed campus are carried out via the current tariff model named medium voltage monomial fixed time (MV-M-FT). Thus, a benchmark is specified for the pros and cons of other scenarios compared to the current model.

(2) Case 2: Scenario of medium voltage monomial three time (MV-M-3T) tariff model: In this scenario, the ICs of the North campus is analyzed as if the MV-M-3T model was utilized during the same period of the base case.

(3) Case 3: Scenario of medium voltage binomial fixed time (MV-B-FT) tariff model using $\ddot{Y}$ values: In this scenario, the ICs of the North campus is analyzed as if the MV-B-FT model was utilized during the same period of the base case. In this scenario, DP is not changed during the period.

(4) Case 4: Scenario of medium voltage binomial fixed time (MV-B-FT) tariff model using λ values: In this scenario, the ICs of the North campus is analyzed as if the MV-B-FT model was utilized during

TABLE III.
DP DATA OF NORTH-TR1

	DP (kW)		Ÿ (kW)		λ (kW)	
Months	**2019**	**2020**	**2019**	**2020**	**2019**	**2020**
January	756.2	728.6	≤1000	≤1000	≤800	≤800
February	750.7	772.8	≤1000	≤1000	≤800	≤800
March	695.5	684.4	≤1000	≤1000	≤800	≤800
April	656.5	309.1	≤1000	≤1000	≤800	≤500
May	723.1	270.4	≤1000	≤1000	≤800	≤500
June	966	402.9	≤1000	≤1000	≤1000	≤500
July	966	458.1	≤1000	≤1000	≤1000	≤500
August	817	463.6	≤1000	≤1000	≤1000	≤500
September	684.4	469.2	≤1000	≤1000	≤750	≤500
October	712	425	≤1000	≤1000	≤750	≤500
November	645.8	419.5	≤1000	≤1000	≤750	≤500
December	673.4	408.4	≤1000	≤1000	≤750	≤500

TABLE IV.
DP DATA OF NORTH-TR2

	DP (kW)		Ÿ (kW)		λ (kW)	
Months	**2019**	**2020**	**2019**	**2020**	**2019**	**2020**
January	529.92	463.68	≤800	≤800	≤600	≤600
February	574.08	507.84	≤800	≤800	≤600	≤600
March	552.00	507.84	≤800	≤800	≤600	≤600
April	518.88	342.24	≤800	≤800	≤600	≤400
May	529.92	298.08	≤800	≤800	≤600	≤400
June	717.60	331.20	≤800	≤800	≤800	≤400
July	750.72	375.36	≤800	≤800	≤800	≤400
August	618.24	353.28	≤800	≤800	≤800	≤400
September	529.92	353.28	≤800	≤800	≤600	≤400
October	540.96	342.24	≤800	≤800	≤600	≤400
November	507.84	342.24	≤800	≤800	≤600	≤400
December	507.84	353.28	≤800	≤800	≤600	≤400

the same period of the base case. On the contrary of Case 3, in this scenario, DP is changed three times during the period.

(5) Case 5: Scenario of medium voltage binomial three time (MV-B-3T) tariff model using $\ddot{Y}$ values: In this scenario, the ICs of the North campus are analyzed as if the MV-B-3T model was utilized during the same period of the base case. Different from Case 3, on the contrary, in this scenario, ToU is 3T.

(6) Case 6: Scenario of medium voltage binomial three time (MV-B-3T) tariff model using λ values: In this scenario, the ICs of the North campus are analyzed as if the MV-B-3T model was utilized during the same period of the base case. Different from Case 4, on the contrary, in this scenario, ToU is 3T.

The prices used for the calculations of the ICs do not include VAT. For the unit prices, the 2019 and 2020 EMRA Tariff Tables of Electricity Bills [47-54] are used. All scenarios in the case studies are calculated based on the Central Bank of the Turkish Republic monthly average effective selling USD rates [55] of the relevant consumption period.[1]

A. Case 1 Base case

In this case, for being made a benchmark rightly, the ICs belonging to the campus consumption are analyzed as a base case via the current billing model of the campus, named the MV-M-FT. The ICs of this case are calculated via Eq. (1) using the unit prices of this model given in [47-54]. The results of the ICs of the current model are \$675.432.6 and \$475.511.7 for the years 2019 and 2020, respectively, and the total IC is \$1.150.944.2.

B. Case 2 Scenario of the MV-M-3T tariff model

In this scenario, the ICs of the campus consumptions are analyzed via the MV-M-3T tariff model. The ICs of this scenario are calculated via Eq. (3) using the unit prices of this model given in [47–54]. The main purpose of this scenario is to analyze the pros and cons of the ToU model with 3T versus the current model with FT. The results of the ICs in this scenario are \$680.924.5 and \$473.102.1 for the years 2019 and 2020, respectively, and the total IC is \$1.154.026.6. As can be seen from the results, ICs increase by \$3.082.42 compared to the base case. It can be concluded that the load profile of the North campus is unsuitable for this scenario, and thus, this model is not optimal for the North campus consumption.

C. Case 3- Scenario of the MV-B-FT tariff model using Ÿ values

In this scenario, the ICs of the campus consumptions are analyzed via the MV-B-FT tariff model. The ICs of this scenario are calculated via Eq (2) using the unit prices of this model given in [47-54]. As a CP, $\ddot{Y}$ values given in Table III and Table IV are used. In this scenario, during the periods of 2019–2020, CPs are the $\ddot{Y}$ values as stated in Table III and Table IV and are fixed. The main purpose of this scenario is to analyze the pros and cons of the B model versus the current model. The results of the ICs in this scenario are \$651,100.9 and \$466,163.1 for the years 2019 and 2020, respectively, and the total IC is \$1,117,264.0. These results show that ICs decrease by \$33.680.20 compared to the base case. It can be concluded that the load profile of the North campus is suitable for this scenario even if CP equals to $\ddot{Y}$ values, which are fixed and the peak DP during the period of the years 2019 and 2020.

D. Case 4- Scenario of the MV-B-FT tariff model using λ values

In this scenario, the ICs of the campus consumptions are analyzed via the MV-B-FT tariff model. The ICs of this scenario are calculated via Eq. (2) using the unit prices of this model given in [47–54]. As a CP, λ values given in Table III and Table IV are used. In this scenario, during the periods of 2019–2020, CPs are the λ values as stated in Table III and Table IV and are not fixed. In other words, CPs, or λ values, indicated in Table III and Table IV are changed three times a year in accordance with [46]. The main purpose of this scenario is to analyze how CP, which is being changed three times a year in the B model, affects the ICs and the pros and cons of this strategy versus the current model and B model with fixed CP. The results of the ICs in this scenario are \$648,817.9 and \$459,301.5 for the years 2019 and 2020, respectively, and the total IC is \$1,108,119.4. These results show that ICs decrease by \$42,824.80 and \$9,144.6 compared to the base case and case 3, respectively. It can be concluded that the load profile of the North campus is more suitable for this scenario than the before ones if the CP equals λ values. Moreover, CPs which are being changed optimally three times a year as a result of careful analysis of the load profile could further decrease the ICs.

E. Case 5- Scenario of the MV-B-3T tariff model using Ÿ values

In this scenario, the ICs of the campus consumptions are analyzed via the MV-B-3T tariff model. The ICs of this scenario are calculated via Eq (4) using the unit prices of this model given in [47–54]. As such in case 3, in this scenario too, CPs are the $\ddot{Y}$ values given in Table III and Table IV. The only difference in this scenario is that the ToU model is 3T. The main purpose of this scenario is to analyze how 3T affects the ICs and the pros and cons of this strategy versus the other cases. The results of the ICs in this scenario are \$656,594.1 and \$463,753.9 for the years 2019 and 2020, respectively, and the total IC is \$1.120.347.9. These results show that ICs decrease by \$30,596.29 and \$33,678.71 compared to case 1 and case 2, respectively. However, on the contrary, ICs increase by \$3,083.91 and \$12,228.51 compared to case 3 and case 4, respectively. So, it can be concluded that the 3T in model B causes to lose its advantage in both cases, that is, when CP is both $\ddot{Y}$ and λ.

F. Case 6- Scenario of the MV-B-3T tariff model using λ values

In this scenario, the ICs of the campus consumptions are analyzed via the MV-B-3T tariff model. The ICs of this scenario are calculated via Eq. (4) using the unit prices of this model given in [47–54]. As such in case 4, in this scenario too, CPs are the λ values given in Table II and Table III. The only difference in this scenario is that the ToU model is 3T. The main purpose of this scenario is to analyze how 3T affects the ICs and the pros and cons of this strategy versus the other cases. The results of the ICs in this scenario are \$654,311.1 and \$456,892.2 for the years 2019 and 2020, respectively, and the total IC is \$1,111,203.3. These results show that ICs decrease by \$39,740.89, \$42,823.31, \$6,060.69, \$9,144.6 compared to case 1, case 2, case 3, and case 5 respectively. However, on the contrary, ICs increase by \$3.083.91 compared to case 4. So, it can be concluded that the 3T model still continues its advantages

1 Based on [55], the average effective selling USD rate for 2019 and 2020, 1 USD = 5.67 TL and 1 USD = 7.00 TL, respectively.

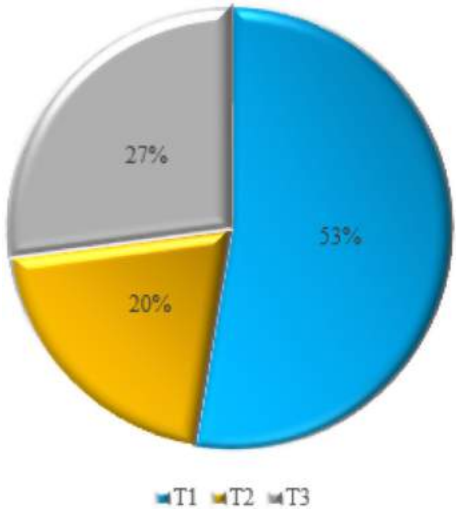

Fig. 9. Consumptions of The North campus in 3T periods.

against all other cases apart from case 4, on the condition that the CPs are specified as λ values. But, 3T in model B still causes to lose its advantage when CP is λ.

The results of the case studies above mentioned are given in Table V as a summary and also illustrated graphically in Fig. 10. It can be concluded that;

- In case 2, ICs are getting increase by 0.27%. Therefore, this model is not optimal for the North Campus.
- All the 3T models in case 2, case 5, and case 6 compared to all FT models in case 1, case 3, and case 4 respectively are worse by approximately 0.28%.
- 3T models are not optimal for consumers with load profiles in the 3T periods shown in Fig. 7.

TABLE V.
SUMMARIES OF CASE STUDIES

Scenario	Total IC of 2019–2020 ($)	Profit Amount ($)	Profit Rate
Base case	1,150,944.21		
S2	1,154,026.63	−3,082.42	−0.27%
S3	1,117,264.00	33,680.20	2.93%
S4	1,108,119.41	42,824.80	3.72%
S5	1,120,347.92	30,596.29	2.66%
S6	1,111,203.32	39,740.89	3.45%

- Unless the rate of load consumed in the T2 period is lower than 20% of all consumption or contrary unless the rate of load consumed in the T3 period is higher than 27% of all consumption 3T tariff models should be analyzed carefully for the related consumer.

The tariff model named B, or DCT, is the best suitable model for the North campus load profile. By using these tariff models, ICs are getting decrease between rates of 2.93% and 3.72% by case 3 and case 4, respectively. Opportunities to earn a total of $39,000–$43,000 in 2 years are available for case 4 and case 6 by this tariff model. Therefore, these cases, particularly case 4, are more optimal for the North Campus.

V. CONCLUSIONS

This study has focused on a crucial but seldom thoroughly investigated domain in public institutions and organizations, especially in state universities that have a campus: energy management on a non-technological and organizational, especially financial opportunities, aspect. In accordance with this purpose, initially, the importance of

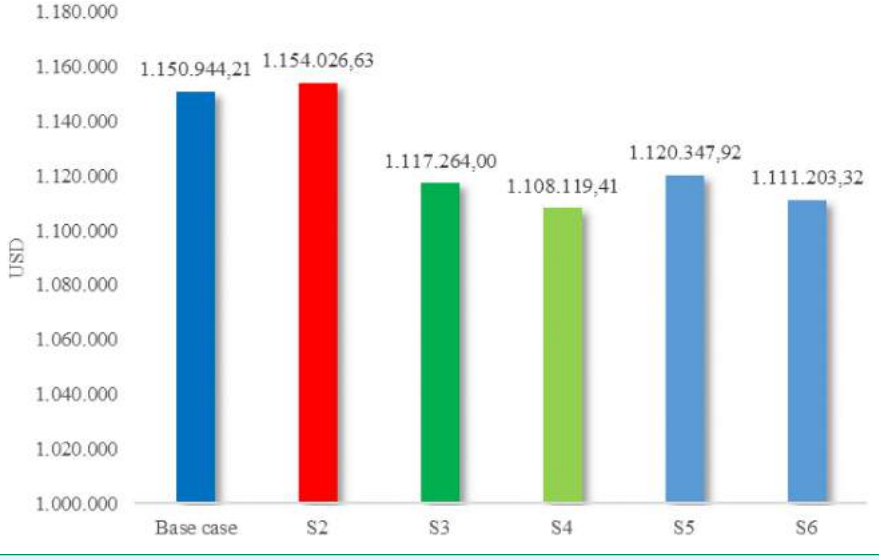

Fig. 10. Summary of the base case versus alternative scenarios.

EnMS and actions in various sectors in the literature are mentioned, and then, with reference to the ISO 50001 standard, the flow chart in Fig. 3 is proposed as an organizational EnMS. As illustrated in the proposed flow chart, after the support of the top management and reviewing legal requirements, the next step of the EnMS has been specified as energy planning. Because the sustainability of EnMS can only be ensured by successful actions in the planning step. Hence, it is highly essential to give priority to actions with both minimum investment costs and high yield in EnMS action plans for improvement activities. With this approach, as a planning step of EnMS, for performance evaluation based on specifying optimal billing model, in terms of the economy, scenario-based case studies were conducted on the IC analysis of Boğaziçi University's electricity consumption, which does not need any investment cost.

In these scenario-based case studies, the ICs of the North Campus, which is the most critical campus of Bogazici University in terms of EnPI, have been analyzed by using different tariff models in Turkey through electrical energy data that was consumed by this campus during 2019–2020 years. In this direction, initially, as a base case, the current billing model of the campus has been analyzed. The main purpose of the base case study is to make a reference point in order to analyze the pros and cons of the other five alternative tariff models against the current situation. Moreover, the pros and cons of each case study against the other ones are discussed in detail and the results are summarized. To sum up these cases, ICs increase by 0.27% in case 2 while decrease between rates of 2.93%, 3.72%, 2.66%, and 3.45% by case 3, case 4, case 5, and case 6, respectively. Thus, via the tariff models in cases 4 and 6, a total savings of $39,000.0–$43,000.0 is available for 2 years. We would like to emphasize in particular that these sums could be saved without any investment costs. These are great opportunities for organizations at the start and thus it is strongly suggested that it must be considered in the EnMS action plans as an initial step. Moreover, the opportunities on behalf of organizations to implement energy-efficient techniques that could be financed via these savings are also particularly important for their future action plans in EnMS. With reference to this study, we strongly suggest that the optimal tariff management strategy should be analyzed in public institutions, especially in universities campuses where energy is consumed intensively. Consequently, we hope that our study is a roadmap for the EnMS issue which started in 2018 at public institutions and state universities in Turkey and contributes to the gap in the literature by creating awareness.

There are many subjects to be investigated as future works. In the present study, we only analyze the ICs considering electricity tariff models in Turkey as an initial step of EnMS. However, to make the research closer to globally, different electricity tariff models in developed or developing countries can be conducted as case studies. In this way, electricity tariff models in Turkey can vary optimally on behalf of both producer and consumer. Moreover, the green tariff model in Turkey, not handled in this study because of its immaturity, can be considered as an alternative model in future works. Thus, the pros and cons of this model can be analyzed for consumer types and load profiles. As a continuation of this study, as the next step of EnMS, our future thought is to forecast the load profiles of the buildings in Bogazici University campuses, especially the peak load demands, by using forecasting-based methods. Thus, we are of the opinion to gain more profit maximization by using the B, or DCT, tariff model, as a result of peak load shaving optimally.

Peer-review: Externally peer-reviewed.

Declaration of Interests: The authors have no conflict of interest to declare.

Funding: The authors declared that this study has received no financial support.

REFERENCES

1. G. A. Kiliç, K. Al., E. Dağtekin, and Ü. Ünver, "Technical, economic and environmental investigation of grid-independent hybrid energy systems applicability: a case study," *Energy Sources Part Recover Util. Environ. Eff.*, vol. 00, no. 00, pp. 1–16, 2020. [CrossRef]
2. A. Imran *et al.*, "Heuristic-based programable controller for efficient energy management under renewable energy sources and energy storage system in smart grid," *IEEE Access*, vol. 8, pp. 139587–139608, 2020. [CrossRef]
3. Y. Fernando, P. S. Bee, C. J. C. Jabbour, and A. M. T. Thomé, "Understanding the effects of energy management practices on renewable energy supply chains: Implications for energy policy in emerging economies," *Energy Policy*, vol. 118, pp. 418–428, 2018. [CrossRef]
4. S. K. Mangla, S. Luthra, S. Jakhar, S. Gandhi, K. Muduli, and A. Kumar, "A step to clean energy - Sustainability in energy system management in an emerging economy context," *J. Clean. Prod.*, vol. 242, p. 118462, 2020. [CrossRef]
5. E. Koç, and E. Kaplan, "General Energy situation-I world assessment in the world and in Turkey," *J. Thermodyn.*, vol. 187, pp. 70–80, 2008.
6. M. Haseeb, S. A. A. Kazmi, M. M. Malik, S. Ali, S. B. A. Bukhari, and D. R. Shin, "Multi objective based framework for energy management of smart micro-grid," *IEEE Access*, vol. 8, pp. 220302–220319, 2020. [CrossRef]
7. M. A. Moktadir *et al.*, "Key factors for energy-efficient supply chains: Implications for energy policy in emerging economies," *Energy*, vol. 189, p. 116129, 2019. [CrossRef]
8. R. Martin, M. Muûls, L. B. De Preux, and U. J. Wagner, "Anatomy of a paradox: Management practices, organizational structure and energy efficiency," *J. Environ. Econ. Manag.*, vol. 63, no. 2, pp. 208–223, 2012. [CrossRef]
9. Energy and Natural Resources Ministry. *National Energy Efficiency Action Plan 2017–2023*. Ankara: Energy and Natural Resources Ministry, 2017.
10. M. S. Alam, and S. A. Arefifar, "Energy management in power distribution systems: Review, classification, limitations and challenges," *IEEE Access*, vol. 7, pp. 92979–93001, 2019. [CrossRef]
11. Y. Jin *et al.*, "An energy management maturity model for China: Linking ISO 50001:2018 and domestic practices," *J. Clean. Prod.*, vol. 290, p. 125168, 2021. [CrossRef]
12. General Directorate of Energy Affairs, "2009 National Energy Balance Sheet," Ankara, 2010. [Online]. Available: https://enerji.enerji.gov.tr//Media/Dizin/EIGM/tr/Raporlar/PRP/UEDT/741828-2009_yili_genel_enerji_dengesi_2016__r1.xlsx.
13. General Directorate of Energy Affairs, "2009 National Energy Balance Sheet," Ankara, 2020. [Online]. Available: https://enerji.enerji.gov.tr//Media/Dizin/EIGM/tr/Raporlar/Ulusal_Enerji_Denge_Tablolari/2019.xlsx.
14. D. Lee, and C. C. Cheng, "Energy savings by energy management systems: A review," *Renew. Sustain. Energy Rev.*, vol. 56, pp. 760–777, 2016. [CrossRef]
15. J. Kaselofsky *et al.*, "Getting municipal energy management systems ISO 50001 certified: A study with 28 European municipalities," *Sustainability*, vol. 13, no. 7, 2021. [CrossRef]

16. UNIDO, *Practical Guide for Implementing an Energy Management System*. Vienna: United Nations Industrial Development Organization, 2015.
17. International Organization for Standardization Energy Management Systems. *Requirements with Guidance for Use; (ISO Standard No. 50001:2018)*. Vernier, Switzerland: ISO, 2018.
18. B. Jovanović, and J. Filipović, "ISO 50001 standard-based energy management maturity model – Proposal and validation in industry." *J. Clean. Prod.*, vol. 112, pp. 2744–2755, 2016. [CrossRef]
19. C. Naden, "ISO 50001 for Energy Management Gets a Boost." Available: https://www.iso.org/news/ref2316.html.
20. L. G. Mkhaimer, M. Arafeh, and A. H. Sakhrieh, "Effective implementation of ISO 50001 energy management system: Applying Lean Six Sigma approach," *Int. J. Eng. Bus. Manag.*, vol. 9, pp. 1–12, 2017. [CrossRef]
21. R. Uriarte-Romero, M. Gil-Samaniego, E. Valenzuela-Mondaca, and J. Ceballos-Corral, "Methodology for the successful integration of an energy management system to an operational environmental system," *Sustainability*, vol. 9, no. 8, pp. 5–8, 2017. [CrossRef]
22. M. R. Teixeira, P. Mendes, E. Murta, and L. M. Nunes, "Performance indicators matrix as a methodology for energy management in municipal water services," *J. Clean. Prod.*, vol. 125, pp. 108–120, 2016. [CrossRef]
23. F. Marimon, and M. Casadesús, "Reasons to adopt ISO 50001 Energy Management System," *Sustainability*, vol. 9, no. 10, pp. 1–15, 2017. [CrossRef]
24. A. McKane *et al.*, "Predicting the quantifiable impacts of ISO 50001 on climate change mitigation," *Energy Policy*, vol. 107, pp. 278–288, 2017. [CrossRef]
25. UNIDO, *Practical Guide for Implementing an Energy Management System*. Vienna: United Nations Industrial Development Organization, 2015.
26. T. Y. Chiu, S. L. Lo, and Y. Y. Tsai, "Establishing an integration-energy-practice model for improving energy performance indicators in ISO 50001 energy management systems," *Energies*, vol. 5, no. 12, pp. 5324–5339, 2012. [CrossRef]
27. T. Fiedler, and P. M. Mircea, "Energy management systems according to the ISO 50001 standard - Challenges and benefits," *Int. Conf. Appl. Theor. Electr. ICATE 2012 - Proc.*, 2012. [CrossRef]
28. H. Kanneganti *et al.*, "Specification of energy assessment methodologies to satisfy ISO 50001 energy management standard," *Sustain. Energy Technol. Assess.*, vol. 23, pp. 121–135, 2017. [CrossRef]
29. A. K. Roy, *Public Sector Energy Management: A Strategy for Catalyzing Energy Efficiency in Malaysia*. Delaware: University of Delaware, 2001.
30. P. Karcher, and R. Jochem, "Success factors and organizational approaches for the implementation of energy management systems according to ISO 50001," *TQM J.*, vol. 27, no. 4, pp. 361–381, 2015. [CrossRef]
31. K. Beihmanis, and M. Rosa, "Energy management system implementation in Latvian municipalities: From theory to practice," *Energy Procedia*, vol. 95, pp. 66–70, 2016. [CrossRef]
32. A. Kamenders, M. Rosa, and K. Kass, "Low carbon municipalities. The impact of energy management on climate mitigation at local scale," *Energy Procedia*, vol. 128, pp. 172–178, 2017. [CrossRef]
33. A. Jekabsone, A. Kamenders, and M. Rosa, "Implementation of certified energy ManagementSystem in municipality. Case study," *Environ. Clim. Technol.*, vol. 24, no. 2, pp. 41–56, 2020. [CrossRef]
34. Ö. Özdemir, "Energy management and cleaner production in an automotive supply industry," İzmir: Dokuz Eylül Univ, 2014.
3s5. C. O. Onus, *Continual Energy Management Dynamics: Energy Efficiency in US Automotive Manufacturing Indsustry*. Walden University, 2014.
36. R. Kannan, and W. Boie, "Energy management practices in SME — Case study of a bakery in Germany," *Energy Conversion and Management*, vol. 44, no. 6, pp. 945–959, 2003.
37. A. Boharb *et al.*, "Auditing and analysis of energy consumption of an industrial site in Morocco," *Energy*, vol. 101, pp. 332–342, 2016. [CrossRef]
38. A. Kluczek, and P. Olszewski, "Energy audits in industrial processes," *J. Clean. Prod.*, vol. 142, 3437–3453, 2017. [CrossRef]
39. M. Tunc, K. Kaplan, S. Sisbot, and U. Camdali, "Energy management and optimization : Case study of a textile plant in Istanbul, Turkey," *World J. Eng.*, vol. 13, no. 4, pp. 348–355, 2016. [CrossRef]
40. D. T. Acosta, *Energy Management in Louisiana's Public School Districts*. Louisiana State University, 1993.
41. S. H. Lee, *Management of Building Energy Consumption and Energy Supply Network on Campus Scale*. Georgia Institute of Technology, 2012.
42. A. R. Akdağ, *Energy Management and Energy Saving in Mosques in the Case of Buildings Used for Gathering Purposes*. Karabük: Karabük Üniversity, 2013.
43. M. N. Sinha, *Intelligent Demand Side Management of Residential Building Energy Systems*. United States of America: The University of North Carolina at Charlotte, 2013.
44. N. C. and N. S. (BMU) Federal Ministry for the Environment. "*Energy Management Systems in Practice - ISO 50001: A Guide for Companies and Organisations. Berlim: Federal Ministry for the Environment, Nature Conservation and Nuclear Safety. (BMU) - Division: ZG III 2*," 2012.
45. S. İsçan, "Creating and modeling the energy management system of Metro Istanbul and its evaluation," *Yalova Üniversity*, 2019.
46. "EMRA," *Procedures and Principles regarding Tariff Applications of Distribution Licensee Legal Entities and Responsible Supply Companies*, *Türkiye*, 2015.
47. "EMRA," *Electricity Tariff Tables Valid as of 1/1/2019*, *Türkiye*, 2019.
48. "EMRA," *Electricity Tariff Tables Valid as of 01/04/2019*, *Türkiye*, 2019.
49. "EMRA," *Electricity Tariff Tables Valid as of 1/7/2019*, *Türkiye*, 2019.
50. "EMRA," *Electricity Tariff Tables Valid as of 01/10/2019*, *Türkiye*, 2019.
51. "EMRA," *Electricity Tariff Tables Valid as of 01/01/2020*, *Türkiye*, 2020.
52. "EMRA," *Electricity Tariff Tables Valid as of 1/4/2020*, *Türkiye*, 2020.
53. "EMRA," *Electricity Tariff Tables Valid as of 1/7/2020*, *Türkiye*, 2020.
54. "EMRA," *Electricity Tariff Tables Valid as of 1/10/2020*, *Türkiye*, 2020.
55. "The Central Bank of the Republic of Turkey," *Monthly Basis Effective Exchange Rates*. Available: https://evds2.tcmb.gov.tr/index.php?/evds/serieMarket/#collapse_2.

TEPES
TURKISH JOURNAL OF
ELECTRICAL POWER
AND ENERGY SYSTEMS

TEPES, Vol. 2, Issue. 1, 58-65, 2022 **DOI:** 10.5152/tepes.2022.21014

RESEARCH ARTICLE

Transformer-Less Single-Stage and Single-Switched PI-Controlled AC-DC Converter Design for Automotive Applications

Davut Ertekin[1], Mesut Berke Bilgiç[2], Bülent Mutlu[2]

[1]Department of Electrical and Electronics Engineering, Bursa Technical University, Bursa, Turkey
[2]Valeo Automotive Industry and Trade Inc. (Valeo Otomotiv Sanayi ve Ticaret A.Ş.), Bursa, Turkey

Cite this article as: D. Ertekin, M. B. Bilgiç & B. Mutlu. Transformer-less single-stage and single-switched PI-controlled AC-DC converter design for automotive applications. *Turk J Electr Power Energy Syst*, 2022; 2(1): 58-65.

ABSTRACT

Alternators are electro-mechanical types of equipment that can convert mechanical energy to electrical energy. These devices frequently are used in automotive industries. Therefore, it is important to test them before being assembled on the automobiles for increasing reliability. In this study, a transformer-less single-stage and single-switched alternating current-direct current converter structure is proposed in order to test the operation quality of the alternator. By using the proportional integral controller, a constant output voltage is provided at three different voltage levels. This is done since different test voltages are requested by the consumers as different alternators with different operational voltages are available in the industry. In addition, since no transformer is used in the proposed structure, the volume and production cost of the converter are appropriate. In this study, the proposed converter and the controller system are analyzed in Matlab/SIMULINK environment. In the analysis, it was seen that the proposed converter works with proper efficiency.

Index Terms—AC-DC converter, PI controller, power factor correction (PFC), full-wave rectifier

I. INTRODUCTION

In the automotive sector, alternating current generators that provide energy to motor vehicles by converting mechanical energy into electrical energy are called alternators. Alternators in automobiles charge the battery while the vehicle's engine run. Thus, they contribute to the feeding of the equipment of the vehicle that needs electricity. To activate the internal circuits of the alternator, a direct current (DC) voltage is requested. There are different types of alternators that need different operational voltages. Therefore, in order to test the performance and working quality of the alternator, the test equipment should work under different voltages. This means the test converter circuit should generate different voltages that will apply as the input voltages for the alternators [1-4].

Alternating current-direct current (AC-DC) converters used in many power electronic devices typically consist of an AC-DC rectifier connected in series with a DC-DC converter. The AC-DC rectifier converts the AC voltage at the input to a DC voltage. Then, the DC-DC converter provides the desired DC voltage at the output. Single-stage AC-DC converters are widely used due to their simplicity and low cost [5-7]. For applications requiring low output voltage, the power conversion process results in low efficiency due to the voltage difference at the input and output [8-10]. To avoid this, a high-stage transformer should be used in the circuit. The inclusion of the transformer in the circuit increases the number of components, the volume of the circuit, and the cost of manufacture. In addition, the efficiency is considerably reduced due to transformer leakage inductance [11-13].

Apart from that, boost-based power factor correction (PFC) is insufficient to provide short-circuit protection at the output and to limit the inrush current at the input. By using a Buck-based PFC circuit, these disadvantages can be reduced.

Different structures for regulating the bus-bar voltage are available in the literature [14-17]. Since transformers are used in the converters suggested in [18], leakage inductance cannot be avoided. This increases the voltage stress on the semiconductor elements and reduces the conversion efficiency [19, 20]. For the converters with more than one switch, the control process is difficult and complex.

In this study, a proportional integral (PI)-controlled AC-DC buck converter is proposed. As a controller, the PI controller structure is preferred due to its simplicity and high efficiency. By adjusting the duty cycle (D) of the active switch in the circuit, it provides a constant

Corresponding author: Davut Ertekin, davood.ghaderi@btu.edu.tr

Received: February 16, 2022
Accepted: March 12, 2022

output voltage at three different levels (10 V, 13.5 V, and 18 V) for variable input voltages. By generating different voltages, the proposed converter can be used to test the performance quality of different alternator types since different operational voltages can be requested by the customers. It means different alternators are available in the automotive industries that can work with 10 V, 13.5 V, or other voltages.

A step-down transformer is not used in the proposed converter to achieve low voltage levels. İnstead, a full-wave rectifier converter is used that can correct the power factor since, in the full-wave rectifier, the average current in the input source is zero. Therefore, it can avoid the problems associated with non-zero average source currents, especially in transformers. The output of the full-wave rectifier has inherently less ripple than the half-wave rectifier.

At the same time, the volume of the circuit and the production cost are considerably reduced by using the minimum number of elements. However, since only one active switch is used, the control process and the analysis of the circuit are significantly simplified.

This paper aimed to verify the performance of the proposed AC-DC converter and is organized as follows: the converter structure proposed in chapter 2 presents the different operating modes of the converter, PI controller calculations, and continuous current mode (CCM) analysis. The calculation of component values is presented in chapter 3, and the simulation results are shown in chapter 4. Finally, in chapter 5, the results obtained and explanations about the results are included.

II. PROPOSED CONVERTER

The proposed single-stage AC-DC converter is shown in Fig. 1. The circuit basically consists of a rectifier and a buck converter. Components D_1–D_4 constitute the bridge rectifier and S, L, D_5, and C_o form the buck converter. It has 2 Ω and 2 mH resistor–inductor load connected in series as load. This amount of the load is based on the practical alternator internal resistor and inductor values.

In the bridge rectifier, the D_1 and D_4 diodes conduct together, and the D_2 and D_3 diodes transmit simultaneously and in the time intervals when the D_1–D_4 pair is open. In the loop with D_1, D_2, and the source, Kirchhoff's law of voltages shows that D_1 and D_2 cannot be on at the same time. Similarly, D_3 and D_4 cannot transmit at the same time. The load current can be positive but never zero. Switch S is controlled by a PI controller, driven by a pulse width modulated (PWM) signal with T as the time period and D as the duty cycle. The requested output voltage can be obtained by adjusting the duty cycle of the switch in the range of 0–1.

In the CCM, the proposed converter can be examined in two conduction and cut-off modes when the power switch is on and off, respectively. The states of the components used in the converter are analyzed separately for each mode. Fig. 2 and Fig. 3 show the circuit structure for the on and off modes. Fig. 4 shows the waveforms of the elements in CCM operation.

Mode 1 [0 – DT]: In this time interval, switch S is on and inductor L is charging through capacitor C_1. Since the D_5 diode is reverse biased, the voltage on it becomes zero and operates in the cut-off state. The load current is provided by the output capacitor C_o. In this study, the voltage on the load is named V_o and the voltage on the capacitor C_1 is named V_{in}. The equations for this operating mode are as follows:

$$V_L = V_{in} - V_o = L\frac{di_L}{dt} \tag{1}$$

$$V_{D_5} = V_{in} \tag{2}$$

The ripple in current when the switch is closed is calculated as:

$$\frac{di_L}{dt} = \frac{\Delta i_L}{\Delta t} = \frac{\Delta i_L}{DT} = \frac{V_{in} - V_o}{L} \tag{3}$$

$$(\Delta i_L)_{kapal1} = \left(\frac{V_{in} - V_o}{L}\right)DT \tag{4}$$

Mode 2 [DT – T]: Switch S is in off state during this time interval. When the switch is deactivated, the diode D_5 becomes forward biased to conduct the inductor current, therefore easily it can be seen that the circuit in Fig. 3 is valid. The equations for this operating mode are as follows:

$$V_L = -V_o = L\frac{di_L}{dt} \tag{5}$$

The ripple in current when the switch is open is calculated as:

$$\frac{\Delta i_L}{\Delta t} = \frac{\Delta i_L}{(1-D)T} = \frac{-V_o}{L} \tag{6}$$

$$(\Delta i_L)_{açık} = \left(\frac{-V_o}{L}\right)(1-D)T \tag{7}$$

In steady-state operation, the amplitude of the current ripple for both on and off states are the same and the net change in inductor current over a period is zero. In that case,

$$(\Delta i_L)_{kapal1} + (\Delta i_L)_{açık} = 0 \rightarrow \left(\frac{V_{in} - V_o}{L}\right)DT - \left(\frac{V_o}{L}\right)(1-D)T \tag{8}$$

By a simplification in (8), the output voltage can be calculated as below:

$$V_o = V_S D \tag{9}$$

Main Points

- Presenting a AC-DC converter for alternator tests in automotive industries.
- Presenting a single-switched and single-stage topology.
- Simple control method with wide range of output voltages.
- Efficient and simple to be implemented.

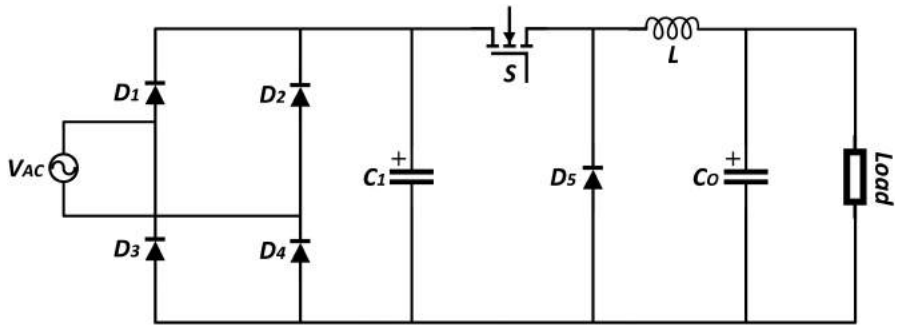

Fig. 1. Circuit diagram of the proposed AC-DC converter.

This equation simply can show that the applied converter can act like a buck converter and decrease the input DC voltage across the capacitor C_1. For the next step, it is important to present a controller to prepare the required pulse to the switch for generating smaller voltages for the alternator as the load.

A. PI Controller and Small-Signal Analysis

The first thing to do for a system to be controlled is to perform the system modeling. Modeling the converter to be realized in power electronics circuits provides a correct understanding of the open-closed loop control response of the converter.

The PI controller provides the control process using the error input and historical error signals. In the PI controller, the reference voltage and the output voltage are compared, and then the sampled voltage passes through the controller, and controller output is compared with the inductor current to obtain the D of the PWM signal. Therefore, the converter provides the requested output voltage [11]. Fig. 5 shows the mathematical model of the pro posed PI controller.

By looking at the state space form of the system to be controlled, it is seen that it has multiple inputs/outputs and state variables. If we express the system in a simple form consisting of one input and one output, the input of the system can be shown as D and the output of the system as *Vo*.

In order to write the single input and single output model in the state space form according to the determined state variables, the state and the output equations should be obtained:

$$\frac{dx(t)}{dt} = Ax + Bu \quad \text{State equation}$$

$$y(t) = Cx \quad \text{Output equation} \tag{10}$$

To obtain the state space model of the Buck converter, the state equations for the state variables need to be obtained. If we obtain the generalized expressions from the equations of inductor current and capacitor voltage in both operating ranges, the inductor current can be calculated:

$$\frac{di_L(t)}{dt} = \frac{1}{L}\left[\left(V_{in} - V_o(t)\right)D + \left(-V_c(t)\right)(1-D)\right] \rightarrow \frac{di_L(t)}{dt} = \frac{V_{in}}{L}D - \frac{V_0(t)}{L} \tag{11}$$

The voltage equation for the output capacitor can be obtained by:

$$\frac{dv_o(t)}{dt} = \frac{1}{C}\left[\left(i_L(t) - \frac{V_0(t)}{R}\right)D + \left(i_L(t) - \frac{V_0(t)}{R}\right)(1-D)\right] \rightarrow \frac{dv_o(t)}{dt} = \frac{1}{C}i_L(t) - \frac{V_0(t)}{RC} \tag{12}$$

The state space form of the system can be written by controlling it with the differential equations we have obtained for the state variables:

$$x_1(t) = i_L(t) \tag{13}$$

$$x_2(t) = v_c(t) \tag{14}$$

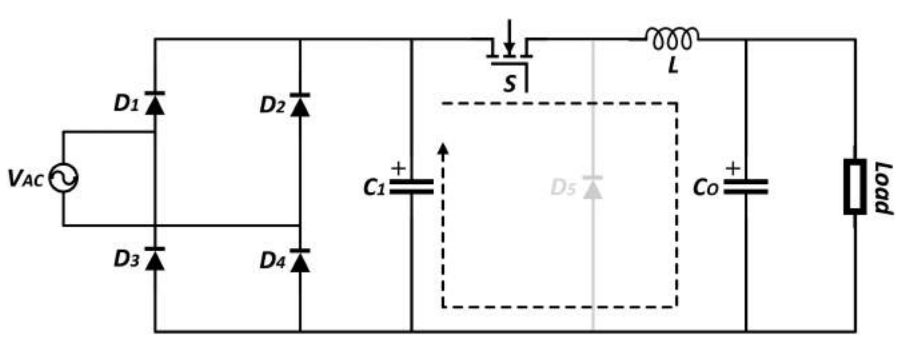

Fig. 2. Circuit structure for the conduction mode of the switch.

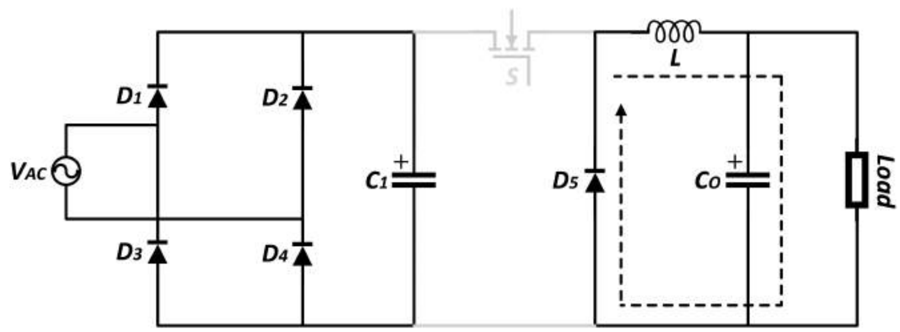

Fig. 3. Circuit structure for the cut mode of the switch.

$$\frac{dx_1(t)}{dt} = -\frac{1}{L}x_2 + \frac{V_{in}}{L}u \text{ 1st state equation} \tag{15}$$

$$\frac{dx_2(t)}{dt} = \frac{1}{C}x_1 - \frac{1}{RC}x_2 \text{ 2nd state equation} \tag{16}$$

The state space form for the buck converter part:

$$\frac{d}{dt}\begin{bmatrix} x_1(t) \\ x_2(t) \end{bmatrix} = \begin{bmatrix} 0 & -\frac{1}{L} \\ \frac{1}{C} & -\frac{1}{RC} \end{bmatrix}\begin{bmatrix} x_1(t) \\ x_2(t) \end{bmatrix} + \begin{bmatrix} \frac{V_{in}}{L} \\ 0 \end{bmatrix} u(t) \tag{17}$$

$$y(t) = \begin{bmatrix} 0 & 1 \end{bmatrix}\begin{bmatrix} x_1(t) \\ x_2(t) \end{bmatrix} \tag{18}$$

The transfer function can be found by writing the equations of state we have obtained for the Buck converter in the S-space:

$$sX_1 = -\frac{1}{L}Y(s) + \frac{V_{in}}{L}U(s) \tag{19}$$

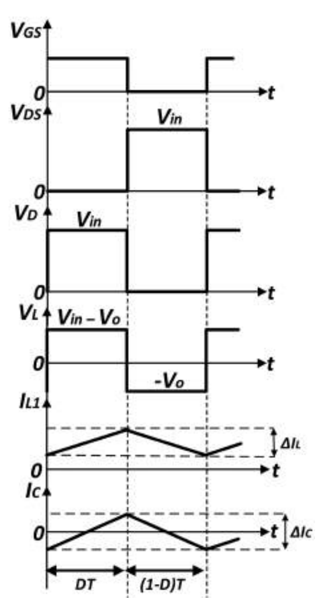

Fig. 4. Converter waveforms in CCM operational mode.

$$sY(s) = \frac{1}{C}X_1 - \frac{1}{RC}Y(s) \tag{20}$$

If X_1 is subtracted from Equation 20 and replaced in Equation 19:

$$G_p(s) = \frac{Y(s)}{U(s)} = \frac{\frac{V_{in}}{LC}}{s^2 + \frac{1}{RC}s + \frac{1}{LC}} \tag{21}$$

If the open-loop response of the system is examined, it is seen that it has a damped form by a low damping ratio (ξ). By designing a controller with a classical PI controller to control the output of the buck converter, the output voltage can be controlled. In this case, the transfer function of the PI controller will be as follows:

$$G_c(s) = K_p + \frac{K_i}{s} \tag{22}$$

In this case, the closed-loop transfer function of the system becomes:

$$\text{Closed Loop Transfer Function} \rightarrow \frac{\frac{V_{in}}{LC}K_p s + \frac{V_{in}}{LC}K_i}{\frac{1}{RC}s^2 + \left(\frac{1}{LC} + \frac{V_i}{LC}K_p\right)s + \frac{V_i}{LC}K_i} \tag{23}$$

III. CALCULATION OF COMPONENT VALUES

While designing the converter circuit, it was assumed that the converter was in a stable state and the semiconductor switching elements were considered ideal, and the losses of the inductor and capacitors were neglected. It is also assumed that the converter works in the CCM.

For the converter circuit shown in Fig. 1, the relationship between V_o and V_s voltages in steady state is as shown in Equation 9. It can be rewritten as:

$$D = \frac{V_o}{V_{in}} = \frac{t_{on}}{T} \tag{24}$$

Here, D is the duty cycle, t_{on} is the switch's conduction time, and T is the switching period.

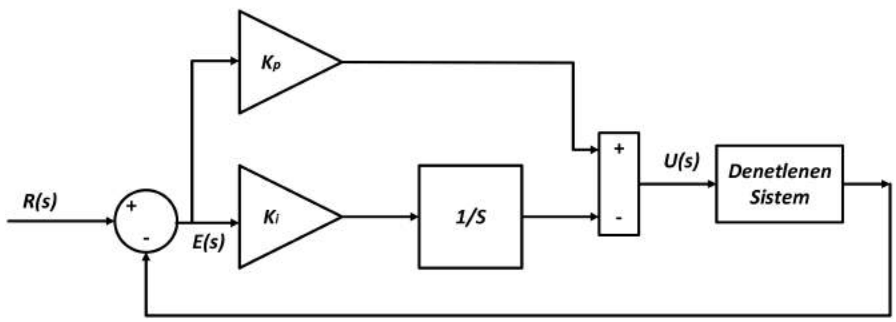

Fig. 5. Mathematical model of the PI controller.

The following equations are used to calculate the minimum inductor and capacitor values in the circuit:

$$L = \frac{(1-D)R}{2f} \tag{25}$$

$$C_o = \frac{1-D}{8L(\Delta V_o / V_o) f^2} \tag{26}$$

These values are the minimum required component values. The component values used in the simulation and the designed circuit are shown in Table I.

IV. SIMULATION RESULTS

This section shows the results of the simulation for the proposed converter and controller circuits. The simulation of the circuit was carried out in Matlab/SIMULINK environment. In Fig. 6, the input voltage with 220 V_{rms} and 50 Hz frequency and the desired output voltage at three different levels are shown. Three different voltages are planned to be obtained. These voltages are 10, 13.5, and 18 VDC voltages that are the industrial and requested real DC voltages. The desired constant output voltage is achieved rapidly at 10 V and 18.5 V values of the output voltage. After a very small delay of 0.3 s for 13.5 V, the desired output voltage is achieved. Since this delay time is very short, it will not have a negative effect on the system, especially by considering the fact that the proposed converter should generate these voltages for a long time for test purposes.

TABLE I.
COMPONENT VALUES USED IN THE CIRCUIT

Parameters	**Value**
Input AC voltgae V_{AC}	220 V_{rms}
Output DC voltage V_o	8, 13.5 ve18 V
Inductor L	100 µH
Capacitor C_o	2200 µF
Capacitor C_1	2200 µF
Switching frequency f_s	20 kHz
Load (alternator)	2 Ω, 2 mH

Fig. 7 shows the waveforms of the output current and voltage. One can see from the figure that the output current changes at three different levels immediately when the output voltage changes.

Fig. 8 shows the voltage and current waveforms for the power switch. As can be seen, there is a voltage of approximately 300 V on the switch during the cut-off time duration and the switch current is zero in this time interval. For the times the switch is in operation, 6 A current flows on the switch and the voltage on it is zero since the switch behaves like a short circuit. In addition, the simulation result also confirms the graph shown in Fig. 4. Fig. 9 shows the voltage waveform for the buck converter's diode, D_5. As can be seen from the figure, when the diode is conducting, the voltage on it is zero. During the cut-off time duration, there is a voltage of about 300 V on this diode. These DC voltages approximately are the peak voltage of the input AC voltage. The power diodes in industrial applications can withstand these voltages easily.

V. CONCLUSION

In this study, a transformer-less single-switch AC-DC converter structure is investigated for test application in automotive industries. The proposed structure can convert and transfer the grid voltage into three different (10, 13.5, and 18 VDC) constant voltage levels at the output for applying to the alternator to investigate the reaction of this device before assembling on the automobile. The ripple in output current and voltage is quite low which is a requested parameter for better analysis of the alternator for probably fault detection investigations. The PI controller structure is preferred as the controller in the converter due to its simple, fast response, and low-cost features. Compared to other structures, its specifications such as the low number of components and the absence of transformers that increase the volume and cost of the circuit make the recommended AC-DC buck converter preferred over other converters. After the circuit was analyzed mathematically in CCM, it was designed using the Matlab/SIMULINK package program and the results confirmed the theoretical analysis.

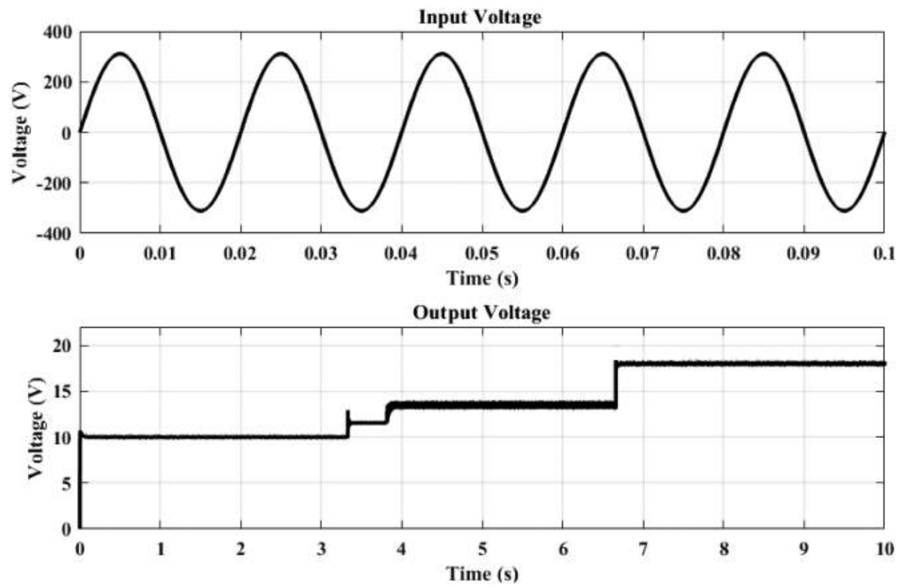

Fig. 6. Input and output waveforms of the converter.

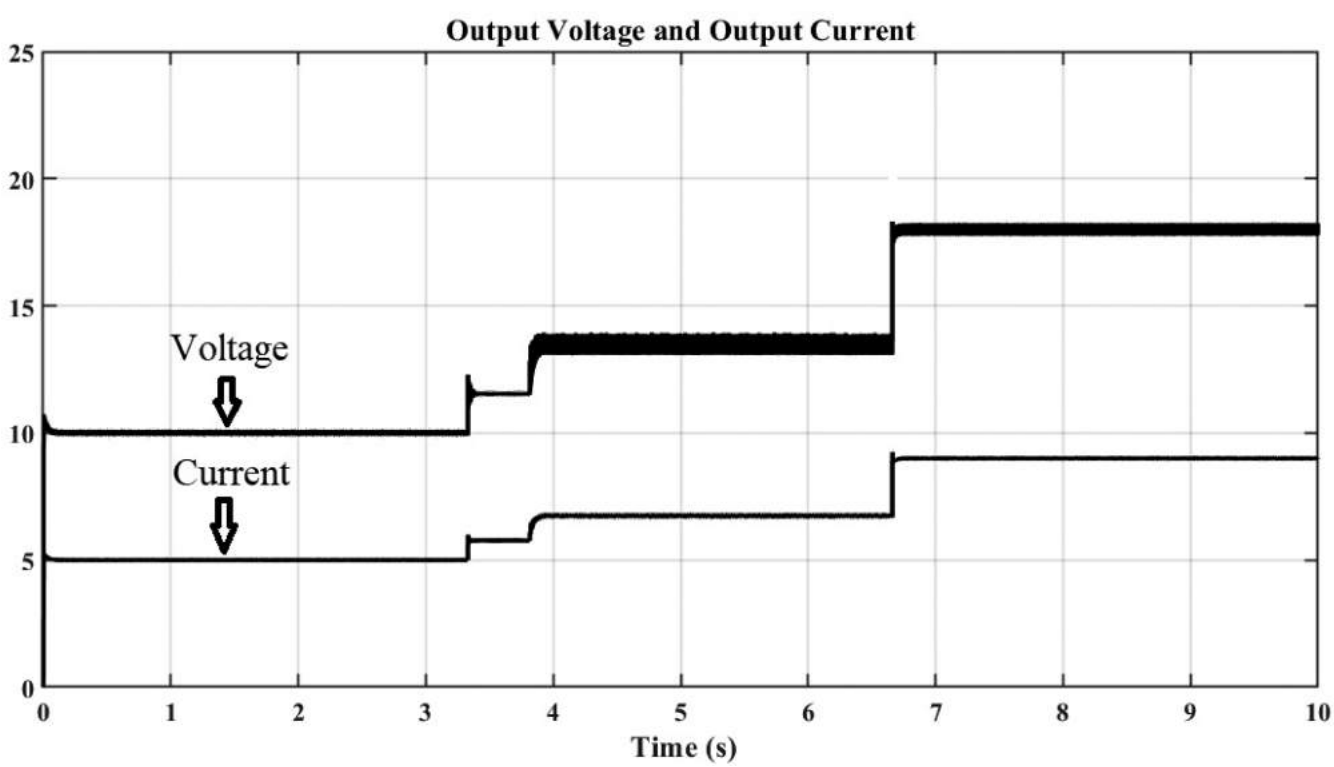

Fig. 7. Output voltage and current waveforms.

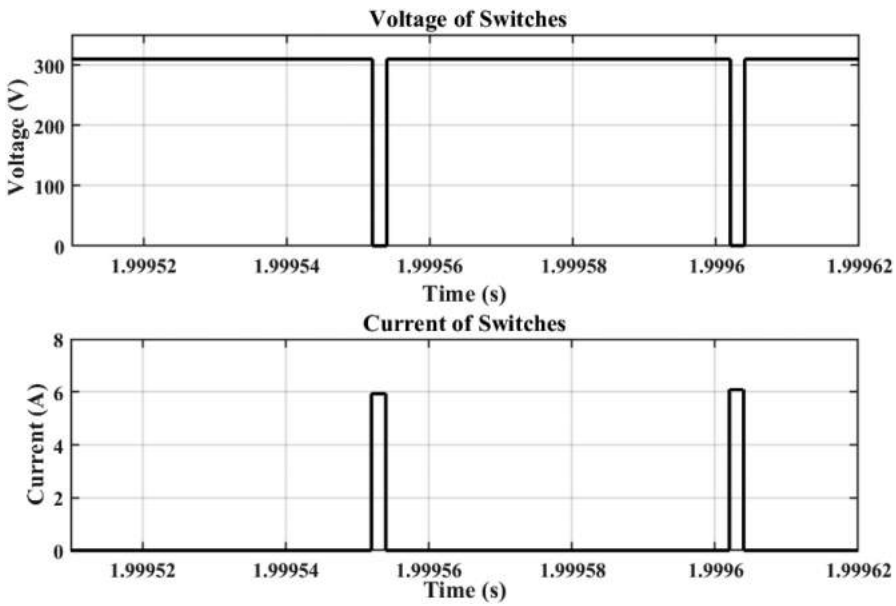

Fig. 8. Waveforms of switch's current and voltage.

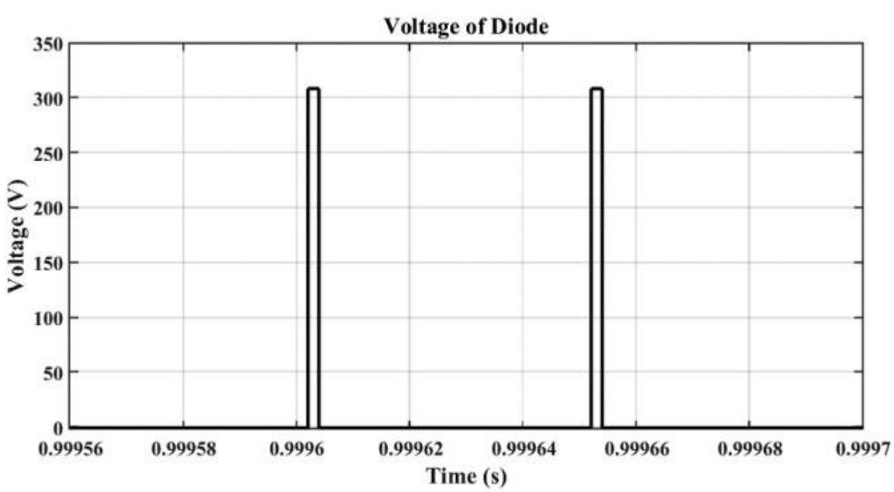

Fig. 9. Voltage waveform for diode D_5.

Peer-review: Externally peer-reviewed.

Acknowledgments: This study has been done as a part of R&D project between the Asst. Prof. Dr. Davut Ertekin from Bursa Technical University and Valeo Automotive Industry and Trade Inc. Bursa, under project untitled: Analog Controlled AC-DC Converter Design for Alternator Tests.

Declaration of Interests: The authors have no conflicts of interest to declare.

Funding: This project is supported by Valeo Automotive Industry and Trade Inc. Bursa, under the project entitled: Analog Controlled AC-DC Converter Design for Alternator Tests.

REFERENCES

1. D. Sarafianos, D. X. Llano, S. S. Ghosh, R. A. McMahon, S. Pickering, and T. J. Flack, "Control strategy for a multiphase Lundell-Alternator/Active -Rectifier system in 14 V automotive power systems," *IEEE Trans. Transp. Electrif.*, vol. 5, no. 2, pp. 347–355, 2019. [CrossRef]
2. S. Wu, S. Zuo, X. Wu, F. Lin, H. Zhong, and Y. Zhang, "Vibroacoustic prediction and mechanism analysis of claw pole alternators," *IEEE Trans. Ind. Electron.*, vol. 64, no. 6, pp. 4463–4473, 2017. [CrossRef]
3. C. -S. Yu, Y. -C. Lin, and C. -J. Chen, "Rotational speed detection for the automotive alternator with low loss rectifier in self-start," *IEEE Trans. Veh. Technol.*, vol. 70, no. 7, pp. 6514–6526, 2021. [CrossRef]

4. S. Wu, S. Zuo, and Y. Zhang, “Optimization for electromagnetic noise reduction in claw pole alternator by rotor claw chamfering,” *IEEE Trans. Ind. Electron.*, vol. 65, no. 12, pp. 1–1, 2018. [CrossRef]
5. H. Wu, Y. Jia, F. Yang, L. Zhu, and Y. Xing, “Two-stage isolated bidirectional DC–AC converters with three-port converters and two DC buses,” *IEEE J. Emerg. Sel. Top. Power Electron.*, vol. 8, no. 4, pp. 4428–4439, 2020. [CrossRef]
6. H. Wu, M. Han, and K. Sun, “Dual-voltage-rectifier-based single-phase AC–DC converters with dual DC bus and voltage-sigma architecture for variable DC output applications,” *IEEE Trans. Power Electron.*, vol. 34, no. 5, pp. 4208–4222, 2019. [CrossRef]
7. S. A. Q. Mohammed, and J. -W. Jung, “A state-of-the-art review on soft-switching techniques for DC–DC, DC–AC, AC–DC, and AC–AC power converters,” *IEEE Trans. Ind. Inform.*, vol. 17, no. 10, pp. 6569–6582, 2021. [CrossRef]
8. D. Ertekin, S. Padmanaban, P K. Maroti, B. Papari, and J. Bo HolmNielsen, “Design and implementation of an improved sinusoidal controller for a two-phase enhanced impedance source boost inverter,” *Computers Electrical Engineering*, vol. 83, no. 3, pp. 1–18, 2020.
9. D. Hu, A. Yin, and D. ERTEKİN, “A transformer-less single-switch boost converter with high-voltage gain and mitigated-voltage stress applicable for photovoltaic utilizations,” *Int. Trans. Electr. Energy Syst.*, vol. 30, no. 10, pp. 1–22, 2020. [CrossRef]
10. K. Bulut, and D. Ertekin, “Maximum power point tracking by the small-signal-based PI and Fuzzy logic controller approaches for a two-stage switched-capacitor DC-DC power boost converter applicable for photovoltaic utilizations,” *El-Cezeri Fen ve Mühendislik Dergisi*, vol. 2020, no. 3, pp. 1167–1190, 2020.
11. S. Du, and B. Wu, “A transformerless bipolar modular multilevel DC–DC converter with wide voltage ratios,” *IEEE Trans. Power Electron.*, vol. 32, no. 11, pp. 8312–8321, 2017. [CrossRef]
12. S. Du, B. Wu, and N. R. Zargari, “A transformerless high-voltage DC–DC converter for DC grid interconnection,” *IEEE Trans. Power Deliv.*, vol. 33, no. 1, pp. 282–290, 2018. [CrossRef]
13. S. Du, B. Wu, D. Xu, and N. R. Zargari, “A transformerless bipolar multistring DC–DC converter based on series-connected modules,” *IEEE Trans. Power Electron.*, vol. 32, no. 2, pp. 1006–1017, 2017. [CrossRef]
14. Y. -T. Huang, C. -H. Li, and Y. -M. Chen, “A modified asymmetrical half-bridge flyback converter for step-down AC–DC applications,” *IEEE Trans. Power Electron.*, vol. 35, no. 5, pp. 4613–4621, 2020. [CrossRef]
15. M. Ryu, J. Baek, J. Kim, S. Park and H. Kim, “Electrolytic capacitor-less, non-isolated PFC converter for high-voltage LEDs driving,” *8th International Conference on Power Electronics - ECCE Asia*, pp. 499–506, 2011. [CrossRef]
16. Y. Cai, J. Xu, P. Yang, J. Wu, and J. Sha, “Evaluation and suppression of a low-frequency output voltage ripple of a single-stage AC–DC converter based on an output impedance model,” *IEEE Trans. Ind. Electron.*, vol. 66, no. 4, pp. 2803–2813, 2019. [CrossRef]
17. C. Chang, C. Cheng, E. Chang, H. Cheng, and B. Yang, “An integrated high-power-factor converter with ZVS transition,” *IEEE Trans. Power Electron.*, vol. 31, no. 3, pp. 2362–2371, 2016. [CrossRef]
18. E. H. Ismail, A. J. Sabzali, and M. A. Al-Saffar, “Buck boost-type unity power factor rectifier with extended voltage conversion ratio,” *IEEE Trans. Ind. Electron.*, vol. 55, no. 3, pp. 1123–1132, 2008. [CrossRef]
19. P. Das, A. Mousavi, and G. Moschopoulos, “An ac-dc single-stage full-bridge PWM converter with bridgeless input,” IEEE Energy Convers. Congress and Exposition, vol. 2009, 2009, pp. 1347–1352. [CrossRef]
20. K. K. H. Dia, M. A. Choudhury, and Ahammad, “A single phase differential Zeta rectifier-inverter,” *IEEE International WIE Conference on Electrical and Computer Engineering (WIECON-ECE)*, vol. 2015, pp. 284–288, 2015. [CrossRef]

TURKISH JOURNAL OF ELECTRICAL POWER AND ENERGY SYSTEMS

TEPES, Vol. 2, Issue. 1, 66-74, 2022 **DOI:** 10.5152/tepes.2022.21011

RESEARCH ARTICLE

The Effect of Non-uniform Pollution on the Field Distributions of Insulator String

İrem Görgöz, Mehmet Cebeci

Department of Electrical & Electronics Engineering, Fırat University, Faculty of Engineering, Elazığ, Turkey

Cite this article as: I. Görgöz & M. Cebeci. The effect of non-uniform pollution on the field distributions of insulator string. *Turk J Electr Power Energy Syst*, 2022; 2(1): 66-74.

ABSTRACT

High-voltage insulators in different atmospheres such as industrial, coastal, and desert regions are faced with temperature, heat, and conductivity changes that are difficult to predict due to factors such as wind, humidity, and precipitation. All of these lead to the formation of pollution layers with different conductivity on the insulator surface. Therefore, surface pollution is generally non-uniform. In this paper, e-field and potential distributions were investigated for non-uniform pollution by applying 20 kV to a 3-unit (U70-BLP) insulator string. The insulator string was modeled in 3D in the COMSOL Multiphysics program using the finite element method. The pollution layer was modeled by a layer of 0.5 mm thickness on the insulator surface. In uniform conditions, pollution conductivity was the same all over the surface. Non-uniform pollution was considered in two ways. First, the conductivity of the pollution was randomly distributed on the surface by forming data at certain ranges. Second, two pollution regions with different conductivity were defined, upper and bottom. The results showed that the non-uniform distribution of the pollution conductivity changed the distribution of the electric field strength and potential across the surface. The most remarkable changes were observed in the pin and cap regions where the radius of curvature was small. In regions where the pollution conductivity increased, the e-field decreased and the potential distribution approached the linear state.

Index Terms—Non-uniform pollution, insulator, field distributions

I. INTRODUCTION

Outdoor insulators are widely employed to maintain electrical insulation ranging from distribution to transmission lines and to support the mechanical load between a conductor and the ground in power systems [1, 2]. With the increase in voltage levels for the transmission system, high-voltage equipment insulation has gained tremendous importance. The basic property of insulating materials is to withstand voltage or electric field strength. While designing high-voltage equipment, knowledge of electric field strength and potential distribution along high-voltage insulators is important [3, 4].

The safety of high- and extra-high-voltage transmission lines is heavily affected by pollution-induced flashover in rated operating conditions. Pollution flashover formed on insulator surface may cause large-scale blackouts accident of the grid system [5, 6]. The line cannot be successfully reclosed after pollution-induced flashover because the contamination reduces the insulation's strength for a long time. Pollution flashover is a very complex problem due to several reasons such as modeling difficulties of the insulator complex shape, different pollution densities at different regions, non-uniform pollution distribution on the surface of the insulator, and unknown effect of humidity on the pollution [7].

The pollution layer behaves as a highly variable nonlinear resistor and the leakage current flowing through it gives rise to heat, electrochemical products of electrolysis, and electrical discharges [8]. Leakage current circulation on the polluted insulator surface gives rise to energy dissipation caused by Joule heating. The non-regular shape of the cap and pin insulator leads to the region where the heating is more important, causing local heating and dry band formation triggering dry band arcing and flashover [9]. On the surface of wetted and polluted insulators, water is evaporated due to heat generation or weather change. When the water evaporation rate is larger than water precipitation and absorption rate, dry bands are formed on areas with higher temperatures [10].

Corresponding author: İrem Görgöz, igorgoz@firat.edu.tr

Received: February 3, 2022
Accepted: March 16, 2022

Numerous dedicated computer packages are of much help in insulator designing process computer simulations for the phenomena occurring both inside and outside of insulator [11]. COMSOL Multiphysics program is one of these software. This software enables the simulation of the target variable to be observed by formulating the data entry of many parameters and the relationship between these variables. Taking into account the time the equipment or the place for experiments is not available, it is very important to use a simulation program that gives accurate results in a very fast and economical way.

In this paper, potential and electric field distributions were investigated by simulating the 3-unit (U70-BLP) insulator string coated with uniform and non-uniform pollution layers.

II. METHOD

The definition of the laws of physics for space- and time-dependent problems is often expressed in partial differential equations (PDE). For the vast majority of geometries and problems, these PDEs cannot be solved by analytical methods. Instead, an approximation of equations is typically created based on different types of meshing. These meshing methods approach PDEs with numerical model equations that can be solved using numerical methods. Several numerical computation methods were developed for solving this problem [12]. The best approach among these is the finite element method (FEM). The FEM is a numerical technique used to find approximate solutions of PDEs, reducing the latter to a system of algebraic equations [13].

The accuracy that can be obtained from any finite element analysis model is directly related to the finite element mesh. Finite element mesh is used to divide the computer-aided design (CAD) model into smaller areas called elements, on which a set of equations is solved. These equations approximately represent the corresponding equation through a set of polynomial functions defined on each element. As these items become smaller and the mesh is improved, the calculated solution will approach the real solution. This mesh refinement process is an important step in validating any FEM and gaining confidence in the software, model, and results. The COMSOL Multiphysics software used in this paper offers a solution with the FEM approach.

A. Definitions of the Problem Regions

As a part of the FEM system, with the help of the COMSOL Multiphysics program used in this study, the entire geometry of the insulator is divided into small triangular elements (meshing). This meshing can enhance the accuracy of the simulation results by increasing the number of meshing elements over the insulator surface where the e-field strength is found to be higher. The FEM estimates approximately the electric potential within each element with a linear interpolation of the potentials at its vertices or nodes [14]. Excessive selection of elements causes unnecessary solution time. The mesh created in the insulator string is shown in Fig. 1.

The insulator model (U70 BLP—mechanical strength 70 kN) drawn in two dimensions in the AutoCAD program was imported to the COMSOL program and transformed into a three-dimensional

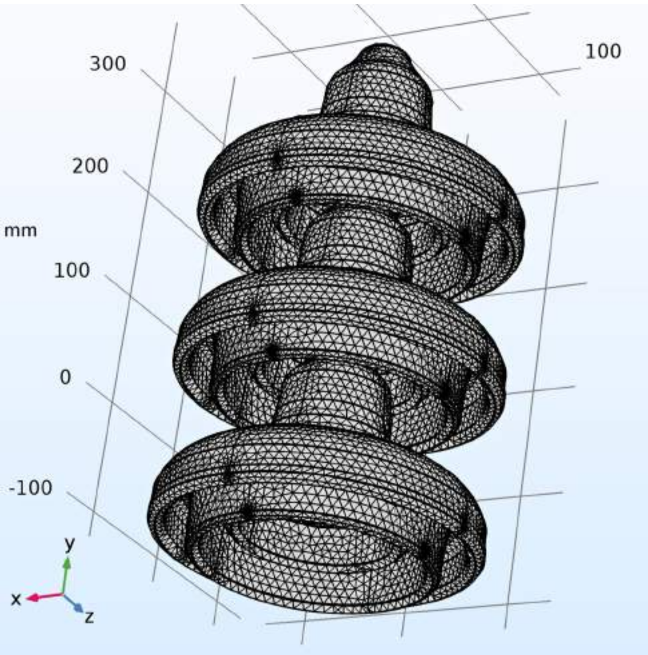

Fig. 1. Meshing of the insulator string.

structure. In the insulator string model, there are the cap (third insulator unit) areas where the insulator is in contact with the representative tower and the pin (first insulator unit) areas where 20 kV voltage is applied. Fig. 2.a-f. iron (a), cement (b), porcelain (c), upper pollution (d), bottom pollution (e), and floating potential (f) shows the required region definitions. The floating potential is defined for the iron regions with high conductivity in the insulator. The floating potential node is used when modeling a metallic electrode at a floating potential. It applies a constant voltage on the boundary (for domain features, this is the boundary enclosing the selected domain) such that the total normal electric current density equals a specific current.

High conductivity areas made of iron material are the pin where voltage is applied and the grounded cap areas. These connections are cemented to the insulator to provide mechanical support. In order to examine the non-uniform pollution distribution with two different conductivities in the two regions, the upper and bottom pollution surfaces were defined.

Material properties of the insulators are given in Table I. The relative permittivity and electrical conductivity values of cement-mortar/concrete show properties close to semiconductor behavior in wet (moisture) conditions and good insulator behavior in dry conditions. For this reason, relative permittivity values between 2.09 and 15 and electrical conductivity values between 10^{-6} and 10^{-16} have been used in the literature for cement material [9, 15-19]. In this study, the cement component was considered as dry. The relative permittivity and electrical conductivity of cement were assumed to be 4.98 and 10^{-14} S/m, respectively.

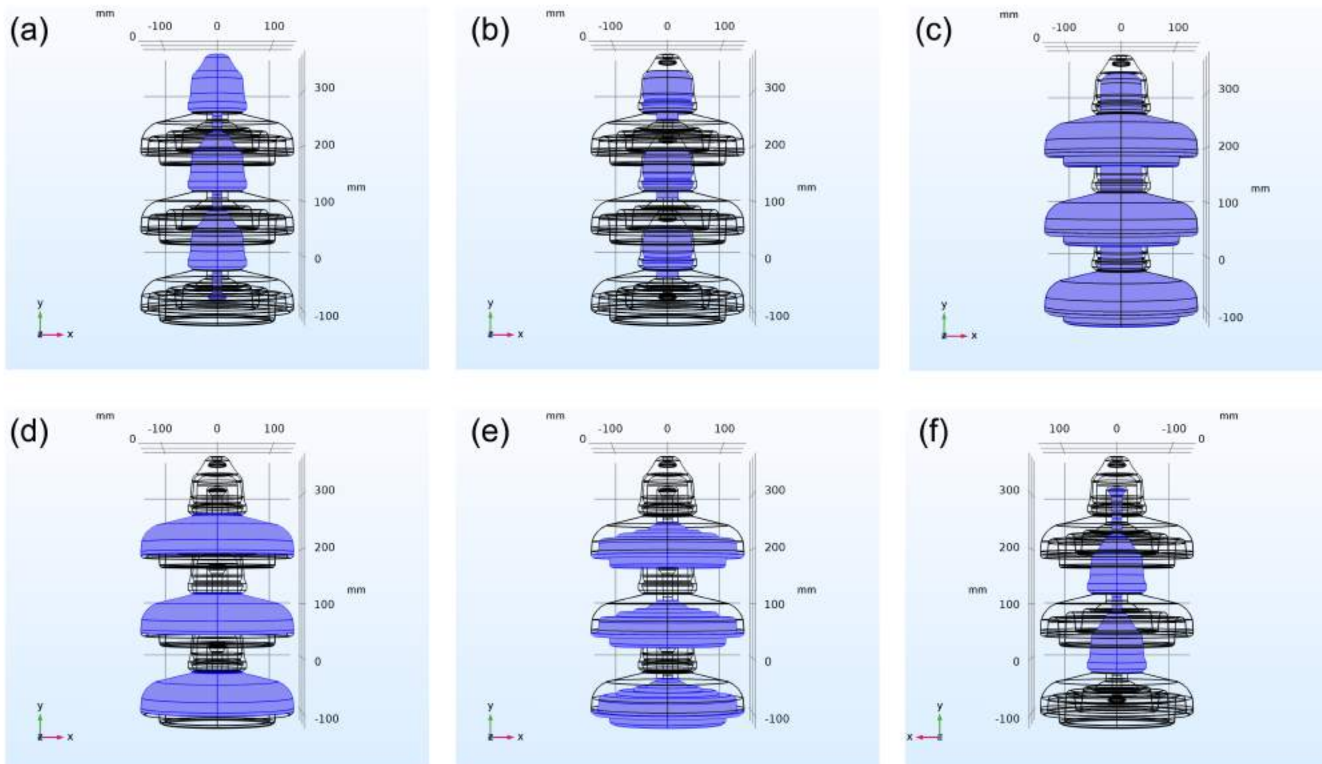

Fig. 2. Definitions of required regions (a) iron, (b) cement, (c) porcelain, (d) upper pollution, (e) bottom pollution, (f) floating potential.

In solving the problem, Electric Currents module of COMSOL Multiphysics software was used. The physics interface is used to compute electric field, current, and potential distributions in conducting media. It solves a current conservation equation based on Ohm's law using the scalar electric potential as the dependent variable. This interface adds a continuity equation for electric potential and provides an interface for defining the dielectric coefficient and electrical conductivity for displacement current.

The differential equation forms required for potential and electric field distributions in the frequency domain and the Electric Currents interface are given in (1), (2), and (3):

$$\nabla . J = Q_j \quad (1)$$

TABLE I.
ELECTRICAL PARAMETERS USED IN MODELING

Material Type	Relative Permittivity (ε_r)	Electrical Conductivity σ (S/m)
Porcelain	6	10^{-15}
Cement	4.98	10^{-14}
Iron	1	$1.12 \times 10^{+7}$
Pollution layer	1	variable

$$J = \sigma E + jwD + J_e \quad (2)$$

$$E = -\nabla V \quad (3)$$

where J (A/m^2) is current density, Q_j (A/m^3) is the current source and J_e (A/m^2) is externally generated current density, w is the angular velocity, V (V) is electric potential, E (V/m) is the electric field, D (C/m^2) is electric flux density.

B. Non-uniform Pollution

Three main types of pollution can be distinguished: industrial, desert, and marine pollution. Industrial pollution appears with industrial development producing contaminants (metallurgical, chemical substances, dust, carbon, and cement) into the atmosphere in both dry and gas forms which may lead to serious situations during wet conditions.

Desert pollution occurs due to a gradual accumulation of dust, sometimes salt, on the insulators which may result in reduced efficiency and possible supply interruption [20].

Transmission lines located in the desert are subjected to desert climate, one of whose features is sandstorms. With the long accumulation of sand and with the advent of moisture from rain, ambient humidity, and dew, a conductive layer forms and the subsequent leakage current may lead to surface discharge, which may shorten the insulator life or lead to flashover, thus interrupting the power supply. The pollution layer accumulated on the insulator surface during normal desert atmospheric weather has a thickness that depends on the type of soil in that region and on the polluting sand grain sizes [21].

Marine pollution exists in coastal environments where a conductive layer, due to the salted dew, can be formed on the insulator's surface [20]. The moisture generated in marine pollution increases the conductivity of the surface layer and causes the solid components to dissolve. This solution contains ions of various salts. The conductivity of these ions determines the conductivity between the electrodes of the insulator. The insulator contamination problem is usually caused by ionic conduction and moisture contamination [22].

The pollution severity will be classified according to its corresponding pollution layer conductivity. Table II shows how pollution severity is classified into four categories in terms of electrical conductivity and equivalent salt deposit density levels [23].

In contamination tests on high-voltage insulators, the pollution on the insulators is always uniform. However, in the real service condition, the depositing processes of the pollution on the top and the bottom surfaces of the insulator are different. Meanwhile, wind, rain, and moisture have different effects on the two surfaces of the insulator. So the deposited pollution on the insulators in service condition is usually non-uniform. The non-uniform pollution distribution is important for the flashover voltage and the withstand voltage of insulators, which should be considered in the outdoor insulation coordination [24].

TABLE II.
ESDD AND ELECTRICAL CONDUCTIVITY VALUES FOR DIFFERENT POLLUTION SEVERITY [23]

Pollution Severity	Environments	ESDD (mg/cm^2)	Electrical Conductivity (μS/cm)
Light	Agricultural areas, mountainous areas, low density of houses equipped heating plants	<0.06	<175
Medium	Areas exposed to wind from sea but located faraway from coast	0.06–0.12	176-500
Heavy	Areas exposed to strong wind from sea, large cities etc.	0.12–0.24	501-850
Very heavy	Exposed to sea spray, deserts, dense industrial areas	>0.24	>850

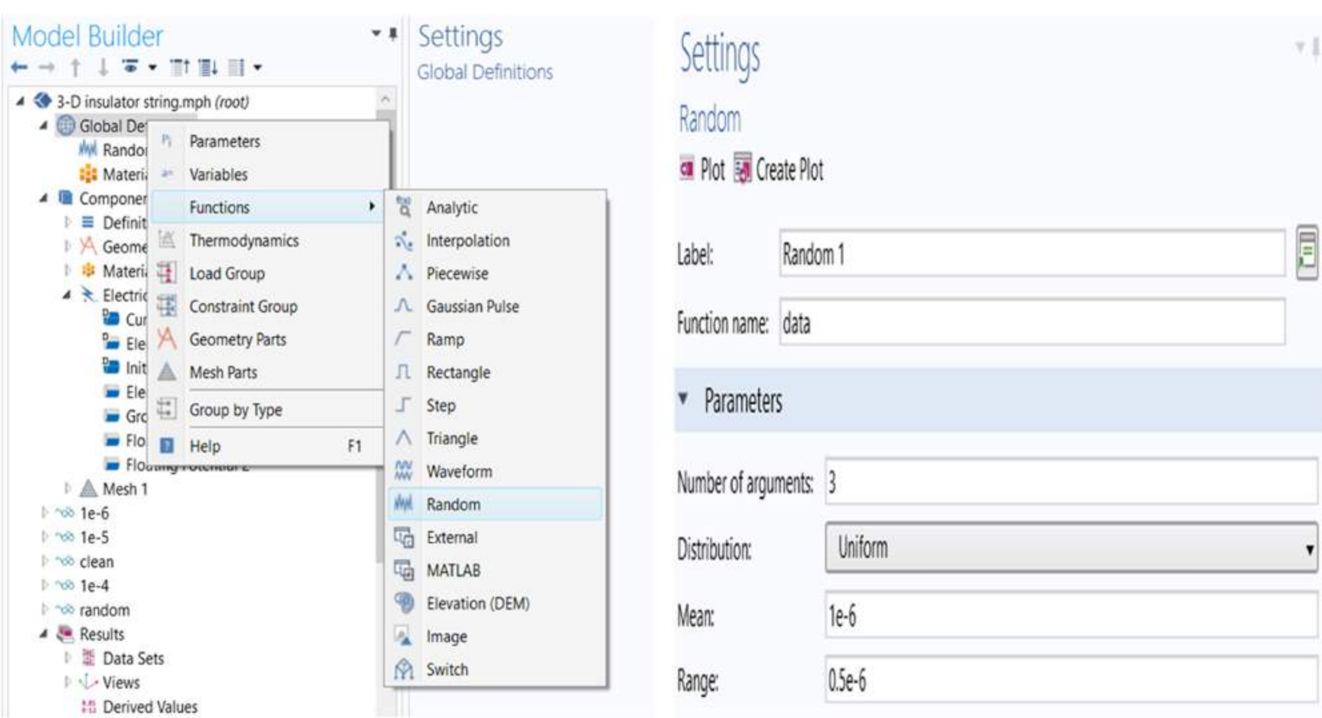

Fig. 3. Generating random data in COMSOL.

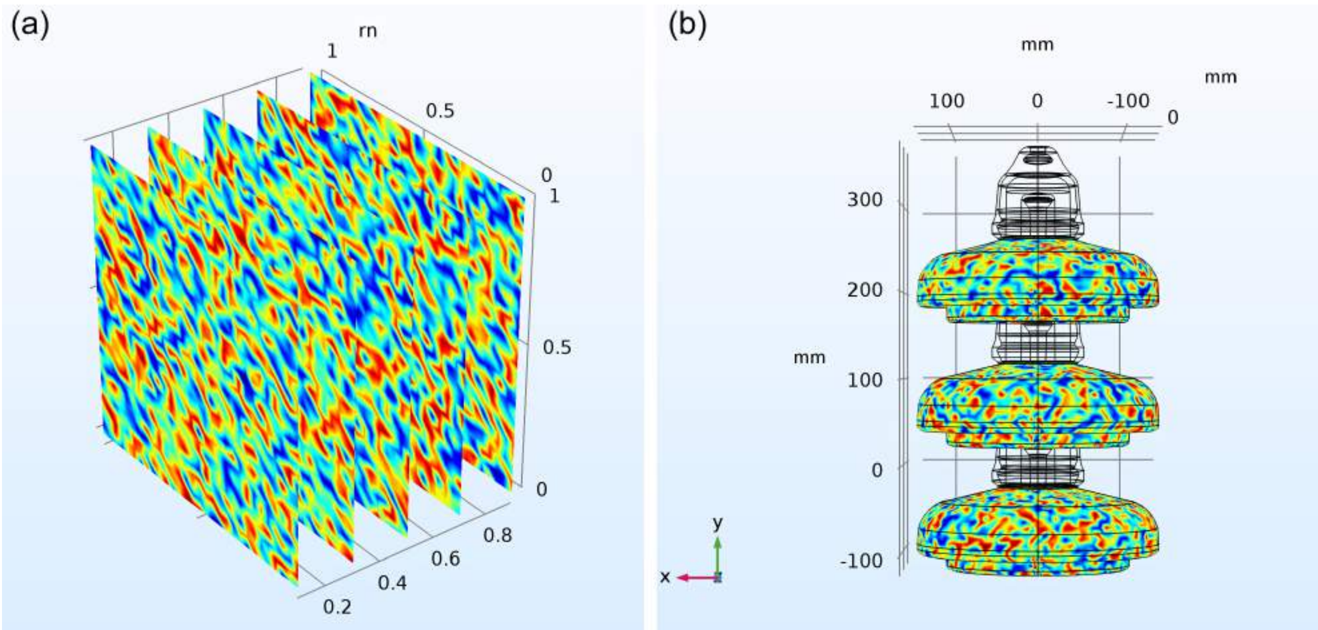

Fig. 4. Distributions of random data (a) 3D distribution of generated random data, (b) surface distribution of the generated data.

Under the influence of wind and precipitation, the upper surface is less polluted than the bottom surface in most cases. However, in coastal or desert regions, the upper surface is more covered with pollution. It can also be partially polluted by factors such as wind. In this case, the pollution distribution on the insulator surface becomes non-uniform. The non-uniformly distribution of pollution layer on top and bottom surfaces of insulator string causes the decrease of equivalent conductivity of the whole surface. The more uneven the pollution distribution on the top and bottom surface of insulators, the smaller the mean pollution surface conductivity along the whole surface of insulators. In this case, the leakage current decreases and the flashover voltage drops due to the dry bands formed [5].

The contamination performance of the insulator is also greatly affected by wind. Under different velocities of wind, the flow field surrounding the insulator will change, causing the corresponding variation of pollution particle movement and collision coefficient. Moreover, the flow field performance at the windward side is very different from that at the leeward side causing a large difference in the contamination performances. In a windless environment, the static pressure at the windward side of the insulator is lower; when wind speed grows, the static pressure at both windward and leeward sides will

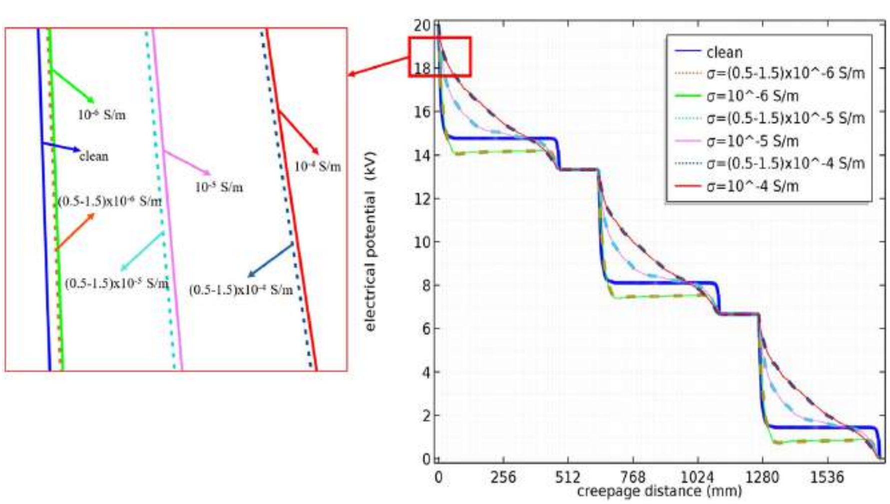

Fig. 5. Electric potential distributions of non-uniform and uniform pollutions.

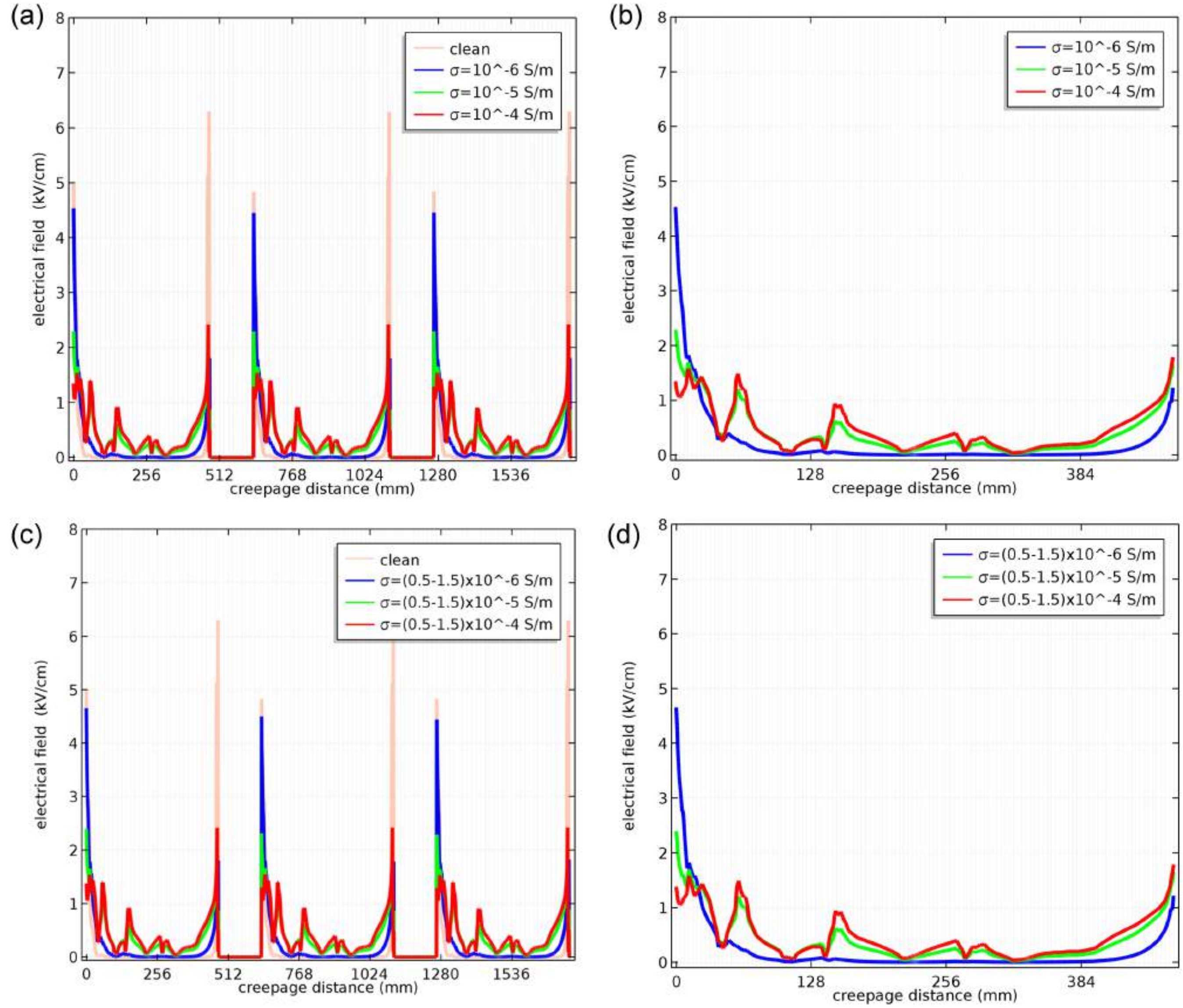

Fig. 6. E-field distributions of uniform and random non-uniform pollutions. Uniform pollutions (a) for insulator string, (b) for the first insulator unit, non-uniform pollutions (c) for insulator string, (d) for the first insulator unit.

improve. The flow velocity at the windward side is higher than that at the leeward side [25]. The wind speed of the leeward side is relatively small, and a vortex can easily form on the bottom surface [26].

The pollution layer is not uniform on the insulator surface for the reasons explained above. Many regions with different conductivity are formed on the insulator surface. For random conductivity values, functions and random were selected from the global definitions menu in the COMSOL program. Random data were created with random functions. The random function definition contains the mean, number of arguments, and range inputs. Random data are defined as a function of x, y, z space coordinates. Since it is a 3D work, the number of arguments is chosen as 3. The mean is the median value of the generated data. The range is the difference between each generated data. The steps given in Fig. 3. were followed to generate random data. The generated data were defined as the electrical conductivity of the pollution layer in the Materials menu.

III. RESULTS

A. Potential and Electric Field Distributions for Uniform and Non-Uniform Conditions

Potential and e-field distributions were investigated under uniform and non-uniform pollution conditions. For non-uniform pollution conditions, random values in the range of $(0.5–1.5) \times 10^{-6}$, $(0.5–1.5) \times 10^{-5}$, and $(0.5–1.5) \times 10^{-4}$ were created. These values were defined as the pollution layer conductivity at the pollution layer surface. Fig. 4. a,b. show the 3D distribution of generated random data and surface distribution of the generated data.

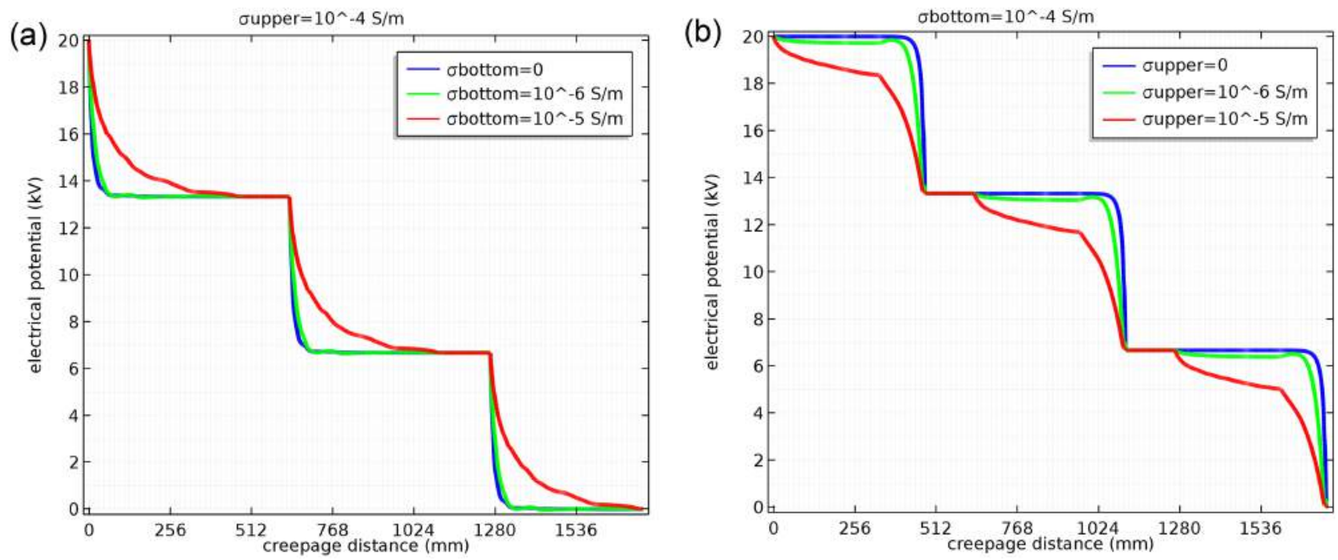

Fig. 7. The potential distributions (different conductivities for upper and bottom regions of insulator units) (a) σupper = 10^{-4} S/m, σbottom = variable, (b) σbottom = 10^{-4} S/m, σupper = variable.

The potential distributions in random non-uniform and uniform conditions are shown in Fig. 5.

Fig. 6.a-d. show the e-field distributions of insulator string and first insulator unit in random non-uniform and uniform pollutions.

In non-uniform conditions, the upper surface may be more contaminated than the bottom surface or the bottom surface may be more contaminated than the upper surface. In order to examine these situations, the upper and bottom surfaces were defined with different conductivities and investigations were made. Heavy pollution is taken into account at a conductivity value of 10^{-4} S/m. The upper surface conductivity was changed when the bottom surface conductivity was 10^{-4} S/m or the bottom surface conductivity was changed when the upper surface conductivity was 10^{-4} S/m. Fig. 7.a, b. show the potential distributions for non-uniform conditions where the bottom and upper surfaces have two different conductivities.

Fig. 8.a-d. show the e-field distributions of insulator string and first insulator unit for non-uniform conditions where the bottom and upper surfaces have two different conductivities.

IV. DISCUSSION

Considering 50 Hz power frequency voltage, imaginary part of the permittivity starts to affect the field distribution when the volume conductivity is in a range of 10^{-6} – 10^{-5} S/m. Increasing the volume conductivity beyond this level, pollution layer behaves like an equipotential surface. Considering bottom polluted condition with a conductivity of 10^{-4} S/m, bottom surface behaves somehow equipotential surface, and the whole pin voltage will appear across the clean top surface. Since the clean top surface has the less creepage distance, and therefore more e-field strengths will occur around the cap region. Similar explanation can be made for the top polluted condition. For the fully polluted condition with high pollution conductivity, a resistive behavior will occur, and the voltage distribution will tend to be linear.

In non-uniform conditions, where the bottom and upper surfaces have two different conductivities, when the conductivity of the bottom polluted layer increases, the distance between equipotential lines increases. Since the conductivity of the cap region will be less, the potential lines will become more frequent in the cap region, reducing the distance between them. When the distance between the equipotential lines decreases, the e-field strength value of the cap region increases. This indicates that arc discharges will start from the cap region. The same interpretation can be made for the case where the conductivity of the cap region is higher than that of the pin region.

In non-uniform pollution created with random data, although the random distribution has smaller values in the data range than the uniform pollution conductivities, it showed a high conductivity effect.

V. CONCLUSION

When the pollution conductivity increased, the potential distribution approached linear state and the e-field strength decreased.

In non-uniform pollution created with random data, the e-field strength values could be lower than the uniform state closest to the data range.

In non-uniform pollutions where the bottom and upper surfaces have two different conductivities, while the electric field strength decreased in the pin region as the bottom pollution conductivity increased, it decreased in the cap region as the upper pollution conductivity increased.

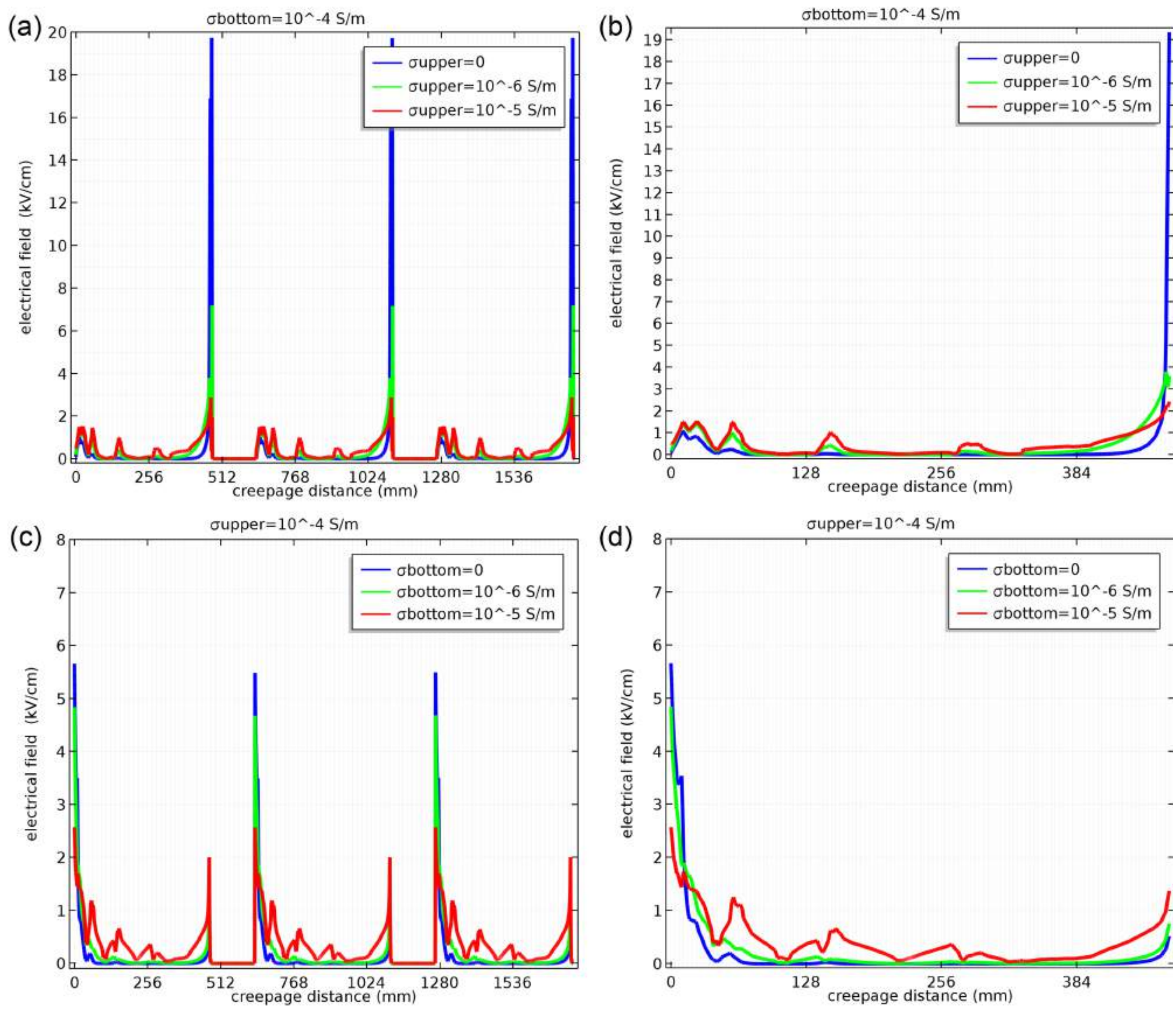

Fig. 8. e-field distributions (different conductivities for upper and bottom regions of insulator units). σbottom = 10^{-4} S/m, σupper = variable (a) for insulator string, (b) for the first insulator unit, σupper = 10^{-4} S/m, σbottom = variable (c) for insulator string, (d) for the first insulator unit.

Peer-review: Externally peer-reviewed.

Declaration of Interests: The authors have no conflict of interest to declare.

REFERENCES

1. M. A. Douar, A. Mekhaldi, and M. C. Bouzidi, “Flashover process and frequency analysis of the leakage current on insulator model under non-uniform pollution conditions,” *IEEE Trans. Dielectrics Electr. Insul.*, vol. 17, no. 4, pp. 1284–1297, 2010. [CrossRef]
2. D. Pylarinos, K. Siderakis, and E. Pyrgiot, “Measuring and analyzing leakage current for outdoor insulators and specimens,” *Rev. Adv. Mater. Sci.*, vol. 29, no. 1, pp. 31–53, 2011.
3. S. Ilhan, A. Ozdemir, S. H. Jayaram, and E. A. Cherney, “Ac and transient electric field distributions along a 380 kV V-string insulator,” IEEE International Symposium on Electrical Insulation (ISEI), San Juan, PR, USA, 2012, pp. 399–403.
4. S. Ilhan, A. Ozdemir, S. H. Jayaram, and E. A. Cherney, “Simulations of Pollution and their effects on the Electrical Performance of Glass Suspension Insulators,” Annual Report Conference on Electrical Insulation and Dielectric Phenomena, Montreal, QC, Canada: 2012, pp. 803–806.
5. Z. Zhijin, Z. Jiayao, W. Donghong, and J. Xingliang, “Effects of non-uniform pollution on the AC flashover performance of suspension insulators,” *J. Electr. Eng. Technol.*, vol. 11, no. 4, pp. 961–968, 2016. [CrossRef]

6. N. Kataria, and K. Tiwari, "Effect of environmental pollution on the performance of power transmission lines: Insulator's flashover," *Int. J. Eng. Res.*, vol. 7, no. 4, pp.531–533, 2018.
7. M. T. Gençoglu, and M. Cebeci, "Investigation of pollution flashover on high voltage insulators using artificial neural network," *Expert Syst. Appl.*, vol. 36, no. 4, pp. 7338–7345, 2009. [CrossRef]
8. M. Vitelli, V. Tucci, and C. Petrarca, "Temperature distribution along an outdoor insulator subjected to different pollution levels," *IEEE Trans. Dielect. Electr. Insul.*, vol. 7, no. 3, pp. 416–423, 2000. [CrossRef]
9. D. Doufene, S. Bouazabia, and R. Bouhaddiche, "Heating dissipation study of a pollution layer on a cap and pin insulator," International Conference on Communications and Electrical Engineering (ICCEE), El Oued, Algeria, 2018, pp. 1–4.
10. D. Zhang, and F. Meng, "Research on the interrelation between temperature distribution and dry band on wet contaminated insulators," *Energies*, vol. 12, no. 22, p. 4289, 2019. [CrossRef]
11. E. Ahmed, and A. Z. E. D. M. Moussa, "Performance of ceramic insulator string for 132 kV under different polluted conditions," *J. Energy*, vol. 1, no. 3, pp. 152–160, 2014.
12. J. L. Rasolonjanahary, L. Krahenbuhl, and A. Nicolas, "Computation of electric fields and potential on polluted insulators using A boundary element method," *IEEE Trans. Magn.*, vol. 28, no. 2, pp. 1473–1476, 1992. [CrossRef]
13. R. Djekidel, A. Bessedik, and A. Hadjadj, "Electric field modeling and analysis of EHV power line using improved calculation method," *Facta Universitatis - Series: Electronics and Energetics*, Vol. 31, no. 3, pp. 425–445, 2018.
14. G. Xu, and P. B. McGrath, "Electrical and thermal analysis of polymer insulator under contaminated surface conditions," *IEEE Trans. Dielectrics Electr. Insul.*, vol. 3, no. 2, pp. 289–298, 1996. [CrossRef]
15. Y. Lin, J. ZheZhang, Y. Liu, and S. Li, "Pei and Y. Liu, *Influence of Pollution on Potential and Electric Field Distribution of Porcelain Insulator in 110 kV Transmission Line*," *J. Phys. Conf. S. IOP Publishing*, vol. 1314, no. 1, p. 012043, 2019.
16. A. S. Krzma, M. Y. Khamaira, and M. Abdulsamad, "Comparative analysis of electric field and potential distributions over porcelain and glass insulators using finite element method," *Proceedings of First Conference for Engineering Sciences and Technology (CEST-2018)*. Elmergib University, Libya, 2018, pp. 176–184.
17. M. I. Mousa, Z. Abdul-Malek, and Z. I. Mousa, "Leakage current based thermal modeling of glass disc insulator surface," *IJEECS*, vol. 6, no. 3, pp. 504–512, 2017. [CrossRef]
18. X. Hui, L. Bangyu, X. Shaobo, and F. Hongzhuan, "The measurement of dielectric constant of the concrete using single-frequency CW radar," First International Conference on Intelligent Networks and Intelligent Systems, United States, 2008, pp. 588–591.
19. O. E. Gouda, A. Z. El Dein, A. Thabet, and A. El Tayeb, "Performance of ceramic insulator type under different polluted conditions," The 2nd International Conference on Energy Engineering ICEE-2, Aswan-EGYPT, 2010, pp. 1–7.
20. M. A. Abouelsaad, M. A. Abouelatta, B. Arafa, and M. E. Ibrahim, "Environmental pollution effects on insulators of Northern Egypt HV transmission lines," Annual Report Conference on Electrical Insulation and Dielectric Phenomena, Shenzhen, 2013, pp. 35–38.
21. M. El-Shahat, and H. Anis, "Risk assessment of desert pollution on composite high voltage insulators," *J. Adv. Res.*, vol. 5, no. 5, pp. 569–576, 2014. [CrossRef]
22. E. Nasser, "Contamination flashover of outdoor insulation," *etz-A*, vol. 93, no. 6, pp. 321–325, 1972.
23. N. A. Arshad, S. G. McMeekin and M. Farzaneh, "Effect of Pollution Severity on Electric Field Distribution along a Polymeric Insulator," IEEE 11th International Conference on the Properties and Applications of Dielectric Materials (ICPADM), Sydney, NSW, Australia, 2015.
24. W. Sima, T. Yuan, Q. Yang, K. Xu, and C. Sun, "Effect of non-uniform pollution on the withstand characteristics of extra high voltage (EHV) suspension ceramic insulator string," *IET Gener. Transm. Distrib.*, vol. 4, no. 3, pp. 445–455, 2010. [CrossRef]
25. Z. Zhang, D. Zhang, X. Jiang, and X. Liu, "Study on natural contamination performance of typical types of insulators," *IEEE Trans. Dielectrics Electr. Insul.*, vol. 21, no. 4, pp. 1901–1909, 2014. [CrossRef]
26. Z. Zhang, J. You, J. Zhao, Y. Cheng, X. Jiang, and Y. Li, "Contamination characteristics of disc-suspension insulator of transmission line in wind tunnel," *IET Gener. Transm. Distrib.*, vol. 11, no. 6, pp. 1453–1460, 2017. [CrossRef]

cigre Turkey

TEPES
TURKISH JOURNAL OF
ELECTRICAL POWER
AND ENERGY SYSTEMS

TEPES, Vol. 2, Issue. 1, 75-84, 2022 **DOI:** 10.5152/tepes.2022.21013

RESEARCH ARTICLE

On-Grid and Off-Grid Hybrid Renewable Energy System Designs with HOMER: A Case Study of Rural Electrification in Turkey

Mikail Pürlü, Sezen Beyarslan, Belgin Emre Türkay

Department of Electrical Engineering, İstanbul Technical University, İstanbul, Turkey

Cite this article as: M. Pürlü, S. Beyarslan and B. E. Türkay. On-grid and off-grid hybrid renewable energy system designs with HOMER: A case study of rural electrification in Turkey. *Turk J Electr Power Energy Syst*, 2022; 2(1): 75-84.

ABSTRACT

In this study, hybrid renewable energy systems were designed to minimize the cost of electrical energy and harmful gas emissions in line with environmental and economic concerns. While the on-grid hybrid renewable energy systems were designed by providing optimum power dispatching between solar panels, wind turbines, a small hydroelectric power plant, and the main grid, off-grid systems were designed by completely disconnecting from the grid and adding a battery energy storage system. Therefore, data such as power demand, peak load, solar irradiation, wind speed, and river flow rate of a rural area in Turkey have been collected to realize the analyses of optimal hybrid energy systems in Hybrid Optimization Models for Energy Resources program. While on-grid systems provide very economical solutions, off-grid systems have become more environmentally friendly. By introducing grid usage restriction, carbon emissions in on-grid systems have also been reduced. Also, more feasible systems have been achieved by including various constraints such as sell-back capacity, shortage capacity, and the maximum number of wind turbines to fit in the area. Finally, the effects of the increase in the renewable energy capacities were examined by performing sensitivity analyses and positive economic and environmental contributions have been observed.

Index Terms—HOMER, hybrid energy systems, grid-connected, standalone, renewable energy

I. INTRODUCTION

The rapid increase in population and technological developments in recent years has increased the electrical energy demand all over the world [1]. On the other hand, the United Nations Environment Program reports that an estimated 2.0 billion people around the world, mostly living in underdeveloped countries or rural areas, are deprived of a reliable electricity grid service [2]. It is a challenge to provide reliable, efficient, and economical electrical energy to these remote and underpopulated areas [3]. Off-grid microgrids including distributed energy sources in small-scale are more cost-effective than stretching transmission and distribution lines to these rural regions [4].

The use of electrical energy has become a basic need for people living in both urban areas and villages/islands, and the demand is increasing day by day [5]. The enormous increase in fossil fuel prices [6] and the decrease in fossil fuel reserves led to an energy crisis. Alternative renewable energy sources are proposed to cope with this energy crisis and reduce harmful gas emissions. Alternative renewable energy sources (RESs) are proposed to cope with this energy crisis and reduce harmful gas emissions. However, a single RES cannot meet the energy demand due to the generation uncertainties of RESs. Therefore, hybrid renewable energy systems (HRESs) including various RESs such as solar, wind, biomass, hydro energy, and energy storage systems are recommended [7]. Hybrid energy systems (HESs) can be designed to operate as off-grid (stand-alone and grid-isolated) or on-grid (grid-connected) systems and can utilize energy storage systems (ESSs) [8].

There are a lot of studies for off-grid and on-grid HESs using various optimization algorithms and tools. The authors in [1] proposed a stand-alone hybrid hydro/wind/solar/diesel/battery energy system to power the Persian Gulf Islands by using Hybrid Optimization Models for Energy Resources (HOMER). In [2], a grid-isolated hybrid solar/wind/diesel/battery energy system was studied on HOMER for a village named Perumal Kovilpathy, Tamil Nadu, in India. An off-grid hybrid solar/wind/hydro/battery energy system design on HOMER to electrify remote and hard-to-reach villages in the Indian Himalayan Region was proposed by [3]. In [4], a comparison of grid-isolated and grid-connected solar/battery systems for a rural community in Rwanda was examined by using HOMER.

Corresponding author: Mikail Pürlü, purlu@itu.edu.tr

Received: February 7, 2022
Accepted: March 16, 2022

The feasible HES designs of solar/wind/biomass/diesel/battery/non-battery on Sbessi Island, South Lampung Regency, Indonesia, were conducted by the authors in [5]. In [6], two HOMER models for off-grid and on-grid HES consisting of solar/wind/diesel/battery were studied without sensitivity analyses for Statesboro.

A grid-connected hybrid solar/wind/biomass energy system without battery was designed considering the effect of sensitivity variables for a university campus utilizing HOMER [7]. Hybrid combinations of wind turbines (WTs), photovoltaic panels (PVs), and battery energy storage system (BESS) were optimized for an 80 m^2 residential building in Durban by using genetic algorithm and particle swarm optimization methods [8].

The authors in [9] proposed a numerical algorithm to determine the optimal size of wind, solar, and wind/solar hybrid energy system with batteries for a typical residential load in a remote area in Montana. Three recent optimization algorithms, bat optimization, equilibrium optimizer, and black hole, were used to optimize the grid-connected HES consisting of PV/BESS/hydrogen storage systems (HSS) for Dobaa Region in Egypt [10].

In [11], renewable and nonrenewable energy sources with BESS and HSS were used to design stand-alone HES for Newfoundland by using HOMER. HOMER-MATLAB combined tool was used to optimize on-grid PVs with BESS for a large commercial load in Makkah, Arabia [12].

The authors in [13] proposed the generalized reduced gradient method to design both optimal off-grid and on-grid HRES including WT, PV, and BESS for a remote rural area. In [14], a moth-flame optimization algorithm was presented to determine the optimal size of wind/solar HES with hybrid ESS including BESS and supercapacitor. HOMER and MATLAB/Simulink models for a residential area in Pakistan were introduced to design grid-isolated wind/solar/battery HESs [15].

HESs such as off-grid PV/HSS for an area in Brazil [16], on-grid PV/BESS at University of Campinas (UNICAMP) campus [17], various combinations of diesel/PV/WT/HPP/BESS for a remote region in Nigeria [18], stand-alone PV/diesel/BESS for a remote area in South Africa [19], and grid-isolated and grid-connected PV/WT/HPP/HSS HES for a rural area in Turkey were designed using HOMER software.

Main Points

- Both off-grid and on-grid scenarios were examined.
- A reliable and robust hybrid energy system was designed using various renewable energy sources.
- Feasible case studies by using the constraints.
- Economic and environmental contributions.
- As future work, another renewable energy source such as biomass can be integrated into the proposed hybrid energy system.

This paper proposes the optimal solution scenarios to both on-grid and off-grid hybrid energy systems consisting of RESs, such as WT, PV, HPP, and BESS, and also examines sensitivity analyses for a rural area by using HOMER software under the various constraints based on power system operation, used components, and feasibility.

The remaining of this paper is organized as follows. In section II, the introduction of the HOMER software and its mathematical modeling are given. The data of the rural area about consumption and renewable generation are presented in section III. The results of the performed analyses for on-grid and off-grid systems are included in section IV. The results are discussed in section V. Finally, the conclusion of this paper is located in section VI.

II. METHODOLOGY

In this study, the HOMERsoftware was used to design RHESs. HOMER is a microgrid optimization tool developed by National Renewable Energy Laboratory [2, 3]. The basic functions of HOMER are imitation, optimization, and sensitivity analysis. Power balance, load profile, location-specific tools, and system components are all considered by HOMER. The schematic summary of the HOMER software is shown in Fig. 1 [4].

In HOMER, the electrical power generated by the HPP is calculated with the following equation [18]:

$$P_{hyd} = \frac{\eta_{hyd} \cdot h_{net} \cdot \rho_{water} \cdot Q_T \cdot g}{1000\left(W / kW\right)} \tag{1}$$

where η_{hyd} is the total efficiency of the hydro plant (%), h_{net} refers to the effective head (m), ρ_{water} is the water density (1000 kg/m^3), Q_T denotes the flow rate of the hydro turbine (m^3/s), and g is the gravitational acceleration (9.81 m/s^2).

The effective electrical power output generated by the WTs is calculated as follows [1, 13].

$$P_{e,wt} = \eta_{wt} \cdot A_{wt} \cdot P_{wt} \tag{2}$$

$$P_{wt} = N_{wt} \times \begin{cases} 0, & v \le v_{ci} \text{ or } v > v_{co} \\ P_r\left(\dfrac{v^3 - v_{ci}^3}{v_r^3 - v_{ci}^3}\right), & v_{ci} < v \le v_r \\ P_r, & v_r < v \le v_{co} \end{cases} \tag{3}$$

where η_{wt} is the wind turbine efficiency, A_{wt} is the swept area of the turbine, N_{wt} is the number of the WTs, P_r is the rated power of each WT (kW), v is the wind speed (m/s), v_{ci}, cut-in wind speed, is the threshold value of the wind speed, and v_{co}, cut-out wind speed, is the threshold value of the wind speed.

The output power of the PV system can be defined by (4) [1, 8 ,10, 18]:

$$P_{pv}(t) = N_{pv} \cdot P_{pv_r} \cdot f_{pv} \cdot \frac{G(t)}{G_n}\left[1 + \alpha_p\left(T_C(t) - T_{C_n}\right)\right] \tag{4}$$

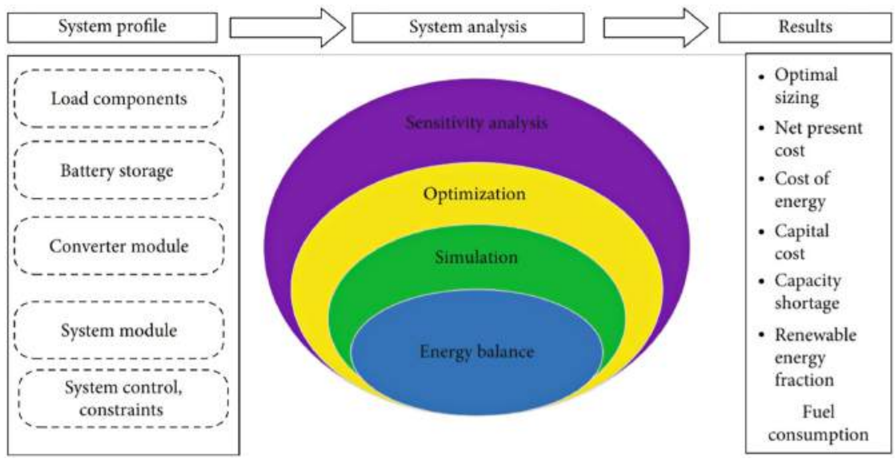

Fig. 1. Schematic representation of HOMER program [4].

where N_{pv} is the number of the PV modules, P_{pvr} is the rated power of each PV module (kW), f_{pv} is the PV derating factor (%), $G(t)$ is the irradiation at the operating temperature (kW/m^2), G_n is the irradiation at the standard test condition ($1kW/m^2$), α_p is the temperature coefficient ($\%/^{\circ}C$), $T_c(t)$ is the cell temperature (°C), and T_{c-n} is the nominal operating (test condition) temperature of the PV module (25°C).

In HOMER, performance indicators are cost of unit energy (CoE), net present cost (NPC), operational cost (OC), and initial cost (IC).

CoE is the most critical metric and it represents the cost of producing 1 kWh of electrical energy. It is calculated as follows [21]:

$$CoE(\$/kWh) = \frac{TAC(\$/yr)}{TAEC(kWh/yr)} \tag{5}$$

where TAC is the total annual cost and $TAEC$ is the total annual energy consumption.

NPC is the total of all expenses including capital, replacement, operation and maintenance, and fuel expenditures minus the salvage cost at the end of the project's lifetime. It is calculated as follows [1]

$$NPC(\$/yr) = \frac{TAC(\$/yr)}{CRF} \tag{6}$$

$$CRF(i,n) = \frac{i(1+i)^n}{(1+i)^n - 1} \tag{7}$$

where CRF is the capital recovery factor, i is the interest rate (%), and n is the life time of the components (year).

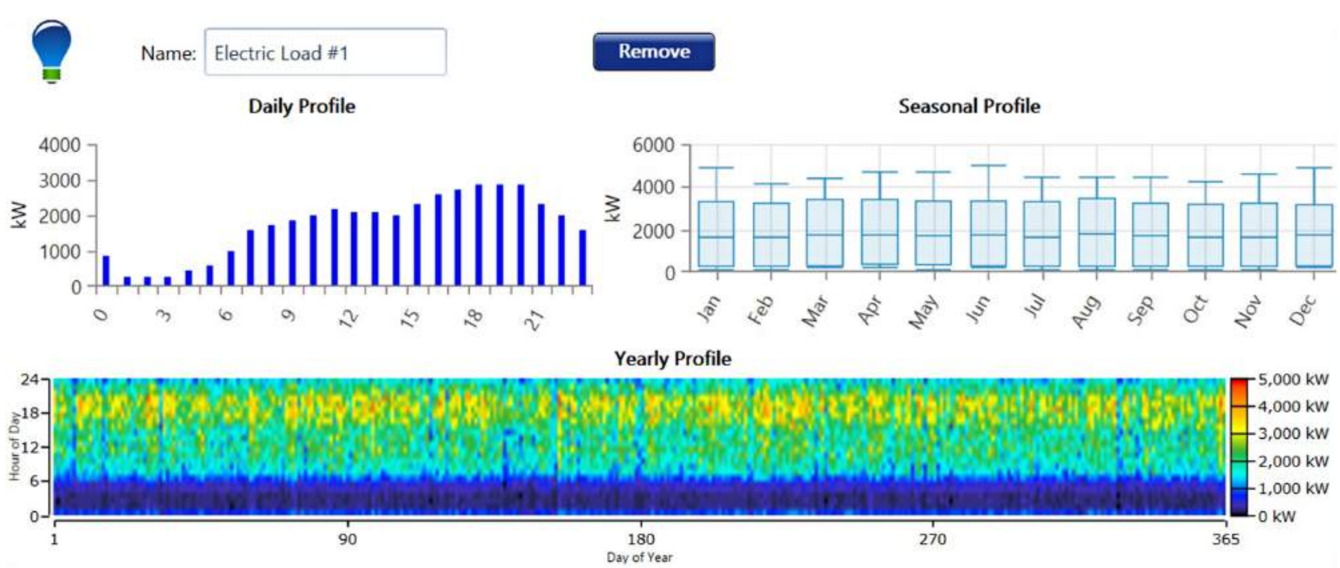

Fig. 2. Load profile.

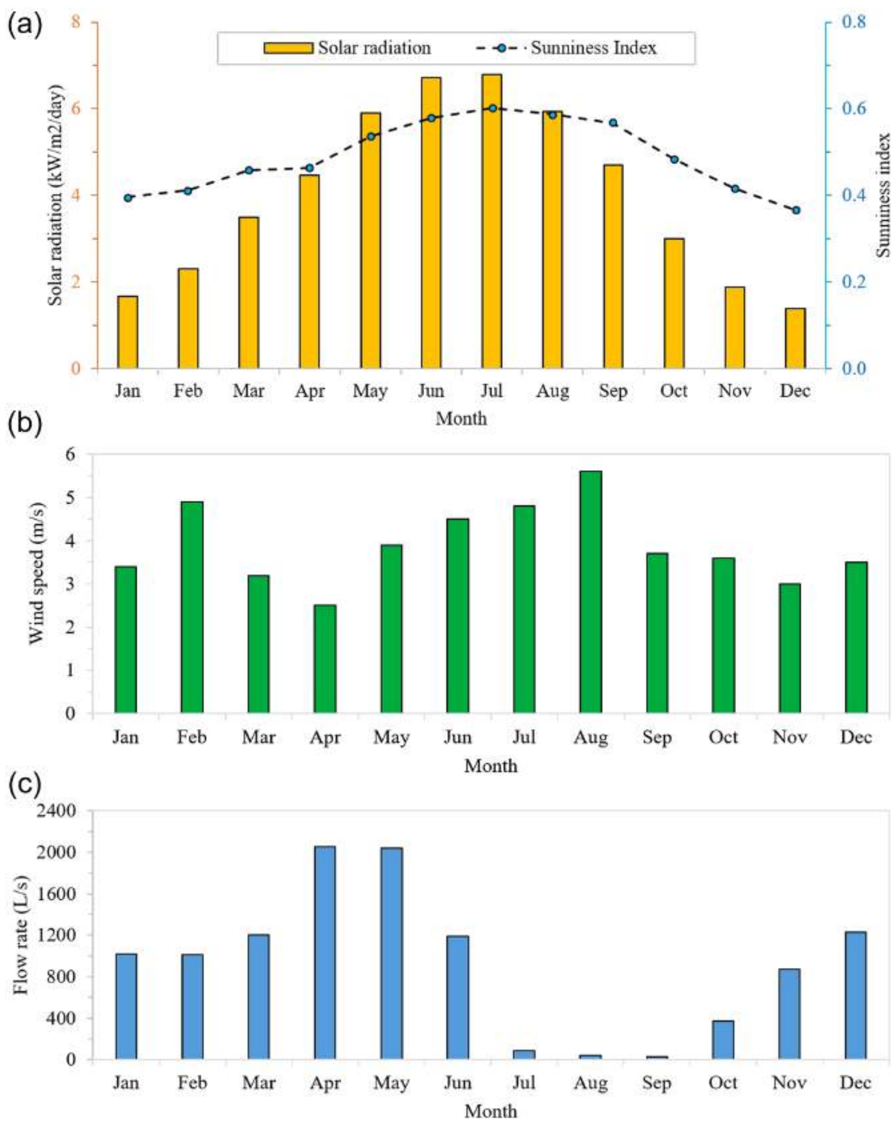

Fig. 3. Renewable sources' data of the region for: a) irradiance; b) wind speed; c) flow rate.

OC is calculated by subtracting the total annual cost from the capital investment and is formulated as follows [1, 21]:

$$OC(\$/yr) = TAC(\$/yr) - ACC(\$/yr) \tag{8}$$

where *ACC* is the annual capital cost.

III. TEST SYSTEM DATA

In this study, a grid-connected village in Bursa, Turkey, was examined. The village is located at 40°08′55.27" north latitude 29°16′06.73" east longitude. The population of this village, located near the Delicay river, was 390 in 2021. The daily, seasonal, and yearly load profiles of the region are given in Fig. 2.

The meteorological data for the village was obtained from the NASA Prediction of Worldwide Energy Resource (NASA POWER) database [22]. Solar radiation data come from NASA POWER by HOMER software. The average sunniness index was recorded as 0.515 and the average daily radiation was recorded as 4.028 kWh/m²/day. The average wind speed for this village, which is located at an altitude of 611 m, is 3.88 m/s. The average flow of Delicay river is 928 L/s. All renewable resources' data used in this study is shown in Fig. 3. Capacity and turbine cost of three types of WT are listed in Table I and the power characteristics of WTs are shown in Fig. 4 [23].

IV. RESULTS OF THE ANALYSES

The analyses were performed for both off-grid and on-grid systems. Village daily energy demand is 29 MWh/day and daily peak load is 3500 kW. Because of the availability of wind and solar energy potential in most areas [8], they were chosen as the major RESs in this study.

TABLE I.
CAPACITY AND TURBINE COST

Type of WT	Abbreviation	Capacity (kW)	Turbine cost ($)
Enercon E33	E33	330	429 000
Leitwind90 LT90	LT90	1500	1 800 000
Enercon E82	E82	3000	3 300 000

WT, wind turbine.

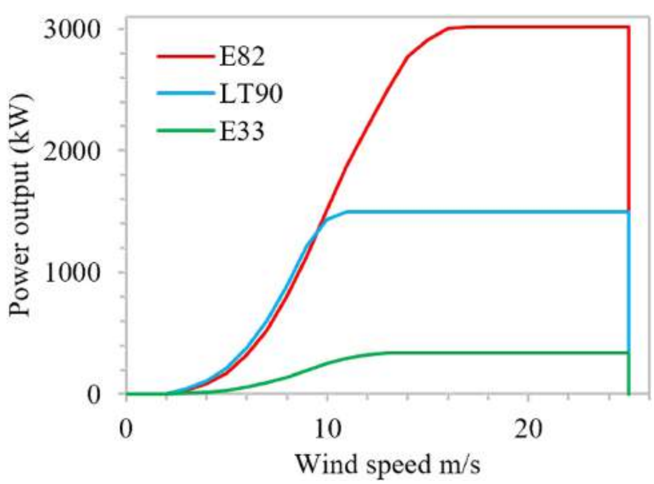

Fig. 4. Power characteristics of wind turbines.

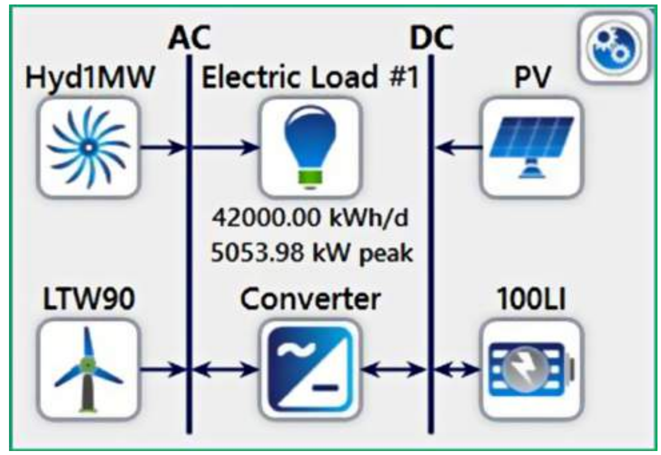

Fig. 5. Off-grid HRES design.

A. Off-grid System Analyses

Off-grid system in Fig. 5 has been designed with renewable energy such as PV, WT, HPP, and ESS such as Li-ion battery.

Analyses were made with 1%, 5%, and 10% shortage capacity to select the most proper one among the three types of WT such as E33, LTW90, and E82. HOMER program analyzes the system economically [24]. In this study, the area of the village is insufficient, the number of WTs is limited to three in terms of feasibility. Due to its low capacity of 330 kW, E33 WT was not used in the limited analyses. The results of the analyses are listed in Table II. According to the

TABLE II.
OFF-GRID ANALYSES RESULTS

SC (%)	WT Type	PV (kW)	WT (kW)	HPP (kW)	Li-ion (100 kWh)	Converter (kW)	NPC (M$)	CoE ($)	OC (M$/Year)	IC (M$)
	E33	12 263	11 550	212	357	4051	73.0	0.371	1.87	48.8
1	LT90	9469	9000	212	338	4156	62.3	0.317	1.65	41.0
	E82	11 673	15 000	212	355	4571	73.6	0.374	1.82	50.1
	E33	9469	9000	212	239	3674	57.6	0.300	1.50	38.2
5	LT90	7293	7500	212	224	3157	47.9	0.249	1.30	31.1
	E82	9841	12 000	212	256	3500	58.8	0.306	1.49	39.6
	E33	8592	8250	212	190	3458	49.9	0.267	1.32	32.8
10	LT90	5677	7500	212	160	3657	41.7	0.224	1.13	27.0
	E82	8623	9000	212	218	3494	50.4	0.270	1.32	33.3
5*	LT90	11 131	4500	212	266	3621	51.7	0.269	1.40	33.6
	E82	11 841	9000	212	272	4811	59.6	0.310	1.51	40.1

*for the case of maximum three WTs limitations.
SC, shortage capacity; WT, wind turbine; PV, photovoltaic; HPP, hydro power plant; NPC, net present cost; CoE, cost of unit energy; OC, operating cost; IC, initial cost.

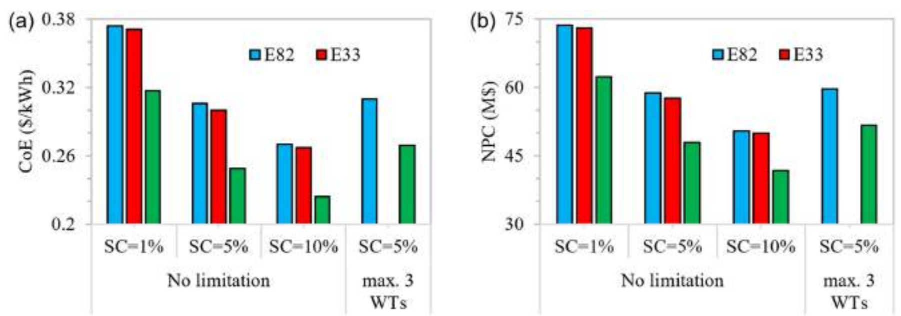

Fig. 6. Comparison of the off-grid designs for a) CoE; b) NPC.

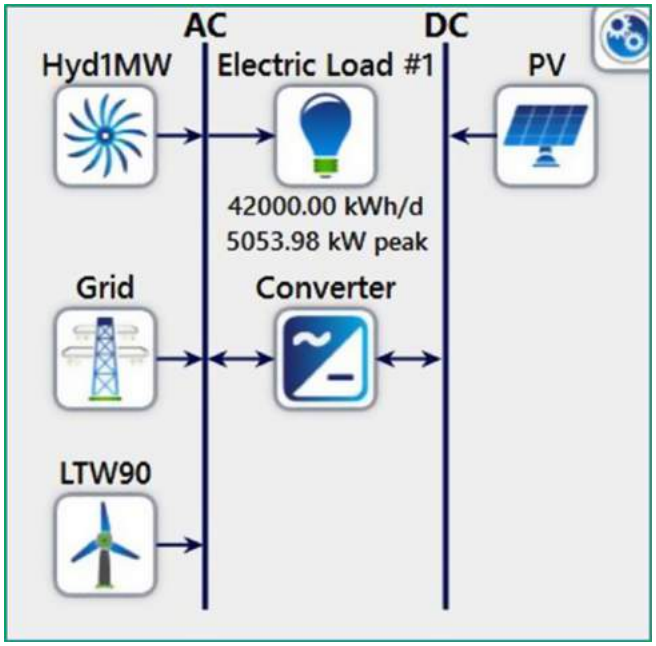

Fig. 7. Grid-connected HRES design.

results, LTW90 is the best option and 10% cheaper than E82. The economical comparison of off-grid designs is shown in Fig. 6.

B. On-grid System Analyses

On-grid system has been designed with PV, WT, and HPP without using any ESS. While designing the on-grid system, HOMER economically prefers grid usage instead of RES. In order to design on-grid with RES and decrease carbon emission level, the grid usage was limited. Since LTW90 was chosen for off-grid, it was also used for on-grid. The on-grid design is shown in Fig. 7.

Grid usage cost of unit energy is defined as 0.1$/kWh and sell-back prices is defined as 0.05$/kWh [25]. Grid usage was separately limited to 4000 kW and 5000 kW for choosing the best option. Sell-back option from renewable energy to grid was defined as 0 kW, 500 kW, 750 kW, and 1000 kW. Since there is no storage system, sellback should be defined for not to waste rest energy generation. Also, for feasible case study, the number of WTs was limited to maximum three. The results of on-grid designs are listed in Table III.

The comparison of on-grid designs is shown in Fig. 8. Although RES usage had no differences, the costs were changed by each sell-back capacity. In case the grid usage is limited to 5000 kW, it is seen that PV and converter are not used.

TABLE III.
ON-GRID ANALYSES RESULTS

GU (kW)	SBC (kW)	PV (kW)	N_{WT}	HPP (kW)	Converter (kW)	NPC (M$)	CoE ($/kWh)	OC (M$/Year)	IC (M$)	GER (%)	CE (kg/Year)
4000	0	1625	7	212	584	31.6	0.16	1.15	16.7	74.1	2 508 538
	500	1615	7	212	723	30.2	0.132	1.03	16.8	77.9	2 471 529
	750	1615	7	212	723	29.5	0.122	0.977	16.8	79.2	2 471 529
	1000	1615	7	212	723	28.8	0.113	0.927	16.8	80.2	2 471 529
5000	0	-	2	212	-	22.8	0.115	1.33	5.60	47.4	5 097 380
	500	-	2	212	-	22.2	0.106	1.29	5.60	50.3	5 097 380
	750	-	2	212	-	22.0	0.103	1.27	5.60	51.2	5 097 380
	1000	-	3	212	-	21.9	0.0953	1.12	7.40	61.9	4 277 795

(*Continued*)

TABLE III.
ON-GRID ANALYSES RESULTS (*CONTINUED*)

GU (kW)	SBC (kW)	PV (kW)	N_{WT}	HPP (kW)	Converter (kW)	NPC (M$)	CoE ($/kWh)	OC (M$/Year)	IC (M$)	GER (%)	CE (kg/Year)
4000*	0	17932	3	212	2274	44.2	0.223	1.31	27.3	76.8	2 246 013
	500	18804	3	212	1171	43.2	0.195	1.29	26.5	74.7	2 749 088
	750	18084	3	212	1171	42.7	0.184	1.25	26.5	75.7	2 749 088
	1000	17812	3	212	1964	41.4	0.167	1.12	26.9	80.9	2 312 578

*For the case of maximum three LT90 WT limitations.
GU, grid usage; SBC, sell-back capacity; N_{WT}, number of wind turbine; HPP, hydro power plant; NPC, net present cost; CoE, cost of unit energy; OC, operating cost; IC, initial cost; GER, green energy usage rate; CE, carbon emission.

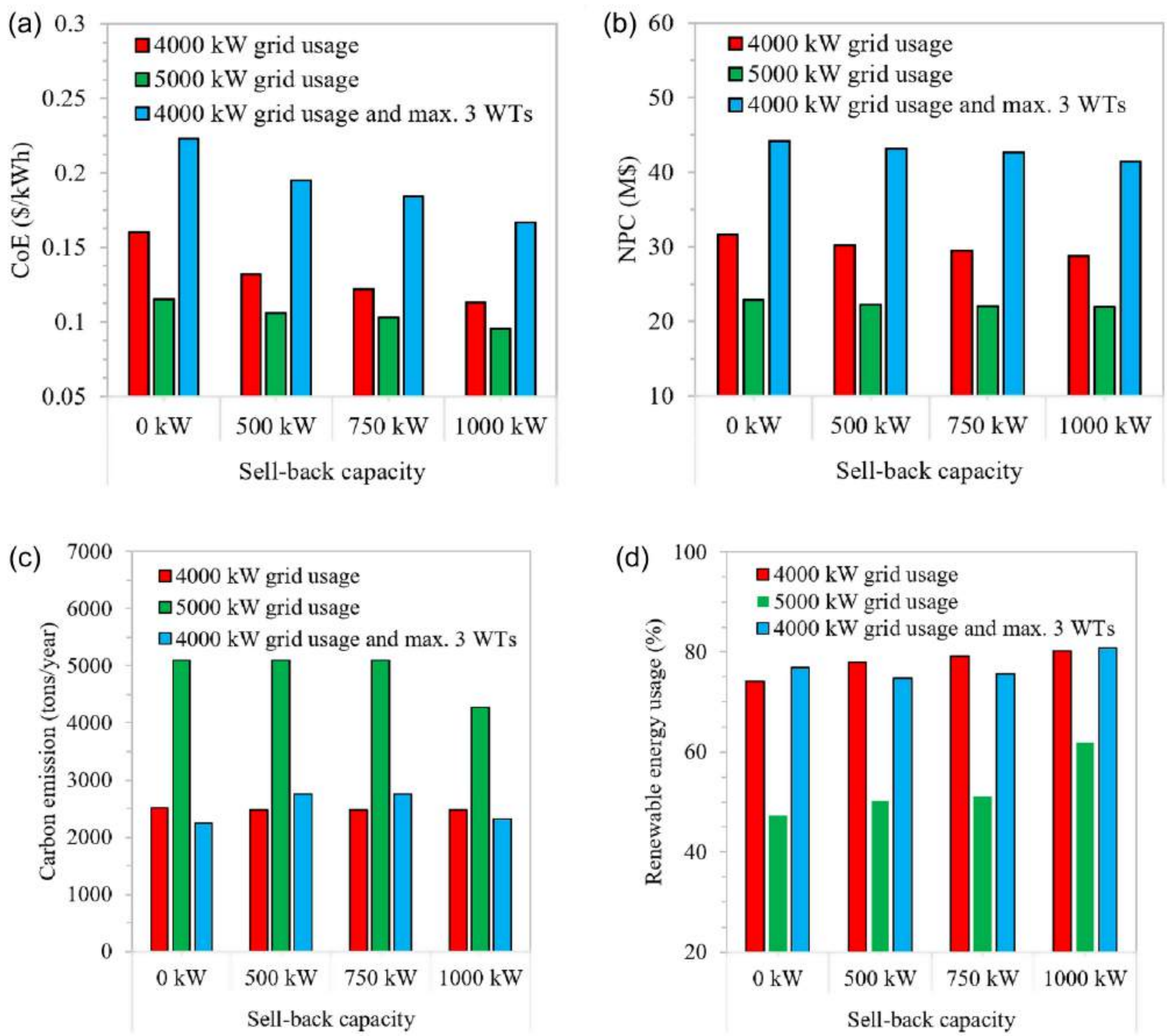

Fig. 8. Comparison of on-grid designs for a) CoE; b) NPC; c) carbon emission; d) renewable energy usage.

Despite the systems with limited grid usage not having cost benefit, they have contributed to the environment by reducing carbon emissions, thanks to the increasing use of RES.

If the grid usage is limited to 4000 kW, the use of renewable energy increases by 25% compared to the case limited to 5000 kW, while carbon emissions decrease by 50%. Considering environmental concerns, limitation of grid usage to 4000 kW is more appropriate than limitation to 5000 kW.

In this case, the best on-grid option is chosen as the system with 4000 kW grid limitation, 3 LTW90 WTs, and 1000 kW sell-back capacity.

C. Sensitivity Analyses

Sensitivity analyses were designed for the off-grid system by increasing renewable energy sources' potential such as wind speed, solar radiation rate, and stream flow speed. In order to catch on-grid system prices, renewable energy potential was increased by 25% and all sensitivity analyses were compared with the base case.

In sensitivity analyses, off-grid systems were designed by three LT90 WTs of 4500 kW and only BESS. The sensitivity analyses results are listed in Table IV and the cost comparisons of all sensitivity analyses are shown in Fig. 9.

While the 25% increase in all renewable energy potential has a positive economic effect, the best result has been obtained for increasing the wind speed.

V. DISCUSSION

The results of on-grid and off-grid system analyses are given in Table V. In the systems limited to three WTs for feasible design, it is seen that the costs of the off-grid system are on average 5 times the on-grid system.

In this study, hybrid energy systems including renewable energy sources and energy storage systems were designed for both on-grid and off-grid by using HOMER. The systems were optimized with economic and environmental concern to be feasible.

TABLE IV.
THE RESULTS OF THE SENSITIVITY ANALYSES

Sensitivty	PV (kW)	WT (kW)	HPP (kW)	Li-ion (100 kWh)	Converter (kW)	NPC (M$)	CoE ($/kWh)	OC (M$/Year)	IC (M$)
Base case	11 131	4500	212	266	3621	51.7	0.269	14 611	33.6
Solar radiation	7284	4500	212	241	3795	45.2	0.235	1.27	28.8
Stream flow	10 347	4500	212	265	3495	50.5	0.263	1.38	32.7
Wind speed	6067	4500	212	210	4771	42.3	0.220	1.18	27.0

PV, photovoltaic; WT, wind turbine; HPP, hydro power plant; NPC, net present cost; CoE, cost of unit energy; OC, operating cost; IC, initial cost.

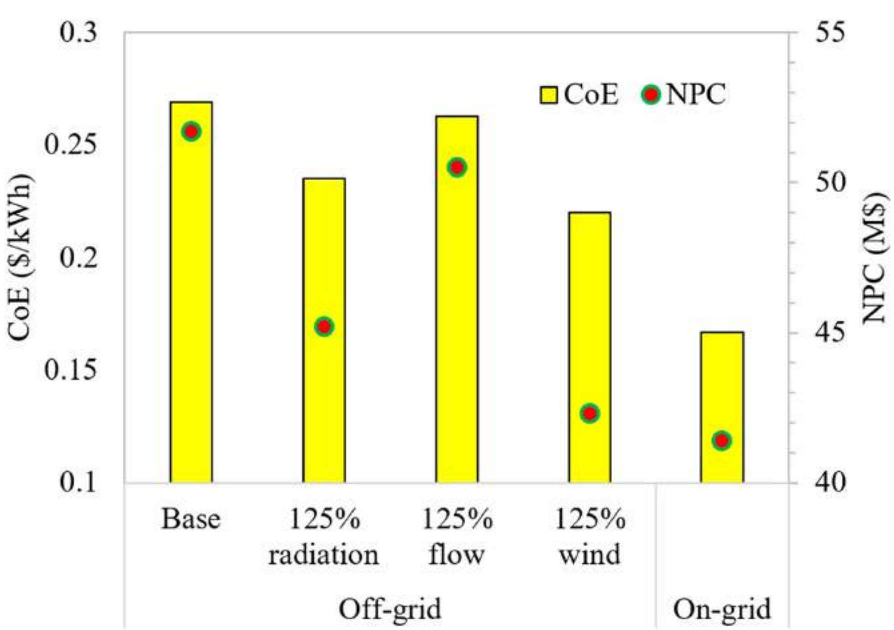

Fig. 9. Comparison of the sensitivity analyses.

TABLE V.
RESULTS OF OFF-GRID AND ON-GRID SYSTEM ANALYSES

Grid Type	NPC (M$)	CoE ($/kWh)	OC (M$/Year)	IC (M$)
Off-grid with 3 WT limitation	41.4	0.167	1.12	26.9
On-grid with 3 WT limitation	51.7	0.269	1.40	33.6

NPC, net present cost; CoE, cost of unit energy; OC, operating cost; IC, initial cost.

According to the results, while on-grid designs are more economical solutions, off-grid systems are the more environmentally friendly solution. Sensitivity analyses show that increasing the renewable energy potential increases both economic and environmental contribution. Although increasing the potential by 25% cannot keep up with on-grid prices, more affordable costs are expected, thanks to developing renewable energy generation technology.

The operating times of PV, WT and HPP are 4400, 6951 and 6552 hours per year (h/yr), respectively. While the increase in stream flow speed and solar radiation rate don't change the operating times in the sensitivity analyzes, it is observed that only the operating time of WT increased by 583 hours to 7534 h/yr when the wind speed increased.

As a result, the on-grid system limited to three wind turbines with 1000 kW sell-back capacity and 4000 kW grid usage has been proposed because it is feasible, economical, and environmentally friendly.

VI. CONCLUSION

In this study, renewable hybrid energy systems have been designed with renewable energy sources and battery energy storage systems. These systems were designed by HOMER with both economic and environmental concerns.

The off-grid system, which has the optimum solution in terms of feasibility, environmental friendliness, and economy, was designed by PVs with a total capacity of 11 131 kW, 3 LT90 WTs with a total capacity of 4500 kW, HPP with a capacity of 212 kW, 266 Li-ion batteries with a capacity of 100 kWh, and the converter with a capacity of 3621 kW.

While the on-grid systems in this study generally provide much more economical solutions, they require some environmental limitations. For this reason, it is aimed to increase the rate of renewable energy usage by limiting the use of fuel-based grids. In designed optimal on-grid system, grid limitation is 4000 kW and the total capacities of sell-back, PV, WT, hydro, and converter are 1000 kW, 17 812 kW, 4500 kW, 212 kW, and 1964 kW, respectively.

In the sensitivity analysis of the stand-alone system, 25% increase in renewable energy potential has increased both economic and environmental contributions, but it is still not as economical as the grid-connected system.

According to all analyses results, while on-grid systems offer more economical solutions, off-grid systems offer more environmental solutions. It is hoped that systems with higher use of clean energy will be more economical with the further development of renewable energy technologies and the decrease in component prices.

Peer-review: Externally peer-reviewed.

Author Contributions: Concept – B.E.T.; Design – S.B.; Supervision – B.E.T.; Materials – S.B.; Data Collection and/or Processing – S.B., M.P.; Analysis and/or Interpretation – S.B., M.P.; Literature Review – M.P.; Writing – M.P.; Critical Review – B.E.T., M.P.

Declaration of Interests: The authors have no conflicts of interest to declare.

Funding: The authors declare that this study has received no financial support.

REFERENCES

1. Q. Ma, X. Huang, F. Wang, C. Xu, R. Babaei, and H. Ahmadian, "Optimal sizing and feasibility analysis of grid-isolated renewable hybrid microgrids: Effects of energy management controllers," *Energy*, Vol. 240, 122503, 2022. [CrossRef]
2. J. Kumari, P. Subathra, J. E. Moses, and D. Shruthi, "Economic analysis of hybrid energy system for rural electrification using Homer," 2017 International Conference on Innovations in Electrical, Electronics, Instrumentation and Media Technology (ICEEIMT), IEEE Publications, 2017, pp. 151–156. [CrossRef]
3. S. Chauhan, R. Pande, and S. Sharma, "Techno-economic study of off-grid renewable energy system in Darma valley, Uttarakhand, India," *Current Science*, vol. 9, p. 121, 2021.
4. K. C. Chang *et al.*, "Standalone and minigrid-connected solar energy systems for rural application in Rwanda: An in situ study," *Int. J. Photoenergy*, vol. 2021, pp. 1–22, 2021. [CrossRef]
5. S. Kanata, S. Baqaruzi, A. Muhtar, P. Prasetyawan, and T. Winata, "Optimal planning of hybrid renewable energy system using Homer in Sebesi Island, Indonesia," *Int. J. Renew. Energy Res. (IJRER)*, vol. 11, no. 4, pp. 1507–1516, 2021. [CrossRef]
6. S. Ghose, A. El Shahat, and R. J. Haddad, "Wind-solar hybrid power system cost analysis using Homer for Statesboro, Georgia," *Southeastcon*. IEEE Publications: Charlotte NC, 2017, pp. 1–3. [CrossRef]
7. H. Sharma, and S. Mishra, "Hybrid optimization model for smart grid distributed generation using Homer," 3rd International Conference on Recent Developments in Control, Automation & Power Engineering (RDCAPE), IEEE Publications, 2019, pp. 94–99. [CrossRef]
8. F. Ghayoor, A. G. Swanson, and H. Sibanda, "Optimal sizing for a grid-connected hybrid renewable energy system: A case study of the residential sector in Durban, South Africa," *J. Energy South. Afr.*, vol. 32, no. 4, pp. 11–27, 2021. [CrossRef]
9. W. D. Kellogg, M. H. Nehrir, G. Venkataramanan, and V. Gerez, "Generation unit sizing and cost analysis for stand-alone wind, photovoltaic, and hybrid wind/PV systems," *IEEE Trans. Energy Convers.*, vol. 13, no. 1, pp. 70–75, 1998. [CrossRef]
10. A. A. Z. Diab, A. M. El-Rifaie, M. M. Zaky, and M. A. Tolba, "Optimal sizing of stand-alone microgrids based on recent metaheuristic algorithms," *Mathematics*, vol. 10, no. 1, p. 140, 2022. [CrossRef]
11. M. J. Khan, and M. T. Iqbal, "Pre-feasibility study of stand-alone hybrid energy systems for applications in Newfoundland," *Renew. Energy*, vol. 30, no. 6, pp. 835–854, 2005. [CrossRef]

12. M. M. Seedahmed *et al.*, "Optimal sizing of grid-connected photovoltaic system for a large commercial load in Saudi Arabia," *Alex. Eng. J.*, 2021. [CrossRef]
13. S. A. Memon, D. S. Upadhyay, and R. N. Patel, "Optimal configuration of solar and wind-based hybrid renewable energy system with and without energy storage including environmental and social criteria: A case study," *Journal of Energy Storage*, vol. 44, 103446, 2021. [CrossRef]
14. A. Abbassi, R. B. Mehrez, R. Abbassi, S. Saidi, S. Albdran, and M. Jemli, "Improved off-grid wind/photovoltaic/hybrid energy storage system based on new framework of Moth-Flame optimization algorithm," *Int. J. Energy Res.*, vol. 46, no. 5, pp. 6711–6729, 2022. [CrossRef]
15. E. A. Al-Ammar *et al.*, "Residential community load management based on optimal design of standalone HRES with model predictive control," *IEEE Access*, vol. 8, pp. 12542–12572, 2020. [CrossRef]
16. N. Dos Santos, G. O. Troiano, M. B. Carneiro, B. D. Bonatto, and P. F. Ribeiro, "Hydrogen storage evaluation feeding a residential load model with the use of Photovoltaic generation," *IEEE PES Innovative Smart Grid Technologies Conference-Latin America (ISGT Latin America)*, IEEE Publications, 2021, pp. 1–5. [CrossRef]
17. L. H. S. Santos, J. A. A. Silva, J. C. López, N. B. Arias, M. J. Rider, and L. C. P. Da Silva, "Integrated optimal sizing and dispatch strategy for microgrids using Homer pro," *IEEE PES Innovative Smart Grid Technologies Conference-Latin America (ISGT Latin America)*, IEEE Publications, 2021, pp. 1–5. [CrossRef]
18. J. O. Oladigbolu, M. A. M. Ramli, and Y. A. Al-Turki, "Feasibility study and comparative analysis of hybrid renewable power system for off-grid rural electrification in a typical remote village located in Nigeria," *IEEE Access*, vol. 8, pp. 171643–171663, 2020. [CrossRef]
19. L. Mbali, and O. Dzobo, "Design of an off-grid hybrid PV/diesel energy system with battery storage for electrification of a remote region: A case study of upper blink water community, South Africa," *IEEE AFRICON*, IEEE Publications, 2021, pp. 1–6. [CrossRef]
20. M. Purlu, S. Beyarslan, and B. E. Turkay, "Optimal design of hybrid grid-connected microgrid with renewable energy and storage in a rural area in Turkey by using Homer," 13th International Conference on Electrical and Electronics Engineering (ELECO), IEEE Publications, 2021, pp. 263–267. [CrossRef]
21. T. Adefarati, R. C. Bansal, and R. Naidoo, "Design and feasibility study of a biomass/diesel/PV/battery microgrid system for an off-grid application," The 9th Renewable Power Gener. Conference (RPG Dublin Online 2021), IET, 2021. [CrossRef]
22. "NASA surface meteorology and solar energy" [Online]. Available: http://www.nasa.gov.
23. IRENA, *Renewable Power Generation Costs in 2018*. Abu Dhabi: International Renewable Energy Agency, 2019.
24. National Renewable Energy Laboratory [Online]. Available: http://www.nrel.gov/international/tools/HOMER/homer.html.
25. E. Fiyatlari [Online]. Available: https://www.enerjiatlasi.com/elektrik-fiyatlari/.

TEPES
TURKISH JOURNAL OF
ELECTRICAL POWER
AND ENERGY SYSTEMS

TEPES, Vol. 2, Issue. 1, 85-93, 2022 DOI: 10.5152/tepes.2022.22009

RESEARCH ARTICLE

Analysis of Solid Insulating Materials Breakdown Voltages Under Different Voltage Types

Firat Akın[1], Oktay Arıkan[1], Cihat Çağdaş Uydur[2]

[1]Department of Electrical Engineering, Yıldız Technical University, İstanbul, Turkey
[2]Technical Science Vocational School, Trakya University, Edirne, Turkey

Cite this article as: F. Akin, O. Arikan and C. Cagdas Uydur, Analysis of solid insulating materials breakdown voltages under different voltage types. *Turk J Electr Power Energy Syst,* 2022; 2(1): 85-93.

ABSTRACT

The effectiveness of the insulation systems has great importance for the continuity of the power equipment. Due to operating conditions, solid insulating materials are subjected to different types of stresses. In this context, one of the factors affecting the breakdown performance is the type of the applied voltage. Since the breakdown strength of the materials determines their lifespan, the effect of the different voltage types must be considered for proper insulation design. For this reason, it is vital to investigate the breakdown performance of insulation materials under different voltage types. In this study, breakdown voltages of press-paper, polyethylene terephthalate and styrene–butadiene rubber/natural rubber under AC, positive DC(+), and negative DC(−) voltages were investigated. For the analysis of the breakdown points, the electric field analysis of the materials for the cylinder–cylinder electrode configuration was performed with COMSOL Multiphysics® software. As a result, it was determined that the electric field distortion increased in the triple junction regions and the potential breakdown points obtained by the simulation matched with seen in the experiments.

Index Terms—Breakdown voltage, electric field analysis, COMSOL multiphysics, solid insulating materials, permittivity

I. INTRODUCTION

Solid insulating materials are the primary elements of the insulation systems of most power equipment. In this context, the dielectric performance of solid insulating materials under different operating conditions should be examined in detail to ensure the continuity of power systems. The breakdown mechanism of solid materials is irreversible, unlike other materials. That is, once degradation occurs, they cannot revert to their former dielectric properties. Therefore, in order to use solid dielectrics efficiently, the mechanisms that can cause degradation should be well known [1,2].

Solid insulation materials are preferred for the insulation of both DC and AC equipment. In addition, the dielectric performances vary considerably under these voltages. Therefore, when examining the breakdown strength of solid insulation materials, different voltage types should be considered, and the conditions covering all the negativities that may occur during the operation of power systems should be investigated.

In a study, breakdown experiments were carried out on Teflon, quartz–silica, and glass–ceramic materials using AC, DC, and impulse voltages. It has been revealed that AC breakdown voltages have the lowest values in all materials and the highest breakdown voltage was reached when AC + DC combined voltage was applied. In addition, it was seen that the AC breakdown voltages of the materials were not affected by the DC pre-stress, while the DC breakdown voltages decreased in the case that DC pre-stress with opposite polarity was applied to the specimens [3]. In the study of Rajan et al., the breakdown voltage of oil-impregnated paper under AC and DC voltages was investigated. They determined that the breakdown performance was better in the experiments performed with DC voltage. Lastly, it was stated that the results are unpredictable when AC and DC voltages are combined [4]. In the studies realized by Grzybowski et al., breakdown voltages of Cross-linked Polyethylene (XLPE) and polyethylene terephthalate (PET) materials were investigated under dry and wet conditions. In this study, it was shown that DC breakdown voltage decreased significantly compared to the AC breakdown

Corresponding author: Cihat Çağdaş Uydur, ccagdasuydur@trakya.edu.tr

Received: February 7, 2022
Accepted: March 27, 2022

voltage under wet conditions compared to dry conditions [5-7]. In another study, the change in the breakdown performance of polymeric insulation materials as a result of thermal aging was investigated using AC, DC, and pulsed voltages [8]. Nagao et al. measured the breakdown strength of various insulating material variations formed with kraft paper and polypropylene laminations under AC, DC, and impulse voltages in liquid nitrogen. It has been found that the breakdown performance was affected by the lamination structures of the materials due to the changes in the electric field and charge behaviors [9]. In a study, the breakdown performance of the solid dielectric barriers inserted between the electrodes under non-uniform electric fields by experimental and simulation studies was investigated by Phloymuk. According to the measurement results, it has been seen that the AC breakdown voltage was lower than the DC breakdown voltage. In addition, it was emphasized that the critical pressure was 1.5 bar in the experiments carried out at different pressures. Below the critical pressure, the positive DC breakdown voltage was higher than the negative DC breakdown voltage, and the opposite case was seen at pressures above the critical value [10]. Illias et al. experimentally investigated partial discharges originating from spherical voids in solid insulating materials [11,12]. A similar research was also carried out by simulation studies and the correlation between simulation results and experiments was clearly seen. As a result, the partial discharges have been defined as a function depending on the temperature and the voltage type [13,14]. Yamada studied the breakdown mechanisms of dielectric elastomers under different applied waveforms (DC, AC, and pulse). It has been found that the breakdown strengths have the order of impulse > DC > AC. Also, the breakdown strengths under these waveforms decreased as the temperature increases. He attributed the lowest breakdown strength under AC voltage to the heating that occurs as a result of dielectric losses under AC voltage. Moreover, the study revealed that the number of laminations leads to an increase in breakdown strength [15]. In another study, DC and AC breakdown characteristics of polypropylene laminated paper as well as various Nomex and Kapton insulating materials were investigated in air and liquid nitrogen. The difference between the Weibull scale parameters of DC and AC breakdown voltages of materials was found as 1.12–1.72 times in air and 1.52–2.14 times in liquid nitrogen [16,17]. In the studies performed by Barouel et al., the breakdown strength of vegetable and mineral oils under AC and DC voltages was studied, and the analysis of dielectric performance of different oil mixtures was carried out for the specified voltages [18,19]. In one study, Huang explores the possibility of improving both the mechanical and degradation properties of insulating printing paper by adding an organic nanoadditive, taking into account four different concentrations of nanofibrillated cellulose (NFC) such as 0.5% by weight, 2.5% by weight, 5% by weight, and 10% by weight. The prepared samples were characterized by scanning electron microscopy, Fourier transform infrared spectroscopy, and X-ray diffraction. It has been found that the addition of 10 wt% NFC provides the best performance in terms of breakdown voltage, and the presspaper containing 10 wt% NFC had 19% and 21% higher AC and DC breakdown voltages than the reference material [20]. Furthermore, studies on the definition and classification of partial discharges were continued by examining them under different voltage types such as impulse voltages and damped voltages [21,22]. In this context, there are also simulative studies to examine the breakdown strength of insulating materials. In these studies, COMSOL Multiphysics® software was preferred [23,24].

Main Points

- Experimental studies have been carried out in the high-voltage laboratory.
- Breakdown voltages of different solid insulating materials were measured with DC+, DC−, and AC voltage types.
- Analysis of electric field distribution studies had been carried out using COMSOL Multiphysics® software.
- Breakdown points that occurred in test specimens had been detected.

In this research, an experimental study was carried out to analyze breakdown performances of solid insulating materials under different types of voltages. Test specimens of 60 × 60 mm^2 dimensions were created from solid insulation materials that were widely used in power systems, PET, presspaper, and a mixture of styrene–butadiene rubber/natural rubber (SBR/NR). As the test voltage, AC, positive DC(+), and negative DC(−) voltages were preferred. Experimental studies were made in Yıldız Technical University High Voltage Laboratory. Finally, an electric field analysis was performed in COMSOL Multiphysics® to explain and analyze the breakdown points seen in the experiment. From the results of the electric field analysis, the location where the breakdown occurred was evaluated.

II. TEST MATERIALS

To examine the effect of voltage type on different classes of insulating materials, PET from thermoplastic polyesters, SBR/NR blend from thermoset polymers, and presspaper, which is an organic insulating material, were used in this study.

Presspaper used in the experiments is fundamental element of oil-type transformer insulation. It is obtained by calendaring kraft paper, and it consists of sulphate–cellulose. Because of their high operating temperatures, resilience to various chemicals, and good dielectric qualities, PET films are commonly preferred in stator slots and interlayer insulations of high-voltage machines. As is known, it is common application to optimize the properties of rubber types by mixing them and use them in the form of blends. Another insulator used in this study is SBR/NR, which is a blend of rubbers. It is commonly used in cable insulation and dielectric matting. The samples of the materials are shown in Fig. 1.

The surface dimensions of the samples were determined as 60 mm × 60 mm with preliminary studies to prevent surface discharges. The specifications of the samples are given in Table 1.

III. EXPERIMENTAL STUDY

In this chapter, the laboratory conditions, the electrode system used in the experimental applications, and the experimental setup were introduced. In addition, the results of the breakdown voltage tests obtained from the experimental measurements are shared in a comparative manner depending on the material and voltage types.

Fig. 1. Test specimens (PET, presspaper, and SBR/NR).

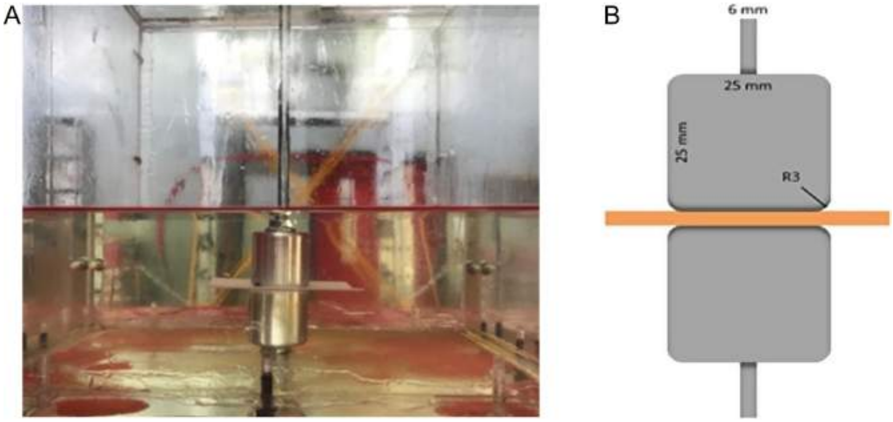

Fig. 2 (a) Electrode configuration and (b) dimensions.

A. Experimental Setup

Ambient conditions in laboratory during the experiments were 28 $\pm$ 2°C temperature, 41 $\pm$ 2% relative humidity, and 756.8 $\pm$ 5 mmHg pressure. Cylinder–cylinder aluminum electrode system was used in accordance with IEC60243:1 [25]. Details are shown in Fig. 2.

Fig. 2a shows the cylinder–cylinder electrode system in the laboratory, and Fig. 2b shows the dimensions of the electrode system in accordance with the IEC 60243:1 standard and its positioning on the insulating material.

For preventing surface discharges, electrodes and specimens were immersed in Nytro Lyra X mineral oil (BDV > 60 kV, $\varepsilon_r = 2.2$). The tests were repeated five times for each material, and 3 minutes was given between trials. The surfaces of all samples were cleaned with ethanol before the measurements. The scheme of the experimental setup is shown in Fig. 3.

To generate the test voltages, 100 kV, 5 kVA single phase, and 50 Hz frequency test transformer was used. DC voltages are obtained with a high-voltage diode. The test voltage was increased until breakdown occurs, and the breakdown voltages were measured with a resistive voltage divider (1000:1 ratio) for DC measurements and capacitive voltage divider (1000:1 ratio) for AC measurements.

B. EXPERIMENTAL RESULTS

In this section, the measurement results according to the specified voltage types are shared for each insulation material. In order to evaluate the results obtained by repeated tests, box-plot notation, which is a statistical presentation form, was preferred. Breakdown voltages are demonstrated as the average value for DC voltages and the peak values for AC voltages.

Fig. 4 demonstrates the breakdown voltages of PET. In the tests performed under AC voltage, the minimum and maximum breakdown voltages of five samples were 26.96 kV and 30.03 kV. In this case, the average breakdown voltage was calculated as 28.37 kV. Under positive DC, the breakdown voltages were between 40.3 kV and 54.2 kV with an average of 44.74 kV. Finally, PET failed at the voltages between 43.81 kV and 50.5 kV under negative DC, while the average value was 47.72 kV. From the results, effectiveness of AC voltage was found significantly higher than DC voltage types for PET.

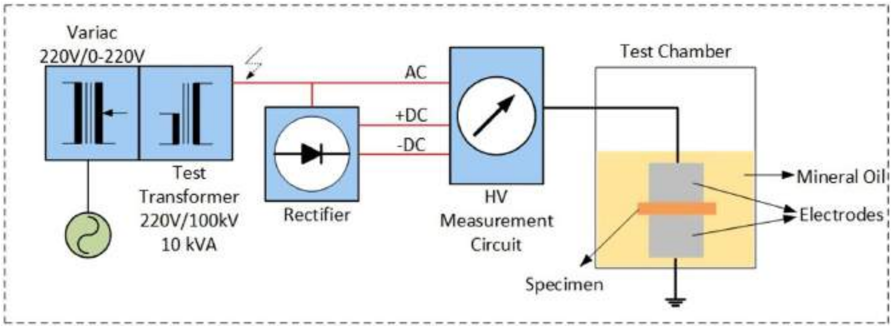

Fig. 3. Scheme of experimental setup.

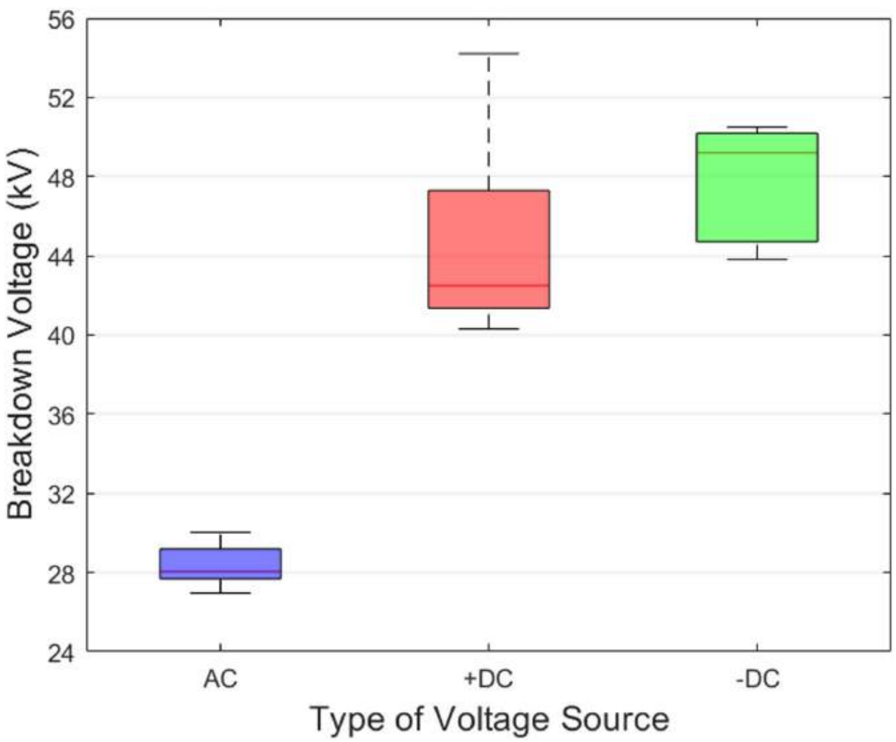

Fig. 4. Box plot of breakdown voltages—PET.

When the breakdown voltage values for presspaper shown in Fig. 5 are examined, it was seen that AC voltage punctured the material at around 50% lower voltage values, according to DC voltage types. It has been found that positive and negative DC voltages provide very close results. The breakdown voltages measured with different voltage types had the values in the ranges of 6.08–8.38 kV, 8.33–12.83 kV, 9–13.56 kV for AC, positive DC, and negative DC, respectively. The average breakdown voltage for AC was 7.26 kV, while these values were 10.85 kV and 10.95 kV for positive and negative DC voltages.

In the case of SBR/NR, it was determined that the effectiveness of AC voltage was greater than DC as with the other materials. Box graph of breakdown voltages for SBR/NR is shared in Fig. 6. As can be seen, the breakdown voltages obtained with AC voltage varied between 47.37 kV and 64.86 kV. The average of these values was 57.75 kV. Also, the breakdown voltages of the material under positive DC voltage varied between 56.87 kV and 62.81 kV with an average of 60.83 kV. When negative DC voltage was applied to the material, the minimum and maximum breakdown voltages of five samples were 58.94 kV and 66 kV. The average of these values was 62.32 kV.

IV. INVESTIGATION ON BREAKDOWN POINTS OF THE MATERIALS

In this section, electric field analyses of the materials are performed with electrostatic interface under the AC/DC module of COSMOL Multiphysics® software to investigate the potential breakdown points.

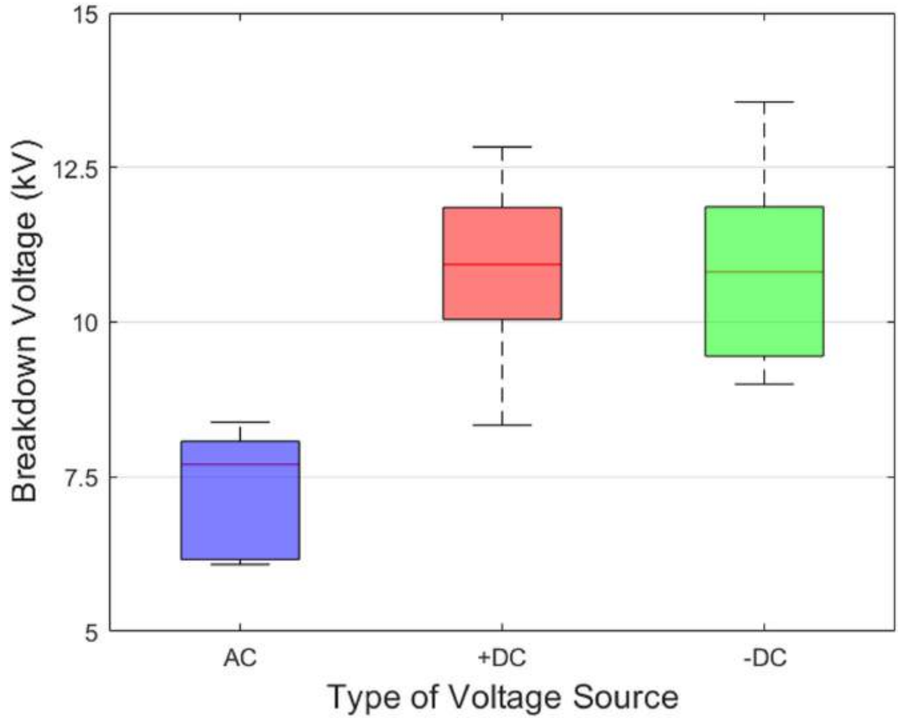

Fig. 5. Box plot of breakdown voltages—presspaper.

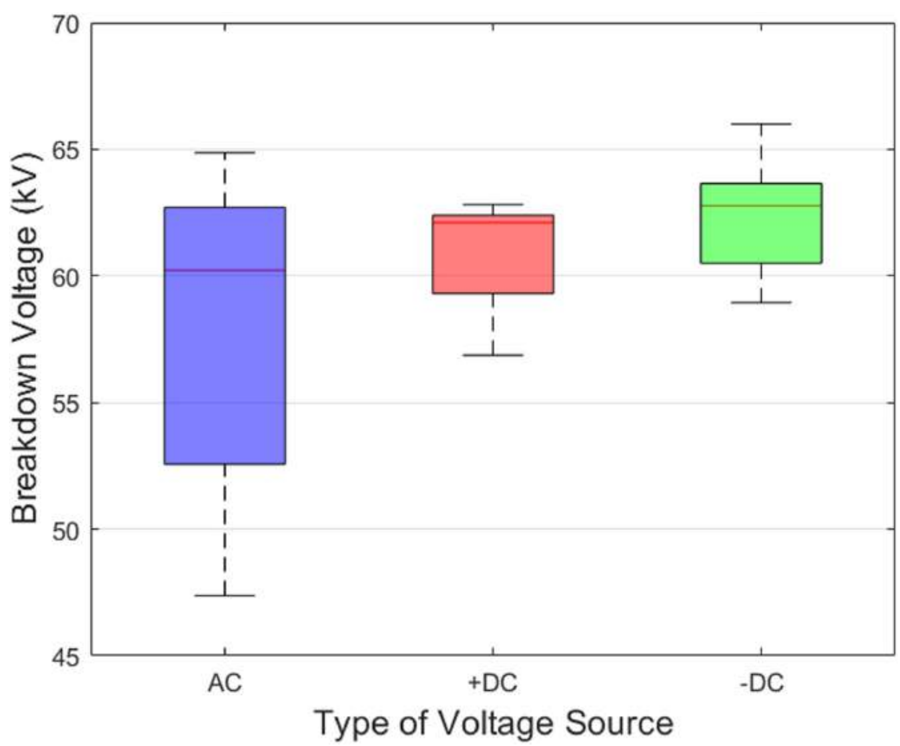

Fig. 6. Box plot of breakdown voltages—SBR/NR.

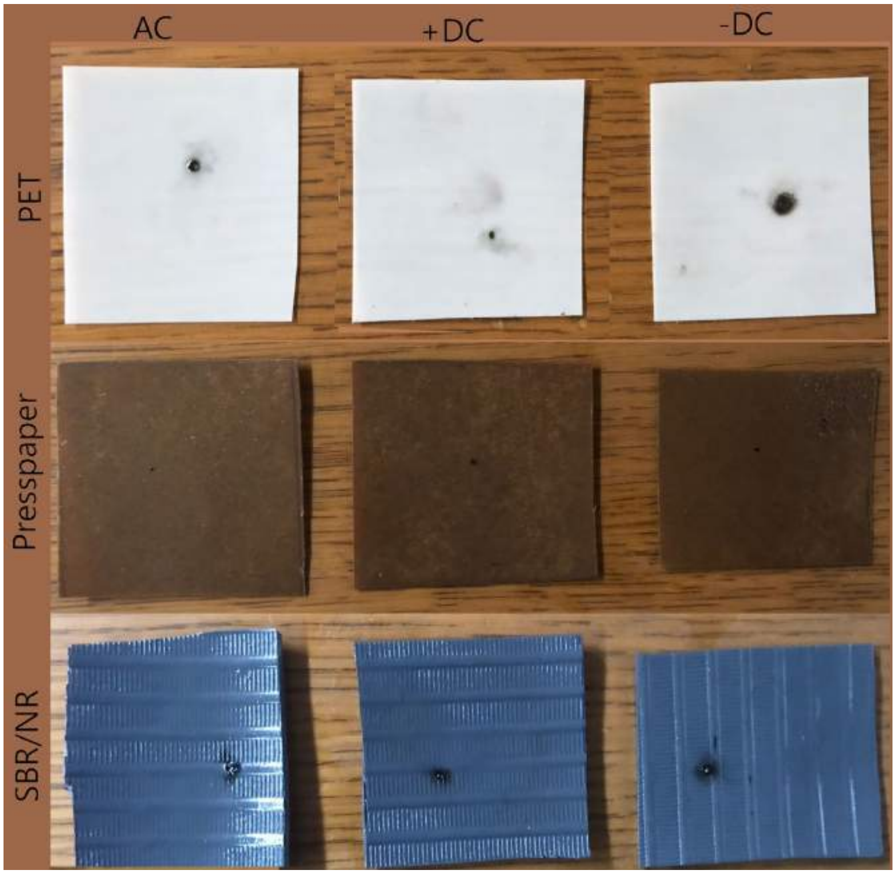

Fig. 7. Breakdown samples of the materials.

As can be seen in Fig. 7, the breakdowns occurred at the electrode boundary areas for all voltage types. For examining this case, the average AC breakdown voltages of the insulating materials are applied during the simulation study, and the electric field densities along their upper surfaces are calculated. The governing equations applied by COMSOL Multiphysics® to solve the defined electrostatic problem are as follows [26]:

$$\nabla \times E = 0 \tag{1}$$

The above formula shows that the electric field is irrotational.

$$\nabla . D = \rho \tag{2}$$

$$-\nabla \mathrm{V} = E \tag{3}$$

$$D = \varepsilon_r \varepsilon_0 E \tag{4}$$

By substituting the electric field and displacement expressions specified in (3) and (4) into (2), (5) is obtained, which shows the relationship between the electrostatic potential and the space charge density.

$$-\nabla .(\varepsilon_r \varepsilon_0 \nabla \mathrm{V}) = \rho \tag{5}$$

where E is the electric field density, D is the electric displacement, ρ is space charge density, ε_0 is the permittivity of free space, and ε_r is the relative permittivity of insulating material.

A simulation model for SBR/NR and the triple area region where the electric field is concentrated are shown in Fig. 8.

As a result of the simulation, it was found that the breakdown occurred at a distance of 20 $\pm$ 2 mm from the one edge of the insulating materials, and the breakdown strengths of presspaper, PET, and SBR/NR were 23.59 kV/mm, 114.98 kV/mm, and 41.04 kV/mm, respectively.

The change in the electric field magnitude along the upper surface of the insulating materials is shown in Fig. 9. The electric field density reaches its highest value at the boundary points where the corners of the electrodes begin to round. When the failed samples are examined, the breakdown points and the possible breakdown points obtained in the simulation study match with each other.

V. DISCUSSION

Average breakdown voltages of the materials according to voltage types are given in Fig. 10. The lowest breakdown voltages for all insulation materials were obtained in the experiments with AC voltage. For PET, the average breakdown voltages under positive DC and negative DC voltages were 57.7% and 68.2% higher than AC, respectively. The average DC breakdown voltages of presspaper were 49.44% and 51% higher than AC breakdown voltages for positive and negative polarities, respectively. The change in the DC breakdown voltage

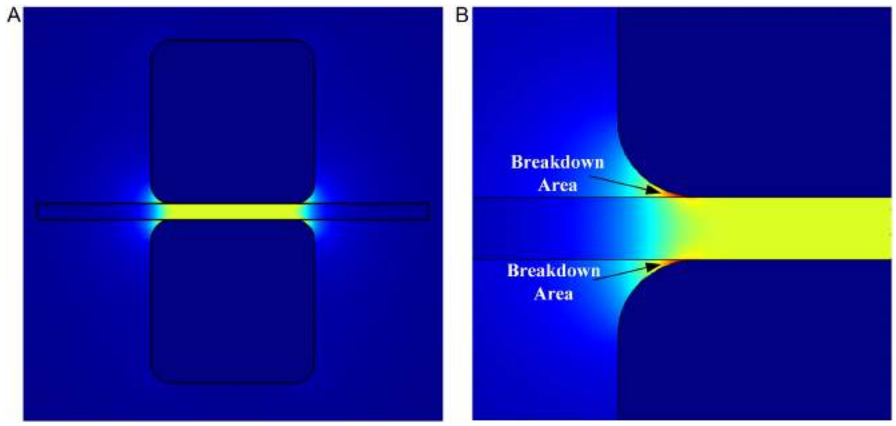

Fig. 8. (a) Electrode system and (b) breakdown areas in simulation model.

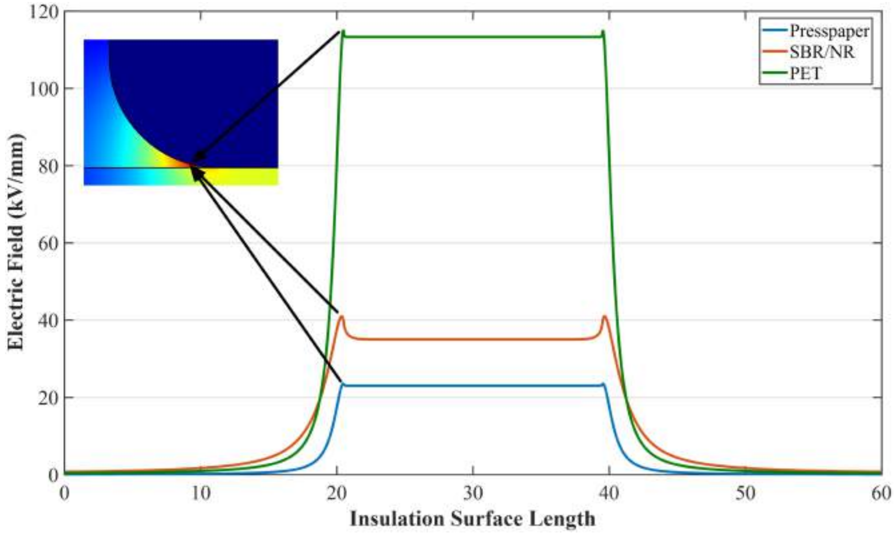

Fig. 9. Variation of electric field density along the electrode–material contact surface.

due to polarity was less for presspaper, unlike other materials. The average breakdown voltage of SBR/NR was 57.75 kV under AC voltage. It increased by 5.33% to 60.83 kV under positive DC voltage and increased by 7.91% to 62.32 kV under negative DC voltage. The breakdown performance of SBR/NR was less affected by the applied voltage type than the other materials. The fact that AC breakdown voltages have lower values in all materials can be explained by two phenomena. These are the dielectric losses that occur in the insulating material exposed to AC voltage and the difference of space charge behavior at AC and DC voltages. A significant heating occurs in the material due to dielectric losses, and it affects the dielectric performance of the insulating material by causing them to fail at lower voltage levels [6].

The structure and accumulation points of space charges become different depending on applied voltage type. When AC voltage is applied, space charges accumulate around the electrodes and have a heterogeneous structure. In the case of DC test voltage, there is a homogeneous structure, and the accumulation point of the charges is the middle of the insulation bulk. Hetero-charges accumulation in the vicinity of the electrodes causes the distortion of the electric field dramatically in these regions. In addition, when charges accumulate in the vicinity of the electrode, smaller transport distance for charges is required compared to DC voltages, where the charge accumulation is in the middle of the insulation bulk. Due to all these facts, breakdown occurs at lower voltage levels, as more severe electric fields will occur under AC voltages [27-29].

While examining the weakest points of the materials in COSMOL Multiphysics®, it is determined that the mismatch between the permittivities of the test specimens and the surrounding material (in this case mineral oil) at the triple contact area causes an increase in the electric field magnitude. Electric field density along the upper surface reaches its maximum value at that area. In addition, as the relative permittivity of the insulating material increases, the difference between the electric field densities at triple contact point and the bottom of the high-voltage electrode increases. While the electric field intensity at the triple contact point of SBR/NR was 17.15%

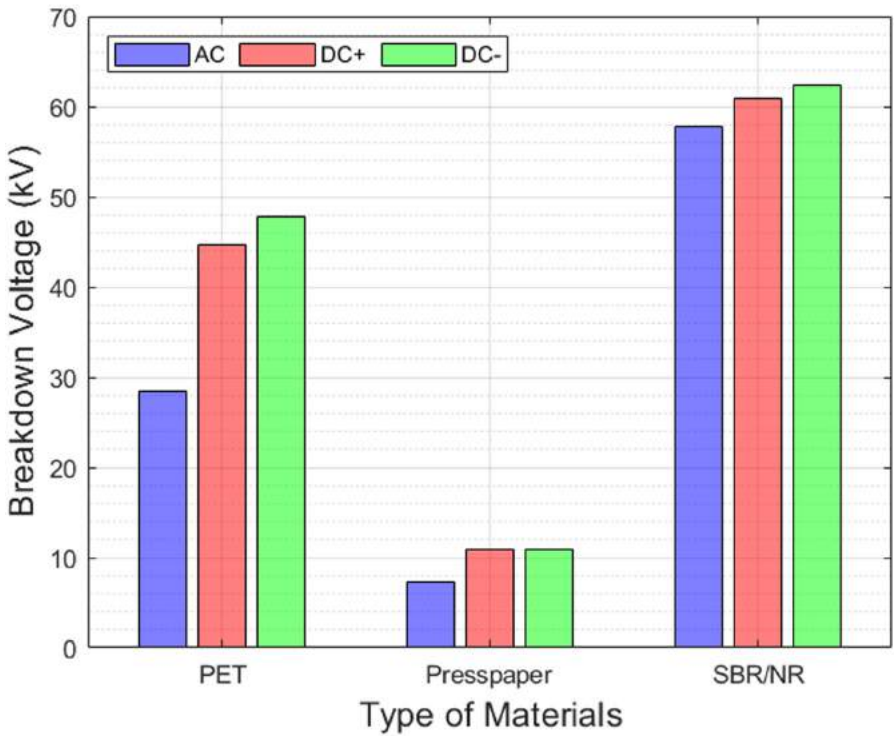

Fig. 10. Average breakdown voltages of materials.

TABLE I
SPECIFICATIONS OF THE SAMPLES

Materials	Thickness	Surface Dimensions (mm × mm)	Relative Permittivity	Tan δ	Max. Operating Temperature (°C)	Density (g/cm³)
PET	0.3	60 × 60	3.2	2×10^{-3}	110	1.39
SBR/NR	2.5	60 × 60	4.5	4×10^{-2}	70	1.45
Presspaper	0.4	60 × 60	3.5	6×10^{-3}	90	1.0-1.2

PET, polyethylene terephthalate; SBR/NR, styrene–butadiene rubber/natural rubber.

higher than the electric field density along the lower surface of the electrode, this difference was 2.3% for presspaper and 1.4% for PET.

VI. CONCLUSIONS

The main subject of this research was the breakdown performances of PET, presspaper, and SBR/NR under AC, positive DC, and negative DC voltages. Also, an Finite Element Method (FEM)-based simulation study was performed in COSMOL Multiphysics for the analysis of the breakdown points obtained in experiments.

During the experimental study, it was found that the breakdown voltages of all materials were in the order of AC < +DC < −DC. In addition, the increase of the average breakdown voltages in the case of negative DC voltage was 50% and 68% for presspaper and PET compared to AC voltage, while the difference in the breakdown voltage of SBR/NR was around 8% for the same comparison. The specified amounts of increases vary according to their physical and chemical structures. The change in breakdown performance between AC and DC voltages was caused by differences in space charge behavior and heating due to dielectric loss. Insulating materials used in power systems can be stressed by different types of voltages. Therefore, understanding the effects of different voltage types on the dielectric performance of insulating materials is vital for power equipment continuity.

In the simulation study, it was determined that the electric field distortion increased in the triple junction areas. Therefore, breakdown occurred in these regions of the samples in accordance with the experimental study. In addition, it has been revealed that the electric field strengths at the electrode boundaries increase in direct proportion to the permittivities of the insulating materials.

The type and rate rise of the test voltage, conductor–insulator geometries, age of the insulating material, permittivity mismatch, and ambient conditions are the primary factors affecting the breakdown performance. For this reason, breakdown performances of the insulating materials should be analyzed by performing simulation and experimental studies including the mentioned factors, and the design of the equipment used in power systems should be developed with the help of the information obtained from the analysis results. In this manner, the reliability and sustainability of the equipment can be ensured by minimizing the failures that occur during the operation of the power systems.

Peer-review: Externally peer-reviewed.

Declaration of Interests: The authors have no conflict of interest to declare.

Funding: Scientific Research Project Coordinator of Yıldız TechnicalUniversity supported this research study with the project number FYL-2021-4166.

REFERENCES

1. N. H. Malik, A. A. Al-Arainy, and M. I. Qureshi, *Electrical Insulation in Power Systems*. Boca Raton: CRC Press, 2018.
2. R. Arora, and W. Mosch, *High Voltage and Electrical Insulation Engineering*. IEEE Press: Piscataway, New Jersey 08854, USA, 2011.
3. A. S. Pillai, and R. Hackam, "Effect of DC pre-stress on AC and DC surface flashover of solid insulators in vacuum," *IEEE Trans. Electr. Insul.*, vol. EI–18, no. 3, pp. 292–300, 1983. [CrossRef]
4. J. S. Sajan, K. Dwarakanath and S. N. Moorching, "Comparative evaluation of dielectric strength of paper-oil insulation under ac, dc, combined, composite ac/dc and impulse voltages," *1998 Annual Report Conference on Electrical Insulation and Dielectric Phenomena* (Cat. No.98CH36257), 1998, pp. 236–239 vol. 1. [CrossRef]
5. S. Grzybowski, and J. Fan, "Electrical breakdown characteristics of the XLPE cables under AC, DC, and pulsating voltages," *Proc. IEEE Int. Conf. Prop. Appl. Dielectr. Mater.*, vol. 1, pp. 389–393, 1997.
6. S. Grzybowski, E. A. Feilat, P. Knight, and L. Doriott, "Breakdown voltage behavior of PET thermoplastics at DC and AC voltages," *Conf. Proc. - IEEE SOUTHEASTCON*, vol. 1999, pp. 284–287, 1999.
7. Y. Wang, J. Li, Y. Wang, and S. Grzybowski, "Electrical breakdown properties of oil-paper insulation under AC-DC combined voltages *Proc*," *Proc. 2010 IEEE Int. Power Modul. High Volt. Conf. IPMHVC*, vol. 2010, pp. 115–118, 2010.
8. W. Yin, and D. Schweickart, "Dielectric breakdown of polymeric insulation films under AC, DC and pulsed voltages," *2009 IEEE Electr. Insul. Conf. EIC 2009*, vol. 2009, pp. 292–296, , 2009.
9. M. Nagao *et al.*, "Dielectric breakdown mechanism of polypropylene laminated paper in liquid nitrogen," *Annu. Rep. - Conf. Electr. Insul. Dielectr, Phenomena, CEIDP*, pp. 419–422, 2011.
10. N. Phloymuk, A. Pruksanubal, and N. Tanthanuch, "DC breakdown voltage of solid dielectric barrier under non-uniform electric field," *Annu. Rep. - Conf. Electr. Insul. Dielectr, Phenomena, CEIDP*, pp. 834–837, 2013.
11. H. A. Illias, G. Chen, and P. L. Lewin, "Partial discharge measurements for spherical cavities within solid dielectric materials under different stress and cavity conditions," *Annu. Rep. - Conf. Electr. Insul. Dielectr, Phenomena, CEIDP*, vol. 2, pp. 388–391, 2009.
12. H. A. Illias, G. Chen, and P. L. Lewin, "Modelling of partial discharge activity in different spherical cavity sizes and locations within a dielectric insulation material," *Proc. IEEE Int. Conf. Prop. Appl. Dielectr. Mater.*, pp. 485–488, 2009.
13. H. A. Illias, G. Chen, and P. L. Lewin, "Modelling of partial discharge behaviour in a spherical cavity within a solid dielectric material as a function of temperature," *Annu. Rep. - Conf. Electr. Insul. Dielectr, Phenomena, CEIDP*, pp. 1–4, 2010.
14. H. Illias, G. Chen, and P. L. Lewin, "Partial discharge behavior within a spherical cavity in a solid dielectric material as a function of frequency and amplitude of the applied voltage," *IEEE Trans. Dielectr. Electr. Insul.*, vol. 18, no. 2, pp. 432–443, 2011. [CrossRef]
15. M. Yamada, Y. Murakami, T. Kawashima, and M. Nagao, "Electrical breakdown of dielectric elastomer and its lamination effect," *2014 IEEE Conf. Electr. Insul. Dielectr. Phenomena, CEIDP*, vol. 2014, pp. 126–129, 2014.
16. W.-G. Li *et al.*, "Comparison between the DC and AC breakdown characteristics of dielectric sheets in liquid nitrogen," *IEEE Trans. Appl. Supercond.*, vol. 24, no. 6, pp. 1–6, 2014. [CrossRef]
17. M. Ritamaki, I. Rytoluoto, M. Niittymaki, K. Lahti, and M. Karttunen, "Differences in AC and DC large-area breakdown behavior of polymer thin films," *Proc. 2016 IEEE Int. Conf. Dielectr. ICD 2016*, vol. 2, pp. 1011–1014, 2016.
18. A. Beroual, H. B. H. Sitorus, R. Setiabudy, and S. Bismo, "Comparative study of AC and DC breakdown voltages in Jatropha methyl ester oil, mineral oil, and their mixtures," *IEEE Trans. Dielect. Electr. Insul.*, vol. 25, no. 5, pp. 1831–1836, 2018. [CrossRef]
19. A. Beroual, U. Khaled, P. S. M. Noah, and H. Sitorus, "Comparative study of breakdown voltage of mineral, synthetic and natural oils and based mineral oil mixtures under AC and DC voltages," *Energies*, vol. 10, no. 4, pp. 1–17, 2017. [CrossRef]
20. J. Huang, Y. Zhou, L. Dong, Z. Zhou, and X. Zeng, "Enhancing insulating performances of presspaper by introduction of nanofibrillated cellulose," *Energies*, vol. 10, no. 5, p. 681, 2017. [CrossRef]
21. H. Illias, J. Low Tau, A. H. A. Bakar, and H. Mokhlis, "Partial discharge simulation under various applied voltage waveforms," *PECon 2012 - 2012 IEEE Int. Conf. Power Energy*, pp. 967–972, 2012.
22. H. Illias, T. S. Yuan, A. H. A. Bakar, H. Mokhlis, G. Chen, and P. L. Lewin, "Partial discharge patterns in high voltage insulation," *PECon 2012 - 2012 IEEE Int. Conf. Power Energy*, pp. 750–755, 2012.
23. M. S. Kamarudin, N. H. Radzi, A. Ponniran, and R. Abd-Rahman, "Simulation of electric field properties for air breakdown using COMSOL multiphysics," In 4th IET Clean Energy and Technology Conference (CEAT 2016), 2016, pp. 1–5.
24. S. Nedphokaew, S. Pukjaroon, and M. Boonthienthong, "Analysis of electric field values in 24 kV high voltage power cable with Program for Finding Partial Discharge Values," In International Conference on Power, Energy and Innovations (ICPEI), vol. 2019, 2019, pp. 110–113.
25. Electric Strength of Insulating Materials - Test Methods - Part 1: Tests at Power Frequencies, IEC standard 60243-1, 2013.
26. "Comsol multiphysics," *An Introduction to the Theory of Electrostatics*.
27. S. Li, Y. Zhu, D. Min, and G. Chen, "Space charge modulated electrical breakdown," *Sci. Rep.*, vol. 6, pp. 32588, 2016. [CrossRef]
28. B. Huang, M. Hao, J. Hao, J. Fu, Q. Wang, and G. Chen, "Space charge characteristics in oil and oil-impregnated pressboard and electric field distortion after polarity reversal," *IEEE Trans. Dielect. Electr. Insul.*, vol. 23, no. 2, pp. 881–891, 2016. [CrossRef]
29. G. Chen, C. Zhou, S. Li, and L. Zhong, "Space charge and its role in electric breakdown of solid insulation," In IEEE International Power Modulator and High Voltage Conference (IPMHVC), 2016, pp. 120–127.

cigre Turkey

TEPES
TURKISH JOURNAL OF
ELECTRICAL POWER
AND ENERGY SYSTEMS

TEPES, Vol. 2, Issue. 1, 94-102, 2022 **DOI:** 10.5152/tepes.2021.21023

REVIEW

Potential of Eco-Friendly Gases to Substitute SF_6 for Electrical HV Applications as Insulating Medium: A Review

Touqeer Ahmad Raza[1,2], Muhammad Kamran[1], Muhammad Umar Khallidoon[3], Majid Niaz Akhtar[4]

[1]Department of Electrical Engineering, University of Engineering and Technology, Lahore, Pakistan
[2]Department of Electrical Engineering, Muhammad Nawaz Shareef University of Engineering and Technology, Multan, Pakistan
[3]Department of Mechanical Engineering, Muhammad Nawaz Shareef University of Engineering and Technology, Multan, Pakistan
[4]Department of Physics, Muhammad Nawaz Shareef University of Engineering and Technology, Multan, Pakistan

Cite this article as: T. Ahmad Raza, M. Kamran, M. Umar Khallidoon & M. Niaz Akhtar. Potential of eco-friendly gases to substitute SF_6 for electrical HV applications as insulating medium: A review. *Turk J Electr Power Energy Syst,* 2022; 2(1): 94-102.

ABSTRACT

Compressed gas is an essential ingredient for high-voltage (HV) applications, especially as an insulating medium. Sulfur hexafluoride (SF_6) gas due to its excellent insulating features is being preferred for decades and is widely utilized in applications such as gas-insulated switchgear, gas-insulated bus bars, circuit-breakers (CB), etc. But its global warming potential has been reported at the utmost harmful level. Many environmental anomalies have been produced by greenhouse gases, the reason why this problem has got extraordinary consideration, and there is an emergent need to introduce some eco-friendly substitute for SF_6. The research was started almost 4 decades ago to find a replacement for SF_6; however, progress in recent years is much better than earlier. Now, many alternatives have been searched out, and tests are being performed to find the best of them. In this study, the progress of some eco-friendly gases such as natural gases, trifluoroiodomethane, dichlorodifluoromethane, tetrafluoroethane, perfluoroketones, and heptafluoroisobutyronitrile has been summarized, keeping in view the basic physical properties and electrical insulating features. Decomposed by-products and boiling point were also discussed in detail, and the conclusion deduced that perfluoroketone and heptafluoroisobutyronitrile, with mixture of natural gases, show much better potential to replace SF_6 in many of the HV applications; later one has a bit upper edge.

Index Terms—Boiling point, circuit breakers, decomposed by-products, dielectric strength, gas-insulated switchgear, global warming potential

I. INTRODUCTION

There is a certain reason for increased usage of sulfur hexafluoride (SF_6) for years because of some limitations of air and oil such as more space required for the technical development of higher voltage range [1]. Air is a mixture of low electronegative gases and so its breakdown strength is very low, and to obtain a higher voltage range, it requires a lot of space. The maintenance of oil is poor, and also, it is a fire hazard. So, SF_6 gas is being considered as the best insulating medium because it requires less maintenance and is very safe to operate [2].

The main feature of SF_6 is its dielectric breakdown strength that is almost three times more than that of air, which is a strong electronegative gas. Space between electrodes is decreased due to its higher breakdown strength, resulting in smaller equipment [1, 2]. Another feature of SF_6 is its arc-quenching capability with excellent dielectric recovery strength, as its molecules reform very quickly after an arc or electrical discharge [3]. It also exhibits good heat transfer and thermal interrupting properties. Some other important properties of SF_6 were as follows: it is a non-toxic [4], non-flammable, colorless, and odorless gas and is chemically and thermally very stable.

But, the two significant issues related to SF_6 utilization in electrical equipment are its very high global warming potential and its bit higher liquefaction temperature.

First, global warming potential of SF_6 is more than 23 000, which can sustain over 100 years, and Kyoto Protocol identified SF_6 as one of the six major greenhouse gases [5, 6], in which the harmful level indicates that SF_6 badly affects the environment. SF_6 was labeled as regulated gas at third Framework Convention on Climate Change [7],

Corresponding author: Majid Niaz Akhtar, majidniazakhtar@mnsuet.edu.pk; majidniazakhtar@gmail.com

Received: August 1, 2021
Accepted: October 26, 2021
Available online: November 18, 2021

apart from this, Paris (France) Agreement 2016 also demands zero emission of greenhouse gases in later half of the century [8]. Its liquefaction temperature is also bit higher, relative to some natural gases, which is −64°C at 0.1 MPa [9]. SF_6 also has some other adverse properties like corrosion and toxic by-products formation resulting from electrical discharges. At the time, China is the leading country in emission of SF_6, and 70% of it comes from electrical equipment, followed by semiconductor manufacturing, magnesium production, and SF_6 preparation, each contributing around 10% of the remaining [10]. The leakage rate of SF_6 is very low, but debugging, recycling of SF_6, normal leakage and maintenance of SF_6-insulated switchgears, circuit-breaker (CB), etc. contribute to emission in atmosphere. More advanced detectors for leakage should be adopted to reduce SF_6 gas emission [11], and campaign should also be initiated to endorse recycling processes. But still, this will not be enough to eliminate greenhouse effect and toxic decomposed by-products. SF_6 gas has been utilized up to the range of 800 kV because there were no alternatives available with the same insulation and quenching properties, the main features of insulating medium. But now, there are many alternatives that show much potential for replacement. Some review articles have also been published in recent years in which some useful comparison between available options has been made. For example, an overview of green gas for the application of switchgear, in comparison with SF_6, was published [12]; however, the article did not consider other potential options. Similarly, some other articles [13, 14] have also reviewed the potential replacement but either covered very few options or missed some properties to discuss. So, in this article, efforts have been made to include every potential option of replacement with discussion on most concerned features.

II. ECO-FRIENDLY SUBSTITUE GASES

Eco-friendly substitute gases of SF_6 must have safety and environmental needs that should be fulfilled, that is, they should be non-toxic and non-flammable, but the two major features of being eco-friendly which cannot be compromised are low global warming potential (GWP) and zero ozone depletion potential.

In addition, some other features needed for usage in electrical HV equipment are:

i. excellent dielectric strength (high withstand and breakdown voltage level);
ii. excellent arc-quenching capability with fast dielectric recovery;
iii. low boiling point with a high cooling capacity;
iv. high heat dissipation;
v. should be chemically and thermally stable;
vi. compatible with the material of circuit breaker, transmission line, switchgear, and design compactness.

Among natural gases, nitrogen (N_2) and carbon dioxide (CO_2) being easily available, non-toxic, non-combustive, and with stable physicochemical properties made them the first choice of consideration as alternatives for SF_6, almost 4 decades ago. N_2, one of the most stable and inert gas, exhibits zero GWP [15], while GWP of CO_2 is taken as one, which makes both of them eco-friendly.

Another compound named trifluoroiodomethane having formula CF_3I is under consideration. It is an odorless and colorless gas with GWP only around 0.5 and lifetime around 2 days. Its ozone depletion potential is almost zero, which is another encouraging feature. CF_3I has some other useful potentials such as being used in semiconductor etching and foaming agents, etc. National Fire Protection Association authenticated CF_3I as a fire extinguishing agent [16] and as an optimal alternative for Halon.

($C_nF_{2n}O$) is the generic formula for fluoroketones which have been used as fire extinguishers for the last one decade and so. C_6F-ketone has dielectric strength around 1.7 times of SF_6 showing an excellent insulating capability [17]. Its toxicity level is also low, and more importantly, it has GWP level of around 1 with an atmospheric lifetime of only a week. C_4-PFK and C_5-PFK are other compounds from the same family with lower molecular weight and lower boiling point, and they exhibit almost equivalent dielectric strength as C_6F-ketone [18].

Dichlorodifluoromethane (R_{12}) and tetrafluoroethane (R_{134}) have recently been introduced as alternatives to SF_6, exhibiting relevant features, such as lower GWP with less atmospheric lifetime and good self-recoverability [16, 19, 20].

Heptafluoroisobutyronitrile is a compound from fluoronitrile family with formula (C_4F_7N), which is commercially accessible with the name 3M™ Novec™ 4710 dielectric fluid. The fluid got attention because its GWP is almost 10 times lower than that of SF_6, which is around 2100, with dielectric strength almost twice that of SF_6 at atmospheric pressure [17]. It also has high thermal transfer capability, and its toxicity level is quite low.

A. Basic Physical Properties

Basic physical properties are important in a sense because these determine the arc-quenching capability and dielectric strength. Relations are very complex, but still, properties are helpful to assess the potential of insulating medium. Studies of basic physical properties with comparison have been carried out that primarily include thermal and electrical conductivities. Temperature dependence of electrical conductivity is almost similar for most of the alternative gases [21], as shown in Fig. 1.

The electrical conductivity of most gases start increasing from 7000 K, but SF_6 and CF_3I start a bit earlier around 5000 K. It is due to the presence of sulfur and iodine, respectively, which have lower ionization energies. Increase is almost steady till 24 000 K. Unlike electrical conductivity, thermal conductivity behavior is much different and depends strongly on the nature of the gas. Typical characteristics are shown in Fig. 2, which clearly reveal that there are some peaks at lower temperature and some at higher temperature [22, 23].

Peaks at a lower temperature are associated with dissociation, and higher temperature peaks are due to ionization. SF_6, CF_3I, and their mixture exhibit many dissociation peaks due to successive dissociation reactions. As far as ionization peak is concerned, SF_6 and its mixture have peaked around 17 000 K almost 2000 K higher than other gases. This is due to the presence of fluorine that has higher ionization energy. In recent years, mixtures such as SF_6/Cu [20], CO_2/Cu

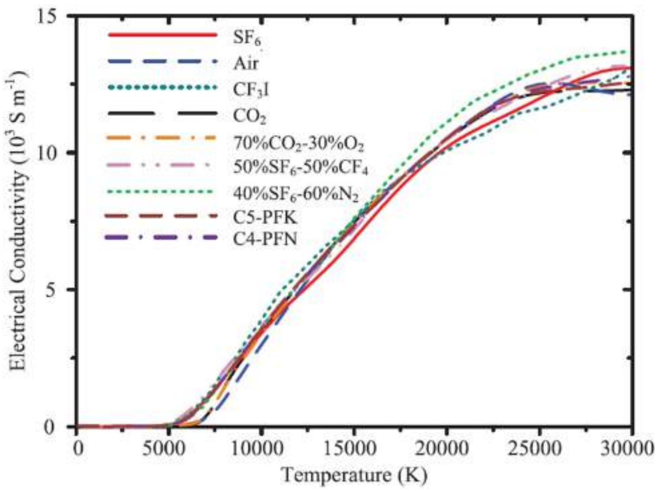

Fig. 1. Electrical conductivity of gases vs. temperature [21].

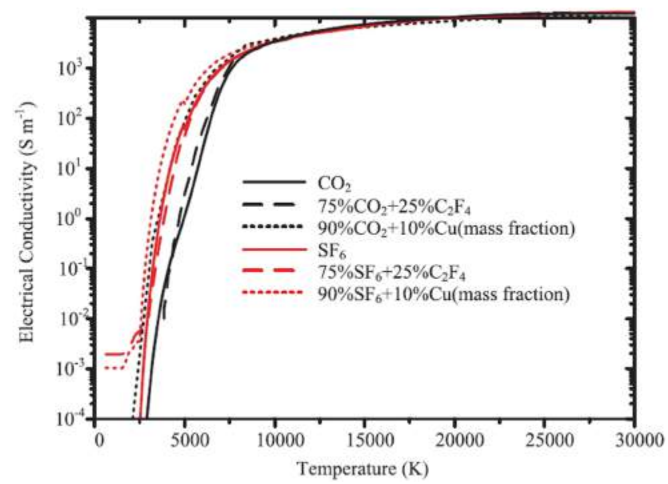

Fig. 3. Thermophysical properties of mixture (electrical conductivity) [26].

[24, 25], and air-CO_2-SF_6/polytetrafluoroethylene (PTFE) have been studied for thermophysical properties [26, 27]. Some of the results are shown in Fig. 3 and 4.

It is obvious from the figures that low ionization energy of metal improves electrical conductivity and makes it to start at lower temperature and rises with higher slope. But, there was no significant change in thermal conductivity; however, PTFE addition increases thermal conductivity and also helps to increase pressure in arc-quenching chamber as well, which boosts the thermal cooling capability of the medium. It was also concluded that the addition of PTFE in CO_2 has more effect as compared to addition of SF_6 for thermal conductivity and that the addition of Cu in CO_2 has a significant change in electrical conductivity at lower temperature regions as compared to SF_6.

Ionization potential of gas is another important factor to understand collision behavior during the breakdown process. Table I gives the comparison of ionization potential of gases, which reveals SF_6 has the highest ionization potential. SF_6 can easily attach to low-energy electrons and hence reduces free electron density owing to good dielectric strength. CF_4, C_3F_8, C_2F_6, and CO_2 also have some reasonable ionization potential.

B. Dielectric Strength

At early stage, when research was started to find the replacement for SF_6, natural gases or mixed gases were experimented, and it was found that the dielectric strength of mixed gases with SF_6 is slightly better than that of pure gases [28-30]. Generally, electronegative gases exhibit good dielectric strength but have high boiling point. In contrast, non-electronegatie gases such as CO_2 and N_2 have low boiling point and low dielectric strength, some fraction of SF_6 (i.e. around 0.4–0.45) [15]. To use natural gases, more volume or high pressure is required to meet the dielectric strength which leads to a significant increase in size and cost, which is undesirable

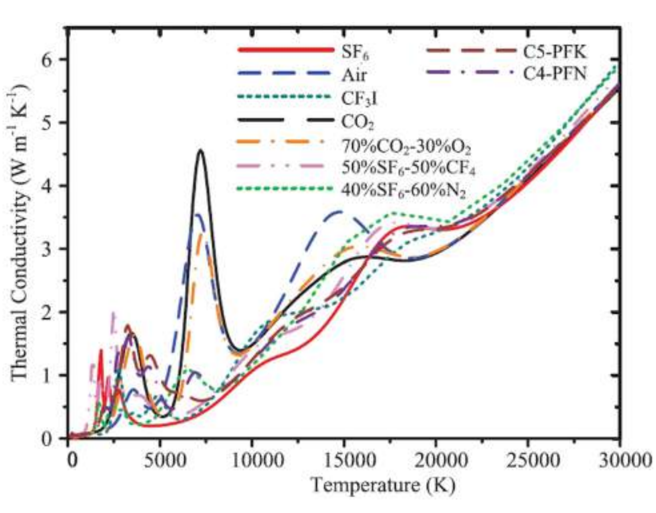

Fig. 2. Thermal conductivity of gases vs. temperature [22].

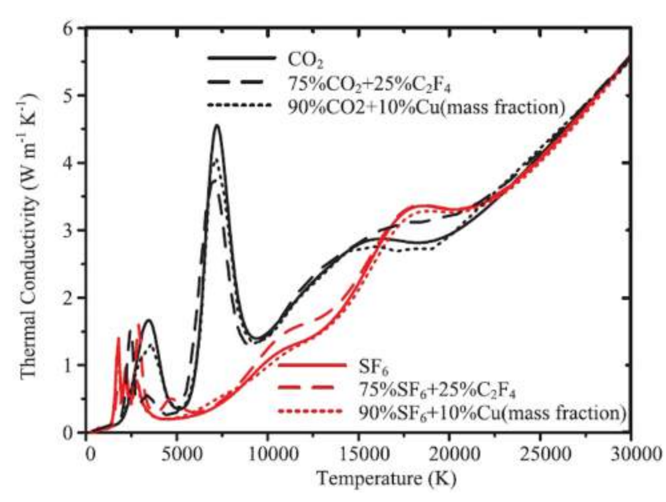

Fig. 4. Thermophysical properties of mixture (thermal conductivity) [26].

for design consideration. Table I summarizes the comparison among pure natural gases and some other substitutes under consideration vs. SF_6. Dry air was also tested in the last 2 decades and successfully used for medium voltages such as 12 kV/24 kV; ring network cabinet uses dry air or N_2 [30, 31], but its dielectric strength is also too low that it requires high pressure. Pure CF_3I has higher dielectric strength as compared to SF_6, almost 1.2 times of SF_6 in comparison with other gases that are depicted in Table I.

CF_3I/N_2 or CF_3I/air mixtures having 60% of CF_3I exhibit almost the same *v–t* characteristics as that of SF_6 under same pressure [32]. Breakdown test was conducted for the mixture (CF_3I/CO_2) with a ratio of 30%/70% which exhibits dielectric strength almost 0.8 times of that of SF_6 [33, 34].

Recently, studies have been conducted for the mixture of CF_3I/N_2 [35, 36]. In non-uniform AC field configuration with plate–needle, the result showed that the CF_3I/N_2 mixture with a ratio of 30%/70% has dielectric strength 0.9 times of that of SF_6 up to distance of 5 mm at 0.3 MPa, which is even better than pure CF_3I in non-uniform field, exhibiting positive synergistic effect [33]. Lightning impulse test was carried out to investigate the withstand voltage performance under lightening impulse for 252 kV gas-insulated transmission lines [33], and it was found that CF_3I/N_2 mixture with ratio of 20%/80% exhibits withstand performance 0.9 times of that of SF_6/N2 of same ratio and 77% of pure SF_6 pure.

Gas-insulated switchgear (GIS) 145 kV was tested for withstand voltage with air and C_6F-ketone, and the result was almost the same as the dielectric strength of SF_6. For this, GIS has filling pressure of 6 bar, while C_6F-ketone has 0.6 bar with temperature of 35°C below which C_6F-ketone will liquefy [17].

TABLE I.
GWP AND DS OF VARIOUS SUBSTITUTES IN COMPARISON WITH SF_6. [9,15,18,42-40,48,62,73,74-77]

Gas Formula	GWP	Dielectric Strength (p.u)	Ionization Potential (eV)	Boiling Point (°C at 0.1 MPa)
SF_6	~23 000	1	15.32	−63
Air	0	0.43–0.5	–	−194
CO_2	1	0.45	13.78	−79
N_2	0	0.4		−196
CF_3I	~0.5	1.21	10.28	−22.5
C_6-PFK	1	>2	–	49
C_5-PFK	1	~2	11.03	27
C_3F_8	8800	0.9	13.38	−37
C_2F_6	12 200	0.76	13.6	−78.1
R_{12}	2400	0.9	–	−29.8
R_{34}	1300	0.85	–	−27
C_4F_7N	~2100	2.2	11.88	−4.7

Mixture R_{12} with N_2 in ratio of 80%/20% shows almost 90% higher dielectric strength than that of SF_6 gas at 50 lb/in^2 under AC voltage, while R_{134} with N_2 in 80%/20% ratio shows 85% higher strength than that of SF_6 [19, 20]. It was also found that further addition of R_{134} and R_{12} does not bring a rapid increase in breakdown voltage due to low energy electron attachment [19, 20]. Synergistic effect was found positive for more than 70% content of dichlorodifluoromethane with pressure at least 25 lb/in^2 [19].

Dielectric strength of heptafloroisobutyronitrile (C_4F_7N) is almost twice of SF_6 at atmospheric pressure [17, 37], as shown in Table I, but its liquefaction temperature being high enforced researcher to use it with mixture. Literature shows that CO_2 was found to be the best one to mix [17, 37-42]. Mixture of (C_4F_7N) with CO_2 is termed as green gas (g^3). Depending on minimum operating temperature and maximum filling pressure, g^3 and (C_4F_7N) mixing ratio may vary, like 4%, 6%, 10%, or 20% of volume. It was found that GWP of the (C_4F_7N/CO_2) mixture in 4%/96% ratio was only 378, around 1.6% of SF_6 [38]. The power frequency dielectric strength of (C_4F_7N/CO_2) mixture with mixing ratio of 18%/20% volume of (C_4F_7N) content is almost equivalent to SF_6 [37, 40]. Fig. 5 explains dielectric strength variation with varying mixing ratio. Lightening impulse test shows that dielectric characteristics at 0.88 MPa and 1.04 MPa are similar to SF_6 at 0.55 MPa and 0.65 MPa [37, 40], respectively. In a uniform field with plane–plane electrode configuration, dielectric strength for (C_4F_7N/CO_2) with a mixing ratio of 15%/85% was found to be 85.29 kV/mm under 0.1 MPa pressure, which is very near to SF_6, with 86.30 kV/mm for identical pressure [42]. And when contents of (C_4F_7N) were increased to 20%, the mixture exhibited a dieclectric strength of 90.25 kV/mm higher than SF_6 [42]. So, (C_4F_7N) with CO_2 is a very promising substitute to replace SF_6 in terms of dielectric strength.

C. Arc Quenching

Dry air and CO_2 have shown auspicious characteristics as far as arc-quenching mechanism is considered. It has been experimented that

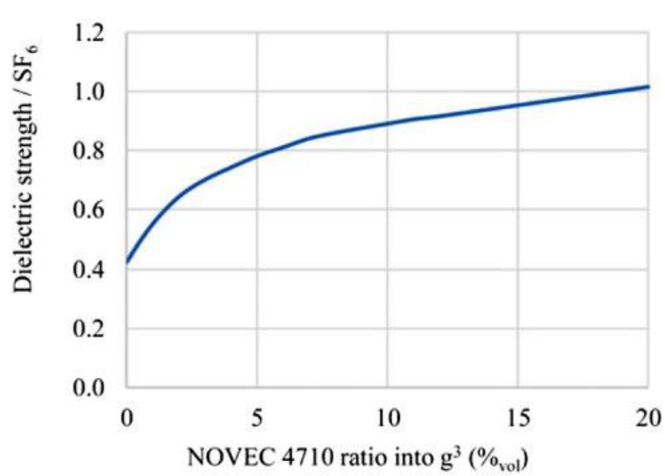

Fig. 5. Comparison of dielectric strength of SF_6 vs. C_4F_7N/CO_2 with different mixing ratio [41].

an increase in pressure from 0.2 MPa to 0.6 MPa increases power loss from 0.32 kW to 0.78 kW for CO_2 as arc-quenching medium, and time constant decreases from 1.3 µs to 0.7 µs with a max value of 1.1 kA [43]. Thermal interruptions of CO_2, SF_6, and some other gases have also been experimented [44-47], to find a comparison of post arc capabilities. Some of the results are depicted in Table II, and characteristic curves have been represented in Fig. 6.

As far as the mixture of gases is concerned, SF_6/N_2 has attracted much attention due to its synergistic effect in dielectric strength and arc interruption. It was also found that a better rate of rise of recovery voltage (RRRV) can be obtained if appropriate ratio of N_2 is mixed with SF_6 [48]. Mixture containing 31% of N_2 and 69% SF_6 exhibited much improved RRRV as compared to SF_6 only [49]. Puffer type gas circuit breaker was experimented with mixture of 0.2 MPa-N_2/0.3 MPa-SF_6 and got 0.76 times more d*i*/d*t* than that of pure SF_6 [49]. Critical RRRV and d*i*/d*t* were very much improved by increasing SF_6 contents in the mixture of SF_6/CO_2 [50]. For 126 kV puffer type gas circuit breaker, if SF_6 concentration is increased from 0%, 20%, and 50%, then RRRV before current zero improves from 39%, 45%, and 70%, respectively [51].

The arc extinguishing capability of pure CF_3I is around 90% of that of SF_6, but pure CF_3I has a bit higher boiling point as compared to SF_6 and cannot be used in extremely cold regions [52]. Again, the mixture with natural gases showed improved boiling point as well as arc extinguishing capability [52]. For mixtures of (CF_3I/N_2), (CF_3I/CO_2), and CF_3I/air, transport coefficient and thermodynamic properties were also investigated, and the result showed that around 30% content of CF_3I may be used as a possible substitute [53].

C_5-PFK, C_6-PFK, and mixture were analyzed for arc quenching and insulating properties by ASEA Brown Boveri (ABB) is a Limited Company (Multinational Corporation) and encouraging results were found [54-57]. C_5-PFK with N_2 and O_2 for medium voltage and C_5-PFK with CO_2 and O_2 for HV GIS were recommended. HV GIS with rating

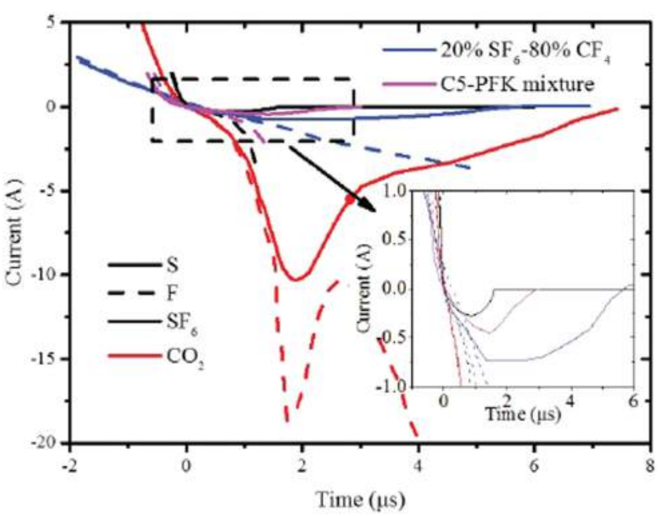

Fig. 6. Comparison of post arc current of CO_2, SF_6, and mixture 20%SF_6–80% CH_4 (S: Success , F: Failure) , [46-48].

170 kV/31.5 kA and medium-voltage switchgear 22 kV/1600 A for feeders and 22 kV/2000 A for bus bars have been installed and operating satisfactorily in Germany and Switzerland since 2015 [52, 57]. Post arc current measurement was carried out with a self-blast live tanker breaker and found that peak/maximum value of post arc current is very near to SF_6. Table II summarizes the post arc current peak values and duration of different gases.

Typically, Vermeer's constant is used to comprehend heat dissipation capability, and to do so, temperature rise test was conducted on 420 kV bus bar keeping pressure as 5.5 bar and operating temperature as -25°C. The constant for heptafluoroisobutyronitrile was determined to be 13.8, higher than SF_6, while the constant for green gas, mixture of heptafluoroisobutyronitrile and carbon dioxide (C_4F_7N/CO_2), was little lower than that of pure SF_6 but still better than CO_2 [17].

D. Partial Discharge and Flashover

Natural gases when mixed with other gases improve partial discharge characteristics, for example, partial discharge properties were found better for mixture (CF_3I/CO_2) than (SF_6/CO_2), but it demands a higher ratio. To get exceeded level than SF_6, the weightage of CF_3I in CO_2 must be 30%/40% [4, 58]. It was also found that inception voltage (+) is better for (CF_3I/CO_2) than that of (CF_3I/N_2) [59], and so, it was concluded that the synergistic effect in terms of inception voltage is higher for CO_2 as compared to N_2.

Unlike other gases, C_5-PFK decomposition process is irreversible during arc, discharge, or thermal decomposition. Partial discharge test on C_5-PFK was performed [60], and it was found that decomposed products do not recombine to their original structure, and some of the by-products were also toxic.

Partial discharge (PD) test has also been carried out on mixture C_4F_7N/CO_2 in 4%/96% ratio, and it was found that inception voltage is around 0.76–0.84 of SF_6 with longer rising time and pulse width PD pulses [61]. So from PD viewpoint, it requires higher pressure or increased content of C_4F_7N (3M™ Novec™ 4710 dielectric fluid) to meet the requirement of SF_6; however, those studies are not available yet. Recently some research has been carried out to present model for discharge process. Discharge of flowing gases includes three basic phases : a) deflection of the main discharge path, b) blowing away of some electrons, and c) decrease in gas density [63]. This modeling will enable the researcher to calculate breakdown voltage.

Solid material–gas interaction is another important factor to be discussed especially for usage in GIS as linked insulation fails at

TABLE II.
POST ARC PEAK CURRENT AND DURATION [46-48]

Gases	Post Arc Current Peak (A)	Duration (µs)
SF_6	0.272	1.59
C_5F-PFK mixture	0.457	2.94
SF_6/CH_4–20%/80%	0.742	5.81
CO_2	10.3	7.42

lower voltage due to flashover in solid material. Pure N_2, CO_2, and air exhibit very lower flashover characteristics as compared to SF_6; however, the trend is much similar. And adding SF_6 to natural gases improves their flashover voltages [64], as shown in Fig. 7.

Flashover characteristics were found better for (CF_3I/N_2) for 30%/70% ratio than that of (SF_6/N_2) for 20%/80% [65] under AC and impulse voltage both, though it had slightly lower dielectric strength. Study of surface flashover for (C_4F_7N/CO_2) has been carried out [66], with epoxy insulator, and it was found that (C_4F_7N/CO_2) with ratio 13%/87% exhibits almost 0.8 times of SF_6 flashover voltage and that further increase in the content of (C_4F_7N) can lead to saturation of surface flashover [66].

III. DISCUSSION

There are also some other necessary aspects to be discussed such as boiling point, decomposed by-products, and toxicity. SF_6 has boiling point (−64°C), though it is sufficient for most of the applications but still high as compared to natural gases such as N_2 (−196°C), air (−194°C), and CO_2 (−79°C). [15]. Compressed air, CO_2, and N_2 have been successfully implied up to 145 kV switching devices as insulating medium [67], but to use natural gases, more volume or high pressure is required to meet the required electrical dielectric strength which leads to a significant increase in size and cost, undesirable for design consideration. That is why natural gases are preferred for mixture as buffer gases to reduce overall boiling point.

Boiling point of some gases is depicted in Table I, which shows that fluoroketones have very high boiling point, limiting their usage in icy/snowy zones. C_6-PFK has boiling point of 49°C and C_5-PFK has 27°C, which means it liquefies under standard conditions. However, it can be used with a mixture of N_2 or air. GIS 145 kV was tested for withstand voltage with air and C-PFK, and results were encouraging [17, 18], but the decomposition process is irreversible during arc, discharge, or thermal decomposition for C_5-PFK [68, 69] and also for

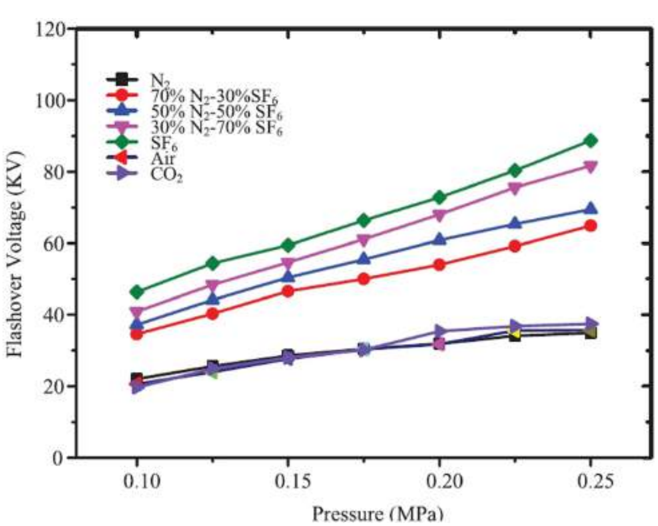

Fig. 7. Flashover comparison of different gases [66].

($C_6F_{12}O/CO_2$) mixture [70], so properties will differ prior and post arc state which limits its usage in GCB.

CF_3I despite its good insulating properties has a higher boiling point of about −22.5°C, which means this gas cannot be used alone and hence mixing with natural gases is recommended. There is another issue associated with CF_3I, that is, its by-products such as C_2F_6, C_3F_6, C_3F_8, CHF_3, and C_2F_5I are toxic [71-73]. Gas itself is categorized as carcinogenic and mutagenic that will be risky to be utilized, due to health hazard issues.

Dichlorodifluoromethane (R_{12}) and tetrafluoroethane (R_{134}) also have higher boiling point at atmospheric pressure, such as −29.8°C and −26.3°C, respectively [19, 20]. This was similar with that of CF_3I and hence mixing with natural gases is recommended. However, the mixture will have its own limits because of the lower dielectric strength of natural gases. Issue with R_{12} is that it contains chlorine that causes ozone depletion [19]. R_{134} has an issue of self-recoverability as AC power frequency breakdown tests show that after tenth shot, breakdown voltage comes down very quickly because of carbon deposit formation on the electrode [20].

(C_4F_7N) has very high boiling point of about −4.7°C [17, 41], and its by-products during decomposition process are C_3F_7, C_3F, CN, CNF, CF, CF_2, CF_3, CFCN, F, free radicals, and CF_4 [74]. Some free radicals recombine to produce C_2F_6, C_3F_8, CF_3CN, CO, and CF_4, some of which are low toxic compounds. However, the addition of CO_2 lowers its boiling point, and less decomposed products are generated [75]. In pure (C_4F_7N) at 2400 K, products were about 96%, while these were reduced to 58% in (C_4F_7N/CO_2) mixture [75].CF_4 and C were very much reduced and precipitate carbon formation was avoided, so green gas (C_4F_7N/CO_2) is a better option than pure (C_4F_7N). Another mixture of ($C_4F_7N/N_2/O_2$) has also been tested, and less solid precipitate was produced with much better dielectric performance [76, 77]. However, toxicity assessment of (C_4F_7N) and its by-products recommends taking measures for eye safety and respiration [78].

IV. CONCLUSION

From the discussion, it is obvious to conclude that natural gases are classified as an excellent choice for mixture component to reduce boiling point, attain lower GWP and better arc-quenching capabilities (especially CO_2 in terms of arc quenching). Trifluoroiodomethane despite considerable dielectric strength and decent arc-quenching capabilities with a mixture of natural gases will be risky to be utilized, due to health hazard issues as being carcinogenic and mutagenic gas. Dichlorodifluoromethane (R_{12}) and tetrafluoroethane (R_{134}) suffer the problem of ozone depletion and self-recoverability issues, respectively. Perfluoroketones, especially C_5-PFK, has a good potential for replacement, but irreversible decomposition process and high liquefaction temperature are still hindrance in complete replacement. Thus, heptafluoroisobutyronitrile (C_4F_7CN) is the one that has upright potential to replace SF_6 as it has wonderful dielectric strength and moderate global warming potential. Adding CO_2 enables to get much lower GWP level, lower liquefaction point, better arc-quenching ability, and much reduced decomposed products are obtained. So green gas, as labeled to mixture (C_4F_7CN/CO_2), is declared to be the best replacement for SF_6 at the time.

V. FUTURE WORKS

Though (C_4F_7CN) has shown a remarkable potential to replace SF_6, it is at the initial stages of research, and much deep study is still required to replace it completely. Studies for compatibility with other materials have been started to investigate, but very few studies have been conducted for streamer radii and leader propagation. Basic physical properties, electron transport coefficients, and radiation properties of relatively new gases must also be investigated. Much study is needed to find an optimum compromise among insulation performance, environmental concerns, health issues, safety concerns, and liquefaction temperature.

Peer Review: Externally peer reviewed.

Conflict of Interest: The authors have no conflict of interest to declare.

Financial Disclosure: The authors declared that this study has received no financial support.

REFERENCES

1. D. Koch, "SF6 properties, and use in MV and HV switchgear [Technical Report No. IEC 1634]," *Cahier Technique Schneider Electric*, no. 188, pp. 23, 2003.
2. L. G. L. Christophorou and R. J. Brunt, "SF_6/N_2 mixtures basic and HV insulation properties," *IEEE Trans. Dielectr. Electr. Insul.*, vol. 2, 1995.
3. B. Belmadani, J. Casanovas, and A. M. Casanovas, "SF_6 decomposition under power arcs chemical aspects, " *IEEE Trans. Electr. Insul.*, vol. 26, no. 6, 1991.
4. X. Zhang, S. Xiao, J. Zhou, and J. Tang, "Experimental analysis of the feasibility of CF_3I/CO_2 substituting SF_6 as insulation medium using needle-plate electrodes," *IEEE Trans. Dielect. Electr. Insul.*, vol. 21, no. 4, pp. 1895–1900, 2014. [CrossRef]
5. United Nations, *Kyoto Protocol to the United Nations Framework Convention on Climate Change*. Italy: United Nations, 1998.
6. T. Takuma, "Gas insulation and greenhouse effect," *J. Inst. Electr. Eng.*, Japan, vol. 119, no. 4, pp. 232–235, 1999. [CrossRef]
7. L. G. Christophorou, J. K. Olthoff, and R. J. Van Brunt, "Sulfur hexafluoride and the electric power industry, " *IEEE Electr. Insul. Mag.*, vol. 13, no. 5, pp. 20–24, 1997. [CrossRef]
8. J. Rogelj *et al.*, "Paris Agreement climate proposals need a boost to keep warming well below 2°C," *Nature*, vol. 534, no. 7609, 631–639, 2016. [CrossRef]
9. C. Preve, D. Piccoz, and R. Maladen, "Validation method and comparison of SF6 alternative gases," in *CIGRE*, Paris, France, 2016, pp. D1–205.
10. X. Fang *et al.*, "Sulfur hexafluoride (SF_6) emission estimates for China: An inventory for 1990–2010 and a projection to 2020," *Environ. Sci. Technol.*, vol. 47, no. 8, pp. 3848–3855, 2013. [CrossRef]
11. Ph. Widger and A. M. Haddad, "Evaluation of SF_6 leakage from gas insulated equipment on electricity networks in Great Britain," *Energies*, vol. 11, no. 8, p. 2037, 2018. [CrossRef]
12. B. Pan, G. Wang, H. Shi, J. Shen, H. K. Ji, and G. S. Kil, "Green gas for grid as an eco-friendly alternative insulation gas to SF_6: A review," *Appl. Sci.*, vol. 10, no. 7, p. 2526, 2020. [CrossRef]
13. Y. Wang, D. Huang, J. Liu,Y. Zhang, and L. Zeng, "Alternative environmentally friendly insulating gases for SF_6," *Processes*, vol. 7, no. 4, p. 216, 2019. [CrossRef]
14. M. Rabie and C. M. Franck, "Assessment of eco-friendly gases for electrical insulation to replace the most potent industrial greenhouse gas SF_6," *Environ. Sci. Technol.*, vol. 52, no. 2, pp. 369–380, 2018. [CrossRef]
15. T. Rokunohe, Y. Yagihashi, F. Endo, and T. Oomori, "Fundamental insulation characteristics of air; N_2, CO_2, N_2/O_2,and SF_6/N_2 mixed gases," *Electr. Eng. Jpn*, vol. 155, no. 3, pp. 9–17, 2006. [CrossRef]
16. W. C. McCain and J. Macko, "Toxicity review for Iodotrifluoromethane (CF_3I)," in *Halon Options Tech. Work. Conf.*, 1999, pp. 242–253.
17. Y. Kieffel, T. Irwin, P. Ponchon, and J. Owens , "Green gas to replace SF_6 in electrical grids," *IEEE Power Energy Magazine*, vol. 14, no. 2, pp. 32–39, 2016. [CrossRef]
18. P. Simka and N. Ranjan, "Dielectric strength of C_5 perfluoroketone," in *19th Int. Symp. High Volt. Eng.*, Czech Republic, 2015.
19. R. Ullah, A. Rashid, F. Khan, and A. Ali, "Dielectric characteristic of dichlorodifluoromethane (R12) gas and mixture with N2/air as an alternative to SF6 gas," *Institution of Engineering and Technology (IET)*, vol. 2, no. 3, pp. 205–210, 2017.
20. R. Ullah, Z. Ullah, A. Haider, S. Amin, and F. Khan, "Dielectric properties of tetrafluoroethane (R134) gas and its mixtures with N_2 and air as a sustainable alternative to SF_6 in high voltage applications," *Electr. Power Syst. Res.*, vol. 163, 532–537, 2018. [CrossRef]
21. A. B. Murphy, "Transport coefficients of air, argon-air, nitrogen-air, and oxygen-air plasmas," *Plasma Chem. Plasma Process.*, vol. 15, no. 2, pp. 279–307, 1995. [CrossRef]
22. A. Gleizes, M. Razafinimanana, and S. Vacquie, "Calculation of thermodynamic properties and transport coefficients for SF_6-N_2 mixtures in the temperature range 1,000–30,000 K," *Plasma Chem. Plasma Process.*, vol. 6, no. 1, pp. 65–78, 1986. [CrossRef]
23. M.Rong *et al.*, "Thermophysical properties of SF_6–Cu mixtures at temperatures of 300–30 000 K and pressures of 0.01–1.0 MPa: Part 1. Equilibrium compositions and thermodynamic properties considering condensed phases," *J. Phys. D: Appl. Phys.*, vol. 47, no. 49, 2014. [CrossRef]
24. A. Yang *et al.*, "Thermodynamic properties and transport coefficients of CO_2–Cu thermal plasmas," *Plasma Chem. Plasma Process.*, vol. 36, no. 4, pp. 1141–1160, 2016. [CrossRef]
25. X. Guo, X. Li, A. B. Murphy, and H. Zhao, "Calculation of thermodynamic properties and transport coefficients of CO_2–O_2–Cu mixtures," *J. Phys. D*, vol. 50, no. 34, p. 5203, 2017.
26. A. Yang *et al.*, "Thermodynamic properties and transport coefficients of high-temperature CO_2 thermal plasmas mixed with C_2F_4," *J. Phys. D: Appl. Phys.*, vol.48, no. 49, 2015. [CrossRef]
27. C. Jan , Y. Cressault ,A. Gleizes, and K. Bousoltane , "Calculation of radiative properties of SF_6–C_2F_4 thermal plasmas—Application to radiative transfer in high-voltage circuit breakers modeling, " *J. Phys. D* , vol. 47, no. 1, p. 5204, 2013.
28. Y. Qiu and E. Kuffel, "Dielectric strength of gas mixtures comprising SF_6, CO_2, c-C_4-F_8 and SF_6, N_2, c-C_4F_8," *IEEE Trans. Power Apparatus Syst.*, vol. 5, pp. 1445–1451, 1983.
29. L. Niemeyer, *A Systematic Search for Insulation Gases and Their Environmental Evaluation*. Berlin: Springer, 1998.
30. D. Y. Lin and S. Bae, "Study on oxygen/nitrogen gas mixtures for the surface insulation performance in gas insulated switchgear," *IEEE Trans. Dielect. Electr. Insul.*, vol. 22, no. 3, pp. 1567–1576, 2015. [CrossRef]
31. N. S. Stoa-Aanensen , M. Runde, E. Jonsson, and A. D. Teigset, "Empirical relationships between air-load break switch parameters and interrupting performance," *IEEE Trans. Power Deliv.*, vol. 31, no. 1, pp. 278–285, 2016. [CrossRef]
32. H. Toyota, S. Matsuoka, and K. Hidaka, "Measurement of sparkover voltage and time lag characteristics in CF_3I-N_2 and CF_3I-air gas mixtures by using steep-front square voltage," *IEEE Trans. Fundam. Mater.*, Japan, vol. 125, pp. 409–414, 2005.
33. H. Katagiri, H. Kasuya, H. Mizoguchi, and S. Yanabu, "Investigation of the performance of CF_3I gas as a possible substitute for SF_6," *IEEE Trans. Dielect. Electr. Insul.*, vol. 15, no. 5, pp. 1424–1429, 2008. [CrossRef]

34. L. Chen, P. Widger, M. S. Kamarudin, H.Griffiths, and A. Haddad, “CF3I gas mixtures: Breakdown characteristics and potential for electrical insulation,” *IEEE Trans. Power Del.*, vol. 32, no. 2, pp. 1089–1097, 2017. [CrossRef]
35. S. Xiao, X. Zhang, Y. Han, and Q. Dai, “AC breakdown characteristics of CF_3I/N_2 in a non-uniform electric field,” *IEEE Trans. Dielect. Electr. Insul.*, vol. 23, no. 5, pp. 2649–2656, 2016. [CrossRef]
36. B. Zhou, D. Tan, J. Xue, F. Cai, and D. Xiao, “Lighting impulse withstand performance of CF_3I-N_2 gas mixture for 252 kV GIL insulation,” *IEEE Trans. Dielect. Electr. Insul.*, vol. 26, no. 4, pp. 1190–1196, 2019. [CrossRef]
37. Y. Kieffel, F. Biquez, and P. Ponchon, “Alternative gas to SF_6 for use in high voltage switchgears: g3,” in *Proc. Int. Conf. Electr. Dist.*, France, 2015, pp. 1–5.
38. H. E. Nechmi, A.Beroul, A.Girodet, and P.Vinson, “Fluoronitrile/CO_2 mixture as promising substitute to SF_6 for insulation in high voltage application,” *IEEE Trans. Dielect. Electr. Insul.*, vol. 23, no. 5, pp. 2587–2593, 2016. [CrossRef]
39. K. Pohlink, Y. Kieffel, J. Owens, and F. Meyer, “Characteristics of fluoronitrile/CO2 mixture-an alternative to SF6,” in *CIGRE*, Paris, France, 2016, pp. D1–204.
40. Y. Kieffel *et al.*, “Characteristics of g3—An alternative to SF_6,”*Proc. Int. Conf. Exhibit. Elect. Dist.*, Glasgow, UK, vol. 2017, no. 1, pp. 54–57, 2017. [CrossRef]
41. X. Mengyuan, Y. Jing, L. Zhiyuan, G. Yingsan, and X. W. Zhen, “Simulation of the decomposition pathways and products of perfluoronitrile C_4F_7N (3M:Novec 4710),” in *4th Int. Conf. Electr. Power Equip. - Switching Tech. (ICEPEST)*, 2017, pp. 310–313.
42. B. Zhang, N. Uzelac, and Y. Cao, “Fluoronitrile/CO_2 mixture as an eco-friendly alternative to SF_6 for medium voltage switchgears,” *IEEE Trans. Dielect. Electr. Insul.*, vol. 25, no. 4, pp. 1340–1350, 2018. [CrossRef]
43. T. Matsumura, I. Morooka, Y. Yokomizu, and M. Suzuki, “Arc parameters in CO_2-blast quenching chamber with high-pressure storage tank of different pressures,” *Vacuum*, vol. 80, no. 11–12, pp. 1305–1310, 2006. [CrossRef]
44. T. Uchii, A. Majima, T. Koshizuka, and H. Kawano, “Thermal interruption capabilities of CO_2 gas and CO_2- based gas mixtures,” in *Int. Conf. Gas Disch. Appl. (GD)*, Germany, 2010, p. 78.
45. S. Nishiwaki, T. Koshizuka, T. Uchii, and H.Kawano, “Discussions on post arc current of a CO_2 circuit breaker,” in *Int. Conf. Gas Disch. Appl. (GD)*, Germany, 2010, p. 125.
46. K. Zhu, J. Zhong, L. I. Xingwen, X. Jiang, H. Zhao, and S. Jia, “Experimental study of SF6 and its gas mixtures with CF4 for a high voltage gas circuit breaker,” in *IS-EMD*, China, 2013, pp. 67–70.
47. J. Mantila, M. Claessens, and M. Kriegel, “Environmentally friendly perfloroketones-based mixture as switching medium in high voltage circuit breakers,” in *Conseil International des Grands Réseaux Electriques (CIGRE)*, Palais de Congres, August 21-26, 2016 Paris, France, 2016.
48. D. M. Grant ,J. F. Perkins ,L. C. Campbell, O. E. Ibrahim, and O. Farish, “Comparative interruption studies of gas blasted arcs in SF_6/N_2 and SF_6/He mixtures,” in *Int. Conf. Gas Disch. Appl.*, United Kingdom, 1976, p. 48.
49. Y. N. M. Tsukushi, K. Hirasawa, and Y. Yoshioka, “Application of theoretical calculation for puffer pressure rise of gas mixtures in puffer type blast circuit breakers,” in *4th Int. Symp. Switch. Arc Phenomena*, Poland, 1981, p. 198.
50. W. Song, D. Yang, Y. Chung, D. Kim, and H. Koh, “A study of large current interrupting capability of SF_6/N_2 mixtures,” in *Conference Record IEEE Int. Symp. Electr. Insul.*, USA, 2002, p. 457.
51. H. Zhao, X. Li, K. Zhu, Q. Wang, H. Lin, and X. Guo, “Study of the arc interruption performance of SF_6-CO_2 mixtures as a substitute for SF_6,” *IEEE Trans. Dielect. Electr. Insul.*, vol. 23, no. 5, pp. 2657–2667, 2016. [CrossRef]
52. M. Taki, D. Maekawa, H. Odaka, H. Mizoguchi, and S. Yanabu, “Interruption capability of CF_3I gas as a substitution candidate for SF_6 gas,” in *IEEE Trans. Dielect. Electr. Insul.*, vol. 14, no.2, pp. 341–346, 2007. [CrossRef]
53. Y. Cressault, V. Connord, H. Hingana, P. Teulet, and A. Gleizes, “Transport properties of CF_3I thermal plasmas mixed with CO_2, air or N_2 as an alternative to SF_6 plasmas in high-voltage circuit breakers,” *J. Phys. D: Appl. Phys.*, vol. 44, no. 49, p. 495202, 2011. [CrossRef]
54. X. Li, X. Guo, A. B. Murphy, H. Zhao, J. Wu, and Z. Guo, “Calculation of thermodynamic properties and transport coefficients of C5F10O-CO2 thermal plasmas,” *J. Appl. Phys.*, vol. 122, no. 14, p. 3302, 2017. [CrossRef]
55. M. Hyrenbach, T. Hintzen, P. Müller, and J. Owens, “Alternative gas insulation in medium-voltage switchgear.” in *23rd Int. Conf. on Electr. Distrib.*, Lyon, 2015, p. 587.
56. M. Saxegaard, M. Kristoffersen, M. Hyrenbach, M. Seeger, P. Stoller, and H. Landsverk, “Dielectric properties of gases suitable for secondary medium voltage switchgear,” in *23rd Int. Conf. Electr. Distrib.*, 2015, p. 926.
57. D. Tehlar, T. Diggelmann, P. Müller, R. Buehler, N. Ranjan, and C. Doiron, “Ketone based alternative insulation medium in a 170 kV pilot installation,” Cigre Colloquium, Japan, 2015.
58. X . Zhang, S. Xiao, Y. Han, and Q. Dai, “Analysis of the feasibility of CF_3I/CO_2 used in C-GIS by partial discharge inception voltages in positive half cycle and breakdown voltages,” *IEEE Trans. Dielectr. Electr. Insul.*, vol. 22, no. 6, p. 3234–3243, 2015. [CrossRef]
59. X. Zhang, J. Zhou, and J. Tang, “Experimental study on insulation characteristics of CF_3I/CO_2 and CF_3I/N_2 mixed gas partial discharge,”*Chin. J. Electr. Eng.*, 2014. [CrossRef]
60. P. Simkka, C. B. Doiron, S. Scheel, and A. Di-Gianni, “Decomposition of alternative gaseous insulation under partial discharge,” in *20th Int. Symp. High Volt. Eng.*, Argentina, 2017, p. 534.
61. G. Wang, W. H. Kim, G. S. Kil, S. W. Kim, and J. R. Jung, “Green gas for a grid as an eco-friendly alternative insulation gas to SF_6: From the perspective of partial discharge under AC,” *Appl. Sci.*, vol. 9, no. 4, 2019. [CrossRef]
62. G. John and P. E. Owens, “Greenhouse gas emission reductions in power equipment through use of a sustainable alternative to SF_6,” *IEEE/PES Trans. Distrib. Conf. Exposit. (T&D)*, USA, 2018.
63. Y. Kang *et al.*, “Modeling of flowing gas discharge – Part I,” *IEEE Trans. Dielectr. Electr. Insul.*, vol. 26, no. 4, pp. 1048–1055, 2019. [CrossRef]
64. C. Wang, *Research on Surface Flashover Characteristics of Insulators in SF_6 Gas Mixtures Between 0.1MPa and 0.25MPa*. Beijing: North China Electric Power University, 2012.
65. S. Zhao, D. Xiao, H. Zhang, and Y. Deng, “Discharge characteristics of CF_3I/N_2 mixtures under lightning impulse and alternating voltage,” *IEEE Trans. Dielectr. Electr. Insul.*, vol. 24, no. 5, pp. 2731–2737, 2017. [CrossRef]
66. Z. Li *et al.*, “Surface flashover characteristics of epoxy insulator in C_4F_7N/CO_2 mixtures in a uniform field under AC voltage,” *IEEE Trans. Dielect. Electr. Insul.*, vol. 26, no. 4, pp. 1065–1072, 2019. [CrossRef]
67. S. Okabe *et al.*, “Fundamental insulation characteristic of high-pressure CO2 gas under actual equipment conditions,” *IEEE Trans. Dielect. Electr. Insul.*, vol. 14, pp. 83–90, 2007.
68. L. Zhong *et al.*, “Compositions, thermodynamic properties, and transport coefficients of high-temperature $C_5F_{10}O$ mixed with CO_2 and O_2 as substitutes for SF_6 to reduce global warming potential,” *AIP Adv.*, vol. 7, no. 7, p. 75003, 2017. [CrossRef]
69. X. Zhang *et al.*, “Study on the discharge characteristics of an environmental-friendly insulating medium $C_5F_{10}O$,” *Proc. CSEE*, 2018.
70. Y. Li, X. Zhang, S. Tian, S. Xiao, Y. Li, and D. Chen, “Insight into the decomposition mechanism of $C_6F_{12}O$-CO_2 gas mixture,” *Chem. Eng. J.*, vol. 360, pp. 929–940, 2019. [CrossRef]

71. K. M. J. Mohamad, O. Shinya, and H. Masayuki, “Gas by-products of CF_3I under AC partial discharge,” *J. Electrostat.*, vol. 69, no. 6, pp. 611–617, 2011.
72. X. Li, H. Zhao, J.Wu, and S. Jia, “Analysis of the insulation characteristics of CF_3I mixtures with CF_4, CO_2, N_2, O_2 and air,” *J. Phys. D: Appl. Phy.*, 2013.
73. S. Zhao *et al.*, “Experimental study on the decomposition products of CF_3I/N_2 gas mixtures,” in *IEEE Electr. Insul. Conf. (EIC)*, USA, 2018.
74. X. Zhang *et al.*, “Reactive molecular dynamics study of the decomposition mechanism of the environmentally friendly insulating medium C_3F_7CN,” *RSC Adv.*, vol. 7, no. 80, pp. 50663–50671, 2017. [CrossRef]
75. X. Zhang, Q. Chen, Y. Li,S. Xiao, J. Zhang, and C. Liu, “Decomposition mechanism of environmental-friendly insulating medium C_3F_7CN/CO_2,” *Process CSEE*, pp. 7174–7182, 2018.
76. Y.Li *et al.*, “Influence of oxygen on dielectric and decomposition properties of C_4F_7N-N_2-O_2 mixture, ”, *IEEE Trans. Dielect. Electr. Insul.*, vol. 26, no. 4, pp. 1279–1286, 2019. [CrossRef]
77. Y. Li *et al.*, “Thermal decomposition properties of fluoronitriles-N_2 gas mixture as alternative gas for SF_6,” *J. Fluor. Chem.*, vol. 229, no. 109434, 2020. [CrossRef]
78. Y. Li *et al.*, “Assessment on toxicity and application risk of C_4F_7N: A new SF_6 alternative gas,” *J. Hazard. Mater.*, vol. 368, pp. 653–660, 2019.